PHOTOCATALYTIC DEGRADATION OF DIMETHYL PHTHALATE AND LOW-DENSITY POLYETHYLENE FILM OVER DUAL Z-SCHEME ZINC OXIDE/BISMUTH TUNGSTATE/SPINEL FERRITE COMPOSITES UNDER SUNLIGHT IRRADIATION

By

CHIN YING HUI

A thesis submitted to the Department of Petrochemical Engineering,

Faculty of Engineering and Green Technology,

Universiti Tunku Abdul Rahman,

in partially fulfilment of the requirements for the degree of

Doctor of Philosophy (Engineering).

DECEMBER 2023

ABSTRACT

PHOTOCATALYTIC DEGRADATION OF DIMETHYL PHTHALATE AND LOW-DENSITY POLYETHYLENE FILM OVER DUAL Z-SCHEME ZINC OXIDE/BISMUTH TUNGSTATE/SPINEL FERRITE COMPOSITES UNDER SUNLIGHT IRRADIATION

Chin Ying Hui

Dimethyl phthalate (DMP) is commonly employed as a plasticizer in plastic packaging, cosmetic products and automotive spare parts. Due to high demand for plastic products and its mobility, DMP has become widespread in the environment, posing health risks to humans and negative impacts on the environment as an endocrine disruptor with carcinogenic, teratogenic and mutagenic properties. Therefore, this study aims to develop an effective approach to mitigate the negative impacts caused by DMP. Photocatalysis has received numerous attentions owe to its promising performance in degrading organic pollutants in wastewater has been selected as the primary treatment method. In this study, Brassica Oleracea-like SF20BWZ, (SF= $SrFe_2O_4$, $BaFe_2O_4$ and $CaFe_2O_4$) composites were synthesized using a hydrothermal-precipitation method. The performance of as-synthesized photocatalysts were evaluated over photodegradation of DMP and LDPE film under sunlight irradiation. The XRD results showed that the ZnO and Bi_2WO_6 revealed wurtzite hexagonal structure and orthorhombic structure, respectively. The existence of SF characteristic peaks in XRD spectra confirmed the successful construction of SF20BWZ composites. The FTIR analysis further confirmed the presence of ZnO, Bi_2WO_6 and SF in SF20BWZ composites via their relative stretching bands. The findings from FESEM and EDX analysis demonstrated the ZnO and SF distributed homogeneously on Bi_2WO_6 and

formed Brassica Oleracea-like SF20BWZ composite. TEM analysis also confirmed the successful construction of Sr20BWZ composite through their respective lattice spacing measurement. XPS result demonstrated that Sr20BWZ composite comprised of Zn 2p, Bi 4f, O 1s, W 4f, Sr 3d and Fe 2p. VSM analysis verified the magnetic properties of 10Sr20BWZ composite. Under sunlight irradiation, 10Sr20BWZ composite exhibited the best photocatalytic performance among the as-prepared composites. 10Sr20BWZ can fully degrade the DMP (100% removal) under optimum conditions: catalyst loading = 1g/L and pH =7. The introduction of foreign substances into the system reduced the photodegradation performance. The extraordinary performance of 10Sr20BWZ composite was attributed to excellent electron-hole pair separation efficiency and the lowest charge resistance. This was ratified in TPR and EIS experiments. The active species study revealed that all •OH, h^+, •O_2^- and e^- participated in degradation of DMP while •OH and h^+ played major role in DMP degradation. Based on intermediates study, degradation of DMP underwent continuous radical attack by •OH and •O_2^- to form smaller intermediates and finally degraded to CO_2 and H_2O. This was supported by COD test where the DMP was fully mineralised after 90 min sunlight irradiation. 10Sr20BWZ composite revealed its high stability with photodegradation efficiency maintained over 80.4% after 4 cycles of run. The phytotoxicity test also revealed the toxicity in DMP solution was greatly declined from 66.2% to 16.5% after the photocatalytic treatment. In present study, Langmuir-Hinshelwood (L-H) 1st order was adopted in expressing the kinetic reaction of photodegradation of DMP over 10Sr20BWZ composite. 1.0 g/L of 10Sr20BWZ revealed the highest rate constant among various catalyst

loading with up to 0.023 min^{-1}. Apart from photodegradation of DMP, 10Sr20BWZ also revealed its promising prospects in LDPE film degradation. LDPE film incorporated with 10Sr20BWZ composite exhibited the greatest reduction in weight loss and tensile strength. Noticeable large cavities with ~30μm diameter in FESEM image and the presence of carbonyl group in ATR analysis validated the successful degradation of LDPE film over 10Sr20BWZ composite.

ACKNOWLEDGEMENTS

APPROVAL SHEET

This thesis/dissertation entitled "**PHOTOCATALYTIC DEGRADATION OF DIMETHYL PHTHALATE AND LOW-DENSITY POLYETHYLENE FILM OVER DUAL Z-SCHEME ZINC OXIDE//BISMUTH TUNGSTATE/SPINEL FERRITE COMPOSITES UNDER SUNLIGHT IRRADIATION**" was prepared by CHIN YING HUI and submitted as partial fulfilment of the requirements for the degree of Doctor of Philosophy (Engineering) at Universiti Tunku Abdul Rahman.

Approved by:

_____

(ChM.Ts.Dr. SIN JIN CHUNG)   Date:......19/12/23...........

Supervisor

Department of Petrochemical Engineering

Faculty of Engineering and Green Technology

Universiti Tunku Abdul Rahman

_____

(ChM.Ts. Dr. LAM SZE MUN)   Date:......19/12/23...........

Co-Supervisor

Department of Environmental Engineering

Faculty of Engineering and Green Technology

Universiti Tunku Abdul Rahman

FACULTY OF ENGINEERING AND GREEN TECHNOLOGY

UNIVERSITI TUNKU ABDUL RAHMAN

Date: ___18/12/23___

SUBMISSION OF THESIS

It is hereby certified that **CHIN YING HUI** (ID No: **20AGD00641**) has completed this thesis entitled: "PHOTOCATALYTIC DEGRADATION OF DIMETHYL PHTHALATE AND LOW-DENSITY POLYETHYLENE FILM OVER DUAL Z-SCHEME ZINC OXIDE/BISMUTH TUNGSTATE/SPINEL FERRITE COMPOSITES UNDER SUNLIGHT IRRADIATION" under the supervision of ChM.Ts.Dr. Sin Jin Chung (Supervisor) from the Department of Petrochemical Engineering, Faculty of Engineering and Green Technology, and ChM.Ts.Dr. Lam Sze Mun (Co-Supervisor) from the Department of Environmental Engineering, Faculty of Engineering and Green Technology.

I understand that the University will upload softcopy of my thesis in pdf format into UTAR Institutional Repository, which may be made accessible to UTAR community and public.

Yours truly,

_____
(CHIN YING HUI)

DECLARATION

I, CHIN YING HUI hereby declare that the thesis is based on my original work except for quotations and citations which have been duly acknowledged. I also declare that it has not been previously or concurrently submitted for any other degree at UTAR or other institutions.

(CHIN YING HUI)

Date: 18/12/23

TABLE OF CONTENTS

Page

LIST OF TABLES

LIST OF FIGURES

with SrFe$_2$O$_4$ (g) before sunlight irradiation (h) after sunlight irradiation; LDPE film incorporated with 20BWZ (i) before sunlight irradiation (j) after sunlight irradiation; LDPE film incorporated with 10Sr20BWZ composite (k) before photocatalytic treatment (l) after photocatalytic treatment

LIST OF SYMBOLS

Symbol	Description	Unit
wt%	weight percentage	%
°C	Degree Celsius	-
C_{DMP}	Concentration of DMP at reaction time t	mg/L
C_{DMP_0}	Initial concentration of DMP	mg/L
C	Concentration of pre-treated DMP at constant time interval	mg/L
Cl^-	Chloride	-
$CO_3^{\bullet-}$	Carbonate radical	-
e_{CB}^-	Electrons at conduction band	-
E_g	Band gap energy	eV
h	Hour	-
h_{VB}^+	Positive hole at valence band	-
$h\nu$	Light	-
$HO_2^{\bullet-}$	Hydroperoxyl	-
HCO_3^-	Bicarbonate	-
Hz	Hertz	-
k	Rate constant	mg/L•min
K	Adsorption equilibrium constant	L/mg
lx	Lux	-
M	Molar	mol/L
μM	Micromolar	μmol/L
mA	Milliampere	-
mL	Milliliter	-
μg	Microgram	-

ng	Nanogram	-
NO_3^-	Nitrate	-
•OOH	Hydroperoxyl radicals	-
OH^-	Hydroxide ions	-
•OH	Hydroxyl radicals	-
$O_2^{\bullet-}$	Superoxide anion	-
SO_4^{2-}	Sulfate	-
–r	Rate of reaction	mg/L•min
t	Reaction time	min
V	Voltage	-
W	Watt	-
λ	Wavelength	nm
PM_{10}	Particulate Matter ($\leq 10\mu m$)	-
$PM_{2.5}$	Particulate Matter ($\leq 2.5\mu m$)	-

LIST OF ABBREVIATIONS

AOP	Advanced Oxidation Processes
ATR	Attenuated Total Reflectance
BBP	Butyl Benzyl Phthalate
DBP	Dibutyl Phthalate
DEHP	Di-(2-ethylhexyl) Phthalate
DEP	Diethyl Phthalate
DIBP	Diisobutyl Phthalate
DMP	Dimethyl Phthalate
DNOP	Di-n-octyl Phthalate
DOP	Di-octyl Phthalate
LDPE	Low Density Polyethylene
MDA	Malondialdehyde
MT	Mega Tonne
PAM	Polyacrylamide
PAEs	Phthalic acid esters
PET	Polyethylene Terephthalate
CB	Conduction Band
C_3N_4	Graphitic Carbon Nitride
COD	Chemical oxygen demand
CuO	Copper oxide
3-D	3-Dimensional
EDX	Energy dispersive X-ray
EIS	Electrochemical Impedance Spectroscopy

FESEM	Field-emission scanning electron microscopy
FTIR	Fourier-transform infrared spectroscopy
GC-MS	Gas Chromatography Mass Spectrometry
JCPDS	Joint Committee on Powder Diffraction Standards
LC-MS	Liquid chromatography-mass spectrometry
L-H	Langmuir-Hinshelwood
M-H	Magnetic Hysteresis
mpg-C_3N_4	mesoporous graphitic carbon nitride
MWCNTs	Multi Wall Carbon Nanotubes
NHE	Normal hydrogen electrode
PEC	Photoelectrochemical
POME	Palm Oil Mill Effluent
PTh	Polythiophene
PW_{12}	Polyoxometalates- $H_3PW_{12}O_40$
RGO	Reduced graphene oxide
SF	Spinel Ferrites
TA-PL	Terephthalic Acid Photoluminescence
TEM	Transmission electron microscopy
TPR	Transient Photocurrent Response
UV	Ultraviolet
UVA	Ultraviolet A
UVB	Ultraviolet B
UVC	Ultraviolet C
UV-vis DRS	UV-visible Diffuse Reflectance Spectroscopy

VB	Valence Band
XPS	X-ray Photoelectron Spectroscopy
XRD	X-ray Diffraction
ZnO	Zinc Oxide

CHAPTER 1

INTRODUCTION

1.1 BACKGROUND OF STUDY

The negative impacts and contamination of industrialization have been the proliferation for industrial toxic wastes released into the environment. Phthalic acid esters (PAEs) usually known as phthalates, classified as a type of vital derivatives from phthalic acids which produced from reaction of phthalic anhydride and particular alcohols through Fischer esterification. Principally, phthalates esters are liquid in colorless form, high in boiling point, low in volatility and water solubility, however they can be dissolved in organic solvents. The chemical structure of PAEs consists of a rigid planar aromatic ring and two malleable nonlinear fatty acid groups, ranging from di-(2-ethylhexyl) phthalate (DEHP) to dimethyl phthalate (DMP). Generally, PAEs are classified as lipophilic chemicals which commonly employed in the plastic industries. They serve as plasticizers and additives, enhancing the extensibility and flexibility of various items, including plastics, synthetic fibers and paints. PAEs with low molecular weight, for example DMP, are commonly applied in personal care items, cosmetic products and insect repellents. (North et al., 2014; Huang et al., 2021).

People have been exposed to PAEs through various routes. Primarily, people could potentially expose to PAEs via direct contact with itemss that contained PAEs. Koniecki et al. (2011) have reported the presence of 18

different PAEs in 252 productions of Canadian, such as toiletries, cosmetic and infant items. Xu et al. (2020) also reported the leaching of phthalates from packaging of delivery collected from leading logistic providers in China. It was proven that the PAEs leached from plastic express packaging bag and therefore it becomes a potential source of PAEs. Besides, people can expose to PAEs through contact with packaging of food and beverages that contained leached PAEs. Furthermore, people could expose to PAEs through contact with polluted air and water such as indoor dust and water.

Since PAEs are generated as global commodity chemicals and listed as organic toxic substances, therefore some studies have been carried out to investigate the impacts of PAEs on organisms, including effects on developmental and reproductive. Phthalates are endocrine disrupter which mimic and disrupt the endogenous hormones from generation and eventually lead to reproductive disorders. Deng et al. (2022) have carried out a study to evaluate connection between body's PAEs level and reproductive health. Their findings showed that the high concentration of phthalate metabolites in urine was closey related to low motility of sperm count, low level of testosterone and elevated probability in abnormal sperm and sperm aneuploidy. Moreover, the pregnant women that exposed to PAE might increase the probability of delivering preterm and cause the reduction in birth weight of baby (Ferguson et al., 2014; Chang et al., 2022). Ferguson et al. (2014) have reported that exposure to PAE during the early pregnancy significantly increased the risk of placental preterm birth. Chang et al. (2022) reported that the risk of low birth weight was associated to maternal PAE exposure during early gestational age. Another nested case-control study from Zhang et al. (2009) also reported the

detected level of di-n-butyl phthalate (DnBP) in blood cord associated with increased probability of giving a baby with low birth weight. In addition, phthalates can affect the reproduction in aquatic life; the growing of crustaceans was impaired and induced genetic aberrations (Zhang et al. 2021; Cong et al., 2020). Cong et al. (2021) have studied the negative impacts of dimethyl phthalate (DMP) on antioxidant enzyme activities of adult zebra fish (Danio rerio). They found that the zebra fish that exposed to DMP for 96 h experienced an increased in malondialdehyde (MDA) content. Since MDA is the end product of lipid peroxidation from oxidative stress, it became the indicator to degree of damage in organism.

The European Union and United States Environmental Protection Agency have listed six PAEs as priority pollutants due to their persistent in biosphere and pose risks to the environment and human health. The six PAEs are diethyl phthalate (DEP), dimethyl phthalate (DMP), di-n-butyl phthalate (DBP), di(2-ethylhexyl) phthalate (DEHP), butyl benzyl phthalate (BBP) and di-n-octyl phthalate (DNOP) (Shivani er al., 2018). In China, the ministry of Environmental Protection has stricten the standard for drinking water supplies by including PAEs in their standard (Liu et al., 2013).

However, phthalates were often detected in lakes, rivers and oceans, sediments, soil and the atmosphere. Figure 1.1 presents a comprehensive overview of the detected concentrations of PAEs in air, water, and soil samples collected from various regions of literatures across Europe and Asia. The data reveals a notable variation in PAE levels among the different areas studied. In terms of air samples, a notable discovery emerged from a daycare facility in Germany with slightly high PAEs concentration detected in indoor

3

environment which can be attributed to plastic toy products, building materials and furniture that made from plastic. Water samples from rivers, lakes, and coastal areas displayed varying PAE concentrations, suggesting the diverse sources and transport mechanisms of these chemicals within aquatic ecosystems. Additionally, soil samples from both agricultural and urban regions demonstrated the presence of PAEs, highlighting their accumulation and potential impact on terrestrial environments.
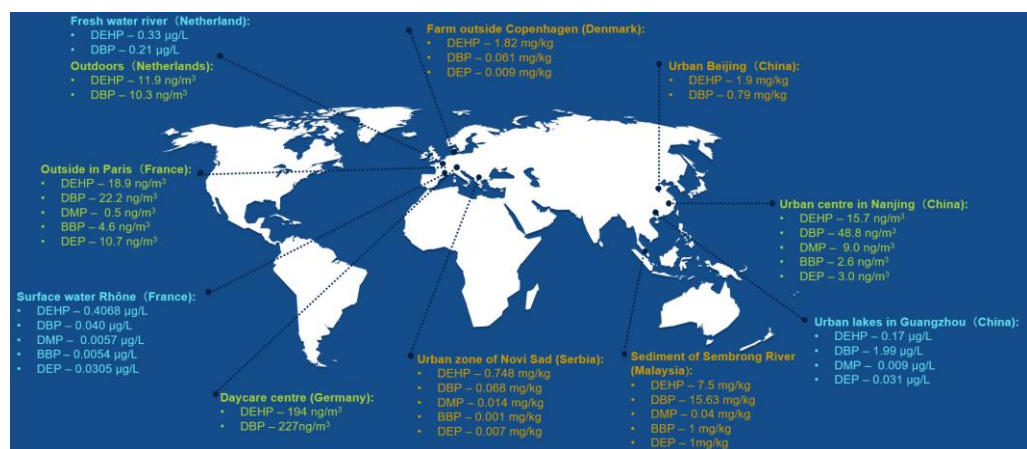
Figure 1.1: Appearance o PAEs in water, air and soil sample collected from Europe and Asia (Pang et al., 2021).

As shown in aforementioned reports, peoples may come into contact with PAEs through routine activities, there is now an utmost urgency to discover an effective and sustainable technology in removing the PAEs from the environment. Conventional water treatment prioritises on removal of pollutants through physical treatment methods. However, PAEs are stable in term of molecular structure, removing them from water through conventional treatment was challenging. Liu et al (2013) have reported low removal efficiencies of DMP and DOP via the conventional coagulation, sedimentation

and filtration treatments. This indicated that the conventional drinking water treatment processes were not practical in purify the PAEs from potable water.

On the other hand, plastics are ubiquitous in the environment. The global plastic production increasing rapidly with the increasing demand of plastic. Global production of plastic has risen sharply from 1.5 million tons in 1950 to 335 million tons in 2016 (Li et al., 2021). However, it was reporeted that more than 78% of used plastic products have not been treated effectively before disposed (Geyer et al., 2017). These plastics eventually entered into the natural environmets and led to detrimental effects on surrounding ecosystem, wildlife and even human. In addition, the chemicals used in manufacturing plastics such as plasticizers (DMP) were reported to release into the environment through diverse pathways. The plastic can become the vectors for other pollutants, some pathogen or microorganism even turned the plastic as their habitat, which accelerating their threats to organism (Neto et al., 2019). A wide diversity of wildlife including fish, zooplankton, birds, turtles, cetaceans and pinnepeds have been reported to ingest a range of plastic form microplastic to plastic bags that resemble as prey objects (Cole et al., 2016). The ingested plastic can affect the animal balances or even bloked the tract of intestine which leading to sub-lethal effect or caused death to the animal. Since most of the plastic contained phthalates as additives, the ingested plastic might release the chemical additives which alter the reproductive hormone or kill the animal. Some plastic additives may biaccumulate in animal bodies and these plastic or additives might enter the human body through the food chain if they consume that particular animal, such as sea fish or tuna or sea food (Smith et al., 2018). In the end, plastic pollution can be hazardous not only to environment and

wildlife animals but human health. Therefore, it is necessary to develop an effective way in dealing the plastic pollution.

Consequently, the amount of research emphasizes on development of new approaches such as membrane processes, bioaugmentation, advanced oxidation processes (AOPs) soared. Among various remediation methods, AOPs are the emerging technology that demonstrated potential in purifing the organic contaminants including PAEs into non-toxic products (Li et al., 2021; Hunge et al., 2019; Mansouri et al., 2019). Besides, it was reported that AOPs can be applied in degradation of plastic debris (Ali et al., 2016; Liang et al., 2013; Venkataramana et al., 2021; Zyhao et al., 2021).

1.2 PROBLEM STATEMENT

Dimethyl phthalate (DMP) is the phthalic acid ester that commonly used as plasticizer in manufacture plastic packaging, automotives components, cosmetics, dental tools and insecticides. DMP is an endocrine disruptor with tetragenic, carcinogenic and mutagenic effects which harmful to human and environment. Due to its high mobility properties, DMP was frequently detected in wasteswater effluent, soil, atmosphere and even biological samples. The removal of DMP from wastewater via conventional treatment process is challenging and unattainable due to its long alkyl-chains and non-biodegradable properties. Therefore, the need for alternative treatment process becoming a vital concern and utmost important for government agencies and regulation authorities in ensuring the quality of water supply. In view of this, it is necessary to look for althernative treatment process that able to advocate the degradation of biorecalcitrant DMP.

6

Other than water pollution, plastic pollution also became another crucial research area. Among the plastic products, Low Density Polyethylene (LDPE) is one of the most widely used polyethylene, with annual production up to 19 Mt per year (Dietrich et al., 2018). Polyethylene are extensily applied in daily products due to its low cost, light weight, good mechanical properties and durability. However, due to intensive usage of LDPE products, these created disposal problems after their useful life. The unproper management of LDPE waste led to a lot of negative impacts on ecosystem, wildlife and even human being. Several approaches including landfills, incineration, biodegradation and thermal degradation have been applied to deal with the plastic waste. However, there are some drawbacks for these treatment processes. The burning of polyethylene products might release hazardous compounds such as methane, ketones and acrolein which polluted the environment (Ali et al., 2016). Besides, the polyethylene is bioinert and resist to assimilation by microorganism, therefore, it took a longer period of time to degrade the polyethlyene waste (Liang et al., 2013). In addition, the plastic waste that buried under the soil can cause negative impacts to organism in soil which eventually reduced the yielding of agriculture (Ali et al., 2016). Thus, it is necessary to find alternative effective and environmentally friendly approach for degradation of LDPE film.

Among the technologies, AOPs were recognized as potential treatment methods to purify organic contaminants without producing secondary pollutants. Heterogeneous photocatalysis has received most attention among AOPs in wastewater treatment due to its non-selective nature and high treatment efficiency (Hong et al., 2022). Besides, several studies have reported

the using of photocatalysis in degradation LDPE film (Mehmood et al., 2015; Zhao et al., 2021; Tofa et al., 2019). Due to its excellent physicochemical properties, affordability, and remarkable environmental stability, ZnO has been utilized extensively in photocatalytic applications for the degradation of organic pollutants (Ong et al., 2018). A lot of attention has recently been focused on three-dimensional hierarchical structures because of their distinctive fine structure and bigger dimension that can provide better performance in photocatalysis applications and prevented aggregation from occurring (Wang et al., 2018). Howbeits, ZnO with wide bandgap energy suffered from the fast electron-hole pair recombination rate which narrowed down its photocatalytic performance (Murali, Sarswat and Free, 2020). Therefore, it is ideally to assemble a photocatalyst capable of showcasing outstanding performance while simultaneously addressing and mitigating as many drawbacks as feasible. Many recent studies have reported that the photocatalytic performance can be enhanced by constructing a heterojunction structure with another suitable semiconductor. Among them, the Z-scheme heterojunction has been proven to promote better separation between photogenerated e^- and h^+ pair as well as boosted redox ability which resuting in photocatalytic performance enhancement (Chen et al., 2020; Cao et al., 2021; Lai et al., 2021). By forming the Z-scheme hetrojunction, the conduction band with more negative potential and valence band with more positive potential were retained in the respective semiconductor hence boosting redox ability (Huang et al., 2019). Thus, coupling ZnO with another suitable semiconductor is a feasible way to overcome its shortcomings.

8

Recently, bismuth-based photocatalyst has attracted researcher interest owed to its unique propertise. Bismuth tungstate (Bi_2WO_6) is a perovskite-type oxide with theoretical bandgap energy of 2.6−2.8eV. It composed of $(Bi_2O_2)n^{2n+}$ layers and $(WO_4)n^{2n-}$ layer alternately. The layered structure accentuates its charge carrier separation. According to reported studies, Bi_2WO_6 is a promising candidate in formation of a Z-scheme system by revealed significant enhancement in photocatalytic performance through forming Z-scheme composites such as $Bi_2O_2CO_3/Bi_2WO_6$ (Qiang et al., 2023), $AgBr/Bi_2WO_6$ (Huang et al., 2019), g-C_3N_4/Bi_2WO_6 (Guo et al., 2018) and $CuBi_2O_4/Bi_2WO_6$ (Yuan et al., 2019). Since the band position of Bi_2WO_6 was perfectly matched with ZnO in the photocatalytic coupled mechanism, therefore, in this study, Bi_2WO_6 with different loading amounts were coupled with ZnO to examine their photocatalytic efficacy via DMP degradation. Based on previous reported studies (Zhao et al., 2022; Duan et al., 2020), the construction of ZnO/Bi_2WO_6 Z-scheme composite is expected to overcome the shortcomings mentioned above. Nonetheless, the application of binary composites in full-scale industry is still challenging, since they can create turbidty and hard to be recovered for recycling use. Therefore, a double Z-scheme composite with magnetic semiconductor can be an effective approach for this situation. Consequently, the photocatalyst with magnetic properties, for example $BaFe_2O_4$, $SrFe_2O_4$ and $CaFe_2O_4$ were introduced in constructing a double Z-scheme composites. The introduction of magnetic spinel ferrites not only aided in recovering the composite photocatalysts from treated solution for recycle use but also enhanced the photocatalytic performance. Among the spinel ferrites, $BaFe_2O_4$, $SrFe_2O_4$ and $CaFe_2O_4$ were chosen in developing

ternary Z-scheme composite as their band positions well fitted with the binary composite. The photocatalytic performance of ternary Z-scheme composite will be assessed by photodegradation of DMP under sunlight irradiation. The experiment was carried out under different operating conditions such as catalyst loading, solution pH and introduction of foreign susbtances to determine the optimum operating conditions for DMP degradation.

Since the development of $SrFe_2O_4/20wt\%Bi_2WO_6/ZnO$ (Sr20BWZ) composite has not been reported before, a possible Z-scheme mechanism was proposed based on findings of radical scavengers. Besides, the degradation pathway of DMP over Z-scheme Sr20BWZ composite was proposed based on intermediates obtained through GC-MS results and reported literatures. Although DMP has been reported to pose toxicity to human health, but the phytotoxicity of DMP on plant was still unknown. Therefore, the phytotoxicity test was performed to validate the viability of releasing treated DMP solution into the environment without causing pollution. The phytotoxicity was carried out using *Vigna radiata* and its level of toxicity can be reflected by the radicle length of the plant (Yadav et al., 2019). In addition, the as-synthesized photocatalysts were loaded on LDPE film for photodegradation under solar light irradiation. To our knowledge, this research is the first to explore the hybridization of ZnO, Bi_2WO_6 and spinel ferrite to establish a Z-scheme hetrojunction composite for photocatalytic degradation of DMP and LDPE film.

1.3 OBJECTIVES

This research aimed to produce Z-scheme ZnO/Bi$_2$WO$_6$/spinel ferrite ternary composites, which are capable of degrading the DMP and LDPE film under sunlight irradiation. The objectives of this research are:

1. To synthesize dual Z-scheme ZnO/Bi$_2$WO$_6$/spinel ferrites (SF) heterostructure systems via a hydrothermal-precipitation method.

2. To charaterize the physicochemical and optical properties of the as-sythesized photocatalysts.

3. To evaluate the catalytic activity of as-prepared photocatalysts in the removal of DMP when irradiated with solar light.

4. To study the charge-transfer mechanism and reaction pathways as to understand the fundamental aspects behind the photocatalytic enhancement.

5. To analyze the weight loss, mechanical properties, surface morphology and functional group of photodegraded LDPE over the as-synthesized photocatalysts.

1.4 SCOPE OF STUDY

Current study focused on development of dual Z-scheme ternary heterojunction photocatalysts containing ZnO, Bi$_2$WO$_6$ and spinel ferrites (CaFe$_2$O$_4$, SrFe$_2$O$_4$ and BaFe$_2$O$_4$) using a hydrothermal-precipitation method. The photocatalysts are synthesized for photodegradation of DMP under solar irradiation. The characteristics of ZnO/Bi$_2$WO$_6$/spinel ferrite ternary composite are analyzed by different techniques including field-emission scanning electron

microscopy (FESEM), fourier-transform infrared spectroscopy (FTIR), energy dispersive X-ray (EDX), X-ray diffraction (XRD), transmission electron microscopy (TEM), X-ray photoelectron spectroscopy (XPS), transient photocurrent response (TPR) and electrochemical impedance spectroscopy (EIS). Furthermore, the research also explores into influences of operating parameters included catalyst loading, pH and foreign substrate on the photodegradation of DMP. The study aims to elucidate the proposed photocatalytic mechanism of the most efficient photocatalyst through radical scavenger test, terephthalic acid photoluminescence probing test (TA-PL), UV-visible diffuse reflectance spectroscopy (UV-vis DRS) and Mott-Schottky test. In addition, the degradation pathway of DMP is proposed based on intermediates detected from GC-MS analysis and reported literature. COD test was used to evaluate mineralization of DMP solution. The stability of spinel ferrite/Bi_2WO_6/ZnO ternary composite also evaluated by cyclic experiments. The phytotoxicity of DMP was assessed using *Vigna Radiata*. The kinetic studies have been carried out to determine reaction order, kinetic model and apparent rate constant in phodegradation of DMP. The low-density polyethylene (LDPE) films together with different phototcatalysts were synthesized. The synthesized LDPE films also charaterised by FESEM, FTIR, tensile strength analysis and their weight was measured before and after solar treatment.

However, there are certain limitations within the scope of this research. Notably, the study is primarily restricted to the investigation of specific photocatalysts with ZnO based composite and their application to DMP photodegradation, thereby excluding the exploration of alternative

photocatalysts and their potential applications. Additionally, the influence of other operational parameters beyond those explicitly stated is not investigated, and alternative mechanisms or tests for photocatalytic mechanisms are not explored. The study focuses solely on the degradation pathway of DMP, based on identified intermediates, and does not address the degradation pathways for LDPE film. Moreover, while COD tests are used to assess DMP mineralization, the study does not explore mineralization methods beyond the scope of COD. Lastly, phytotoxicity assessments are limited to the examination of Vigna Radiata in the context of DMP exposure, excluding the assessment of phytotoxicity for other species.

1.5 THESIS STRUCTURE

This thesis comprises of five chapters.

Chapter 1 provides an overview of the research structure and outlines the entire study. It encompasses the DMP pollution, limitations of traditional wastewater treatment approaches and concept of heterogeneous photocatalysis. Problem statement illustrates the detrimental impact of DMP on surroundings, highlight the constraints of ZnO and discuss the strategies employed to overcome these limitations through modifications. The objectives of the research are clearly stated, and the chapter concludes by summarizing the extent of the study and presenting the thesis's organizational framework.

Chapter 2 comprises a compilation of relevant literature reviews that pertain to the research topic. It covers the types of PAEs, structure of DMP, toxicology of DMP, conventional remediation, background of heterogeneous

photocatalyst, Z-scheme mechanism and articles involving coupled ZnO and the influence of experiment parameters on photocatalytic performance.

Chapter 3 presents the synthesis process of spinel ferrite/Bi_2WO_6/ZnO composites. Subsequently, the as-fabricated products are subjected to characterization studies to assess their physical, chemical, and optical properties. Additionally, this chapter presents the experimental procedure and operating conditions for evaluating the photocatalytic activities of DMP, as well as the analytical procedure used for analysis.

Chapter 4 examines the research results and provides in depth discussions and interpretations. This chapter analyzes thoroughly the outcomes of characterization, encompassing XRD, EDX, FESEM, TEM, FTIR, XPS, transient photocurrent response, electrochemical impedance spectroscopy and Mott-Schottky analysis for as-prepared catalyst. Furthermore, the chapter discussed the photocatalytic performance of DMP degradation in relation to the operating conditions. Moreover, the result of scavenger test, cyclic experiment, phytotoxicity test and mineralization study also have been investigated. The mechanism of synthesized composite has been proposed. The degradation route of DMP was proposed according to findings from GC-MS and reported literatures. Moreover, kinetic study of photodegradation of DMP using as-synthesized photocatalyst was included. Finally, this chapter ends with the photodegradation of low-density polyethylene (LDPE) film together with their post-treatment characterization.

Chapter 5 consolidates the conclusions drawn from the research and offers recommendations pertaining to the study's findings.

CHAPTER 2

LITERATURE REVIEW

2.1 ADVANCED OXIDATION PROCESS (AOP)

The term "advanced oxidation process" (AOPs) is used to describe oxidation technologies that involved generaton of highly oxidizing radical and reactive species (hydroxyl, superoxide anion, organic peroxyl radicals) in situ. These species interact with organic pollutants and effectively break them down into smaller fragments. In 1987, AOP was firstly introduced by Graze et al. (1987) for the purification of water pollutants by generating hydroxyl radicals. Initially, the reactive radicals generated with the assiatant of one or combination of primary oxidants, for example catalyst, ozone, hydrogen peroxide or energy source (UV irradiation). Gradually, the AOP treatment methods expanded to include photocatalytic reaction, electrochemical process, Fenton's reagent and ultrasound.

Practically, the AOP commonly been applied in treating secondary effluent, biodegradable or non-degradable pollutants such as volatile organics in water, pesticides, aromatic compounds and petroleum constituents. During AOP treatement, these contaminants are mineralized and attacked by the generated reactive species including $\bullet OH$, $O_2^{\bullet-}$ and $HO_2^{\bullet-}$, which then converted or transformed into less toxic or even non-toxic inorganic compounds such as inorganic salts, carbon dioxide and water.

Basically, AOPs composed of three essential steps:

1. Generation of reactive species such as hydroxyl radicals (•OH), superxoxide anions (O_2^-) and hydroperoxyl (HO_2^-).

2. The highly reactive species attacked the organic pollutants in the waste sample and converted them into intermediates form.

3. Finally, the intermediates were oxidized and mineralized into harmless products such as water, organic salts and carbon dioxide.

Moreover, AOPs exhibited remarkable performance when compared to other conventional treatments owed to its several strengths:

➤ Have potential to remove toxicity and completely degrade organic pollutants in wastewater.

➤ Avoid the generation of secondary pollutants and circumvent the further treatment.

➤ No generation of sludge and thereby the solid waste management was not needed.

➤ Nonselective degradation pathways that allowed remediation of varied organic pollutants simultaneously.

➤ Capital-intensive installations are required; but the cost can be kept relatively low by tailoring their chemistry to specific applications.

Through AOPs, the toxic pollutants were oxidized by highly reactive species and can be mineralized and transformed to less toxic or even non-toxic compounds, thereby providing an ultimate solution for wastewater treatment. In addition, AOPs can be divided into non-photochemical or photochemical reactions as shown in Figure 2.1 and further categorized as heterogeneous (catalyst and pollutant in different phases) or homogeneous (catalyst and

pollutant in the same phase) reaction. The AOPs with the most frequently investigated technology is the Fenton process, which was initially reported as oxidation of tartaric acid in the existence of ferrous salt. This theory was further altered to involve the generation of •OH through activation of H_2O_2 by ferrous ions. Moreover, the efficacy of Fenton process was improved by ultraviolet irradiation or solar irradiation. As of April 2023, about 19991 articles regarding AOPs were available in Scopus database. However, some of the articles have indicated the traditional AOPs in generation of •OH radicals required high energy consumption, which is the drawbacks of these technology. To overcome this shortcoming, emerging technologies such as heterogeneous photocatalysis has been proposed and introduced for degradation of organic pollutants in wastewater. Heterogeneous photocatalysis have tangible performance in purification of wastewater and many of its contribution were well-documented and reported in water treatment field.
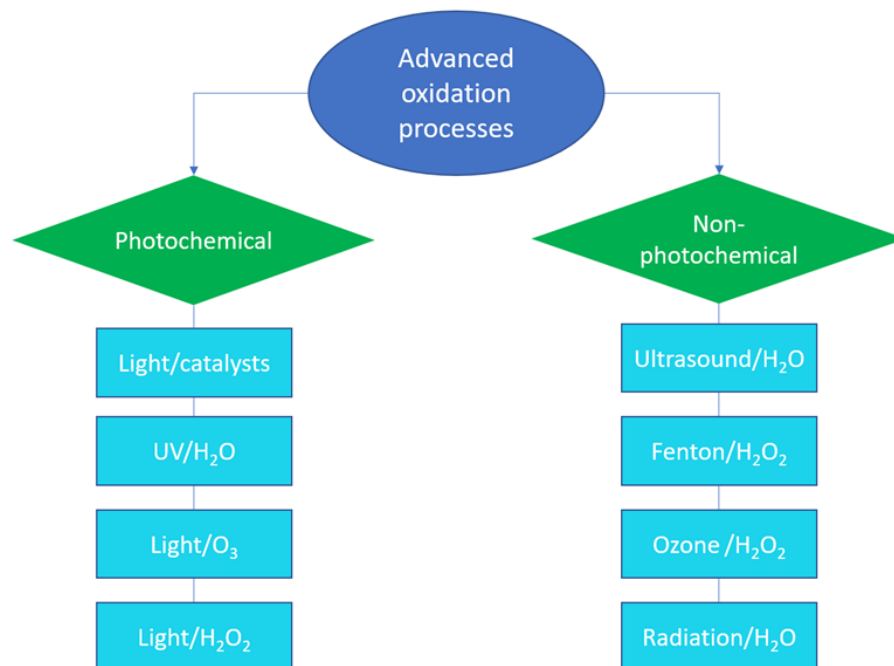
Figure 2.1: Advanced oxidation processes.

AOPs demonstrated their potential in purification of various wastewaters such as textile wastewater, pharmaceutical wastewater, pesticide wastewater and polymer wastewater. Among them, phthalic acid esters (PAEs) were categorized as important industrial pollutants and frequently received significant attention among environmental research for a few decades. These could be due to the commercial value of phthalate esters became increasingly recognized amidst 1950s. On account of outstanding performance as cost-effective plasticizers in extensive range of industrial applications, the demand for phthalic esters surged.

2.2 HETEROGENEOUS PHOTOCATALYSIS

Typically, the remediation process for heterogeneous AOPs requires the introduction of suitable catalysts/semiconductors for example metal oxides, catalysts, or transition metals into the system in order to stimulate an oxidation reaction in the liquid/solid interface. The chronicle of photocatalysis can be tracked back to year 1972. Heterogeneous photocatalysis has attracted much attention in the field of environmental sciences since Fujishima and Honda discovered and published their pioneer work in 1972. They discovered the splitting of water into hydrogen and oxygen using titanium dioxide (TiO_2) photoanode in a PEC cell by irradiating the photoanode under UV light. Since then, this paved the way for the subsequent interest in the field of heterogeneous photocatalysis, which can become a sustainable and environmentally sound means to degrade organic pollutants in polluted wastewater. Heterogeneous photocatalysis involves the alteration of chemical reaction rates through harnessing photon energy from light by photocatalysts,

leading to their participation in the chemical transformation of the reactants under suitable wavelength irradiatioon. (Braslavsky et al., 2011; Banerjee et al., 2014). Photocatalysts referred to materials for example semicondutors that able to decompose detrimental substances under suitable light irradiation.

During photocatalytic reaction, the photocatalyst was firstly illuminated to a lightsource. When the photon energy of the lightsource was found similar to or exceeds the bandgap energy of the photocatalyst, it results in the excitation of electrons (e_{CB}^-) from the valence band (VB) to the conduction band (CB), while simultaneously generating a positive hole (h_{VB}^+) in VB (Equation 2.1).

$$h\nu + \text{photocatalyst} \rightarrow \ e_{CB}^- + h_{VB}^+ \qquad (2.1)$$

Nonetheless, if the electron-hole pair recombination happened, the energy will be released which caused by low conversion of photon to energy in semiconductor (Equation 2.2).

$$e_{CB}^- + \ h_{VB}^+ \rightarrow \text{energy} \qquad (2.2)$$

Conversely, the h_{VB}^+ and e_{CB}^- will migrate towards catalyst surface if the recombination of photogenerated charges doesn't happen. When h_{VB}^+ species encounters with H_2O or OH^-, it initiates a reaction that resulted in the generatin of highly reactive •OH species (Equations 2.3 - 2.4).

$$H_2O + h_{VB}^+ + \rightarrow H^+ + \text{•OH} \qquad (2.3)$$

$$OH^- + h_{VB}^+ \rightarrow \text{•OH} \qquad (2.4)$$

Concurrently, the e_{CB}^- will react with O_2 to form oxygen related active species for example superoxide anion ($O_2^{•-}$) through Equation 2.5. Eventually, the generated $O_2^{•-}$ can protonate into radicals of hydroperoxyl (•OOH) and further transformed to hydrogen dioxide (H_2O_2) via Equation 2.6 - Equation

2.7. In the end, the H_2O_2 can be converted to •OH and OH¯ by e_{CB}^- which illustrated in Equation 2.8.

$$e_{CB}^- + O_2 \rightarrow O_2^{\bullet-} \tag{2.5}$$

$$O_2^{\bullet-} + H^+ \rightarrow \bullet OOH \tag{2.6}$$

$$H^+ + \bullet OOH + e^- \rightarrow H_2O_2 \tag{2.7}$$

$$H_2O_2 + e^- \rightarrow \bullet OH + OH^- \tag{2.8}$$

Finally, wastewater's organic components can be mineralized into harmless compounds like water (H_2O), carbon dioxide (CO_2) and inorganic ions by reactive species (•OH, $O_2^{\bullet-}$, H^+) generated in the reation through Equation 2.9.

$$\bullet OH, H^+ \text{ and } O_2^{\bullet-} + \text{pollutants} \rightarrow CO_2 + H_2O + \text{inorganic ions} \tag{2.9}$$
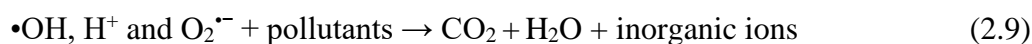
As discussed above, photocatalysis is the light-induced reactions of the surrounding molecules to generate radical species for the utilization in various applications as shown in Figure 2.2.

Figure 2.2: Applications of heterogeneous photocatalysis (Porcu, Secci and Ricci, 2022).

Among the application, photocatalysis demonstrated their potential in purification of various wastewaters such as textile wastewater, pharmaceutical wastewater, agrochemical wastewater and polymer wastewater. Table 2.1 summarizes the various groups of pollutants that can be treated by photocatalysis using different photocatalysts. The photocatalysis demonstrated its potential to degrade numerous types of contaminants, including azo dyes, antibiotics, phatmaceutical wastes, pesticides, herbicides, plastic additives and real wastewater.

Figure 2.3 shows a schematic diagram of photocatalysis basic mechanism which illustrated the reaction of photocatalyst and the response of active species generated through Equation 2.3- Equation 2.8 towards organic substances in the wastewater.
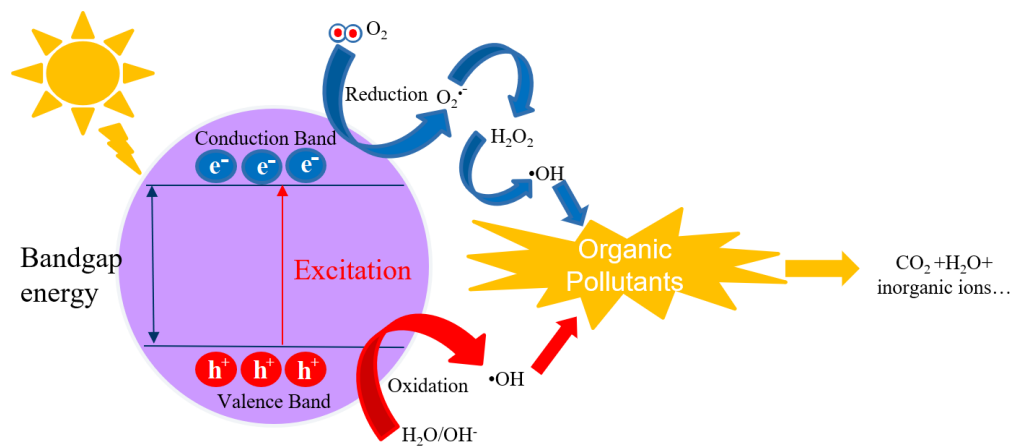
Figure 2.3: Basic mechanism of photocatalysis (Zhu and Zhou, 2019).

Table 2.1: List of pollutants degraded using photocatalysis.

Class	Pollutants	References
Azo dye	Rhodamine 6G	Arogon et al. (2023)
	Methylene blue	Zhou et al. (2023)
	Crystal violet	Xing et al. (2023)
	Reactive red 120	Luo et al. (2023)
	Methyl Orange	Jiao et al. (2023)
	Congo Red	Kalita et al. (2022)
Antibiotics	Oxytetracycline	Wu et al. (2023)
	Sulfamethazine	Yang et al. (2023)
	Tetracycline	Ma et al. (2023)
	hydrochloride	Wu and Song (2023)
	Doxycycline	Xu et al. (2023)
	hydrochloride	Musial et al. (2023)
	Ciprofloxacin	
	Sulfamethoxazole	
Pharmaceutical	Metformin	Parra-Marfil et al. (2023)
	Chloramphenicol	Wu et al. (2023)
	Acetaminophen	Lee et al. (2023)
	p-chlorophenol	Janni et al. (2023)
	Carbamazepine	Lung et al. (2023)
	Diclofenac sodium	Latif et al. (2023)

Table 2.1: Continued.

Pesticides	Malathion	Vela et al. (2018);Kumar et a. (2022)
	Dichlorvos	Kumar et al. (2022)
	Fipronil	Fahri et al. (2023)
	Triclopyr	Sharma et al. (2023)
	Organophosphorus	Zhang et al. (2023)
	Glyphosate	Sun et al. (2023)
	Profenofos	Lv et al. (2022)
Herbicides	Tebuthiuron	Gonçalves et al. (2023)
	Phenylurea	Wang et al. (2023)
	Atrazine	Feng et al. (2023)
	Pendimethalin	Gad et al. (2023)
	Monuron	Rusek et al. (2023)
	S-metolachlor	Barquín et al. (2022)
Plastic additives	Bisphenol A	Zhang et al. (2023)
	Dimethyl phthalate	He et al. (2022)
	Diethyl phthalate	Ye et al. (2022)
	Diisobutyl phthalate	Pang et al. (2022)
	Dibutyl phthalate	Zhang et al. (2022)
	Nonylphenol	John et al. (2022)
	Tetrabromobisphenol A	Keshu et al. (2022)
	4,4′-dibromobiphenyl	Liu et al. (2011)

Table 2.1: Continued.

Industrial	Textile	Laksono et al. (2023)
wastewater	Palm oil mill effluent	Subramaniam et al. (2020)
	Agrochemicals	Masula et al. (2022)
	Pharmaceutical	Rapti et al. (2022)
	Olive oil	Vuppala et al. (2020)
	Pulp and paper	Moses et al. (2022)
	Gold mining	Mestre-Martinez et al. (2020)
	Poultry refinery	Theerakarunwong and Phothi (2018)
	Petrochemical	Joy et al. (2022)

2.3 ZNO AS A PHOTOCATALYST

Photocatalysis has contributed to numerous applications in human society, including the provision of alternative energy source in solving global energy crisis and offering environmental treatments. Photocatalyst plays the key role in realizing such a conversion. Semiconductors have emerged as highly promising candidates in photocatalytic applications due to their ability to interact with light and molecules, possessing suitable band gap energies and well-defined electronic configurations. This has paved the way for significant advancements in the field of photocatalysis. Examples of semiconductors commonly employed in photocatalysis include ZnO, C_3N_4, Bi_2WO_6, TiO_2, CuO, SnS_2 and etc. Among them, ZnO has attracted attention form the researchers

owing to its extraordinary properties. ZnO, a semiconductor with a wide band gap of approximately 3.3 eV, has demonstrated excellent catalytic performance, non-toxicity, piezoelectric properties, and elongate spectral absorption make ZnO a highly suitable candidate in photocatalysis. These unique properties play an important role in photocatalytic performances.

2.3.1   Basic knowledge of ZnO

ZnO is a semiconductor with tetrahedral bonding configuration, where the anion is surrounded by four cations at the corner of a tetrahedron. Besides, ZnO occurs naturally as a rare mineral known as zincite, which can be found in various crystal structures, including zincblende, rocksalt and wurtzite. ZnO predominantly adopts the hexagonal wurtzite crystal structure under the ambient consitions, which is recognized as the thermodynamically most stable form. Else, when cubic substrates used in growing ZnO, it can stabilize and grow in a cubic zincblende structure. On the other hand, under relatively high pressure, ZnO undergoes a phase transition and exists in a cubic rocksalt or rochelle salt (NaCl) structure. This flexibility in crystal structures allows ZnO to exhibit diverse properties and opens up possibilities for tailored applications in various fields. Figure 2.4 exhibits the three possible crystal structure of ZnO.
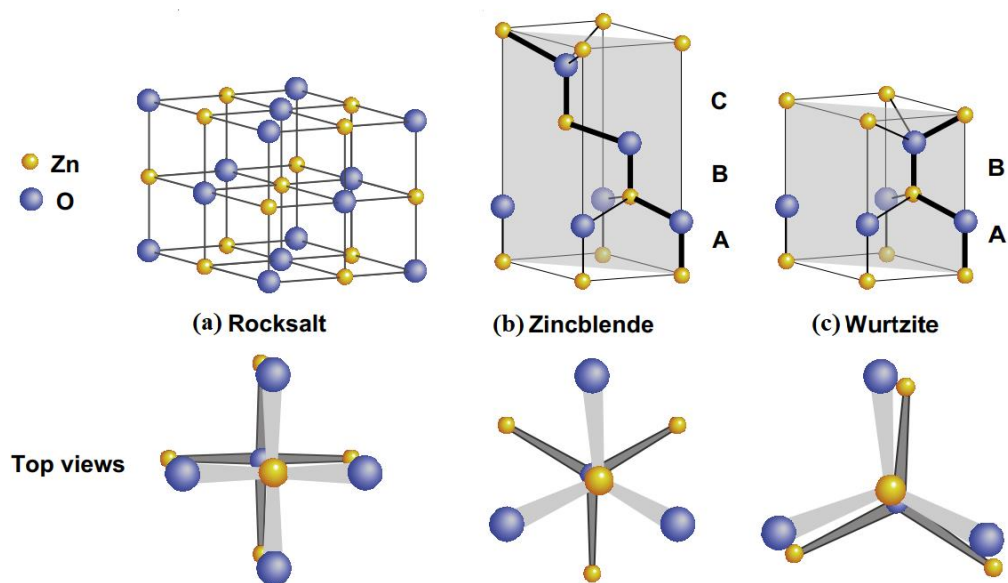
Figure 2.4: Crystal structure of ZnO by stick and ball representation: (a) cubic rocksalt (b) cubic zinc blende and (c) hexagonal wurtzite. (Ong et al., 2018).

Photocatalytic reaction mostly depended on the bandgap energy, band position and reactive radicals generated. To achieve exceptional photocatalytic performance, it is essential for the •OH radicals (2.8 V vs. NHE) and the $O_2^{•-}$ (-0.33 V vs. NHE) to fall within the energy levels between the valence band and conduction band of the photocatalyst. (Miao et al., 2020; Amatore and Arbault, 2007). Thereby, the highly reactive radicals were able to be generated and participated in photocatalytic reaction. ZnO has been identified as a semiconductor that exhibits a favorable alignment with respect to band gap position as discussed above. Moreover, ZnO has demonstrated better photocatalytic performance compared to other semiconductors in both aqueous and air environments. (Kumar et al., 2016). Furthermore, ZnO exhibits a cost-effective production, distinctive physical and chemical characteristics, high environmental stability, when compared to other semiconductors (Ong et al., 2018). All these criterias have made ZnO chosen and studied in this research.

2.4 MODIFICATION OF ZNO

A lot of research has been conducted to enhance the photocatalytic efficiency in different aspects. Lately, Z-scheme heterojunction has drawn considerable attention from researcher as it can greatly boost the photocatalytic performance by inhibiting the e_{CB}^- - h_{VB}^+ pair from recombination and retained its strong redox ability simultaneously. Thus, comprehensive study has been conducted on Z-scheme ZnO based heterojunction in this section.

2.4.1 Traditional Heterogeneous Composite

As discussed earlier, ZnO has been reported to show higher photocatalytic ability when compared to other photocatalysts. However, the photocatalytic performance of a catalyst is highly depended on and governed by its ability in generating electron-hole pairs. Although ZnO was well-recognised as promising candidate in photocatalytic field, however, the rapid electron-hole recombination rate has pertubed its photodegradation performance. Therefore, numerous efforts have been applied to improve the photocatalytic performance by reducing the electron-hole pair recombination.

Constructing heterojunction between two semiconductors is one of the approaches that has been reported to prolong the lifetime of charge carriers besides expand the spectral response (Zhu et al., 2021). Moreover, the formation of heterostructure system through a well-fitted composite can impede the electron-hole pair from recombination.

Different electronic arrangements and formation of heterojunction system can be categorised based on their VB and CB position together with

their bandgap energies. Figure 2.5 shows the mechanism for different types of heterojunction system.
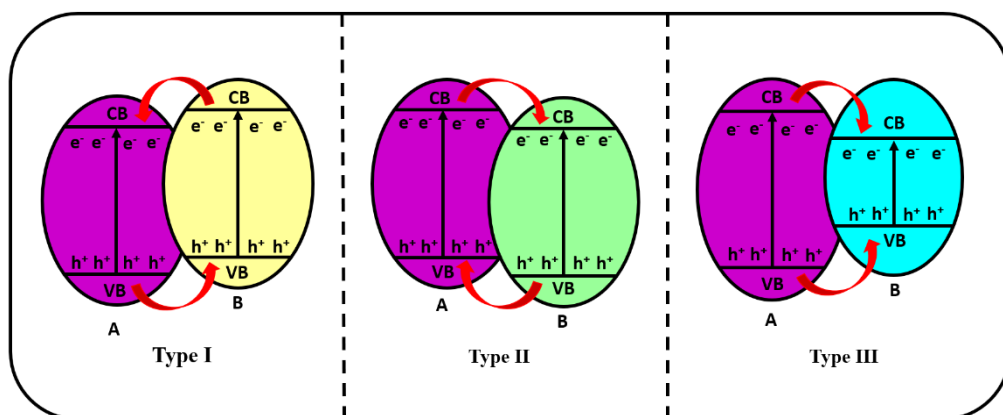
Figure 2.5: Electronic arrangements of different hetrojunction systems based on their bandgap energy and band position (Kumari et al., 2020; Joudi et al., 2018).

In type I heterostructure mechanism, both semiconductors will be excited and the e_{CB}^- will shift from the CB of semiconductor B, which has a higher potential, to the CB of semiconductor A, which has a lower potential. Moreover, the h_{VB}^+ will migrate in the opposite direction, moving from the VB with a more positive site (semiconductor A) to the VB with a less positive site (semiconductor B). As a consequence, the e_{CB}^--h_{VB}^+ can be separated effectively towards opposite direction of semiconductor edge. Thus, the electon-hole pair recombination rate can be reduced, and the photocatalytic performance was enhanced.

The principal for electron arrangement in type II heterostructure was analogous to type I, except the variation of band position in type II system. In this scenario, the CB and VB position of semiconductor A stay higher than semiconductor B. Therefore, the e_{CB}^- undergo a migration from the CB with a higher potential (semiconductor A) to the CB with a lower potential (semiconductor B) when both semiconductors (A and B) were excited.

Nevertheless, the h_{VB}^+ will will shift from the semiconductor B's VB to the semiconductor A's VB.

In type III heterostructure system, both of the VB and CB of semiconductor B is sandwiched between semiconductor A. In this scenario, both the e_{CB}^- and h_{VB}^+ will migrate from semiconductor A to semiconductor B due to lower band potential of semiconductor B. Consequently, the charge carrier will assemble on the semiconductor B with smaller bandgap. In this case, both semiconductors operate individually in the photocatalytic and the photocatalytic performance may disminish due to reduction in actives species for both materials.

In photocatalytic reaction, the e_{CB}^- and h_{VB}^+ plays an important role in participating the reactive species generation if they achieve the required redox potential. Table 2.2 shows the generation of reactive species with their relative standard redox potential.

Table 2.2: Standard redox potential required in forming reactive species (Lam et al., 2014)

Equations	Standard Redox Potential, E_0 (V)
$O_2 + e^- \rightarrow O_2^{\cdot-}$	-0.33
$O_2 + H^+ + e^- \rightarrow HO_2^{\cdot}$	-0.046
$O_2 + 2H^+ + 2e^- \rightarrow H_2O_2$	$+0.682$
$H_2O + h^+ \rightarrow H^+ + \cdot OH$	$+1.99$
$OH + h^+ \rightarrow \cdot OH$	$+2.72$

Hence, it was important in selecting an appropriate semiconductor to be the candidate in pairing with ZnO because these criteria not only assist in e_{CB}^- - h_{VB}^+ separation but also help in generating highly reactive species which

is useful in boosting photocatalytic performance. Different semiconductors and their respective bandgap, VB and CB were obtained through literature review and are displayed in Table 2.3.

Table 2.3: Semiconductors and their respective bandgap and band position.

Photocatalyst	VB (V vs NHE)	CB (V vs NHE)	Band gap (eV)	References
C_3N_4	1.87	-0.95	2.82	Kim and Yong et al. (2021)
Bi_2MoO_6	2.63	-0.39	2.24	Zhang et al. (2019)
TiO_2	2.82	- 0.2	3.02	Zhou et al. (2020)
$BaTiO_3$	2.16	-0.9	2.96	Zhou et al. (2019)
$CuBi_2O_4$	1.13	-0.63	1.76	Sabri et al. (2020)
CuO	1	-0.8	1.8	Kumaresan et al. (2020)
MoS_2	1.74	-0.11	1.85	Kumar et al. (2019)
SnO_2	3.67	0	3.67	Uddin et al. (2020)
Ag_2CO_3	2.67	0.37	2.30	Li et al. (2019)
ZnO	2.96	- 0.27	3.23	Kim and Yong et al. (2021)

The literatures of different ZnO-assisted heterostructures are compiled in Table 2.4. From the literature review, it was noteworthy that the coupled ZnO composites exhibited better photocatalytic performance when compared to bare catalyst and mainly due to the enhancement in e_{CB}^{-} - h_{VB}^{+} pair separation. The ZnO-assited composites included: ZnO/C_3N_4, ZnO/Bi_2MoO_6, TiO_2/ZnO, $ZnO/BaTiO_3$, $ZnO/CuBi_2O_4$, ZnO/CuO, ZnO/MoS_2 and ZnO/Ag_2CO_3.

Table 2.4: ZnO-assisted heterostructures for photodegradation of different organic substances.

Photocatalyst	Pollutants	Conditions	Performance	References
ZnO/Zeolite	Fluorene	Initial concentration: 1 mg/L Loading of photocatalyst: 2.5g/L Light source: 300W Halogen lamp Irradiation time: 180 min	ZnO: 48% ZnO/Zeolite: 97.5%	Manna and Sen (2023)
ZnO/FeHCF	Nonylphenol	Initial concentration: 2 mg/L Loading of photocatalyst: 1.6 g/L Light source: sunligt Irradiation time: 24 h	ZnO: 67% FeCF:73% ZnO/ FeCF: 91%	Rachna, Rani and Shanker (2019)
ZnO/ZnHCF	Bisphenol A	Initial concentration: 2 mg/L Loading of photocatalyst: 1 g/L Light source: sunlight Irradiation time: 24 h	ZnHCF: 88% ZnO: 75% ZnO/ZnS: 94%	Rani and Shanker (2018)
ZnO/SnWO$_4$	Methylene blue	Initial concentration: 3 mg/L Loading of photocatalyst: 1g/L Light source: Visible light (Sodium lamp) Irradiation time:120 min	ZnO: 40.41% SnWO$_4$: 69.48% ZnO/SnWO$_4$: 82.86%	Elviera et al. (2022)

Table 2.4: Continued.

ZnO/SnO$_2$	4-methylbenzoic acid	Initial concentration: 5 mg/L Loading of photocatalyst: 1g/L Light source: 35 W Hg lamp Irradiation time:600 min	ZnO: 10 % SnO$_2$: 22% ZnO/SnO$_2$: 90%	Khodami and Ejhieh (2017)
ZnO/BiOBr	Rhodamin B	Initial concentration: 5 mg/L Loading of photocatalyst: 1g/L Light source: 50W LED lamp Irradiation time: 300 min	ZnO: 19.7% ZnO/BiOBr: 43.6%	Zarezadeh et al. (2019)
ZnO/CuO	Rhodamin B	Initial concentration: 5 mg/L Loading of photocatalyst: 1 g/L Light source: 150 W Tungsten lamp Irradiation time: 25 min	ZnO: 7% CuO: 40% ZnO/CuO: 55%	Kumaresan et al. (2020)
ZnO/CuBi$_2$O$_4$	Rhodamin B	Initial concentration: 5mg/L Loading of photocatalyst: 0.4 g/L Light source: 50W LED lamp Irradiation time: 300 min	ZnO: 19% ZnO/CuBi$_2$O$_4$: 75%	Sabri et al. (2020)

Zhang et al. (2019) have prepared the Bi_2MoO_6/ZnO through a solvothermal method. The performance of Bi_2MoO_6/ZnO composite was evaluated by reduction of Cr (VI) under visible light irradiation. The result revealed that the Bi_2MoO_6/ZnO composite demonstrated improved degradation efficiency (100%) towards Cr (VI) reduction when compared to pure ZnO (10%) and Bi_2MoO_6 (22.78%). The improved in photocatalytic performance for the composite was mainly attributed to the development of 3D heterojunction between ZnO and Bi_2MoO_6, which promoted the interfacial separation of e_{CB}^- - h_{VB}^+ during photocatalytic reaction.

Kumaresan et al. (2020) have synthesized the ZnO/CuO composite through a solid-state method. The photocatalytic activity was examined by RhB dye degradation under visible light irradiation. The result revealed that the bare ZnO and CuO showed approximate 7% and 40% of RhB degradation, respectively. The ZnO/CuO composite enhanced degradation efficiency up to 55%. The improvement in photocatalytic efficacy was accredited to the formation of binary composite that reduced the e_{CB}^- - h_{VB}^+ pair separation.

Sabri et al. (2020) have fabricated ZnO/$CuBi_2O_4$ composite through a hydrothermal method. The efficiency of synthesized composite was studied by photodegradation of RhB dye under visible light. The outcome of their study revealed that the photocatalytic performance of ZnO/$CuBi_2O_4$ composite (75%) was much better than the pristine ZnO (19%) after 210 min visible light irradiations. Their photochemical test also revealed that the binary composite has better charge separation and migration, contributing to a better photoactivity. In another study, Elviera et al. (2022) have reported the construction of ZnO/$SnWO_4$ composite, and its photocatalytic performance was

assessed by photodegradation of methylene blue under visible light irradiation. The result showed that the ZnO/SnWO$_4$ heterostructure exhibited degradation percentage of 82.86% which was higher than the bare ZnO (40.41%) and SnWO$_4$ (69.48%). The improvement was attributed to the formation of heterostructure and low e_{CB}^- - h_{VB}^+ pair recombination rate.

In sum, development of binary composite was proved to enhance photocatalytic performance that owing to better e_{CB}^- - h_{VB}^+ pair separation. Howbeit, there is still some rooms for improvement on generating a multifunctional photocatalyst in real application.

2.4.2   Z-scheme Binary Composite

In direct Z-scheme, the band energy arrangement is similar to heterojunction of type II as discussed above, but with different migration pathways of charge carrier. Figure 2.6 shows the arrangement of heterojunction in Z-scheme mechanism. When the system exposed to light, both semiconductors can be excited and generated e_{CB}^- - h_{VB}^+ pair in their CB and VB, respectively, as previously discussed. Nevertheless, the e_{CB}^- from semiconductor B may migrate to VB of semiconductor A and recombined with the h_{VB}^+ present therein. Such electrons transition path not only led to charge separation within the semiconductor but also produced a beneficial condition that keeps e_{CB}^- in semiconductor A and h_{VB}^+ in semiconductor B to remain at their original and greatest potential. Since the e_{CB}^- transport pathway resembles in letter Z shape, such heterojunction structure is referred to Z-scheme configuration.
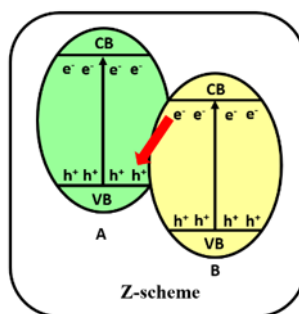
Figure 2.6: Direct Z-scheme mechanism (Xu et al., 2018).

Zhu et al. (2018) has developed a Z-scheme ZnO/CeO_2 heterojunction through a combination of wet chemistry and heat-treatment. The photocatalytic performance of as-synthesized composite was evaluated through rhodamine B (RhB) degradation. Their study reported that the ZnO/CeO_2 composites exhibited boosted photodegradation performance when compared to bare catalyst. ZnO/CeO_2 composite demonstrated the best photocatalytic activity with degradation efficacy up to 96% after 80 min irradiation which was higher than pristine ZnO (38%) and CeO_2 (56%). Moreover, there were evidence to prove that ZnO/CeO_2 composite belonged to Z-scheme heterojunction. In this study, ZnO/CeO_2 heterostructure obviously revealed extraordinary performance when compared to pure element owing to effective separation of charge carriers through Z-scheme mechanism. Besides, via the Z-scheme mechanism, both the •OH and O_2^- radicals can be generated and served as reactive species in degrading RhB molecules.

In another study, Ramachandra et al. (2020) synthesized ZnO/g-C_3N_4 composite using an exfoliation method. The performance of as-prepared composite was investigated by photocatalytic removal of malachite green (MG) under irradiation of visible light. The findings of this study showed that ZnO/g-C_3N_4 heterostructure exhibited a smaller arc radius when compared to pure

36

ZnO and g-C$_3$N$_4$. This indicating a reduction in charge transfer resistance and further comfirming the enhancement of charge carrier separation that can enhance the photocatalytic activity. The ZnO/g-C$_3$N$_4$ heterostructure was proved to follow Z-scheme mechanism through radical scavenger test. This further confirmed the highly potential and effectiveness of applying Z-scheme mechanism in their following study.

Li et al. (2018) have fabricated Bi$_2$WO$_6$/Bi$_2$Fe$_4$O$_9$ Z-scheme heterojunction through a facile hydrothermal route. The photocatalytic efficacy of as-fabricated composite was examined by photodegradation of RhB with visible-light irradiation. The Bi$_2$WO$_6$/Bi$_2$Fe$_4$O$_9$ composite revealed high photocatalytic activity with 100% of RhB degradation within 90 min which was 1.6 times better than pure Bi$_2$WO$_6$. The improvement in photocatalytic performance was attributed to rapid carrier separation through constructing Z-scheme heterojunction.

Long et al. (2018) have synthesized Bi$_2$WO$_6$/g-C$_3$N$_4$ Z-scheme heterojunction via a mixing heating method. The performance of as-synthesized composite was evaluated by photocatalytic degradation of 2,4-dichlorophenol under UV irradiation. Bi$_2$WO$_6$/g-C$_3$N$_4$ composite obtained the best photocatalytic performance as well as the highest rate constant (1.13h^{-1}) among the catalysts, which was 7.6 and 8.9 times higher than those of pure Bi$_2$WO$_6$ and g-C$_3$N$_4$, respectively. The improved photoactivity was originated from the effective suppression of $e_{CB}^- - h_{VB}^+$ pair recombination and prolonged in absorption spectrum through developing a Z-scheme composite.

Apart from the literature studies above, enormous number of Z-scheme binary composites have been constructed and employed in environmental applications, including AgI/Bi$_2$MoO$_6$ (Du et al. 2021), In$_2$S$_3$/Bi$_2$Fe$_4$O$_9$ (Das et al. 2022), CuBi$_2$O$_4$/Bi$_2$WO$_6$ (Yuan et al. 2019), ZnWO$_4$/NiFe$_2$O$_4$ (Venkata Reddy et al. 2020), CuWO$_4$/Bi$_2$OS$_3$ (Askari et al. 2020), CoTiO$_3$/NiO (Yang et al. 2021) and numerous studies on Z-scheme hetrojunction have been studied.

In particular, Z-scheme heterojunction showed outstanding charge separation ability, thus enhancing photocatalytic performance when compared to traditional hetrojunction. However, there is still considerable room for improvement in terms of surface redox reaction and catalyst recovery capability of these Z-scheme composites.

2.4.3 Magnetic prepared dual Z-scheme ternary composite

Motivated by the Z-scheme heterojunction study, dual Z-scheme ternary composite containing a magnetic semiconductor was more efficient, revealed a stronger oxidation and reduction ability and excellent magnetic recovery after treatment process. Recently, Zhang et al. (2020) prepared Z-scheme PANI/BiOBr/ZnFe$_2$O$_4$ heterojunction via a facile hydrothermal method. The performance of as-fabricated sample was assessed by photodegradation of RhB and nitrobenzene with the utilization of visible light. The PANI/BiOBr/ZnFe$_2$O$_4$ heterostructure revealed enhanced photocatalytic performance when compared to pristine catalyst. The ternary composite can be easily recovered after treatment process and its degradation efficiency remained stable after 3 consecutive uses. This can be attributed to the magnetic

properties of ZnFe$_2$O$_4$ and construction of dual Z-scheme hetrojunction. Their dual Z-scheme mechanism of PANI/BiOBr/ZnFe$_2$O$_4$ is shown in Figure 2.7.
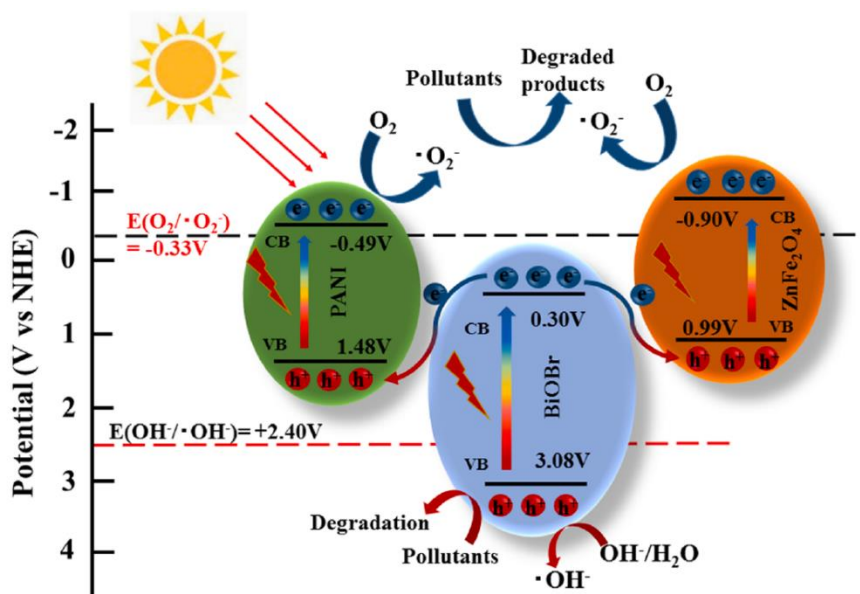
Figure 2.7: Dual Z-scheme mechanism of PANI/BiOBr/ZnFe$_2$O$_4$ hetrojunctionunder visible light irradiation (Zhang et al. 2020).

Based on the dual Z-scheme mechanism, the e_{CB}^- of BiOBr will move to VB of PANI and ZnFe$_2$O$_4$ and recombined with their h_{VB}^+, respectively. Consequently, the e_{CB}^- with strong redox potential remained in CB of PANI (-0.94V vs NHE) and ZnFe$_2$O$_4$ (-0.9 V vs NHE), and the e_{CB}^- can reduce O$_2$ to form $O_2^{\cdot-}$. At the same time, the h_{VB}^+ that stayed in VB of BiOBr not only can oxidize the organic pollutants but oxidize H$_2$O or OH$^-$ to form •OH. The proposed dual Z-scheme mechanism also consistent with their results obtained from the radical scavenger tests, which indicated that $O_2^{\cdot-}$ and h$^+$ played major role in photodegradation.

Saravanakumar and Park (2021) have designed a LaFeO$_3$/g-C$_3$N$_4$/BiFeO$_3$ dual Z-scheme structure using a wet chemical process. The photocatalytic ability of as-synthesized composite was measured by removal of ciplofloxacon. The double Z-scheme composite showed remarkable

photocatalytic performance when compared to pure LaFeO$_3$, g-C$_3$N$_4$ and BiFeO$_3$. The boosted photoactivities were credited to improvement in light absorption, effective separation of charge carrier that derived from a double Z-scheme mechansism. A double Z-scheme mechanism has been proposed as illustrated in Figure2.8.
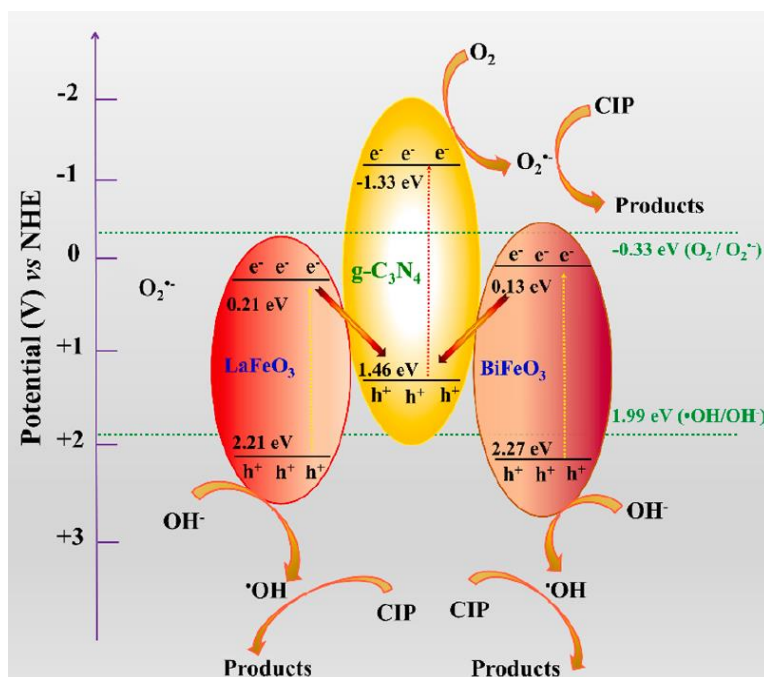
Figure 2.8: Dual Z-scheme mechanism of LaFe$_2$O$_3$/g-C$_3$N$_4$/BiFeO$_3$ heterojunction (Saravanakumar and Park, 2021).

In this Z-scheme mechanism, the e$_{CB}^-$ from g-C$_3$N$_4$ achieved the required standard reduction potential in reducing the O$_2$ to O$_2^{\cdot-}$, which can be utilized in oxidizing the pollutants. The e$_{CB}^-$ from LaFeO$_3$ and BiFeO$_3$ migrated and recombined with the h$_{VB}^+$ in g-C$_3$N$_4$. However, the remaining h$^+$ in the LaFeO$_3$ and BiFeO$_3$ can directly oxidize the H$_2$O or OH$^-$ to generate •OH radicals which is useful in degrading the pollutants.

The formation of double Z-scheme Fe$_3$O$_4$/NiFe$_2$O$_4$/phosphorus-g-C$_3$N$_4$ composite through co-precipitation of sol gel via in situ method was reported by Mishra et al. (2020). The photocatalytic performance of Fe$_3$O$_4$/NiFe$_2$O$_4$/

phosphorus-g-C_3N_4 was evaluated by degradation of ciprofloxin. The degradation percentage for the dual Z-scheme composite was almost 2-fold better than those of pristine catalyst. The enhancement was ascribed to double Z-scheme mechanism that stimulated charge carrier separation and migration, assisting in internal electrin-field creation, thus leading to dramatic augmentation of photocatalytic performance. Moreover, the Fe_3O_4/NiFe$_2O_4$/phosphorus-g-C_3N_4 nanocomposite was magnetically retrievable which avoided the further treatment after photocatalytic reaction.

In another study, Dang et al. (2022) prepared the Fe_2O_4/BiOCl/BiOI ternary composite by a solvothermal method. The photocatalytic ability of as-prepared composite was determined based on degradation efficiency of tetracycline under Xe lamp. The experimental results demonstrated that the Fe_3O_4/BiOCl/BiOI exhibited superior photocatalytic activity and mostly ascribed to double Z-scheme hetrojunction. It was imputed the development of dual Z-scheme system can impede the charge recombination and at the same time retained the CB and VB with strong redox abilities. The introduction of magnetic material (Fe_3O_4) in this study also provided a promising pathway for convenient separation and recovery of photocatalyst.

Apart form the above studies, there are many more works out there that focused on magnetic dual Z-scheme composites, including Ta_3N_5/Ag$_3PO_4$/AgBr (Cui et al., 2022), CeO_2/Ag/CdS (Wang et al., 2022), Fe_3N/Fe$_2O_3$/C_3N_4 (Padervand et al., 2021), $CoFe_2O_4$/BiOBr/Graphene (Li et al., 2019), α-Fe_2O_3/g-C_3N_4/ZnO (Balu et al., 2019) and rGO/InVO$_4$/Fe_2O_3 (Kumar et al., 2018). Compared to the Z-scheme heterojunction composites, magnetic assisted dual Z-scheme ternary composite has drawn a lot of attention since it

can impede the $e_{CB}^{-} - h_{VB}^{+}$ pair from recombination, retained strong redox potential and easily recovered the photocatalyst after treatment process. All these criterias made the magnetic assisted ternary Z-scheme type composite to be employed in this study.

2.5 SYNTHESIS OF PHOTOCATALYSTS

Various synthesis methods have been reported by researchers to fabricate the photocatalysts. Among them, a great attention has been focused on co-precipitaion method with facile and simple synthesis route. Numerous studies have reported the fabrication of ZnO via co-precipitation (Selvaraj et al., 2022; Nandi and Das, 2019; Rupa et al., 2019; Goel, Sinha and Kumar, 2019; Raji and Gopchandran, 2017). Raji and Gopchandran (2017) have reported the morphology of as-prepared catalyst was highly depended on the concentration of KOH added. It was found that low concentration of alkaline solution ($\leq$ 0.2M) resulted in spherical nanoparticles. The increasing of alkaline solution led to formation of rod shape structure and then to flower-like structure. Figure 2.9 shows various structure of ZnO formed by with the adding of different concentrations of alkaline solution.
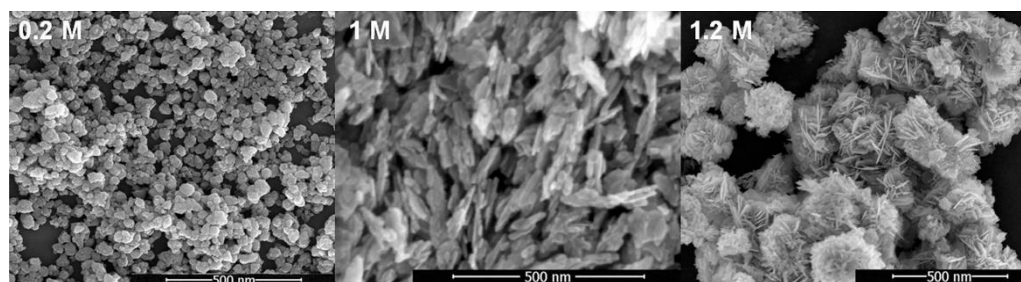
Figure 2.9: Morphology of ZnO fabricated with different concentration of alkaline solution (Raji and Gopchandran, 2017).

Goel, Sinha and Kumar (2019) also reported the synthesis of ZnO via a co-precipitation route. They found that the ZnO synthesized through high concentration of NaOH resulted in microflower shape with hierarchical structure. Another study from Selvaraj et al. (2022) also demonstrated the fabrication of ZnO via a co-precipitation method. In their study, 0.1 M of zinc nitrate hexahydrate was dispersed in 50 mL of deionized water. After stirring for 30 min, 0.1 M of NaOH solution was added into the zinc nitrtate solution until pH reached 12. The white precipitated product was then filtered, rinsed and dried overnight at 60°C using oven. Lastly, it was calcined at 500 °C for 2 hr. The FESEM studies revealed the morphology of as-prepared ZnO was nanoflower shape. The whole process for co-precipitation was facile, convenient and simple. Therefore, it was one of the methods that popularly selected by researchers in fabricating materials for different photocatalytic applications.

Apart from co-precipitation method, hydrothermal is another method that commonly approached by researchers in preparing catalysts. By adopting hydrothermal method, it can generate the catalysts that are not stable at elevated temperatures. Through hydrothermal synthesis, nanomaterials with high vapour pressures can be synthesized with the minimal loss of materials (Gan et al., 2020). Many articles have reported the fabrication of Bi_2WO_6 through a hydrothermal route (Teodóra et al., 2019; Huang et al., 2019; Shivani et al., 2019; Huang et al., 2021; Miao et al., 2021). For example, Huang et al. (2019) presented the fabrication of flower-like Bi_2WO_6 using a hydrothermal method. Particularly, 0.97 g of $Bi(NO_3)_3.5H_2O$ was dissolved in 0.4 M nitric acid. 0.05 M of Na_2WO_4 solution was added dropwise and stirred vigorously

for 1 h. The mixture was transferred to a Teflon-lined autoclave and heated for 20 h at 160°C. Subsequently, the precipitated product was filtered, rinsed with distilled water and dried in oven at 70°C for 10h. A flower-like hierarchical Bi_2WO_6 with high crystallinity was obtained through this hydrothermal route. Another study from Teodóra et al. (2019) have studied the effect of pH, reaction temperature and reaction duration on morphology and crystallinity of Bi_2WO_6. Their study revealed that the crystallinity of Bi_2WO_6 increased when the reaction temperature increased from 150°C to 200°C. The SEM images showed the morphology of Bi_2WO_6 changed from fiber-like structure to homogeneous sheet-like structure when temperature changed from 150°C to 200°C. Moreover, the Bi_2WO_6 changed from curved disks and fibers-like structure to angular sheet when duration of hydrothermal increased from 6 h to 24 h. The crystallinity of Bi_2WO_6 increased when pH value increased from 0.6 to 7.5, whereas it declined when the pH value beyond 7.5. On the other hand, the morphology of Bi_2WO_6 changed from irregular fiber-like structure to sheet like structure and into small cubic octahedral shapes when pH increased from 0.6 to 13.5. Figure2.10 shows the SEM images of Bi_2WO_6 fabricated at 200 °C using different pH of solution.
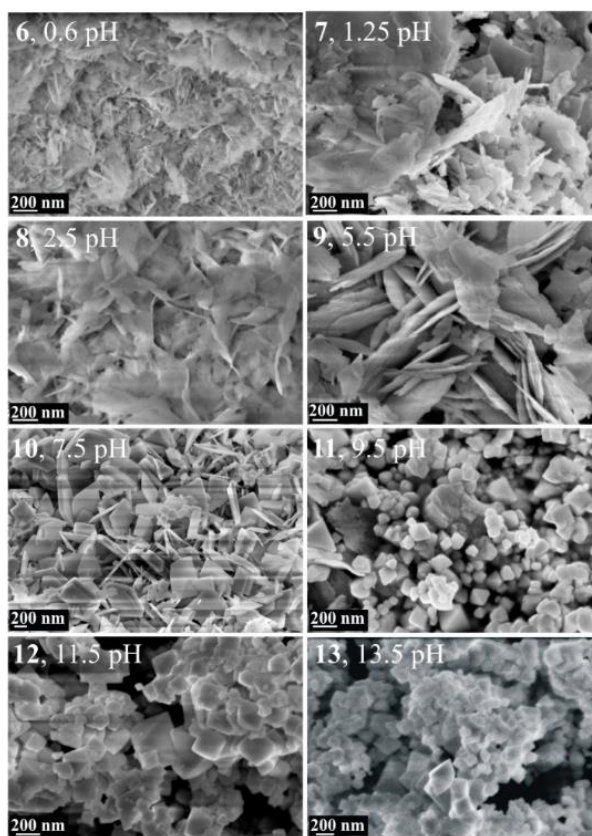
Figure 2.10: SEM images of Bi$_2$WO$_6$ fabricated using different pH of solution (Teodóra et al., 2019).

Another study from Xiao et al. (2015) also prepared hierarchical Bi$_2$WO$_6$ via a hydrothermal route. In their study, the effect of reaction temperature on morphology of Bi$_2$WO$_6$ was investigated. The surface morphology of Bi$_2$WO$_6$ was observed to change from amorphous nanoparticles to hierarchical microsphere structure when the reaction temperature increased from 110 °C to 140 °C. Further increasing in reaction temperature resulted in homogeneous size and shape of hierarchical microsphere. The photocatalysts generated through hydrothemal method were in high quality which can be observed in terms of morphology, structure and crystallinity.

Spinel ferrites have also been prepared via different routes such as co-precipiatation, sol-gel and hydrothermal methods. The following studies

demonstrated the fabrication of spinel ferrites using co-precipitation and combination of hydrothermal and co-precipitation method. For example, Sulaiman et al. (2018) have prepared $CaFe_2O_4$ via a co-precipitation method. In their study, $Ca(NO_2)_3$ and $Fe(NO_3)_3$ with (1:2) molar ratio were dispersed in 0.15L distilled water under continuous stirring condition. After that, 6 mL of ethylene glycol was added into the mixture. It was followed by adding of NaOH solution until the pH = 8. The mixture was stirred continuously for 1 h. The precipitate was centrifuged, washed with distilled water and dried in oven at 90 °C for 6 h. The $CaFe_2O_4$ synthesized using co-precipitation revealed high crystallinity and bigger value of saturation magnetization when compared to auto-combustion method. Figure 2.11 shows the XRD result and M-H curve for $CaFe_2O_4$ synthesized through co-precipitation and auto-combusition method.
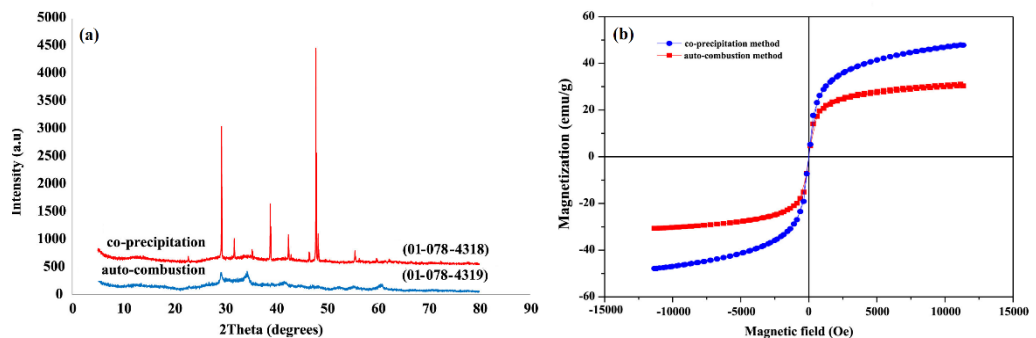
Figure 2.11: XRD result (a) and M-H curve (b) for $CaFe_2O_4$ synthesized through co-precipitation and auto-combusition method (Sulaiman et al., 2018).

Another study from Kishimoto et al. (2019) have prepared Co-Ni spinel ferrites via a combination of co-precipitation and hydrothermal method. Initially, 0.02 mol of $FeCl_3$, 0.005 mol $CoCl_2$ and 0.003 mol $NiCl_2$ were dissolved in 20 mL of water. The mixture was added to aqueous solution containing 0.228 mol of NaOH under continuous stirring. The mixture was undergoing hydrothermal treatment in an autoclave with temperature ranged

46

from 100 to 240 °C for 2h. After hydrothermal treatment, the spinel ferrite was filtered and rinsed with pure water until neutral pH was achieved. In their result, the average particle size of spinel ferrites synthesized in this way tends to increase with the increasing temperature of hydrothermal treatment. Figure 2.12 displays the size distribution of synthesized nanoparticles at various temperatures.
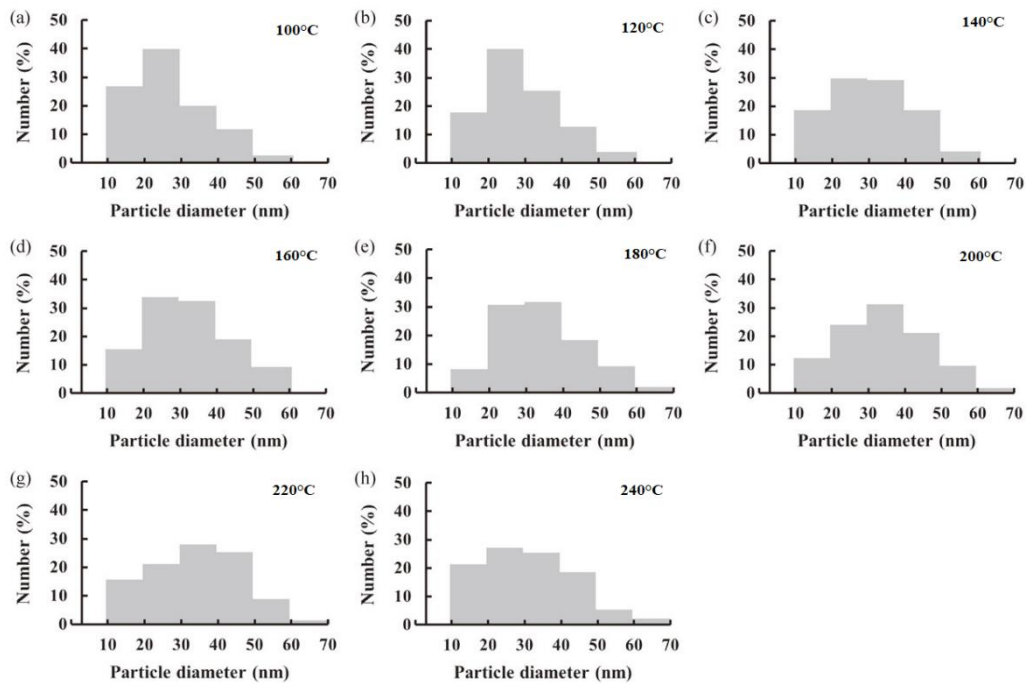
Figure 2.12: Particle size distribution of Co-Ni spinel ferrites treated at different temperature (Kishimoto et al., 2019).

On the other hand, dual Z-scheme ternary composites have been synthesized in various forms by distinctive fabrication process. Following are the different synthesis processes for Z-scheme ternary composites. Cui et al. (2022) have reported fabrication of Z-scheme ternary $Ta_3N_5/Ag_3PO_4/AgBr$ composite through a combination of hydrothermal, chemical precipitation and anion exchange methods. Ta_3N_5 was prepared via a hydrothermal method. Appropriate amount of tantalum precursor was dispersed in deionized water,

following by the ultrasonication and the adding of HF, HCl and H_2O_2. The mixture was then transferred to Teflon reactor and underwent hydrothermal treatment at 220°C for 22 hr. The obtained precipitate was filtered and dried at 60°C. Finally, the precipitate underwent nitridation at 850°C for 10 hr and Ta_3N_5 was obtained. Ta_3N_5/Ag_3PO_4 was synthesized by a chemical precipitation method. It was started with the dissolving of $AgNO_3$ in deionized water, followed by adding of Ta_3N_5 powder obtained from previous steps. After mixing for 1 hr, Na_2HPO_4 solution was added into the mixture. Finally, the obtained precipitate which is Ta_3N_5/Ag_3PO_4 composite was dried at 60°C. The ternary $Ta_3N_5/Ag_3PO_4/AgBr$ composite was prepared by in-situ anion exchange method. Briefy, the Ta_3N_5/Ag_3PO_4 composite with optimized performance was selected and dispersed in deionized water. It was followed by adding of NaBr and stirring for 3hr. The obtained powder was rinsed few times using distilled water and insert to oven for drying at 60°C. The as-received powder was referred to $Ta_3N_5/Ag_3PO_4/AgBr$ composite. The SEM and TEM results revealed the successfully development of $Ta_3N_5/Ag_3PO_4/AgBr$ composite with the presence of crystal planes of Ta_3N_5 (112), AgBr (220), Ag_3PO_4 (200). Moreover, the XRD result also further confirmed the successfully development of $Ta_3N_5/Ag_3PO_4/AgBr$ composite by showing characteristic peaks and crystal structure of Ta_3N_5, Ag_3PO_4 and AgBr. XPS result also confirmed the presence of the peaks of Ag, P, Br, O, Ta and N in $Ta_3N_5/Ag_3PO_4/AgBr$ composite which was in consistent with the characterization result.

Apart form the synthesis method discussed above, wet chemical process that combined hydrothermal treatment and deposition-precipitation also has

been adopted in fabrication of $LaFeO_3/g\text{-}C_3N_4/BiFeO_3$ ternary composite as reported by Saravanakumar and Park (2021). In their study, both $LaFeO_3$ and $BiFeO_3$ were synthesized via a hydrothermal treatment with different precursors and operating conditions. Basically, pure $LaFeO_3$ was prepared by dissolving $Fe(NO_3)_3 \cdot 9H_2O$, $La(NO_3)_3 \cdot 6H_2O$ and $C_6H_8O_7 \cdot H_2O$ in 60 mL ethylene-contained solution and stirred for 30 min. The mixture was then transferred to Teflon-lined autoclave and heated at 180°C for 12 hr. The resulting precipitate was dried at 80°C and calcined at 800°C for 3 hr to obtain the $LaFeO_3$ catalyst. Synthesis of $BiFeO_3$ was similar to $LaFeO_3$, except the using of different precursors. Particularly, appropriate amount of $Fe(NO_3)_3 \cdot 9H_2O$ and $Bi(NO_3)_3 \cdot 5H_2O$ were dispersed in HNO_3 solution. Accordingly, KOH was poured into the suspension and stirred vigorously. The suspension proceeded with ultrasonication before transferred to autoclave heating for 6 hr at 200°C. The resulting precipiatate was washed and dried at 80°C which labeled as $BiFeO_3$ catalyst. The double Z-scheme $LaFeO_3/g\text{-}C_3N_4/BiFeO_3$ ternary composite was prepared by a wet chemical process. $g\text{-}C_3N_4$ was selected as base catalyst in ternary composite. Primarily, $g\text{-}C_3N_4$ was first dispersed in 50 mL deionized water, followed by adding of desired amount of $LaFeO_3$ and $BiFeO_3$ into the dispersion. The dispersion was then stirred vigorously for 6 hr and the obtained product was dried and calcined at 300°C for 2 h. The SEM and TEM images also confirmed the formation of intimate interface between $g\text{-}C_3N_4$, $LaFeO_3$ and $BiFeO_3$. The successful construction of double Z-scheme $LaFeO_3/g\text{-}C_3N_4/BiFeO_3$ ternary composite was reflected in its photocatalytic performance. In their study, the $LaFeO_3/g\text{-}C_3N_4/BiFeO_3$ ternary composite exhibited the highest k value of 0.058 min^{-1} in

photodegradation of ciprofloxacin (CIP) degradation. It was 2.6-, 2.9-, 4.8-, 5.2-, and 8.2-fold higher than those of $BiFeO_3$/g-C_3N_4 (0.022 min^{-1}), $LaFeO_3$/g-C_3N_4 (0.020 min^{-1}), g-C_3N_4 (0.012 min^{-1}), $BiFeO_3$ (0.011 min^{-1}) and $LaFeO_3$ (0.007 min^{-1}), respectively.

Deposition-precipitation method involves the precipitation from a metal precursor onto the surface of a support material. Normally, precipitation was triggered by a controlled increase in pH of an aqueous solution that contained relative metal salt. Recently, Kumar et al. (2018) developed dual Z-scheme rGO/$InVO_4$/Fe_2O_3 ternary composite through combination of reduced graphene oxide with $InVO_4$/Fe_2O_3 using a deposition-precipitation route as demonstrtated in Figure 2.13.
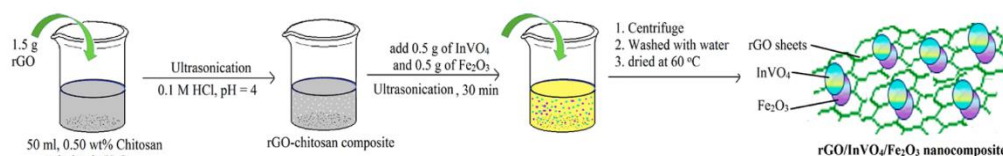
Figure 2.13: Synthesis of rGO/$InVO_4$/Fe_2O_3 ternary composite using deposition-precipitation method (Kumar et al., 2018).

Basically, it started with the adding of reduced graphene oxide into chitosan contained water. The mixture then underwent ultrasonication and pH adjustment to pH 4. Appropriate amount of $InVO_4$ and Fe_2O_3 were added into the suspension and ultrasonicated for 30 min. Finally, the suspension was centrifuged, washed with water and dried at 60 °C. The obtained powder was referred to rGO/$InVO_4$/Fe_2O_3 ternary composite. The successful sysnthesis of rGO/$InVO_4$/Fe_2O_3 ternary composite was substantiated by HRTEM image with their relative characteristic planes such as (220) plane of $InVO_4$ and (113) plane of Fe_2O_3. Moreover, the XRD pattern also further confirmed the

successful synthesis of rGO/InVO$_4$/Fe$_2$O$_3$ ternary composite with the presence of diffraction peaks and their corresponded characteristic planes including (111), (200), and (202) planes of InVO$_4$ (JCPDS card No. 48-0898) and the (113) plane of Fe$_2$O$_3$ (JCPDS card no. 33-0664). The existence of elements C, Fe, V, In and O revealed via EDX analysis and further verified the successful fabrication of rGO/InVO$_4$/Fe$_2$O$_3$ ternary composite.

Inspired by the reported studies, a hydrothermal-precipitation method was adopted in this study for fabrication of dual Z-scheme spinel ferrites/Bi$_2$WO$_6$/ZnO composite. The adoptation of the hydrothermal-precipitation method in fabrication of composite offers several notable benefits (Chang et al., 2020; Lin et al., 2020; Liu et al., 2018):

1) Controlled morphology and particle size: The hydrothermal-precipitation method allows for morphology and size control of the photocatalyst. This criterion is crucial in optimizing photocatalytic performance.

2) Homogeneous size distribution: The hydrothermal-precipitation method facilitates the uniform size distribution of the photocatalyst. The synthesized catalyst with homogeneous size is essential for maintaining the synergy effect between material and it lead to improved performance.

3) Facile and easy for tuning of properties: The characteristic and properties of photocatalyst can be easily tuned through adjusting temperature, pH, and molar concentration. This enable the researcher to tailor the photocatalyst into specific characteristic.

51

4) Environmental friendly: The use of hydrothermal-precipitation method is environmentally friendly because it avoid the using of toxic solvent. This is important because the photocatalyst can be innovated without causing pollution to environment.

In summary, the hydrothermal-precipitation method stands out for its ability to produce well-defined, homogeneous, and efficient composite photocatalysts, making it a promising choice for various applications in materials science and environmental engineering.

2.6 PHTHALATE ACID ESTERS (PAEs)

Phthalate acid esters (PAEs) are a group of derivatives of phthalic acid which synthesized from phthalic anhydride and specific alcohols by Fischer esterification. PAEs systematic name is 1,2-benzenedicarboxylic acid where there are two benzenedicarboxylic acids, namely isophthalic acid,3 and the terephthalic acid,4. Terephthalic acid is essential in manufacturing polyester fabric. PAEs are commonly applied in the plastic production in order to introduce elasticity into plastic products. A low phthalic acid ester intoduced into the plastic would lead to hard products and a high phthalic acid ester concentration would generate solf and elastic plastic products. Recently, the world production was approximately 150 million tons of plastics per year, where the annual consumption is approximately 6-8 million tons.

2.6.1 Types of PAEs

PAEs are synthethically generated by esterification of phthalic acid through different alcohols. It is diesters of 1,2-benzenedicarboxylic acid that

contained a benzene ring and two ester groups. Molecules with different physicochemical properties are obtained based on the alcohol attached. The water solubility of PAEs is low and the solubility reduces with increasing side chain length and molecular weight. In this study, DMP with low molecular weight and short alkyl groups has higher water solubility. Generally, the PAEs with higher molecular weight are applied in construction ingredients and several PVC contained products such as water repellent clothing (raincoats, boots), flooring and wall covering, children's product, medical devices and food packaging. PAEs with low molecular weight such as DEP, DMP and DBP are exploited as solvents in cosmetic products, insecticides, lacquers and pharmaceutical products. There are differet types of PAEs which included DMP, DBP, DEP, DEHP, DnOP, DOP and BBP. Their chemical structure and physicochemical properties are summarized in Table 2.5 below.

Table 2.5: Types of PAEs and their characteristics
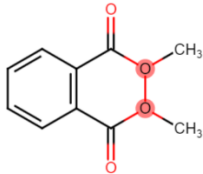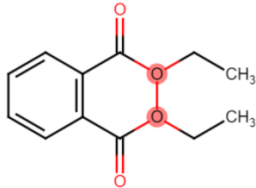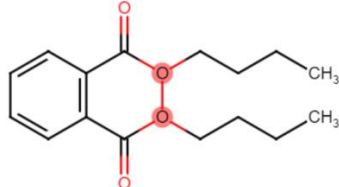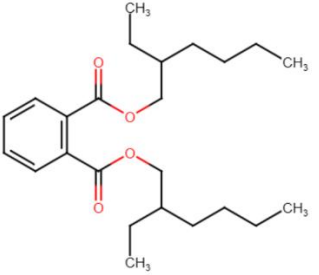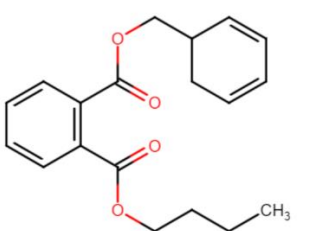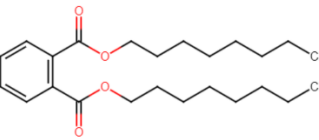
Compound	Chemical structure	Physicochemical properties
Dimethyl phthalate (DMP) Molecular formula: $C_{10}H_{10}O_4$ C_6H_4-1,2-$(COOCH_3)_2$		MW= 194.18 g/mol Spec. density:1.19g/cm^3 (20°C) Water solubility: <0.1g/L (20°C)
Diethyl phthalate (DEP) Molecular formula: $C_{12}H_{14}O_4$		MW= 222.24 g/mol Spec. density:1.12g/cm^3 (20°C) Water solubility: <1.08 g/L (25°C)
Dibutyl phthalate (DBP) Molecular formula: $C_{16}H_{22}O_4$		MW= 278.34 g/mol Spec. density:1.05g/cm^3 (20°C) Water solubility: <0.013 g/L (25°C)

Table 2.5: Continued.

Di(2-ethylhexyl) phthalate (DEHP) Molecular formula: $C_{24}H_{38}O_4$		MW= 278.34 g/mol Spec. density:1.05g/cm^3 (20°C) Water solubility: <0.013 g/L (25°C)
Benzyl butyl phthalate (BBP) Molecular formula: $C_{19}H_{20}O_4$		MW= 312.36 g/mol Spec. density:1.12g/cm^3 (20°C) Water solubility: <0.0037g/L (25°C)
Di-n-octyl phthalate (DnOP) Molecular formula: $C_{24}H_{38}O_4$		MW= 390.62 g/mol Spec.density:0.98g/cm^3 (25°C) Water solubility: <0.003g/L (25°C)

2.6.2 Exposures of PAEs and its effects on human and environment

The threat of PAEs posed is often determined by the frequency and exposure route to human and living creatures. In general, human exposed to PAEs via several different pathways. At first, people might expose to PAEs through diet intake or inhalation with products containing PAEs. For example, oral intake of PAEs occured when the child chew or suck on toys containing phthalates. Koniecki et al. (2011) identified the existence of 18 PAEs appeared in personal care items and baby products. The presence of PAEs in personal care and baby products is particularly noteworthy due to the potential implications for human exposure. These products often come into direct contact with the skin, and the presence of PAEs raises concerns about their absorption through dermal contact or ingestion, especially among vulnerable

populations such as infants and young children. Xu et al. (2020) reported the logistic packaging was the source of phthalate, with 181 to 5320 ng/g of phthalates leached from plastic express packaging after 2 days. In the study of Paluselli et al. (2018), DEP and DMP were the major PAEs that leached from PVC cables, with mass fraction up to 68.9 ng/g and 9.5 ng/g, respectively.

Moreover, people are exposed to PAEs indirectly by utilization of plastic product that contained PAEs, for example the plastic drinking bottle and plastic food container. Li et al. (2018) have reported the occurrence of 21 PAEs in drinking water contained in polyethylene terephthalate (PET) bottle, with DMP, DBP and DiBP being the major compounds detected. Another study from Wormuth et al. (2006) also suggested that food was another significant source that human exposed to to PAEs. In addition, Gong et al. (2016) also investigated the relationship between clothing and dermal exposure of phthalate by examine the phthalate levels on different skin locations. The outcomes from this study revealed that the concentration of phthalates on skin covered by fabric clothing were less than those uncovered areas. Besides, the concentration of phthalate on clothes and skin increased when wearing durations increased. In addition, people can be exposed to PAEs via environmental conatamination such as polluted water, air and indoor dust. Li et al. (2019) reported the detection of PAEs in indoor particle samples from living room and bedroom area, with up to 462 µg/g.

According to various exposure mechanism, the daily intake of PAEs was limited to 70µg/kg/day (Net et al., 2015). Koch et al. (2011) also reported that up to 24% of the children from 111 German primary school have exceeded the tolerable daily intake value. On the other hand, Qu et al. (2022) studied the

daily exposure value of PAEs from different group ages and revealed that the exposure of PAE was varied among different groups with toddler and infants suffering from higher PAE exposure compared to adult groups. This could be due to most infants chew or suck on toys containing phthalates and wearing cotton-based clothing, which easily adsorb phthalates compound than other types of fabrics (Li et al., 2019)

Since PAEs have been generated as bulk chemicals universal and classified as toxic organic substances, there are numerous studies on the negative impacts of PAEs on living creatures, including mental development and reproductive syste. PAEs were proved to pose endocrine disrupting properties, they managed to compete and disturb regular generation of endogeneous hormones, leading to reproductive issues (Knez, 2013). Jurewicz et al. (2013) investigated the relationship between reproductive health and PAE level in the body and discovered that the reduction in sperm motility, testosterone level increased with urinary PAE meatabolite levels. In addition, the cases of sperm gene damage and sperm aneuploidy also increseaed with PAE level in the body. Moreover, it was reported that pregnant women that exposed to PAEs may experience preterm delivering and reduction in baby birth weight (Ferguson et al., 2014; Song et al., 2018). Moreover, the male babies would have potential in developing testicular and Leydig cell when being exposed to PAEs and lead to low secretion of androgen and shorter anogenital distance (Pang et al., 2021). In addition, the studies from toxicology field also confirmed the prenatal exposure to phthalates with high molecular weight can increase the riak of asthma and respiratory issues during childhood (Adgent et al., 2020).

Several research have also focused on the identification of PAEs in various environmental contexts. Researchers from Serbia discovered the appearance of six different PAEs in the soil collected from Novi Sad with concentrations in the range of 0.0002−4.82 mg/kg, with the highest concentration detected from city parks. In another research, a total of six PAEs was detetcted in indoor quality from Tianjin, China with concentration range from 7.266 – 1591.277 ng/m^3. DMP, DEP, DBP, BBP, DEHP and DOP were the PAEs that frequently detetected from nine different cities in China. In Istanbul, Turkey, the researchers found the presence of five PAEs (DEP, DMP, DEHP, BBP and DBP) in soil samples. In Austria, six PAEs (DMP, DEP, DBP, BBP, DEHP and DOP) were detected in nearly all the wastewater treatment facility effluent and also in all runoffs from street (Pang et al., 2021).

As discussed above, human can be exposed to various PAEs through a series of daily exposure without being aware of it. In particular, DMP with a hydrolysis half-life of about 20 years that almost ubiquitous in the environment (Sun, Yan and Xue, 2012). Therefore, an effective and promising eradication of DMP from water source is currently an important environmental issue. DMP is stable in term of molecular structure, removing it from water through conventional treatment can be challenging. According to Liu et al (2013), the removal percentage of PAEs from water source in Harbin, China through a conventional treatment was approximately 25.8-76.5% in which DMP removal demonstrated the lowest efficiency of less than 30%. These indicated that the conventional drinking water treatment process was not practical in purify the PAEs from potable water.

2.7 PHOTODEGRADATION OF DMP

Ye et al. (2022) reported the efficient photodegradation of DMP using MgSnO$_3$. The experiment was carried out under Xenon lamp irradiation. It was reported that 75% of DMP was successfully degraded after 120 min reaction. Quenching experiments were also carried out to identify the main active species in photodegradation of DMP. •OH, •O$_2^-$ and h$^+$ were proved as the active species that responsible in degradation DMP while •O$_2^-$ played major role in photodegrdation of DMP. In order to eluicidate DMP degradation pathway, the intermediates of DMP were determined by LC-MS analysis. In their study, the photodegradation of DMP was majorly ascribed to the attack by reactive species. There are two possible pathways in photodegradation of DMP. In the first pathway, the benzene ring of DMP was attacked by reactive species and generating 5-hydroxy-2-methoxycarbonylbenzoic acid and 4-hydroxyphthalaldehyde. In second possible pathway, radical attack on ester group of DMP resulting in formation of (methoxycarbonyl)benzoic acid. This intermediate was oxidized to form 1-(2-acetylphenyl)ethenone, benzene-1,2-diol, phthalic anhydride. In the end, the intermediates were degraded to harmless small molecule such as H$_2$O and CO$_2$. The photodegradation pathway of DMP by MgSnO$_3$ was shown in Figure 2.14.
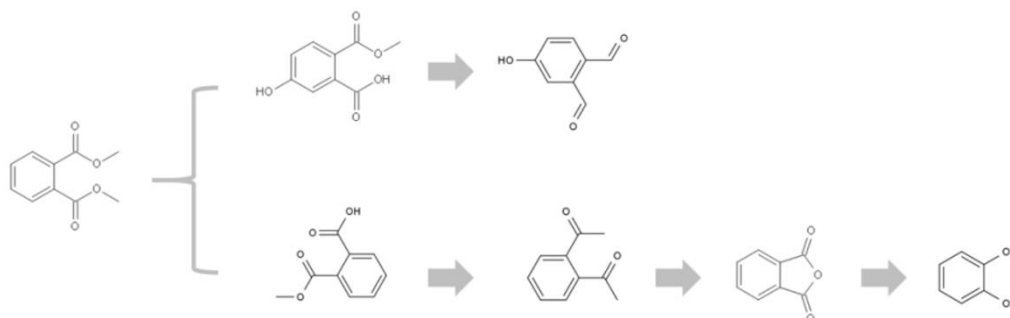
Figure 2.14: Proposed photodegradation pathway of DMP with their detected intermediates (Ye et al., 2022).

Chen et al. (2021) have reported the photodegradation of DMP using La/TiO$_2$. In their study, 74.4 % of DMP was successfully degraded by La/TiO$_2$ under 10 h UV irradiation. In their study, the degradation of DMP has been experimentally proven due to the attack of radicals. Several intermediates including monomethyl phthalate, maleic acid and hydroxylated MMP were present in their proposed degradation pathway. The detected intermediates oxidized into CO$_2$ and H$_2$O in the end of photodegradation. The possible DMP degradation pathways are displayed in Figure 2.15.
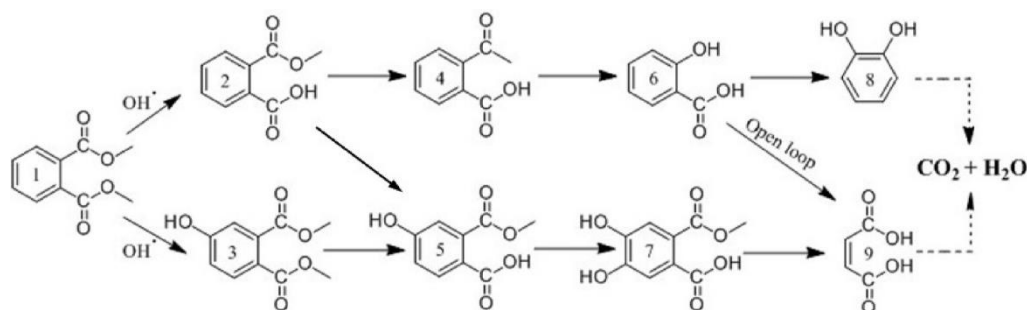
Figure 2.15: Possible degradation pathways of DMP over La/TiO$_2$ composite (Chen et al., 2021).

As illustrated in Figure 2.15, the DMP was attacked by •OH radicals and formed monomethyl phthalate (2) and transformed to O-carboxybenzene ethyl ketone (4) or hydroxylated MMP (5). Then, the product (4) can undergo dealkylation to form salicylic acid (6) and further oxidized into catechol (8) or maleic acid (9). In second pathway, the •OH radical reacted with DMP to form mono-hydroxylated DMP (3). Under continuous attack from •OH radicals, hydroxylated MMP (5) was produced from product 3 and product 2. Product 5 was oxidized into di-hydroxylated MMP (product 7) and further oxidized into product 9. Finally, the products 8 and 9 were degraded into CO$_2$ and H$_2$O.

Salazar-Beltrán et al. (2019) have studied the photodegradation of DMP using TiO$_2$ under UV irradiation. It was revealed that the DMP degradation can

up to 82% after 300 min irradiation. Tan et al. (2018) have investigated the photodegradation of DMP using MWCNTs/TiO$_2$ nanocomposites. They illustrated the degradation of DMP via the attack by reactive species. Particularly, the photocatalytic degradation was initiated by TiO$_2$ excitation and generation of electron-hole pairs on catalyst surface. These electron-hole pair tended to form reactive species which was useful in DMP degradation. Finally, the generated reactive species mineralized the DMP into CO$_2$ and H$_2$O.

2.8 EFFECT OF OPERATING PARAMETER

2.8.1 Effect of Catalyst Loading

In general, the photocatalytic performance is greatly affected by loading of photocatalyst. When the catalyst loading increased, active sites on the photocatalyst also increased and hence more reactive species can be generated. The generatetd reactive species were then participated in photodegradation, and thus, the photocatalytic performance also increased. However, when the catalyst loading was beyond to certain limit, the rate of phototcatalytic degradation will decline. This could be due to high turbidity of the solution, which increases with the catalyst loading and blocks the light from penetrating inside the solution. In this scenario, light scattering effect caused the reduction in active species and subsequently reduced the photodegradation percentage. Another reason for reduction in degradation efficiency was the agglomeration of catalyst during high catalyst loading, which reduces exposure and surface for active sites and hence resulted in reduction of photocatalytic performance.

According to Fazli et al. (2021), Fe_3O_4@CuCr-LDH was used to degrade DEP with the assistance of visible light illumination. It was found that the photocatalytic degradation efficiency originally increased as the catalyst loading was increased from 0.5 g/L to 1.0 g/L but the removal rate started to reduce once the catalyst reached the optimum loading (1.0 g/L) in their study. This was due to high turbidity in solution during high catalyst loading that caused reduction in number of incident photons into the solution. As a consequence, the number of active sites that can be used in photodegradation reduced and hence resulted in lower photocatalytic efficiency.

A study from Xu et al. (2020) has investigated the effect of catalyst dosage on degradation of DMP using g-C_3N_4. An increasing in catalyst dosage resulted in enhanced DMP photodegradation. However, further increase in catalyst loading has strengthened the "inner filter" effect of incident light and reduced the photon density for unit mass of catalyst, which caused milder increase of rate constant at higher catalyst loadings. Similar result was reported by Mphahlele et al. (2022) in DBP degradation over Gd-WS_2. The effect of catalyst loading on degradation performance was carried out, and the findings revealed that moderate dosage of catalyt was sufficient to provide superior photocatalytic performance. They went further to explain the excessive catalyst dosage not only introduced turbidity in the catalytic system, but also reduced the light penetration from reaching the catalyst and eventually diminished the photocatlytic performance.

In another study, Abbas and Jamil (2016) have employed Fe/$SrTiO_3$ in photocatalytic degradation of DBP. During their investigation, the researchers observed an enhancement in photocatalytic efficacy as the catalyst loading was

increased from 0.25 to 1.0 g/L, primarily due to the generation of a higher number of reactive radicals. The catalyst dosage with the highest degradation efficiency was determined to be 1.0 g/L in this study. A minor reduction in photocatalytic efficiency was noticed when loading of catalyst beyond 1.0g/L. This can be attributed to the phenomenon of light scattering and high turbidity that occurred in high catalyst concentrations. Thus, 1.0 g/L was selected as catalyst loading in other section of experiment throughout their study. Table 2.6 summarises different studies on how photocatalyst loading affects the degradation of various PAEs.

Table 2.6: Effect of catalyst loading on photocatalytic degradation of different PAEs.

Photocatalyst	Degraded Pollutant	Condition	Range of catalyst loading (g/L)	Optimum catalyst loading (g/L)	Reference
Fe/SrTiO$_3$	DBP	Substrate concentration = 50mg/L; Irradiation time = 120 min; light source = Halide lamp	0.25-1.25	1.0	Abbas and Jamil (2016)
Bi$_2$O$_3$/TiO$_2$/RGO	DEHP	Substrate concentration = 10 mg/L; Irradiation time = 90 min light source = 300W Xenon lamp	0.1-2.0	1.0	Zhang et al. (2021)
g-C$_3$N$_4$	DMP	Substrate concentration = 1.948 mg/L; Irradiation time = 120 min; light source = Mercury lamp	0.1-1.5	1.5	Xu et al. (2020)
Fe$_3$O$_4$@CuCr-LDH	DEP	Substrate concentration = 20 mg/L; Irradiation time = 150 min; light source = solar simulator lamp	0.5-2.0	1.0	Kumar et al. (2021)

Table 2.6: Continued.

Cu/TiO$_2$	DBP	Substrate concentration = 20mg/L Irradiation time: 5 h light source = UV lamp	1.0-3.0	3	Sathasivam et al. (2013)
rGO-ZnO	DEP	Substrate concentration = 10 mg/L Irradiation time: 180 min light source = UVA lamp	0.6-1.2	0.8	Wang et al. (2018)
Fe/Ag/ZnO	DBP	Substrate concentration = 5 mg/L; Irradiation time = 120 min light source = LED light	0.1-0.2	0.2	Akbari-Adergani et al. (2017)
ZnO	Diamyl phthalate	Substrate concentration = 30 mg/L; Irradiation time = 240 min light source = UVA lamp	0.1-0.3	0.3	Vela et al. (2018)
Gd-WS$_2$	DBP	Substrate concentration = 5 mg/L; Irradiation time = 60 min; light source = Xenon lamp	0.05-0.25	0.2	Mphahlele et al. (2022)

2.8.2 Effect of pH

pH stands as an essential determinant among various factors which can alter the photocatalytic degradatin rates in multiple ways. It was found that the the adsorption of DMP onto the surface of semiconductor depended on the pH of the given solution. It was reported that the impact of pH on photocatalytic performance was closely associated with surface charge of the photocatalysts.

In the presence of PW_{12}/TiO_2, Xu et al. (2010) demonstrated degradation of DEP from pH 3.4 to pH 11.2. They have noted that the photocatalytic performance increased when the pH value changed from pH 3.4 to pH 9.1. A slight decline in photocatalytic efficacy was noticed when the pH beyond pH 9.1. Their result suggested the neutral or slightly alkaline conditons favoured the degradation of DEP. This was attributed to increase in amount of •OH generated at alkaline environment. Similar observation was also reported by Fazli et al. (2021) in which optimum pH for degradation of DEP was achieved at slightly alkaline solution of pH=8. In neutral environment, deprotonation of essential groups of PW_{12}/TiO_2 composite created the negative charges surface and induced the attractive forces between catalyst and organic molecules in wastewater. This led to boosting of photocatalytic performance. Conversely, at highly alkaline condition, repulsive force was induced between pollutants and catalyst which deteriorated the degradation efficiency.

Pang et al. (2022) have studied the influence of pH on removal of diisobutyl phthalate (DiBP) over ZnO, the experiment was conducted over the range of 2<pH<10. The DiBP removal rate was found to be increased when the pH changed from 4 to 9. It was suggested that a higher amount of hydroxide

ions in alkaline environment can generate more •OH radicals which resulted in boosting photocatalytic removal efficiency. However, an inhibition in DiBP removal was observed when the pH value beyond pH 9. Similar finding has been reported by Abbas and Jamil (2016). They studied the degradation of DBP using $Fe/SrTiO_3$. In their study, the degradation efficacy increased when pH increased from pH 3 to pH 9. The photocatalytic performance was observed to decline when pH beyonded pH 9 due to replusion occurred between pollutant and catalyst.

Meenakshi and Sivasamy (2018) studied the DEP photodegradation using ZnO/SiC composite. The experiment outcomes clearly demonstrated that the optimum degradation performance occurred at pH 7 for the catalyst. When the pH of the medium was in acidic environment, H^+ ions scavenged OH^- ions in the solution and led to lower generation of active species and eventually resulted to lower photocatalytic degradation. When the pH of the medium was in highly alkaline conditions, the removal rate deteriorated which was due to weaker adsorption of pollutants onto the catalyst surface.

The effect of pH on photodegradation of DMP was also investigated by Li et al. (2021) using $M\text{-}mpg\text{-}C_3N_4/BiOBr/PTh$ composite. The degradation efficiency was observed to be the highest at nearly neutral condition (pH=7.36). It was reported that the DMP and the catalyst were protonated and became positively charged under acidic environment. These created the repulsive forces between the surface of catalyst and pollutants which leads to deterioration of photocatalytic performance. Analogously, under extremely alkaline environment, both the DMP pollutants and catalyst were in negatively charged which created electrostatic repulsion force among themselves and

eventually weakened the photocatalytic performance. Table 2.7 summarises the studies of different photocatalysts used in photocatalytic degradation of various phthalates and their operating condition together with the optimum pH used.

Table 2.7: Effect of pH on photodegradation of different PAEs.

Photocatalyst	Degraded Pollutant	Condition	Range of pH	Optimum pH	Reference
M-mpg-C$_3$N$_4$/BiOBr/PTh	DMP	Substrate concentration = 20mg/L Irradiation time: 6 h light source = 500W Xenon lamp	5.37-11.17	7.36	Li et al. (2021)
MgSnO$_3$	DMP	Substrate concentration = 10mg/L; Irradiation time = 120 min; light source = 500 W Xe lamp	3-9	7	Ye et al. (2022)
Gd-WS$_2$	DBP	Substrate concentration = 5 mg/L; Irradiation time = 60 min; light source = Xenon lamp	1-11	7	Mphahlele et al. (2022)
Fe$_3$O$_4$@CuCr-LDH	DEP	Substrate concentration = 20 mg/L Irradiation time = 150 min light source = Stimulated solar lamp	3-12	8	Fazli et al. (2021)
ZnO	DiBP	Substrate concentration = 10 mg/L Irradiation time: 60 min light source = UV lamp	2-10	9	Pang et al. (2022)

Table 2.7: Continued.

ZnO/SiC	DEP	Substrate concentration = 100 mg/L Irradiation time: 4 hr light source =UV lamp	2-12	7	Meenakshi and Samy (2018)
PW12/TiO$_2$	DEP	Substrate concentration = 5mg/L Irradiation time: 150 min light source =UV lamp	3.4-11.2	7	Xu et al. (2010)
Fe$_3$O$_4$/BC	DEP	Substrate concentration = 20mg/L Irradiation time: 120 min light source =solar	3-9	7	Yi et al. (2021)
Fe/SrTiO$_3$	DBP	Substrate concentration = 50mg/L; Irradiation time = 120 min; light source = Halide lamp	3-11	9	Abbas and Jamil (2016)
Gr/TiO$_2$	DBP	Substrate concentration = 10 mg/L; Irradiation time = 90 min light source = Xenon lamp	3.2-11.5	9.2	Wang et al. (2019)

2.8.3 Effect of Foreign Substances

The foreign subatances such as nitrate, sulphate, humic acid, etc, commonly exist in natural water. Therefore, it is necessary to investigate the impact of various substances on photodegradation efficiency. The foreign substances may compete with organic contaminants to get adsorbed onto surface of catalyst and occupied the active sites. Therefore, photocatalytic performance of the catalyst was greatly affected by introducing foreign substances.

Wang et al. (2018) studied the effect of bicarbonate (HCO_3^-), nitrate (NO_3^-), chloride (Cl^-) and sulfate (SO_4^{2-}) on photodegradation of DMP. They found that the presence of foreign substances had contrasting effects on DMP removal. The effect of the foreign substances was found in the order of $NO_3^- > HCO_3^- > Cl^- > SO_4^{2-}$ The introduction of HCO_3^- resulting in restraint of degradation efficiency from 75% to 51.8% as the HCO_3^- can react with h^+ and •OH and generated $CO_3^{•-}$ which has lower redox potential than •OH. The Cl^- suppression was caused by (1) The Cl^- ions adsorbed on catalyst surface and competed with organic pollutants; (2) The Cl^- scavenged the •OH and h^+ to generate $Cl•$ with weaker redox potential which hinder the photocatalytic reaction. For NO_3^-, it reacted with photons in generating NO_2^- which was •OH scavenger that deprieved the photocatalytic reaction.

In another study, Wang et al. (2019) have assessed the impacts of foreign on photodegradation of DBP by introducing foreign substances such as HCO_3^-, Cl^-, NO_3^-, SO_4^{2-} into the system. Similar to previous study, it was observed that the introduction of foreign substances into the water sample had inhibitory effect on photocatalytic performance. The degree of inhibition

followed the trend $NO_3^- > HCO_3^- > SO_4^{2-} > Cl^-$. Inhibitory effect mainly arose from reaction with reactive species and eventually consumed the active species that participated in photodegradation.

Song et al. (2015) have studied the effect of foreign substances on photocatalytic performance of DEP using TiO_2. In their study, several foreign substances such as humic acid, HCO_3^-, CO_3^{2-}, NO_3^-, SO_4^{2-} were included in their assessment. A reduction in degradation efficiency was observed when humic acid was added. This can be explained by shading effect caused by high turbidity and occupied the active species in photocatalytic activity. Moreover, the degradation of DEP was inhibited when HCO_3^-, CO_3^{2-}, NO_3^-, SO_4^{2-} were introduced. The negative effect was arranged in the order: $CO_3^{2-} > NO_3^- > HCO_3^- > SO_4^{2-}$. This was resulted from the competition between the pollutant molecules and the anions for the active species. The reactive species with less redox potential than •OH were generated such as $NO_2^\bullet$, $SO_4^{\bullet-}$, $CO_3^{\bullet-}$ which resulted in deterioration of photocatalytic efficacy in DEP degrdation.

The study from Liu et al. (2020) also reported that the degradation of DBP was greatly affected when foreign substances such as HCO_3^-, CO_3^{2-}, Cl^-, NO_3^- and SO_4^{2-} introduced into their photocatalytic system. With the introduction of HCO_3^-, CO_3^{2-}, Cl^-, NO_3^-, the degradation efficiency was observed to drop from 73.6% to 44.4%, 11.8%, 47.9% and 34.6% due to the consumption of active scpecies by the foreign substances. However, the addition of SO_4^{2-} improved the degradation efficiency from 73.6% to 85.8% which attributed to the formation of $SO_4^{\bullet-}$ with redox ability that can assist in photocatalytic performance. Overall, most of the added foreign substances

competed with the pollutants for photogenerated active species which resulting in deterioration of photocatalytic efficacy. Table 2.8 summarises the studies of different photocatalysts used in PAEs degradation under different operating condition and different foreign substances added.

.

Table 2.8: Effect of foreign substances on photocatalytic degradation of various PAEs.

Photocatalyst	Degraded Pollutant	Condition	Foreign substances	Results	Reference
Gr/TiO$_2$	DBP	Substrate concentration = 10 mg/L; Irradiation time = 90 min light source = Xenon lamp	HCO$_3^-$ Cl$^-$ NO$_3^-$ SO$_4^{2-}$	The adding of foreign substances resulting in restraint of degradation efficiency from 98% to 60.9%.	Wang et al. (2019)
GR/WO$_3$/TiO$_2$	DMP	Irradiation time = 120 min light source = 150 W Xenon lamp	NO$_3^-$ HCO$_3^-$ Cl$^-$ SO$_4^{2-}$	The adding of of foreign substances resulting in restraint of degradation efficiency from 75% to 43.9%.	Wang et al. (2018)
FeO$_2$H	DBP	Substrate concentration =8 mg/L; Irradiation time = 150 min light source = UVA lamp	NaCl	The adding of NaCl resulting in restraint of degradation efficiency from 80% to 11%.	Hejda et al. (2023)

Table 2.8: Continued.

$Bi_2O_2CO_3/Bi_2S_3$	DBP	Substrate concentration =10 mg/L; Irradiation time = 180 min light source = 500 W Xenon lamp	NO_3^- CO_3^{2-} HCO_3^- Cl^- SO_4^{2-}	The adding of foreign substances resulting in restraint of degradation efficiency from 73.6% to 11.8%, except the SO_4^{2-} boosted the photocatalytic performance to 85.8%.	Liu et al. (2023)
TiO_2	DEP	Substrate concentration = 1.28 mg/L Irradiation time: 30 min light source = 30 W mercury lamp	HCO_3^- CO_3^{2-} NO_3^- SO_4^{2-} humic acid	The adding of foreign substances resulting in decline of rate constant from 0.0636 to 0.0321.	Song et al. (2015)

2.9 LOW DENSITY POLYETHYLENE (LDPE)

Low density polyethylene (LDPE) is a thermoplastic polymerized from ethylene, has a highly branched structure from both long and short chain branches which interfere with crystallization (Dietrich et al. 2018). It categorised as 1st grade in polyethylene. It was firstly manufactured in 1993 by Imperial Chemical Industries using high pressure technique via free radical polymerization.

LDPE is one of the most widely used polymers, with production around 19 M tonne per year. In year 2013, the worldwide market of LDPE has reached a volume of about 33 billion USD (Tsala-Mbala et al., 2022). It has been applied in broad variety of applications. LDPE is widely used in packaging like trays, foils and plastic wrap for food and nonfood purpose. For instance, one of its most popular applications is in milk cartons. Other applications including foil wrapping for packaging, plastic bag, garbage bags, multipurpose containers, plastic toys, and etc. In year 2018, the most important sales market for LDPE falls on application area of "packaging film" with demand of 5.74 million tonnes. In terms of demand volume, the application of construction area apparently achieve the highest percentage and continue to increase until 2026 with average growth rate of 2.7% per year (Aupetit, 2021).

LDPE has a density ranged from 917-930kg/m^3. It was produced in translucent and opaque cariations, with tough and flexible properties. Its resistence to chemicals was summarized in Table 2.9 below:

Table 2.9: Chemical resistance of LDPE towards different chemcials (Lahari and Sharma, 2022).

Resistance level	Chemicals
Excellent	Acids, alcohols, Alkalis, esters
Good	Aldehyde. Ketones, vegetable oils
Limited	Aromatic and aliphatic hydrocarbons, mineral oils, oxidizing agents
Poor	Halogenated hydrocarbons

In year 2010, it was estimated that around 275 million metric tons (MT) of plastic waste was generated among 192 coastal countries. In this regards, 31.9 million MT of plastic waste were categorized as mismanaged and hence ends up with estimated 4.8 to 12.7 million MT of plastic waste entered marine ocean. Plastics pollution in ocean environment are of increasing concern due to their persistence properties such as chemical resistance and phthalate additives introduce into plastic during manufacturing process. All these resulted in negative impacts on marine life, wildlife and potentially, humans. As times goes by, weathering of plastic waste led to plastic fragmentation that eventually turned it into particle size that easily ingested by aquatic life and marine invertebrates. In addition, plastic debris could be found floating on sea surface or accumulated at seafloor. These plastics were so small in size that was source intraceabe and extremely difficult to remove it from open sea area.

Traditional plastic managements include recycling, incineration or send to sanitary landfill. However, some of the materials are bioinert and are highly resistant to assimilation by microorganism. Thus, the plastic including LDPE

unable to undergo biodegradation that involves bioassimilation of substrate molecules.

Fortunately, scientists have a breakthrough in plastic research. The mechanism of polyethylene degradation has been established and known as oxo-biodegradable which involves two stages. The first stage was known as abiotic photo-oxidation or thermos-oxidation. The second stage was referred to microbial biodegradation. The rate of polyethylene degradation was subjected to abiotic oxidation stage which can be speeded up by incorporation of pro-oxidant into material. In this way, the polymer can be oxidized, where its molar mass can be reduced by the oxygenated groups generated by pro-oxidant. Recently, photocatalyst was identified as an effective pro-oxidant which capable in polyethylene degradation by generating reactive radicals.

2.10 PHOTODEGRADATION OF LDPE

Several studies have shown photocatalysts was the promising pro-oxidant and can be incorporated into polyethylene for photodegradation. For example, Liang et al. (2013) have prepared a photocatalytic polyacrylamide grafted TiO_2 (PAM-g-TiO_2) and embedded into LDPE plastic. During photocatalytic experiment, both the pure LDPE film and the LDPE/PAM-g-TiO_2 composite film were irradiated under UV light. After the irradiation, both of the films were analysed and compared with their weight loss, functional or carbonyl groups and tensile strength. It was observed that the composite film reduced its weight by 39.85% after 520 h of UV irradiation, while the pure film only reduced 1.03% of its weight. This was because the TiO_2 can react with

absorbed H_2O in the film and generated reactive species which accelerated the LDPE degradation. It was noticed that the intensities of carbonyl peak in the LDPE composite film was stronger than bare LDPE film. The tensile strength of composite film was found to be weaker when compared to pure LDPE film due to the photo-oxidation of film that created voids and cavities which destroyed the film structure.

Similar study was carried out by Ali et al. (2016) where they embedded TiO_2 into low density polyethylene (LDPE) film for photodegradation. The LDPE films before and after exposed to visible light were evaluated by weight loss, FTIR, SEM analysis and tensile strength testing. The LDPE film incorporated with TiO_2 showed higher degradation up to 50% when compared to bare LDPE film which only showed 2% degradation under visible light. In FTIR analysis, an increase in -OH stretching region was observed due to generation of hydroperoxide and alcohol during photo-oxidation of LDPE film. The SEM images revealed that those composite films contained cavities arised from interconnected holes arised from photodegradation. Moreover, tensile strength measurement also confirmed the defects and breakdowns formed on LDPE film by showing relatively reduction in film elongation measurement.

In another study, Thomas et al. (2013) incorporated TiO_2 with different sizes (50-200nm) into the LDPE film for photodegradation. It was noticed that the polyethylene film with 50 nm TiO_2 revealed the highest degradation efficiency under 300 h UV irradiation. Furthermore, the SEM images revealed the film loaded with 50 nm contained larger cavities when compared to others. Some variations in IR spectra were noticed which attributed to changes in film structure during degradation.

All the literatures above proved that the incorporation of photocatalysts into LDPE film was a promising strategy to photo-oxidize and accelerated the degradation of LDPE film.

2.11 SUMMARY OF LITERATURE REVIEW

The comprehensive literature review reveals that there are no reports regarding the application of double Z-scheme ZnO/Bi_2WO_6/spinel ferrites as photocatalyst. The selection of spinel ferrites according to suitable band position and bandgap can be investigate in constructing a double Z-scheme composite. The assessment on the role of active species, charge transfer pathway and mechanism of ternary composite in DMP degradation were verified and proposed in details. However, there still some challenges in applying the photocatalyst in real industry, for example the cost consideration, environmental variability and long-term stability. Cost consideration such as budget constraint for implementing photocatalytic processes in industrial setting lies in managing the cost of catalyst materials, reactors and maintenance within a given financial framework. Industrial wastewater can vary widely in composition and foreign substances, and the photocatalytic system must be robust enough to handle this variability. Photocatalysts may face degradation over time due to factors such as exposure to harsh industrial conditions, it was crucial to maintain its photocatalytic performance in industrial application. Therefore, operating paramenters such as catalyst loading, pH and foreign substances were included to simulate the real wastewater environment in order to investigate and overcome the limitation. Moreover, the stability of the

photocatalyst was assessed through a cyclic experiment. In addition, the prepared composite can be applied in photo-oxidate and accelerate the degradation of LDPE film. To date, there are no reports on LDPE film degradation using ZnO/Bi_2WO_6/spinel ferrites composite. From the practical perspective, the engagement of photocatalyst in LDPE film degradation was applicable as it can help in fragmentation of plastic and useful in reducing solid waste.

CHAPTER 3

METHODOLOGY

3.1 FLOWCHART OF LAB WORK

The study could be divided into several stages, and the flowchart in Figure 3.1 provides a summary of the overall experiments conducted.

Synthesis of of ZnO/Bi$_2$WO$_6$ composites; Bi$_2$WO$_6$ loading: 15-25 wt%

Synthesis of of ZnO/Bi$_2$WO$_6$/SF composites SF: CaFe$_2$O$_4$, BaFe$_2$O$_4$ and SrFe$_2$O$_4$

Synthesis of of ZnO/Bi$_2$WO$_6$/ SrFe$_2$O$_4$ composites; SrFe$_2$O$_4$ loading: 5 - 20wt%

Characterization of as-synthesized products: XRD, FESEM, EDX, TEM, HRTEM, UV-vis DRS and TA-PL analysis

Screening of ZnO/Bi$_2$WO$_6$/SF composites on photocatalytic degradation of DMP:

Check — No

Yes

Operating parameter study:
1. Effect of catalyst loading (range: 0.5 g/L – 2.0 g/L)
2. Effect of pH (range: pH 5 – pH 11)
3. Effect of foreign substances (humic acid, NO$_3^-$, Cl$^-$, SO$_4^{2-}$)

Photoelectrochemical studies: photocurrent response, EIS

Photocatalytic mechanism study:
1. Photoelectrochemical test (TPR, EIS)
2. Active species detection study
3. Terephthalic acid photolumoinescene study

Reusability studies, Phytotoxicity test, Mineralization studies

Kinetic studies

Pre-treated characterization on LDPE

Photocatalytic degradation and post-treated characterization on LDPE

Figure 3.1: Overall lab work flowchart.

81

3.2 LISTING OF MATERIALS AND CHEMICALS

Table 3.1 presents the chemicals used throughout the research.

Table 3.1: List of the chemicals and materials used in the experiment.

Chemicals / Materials	Purity	Supplier	Application
Bismuth (III) Nitrate Pentahydrate $Bi(NO_3)_3.5H_2O$	~98%	Acros Organics	Synthesis of photocatalyst
Zinc Nitrate Hexahydrate $Zn(NO_3)_26 \cdot H_2O$	~98%	Sigma-Aldrich	Synthesis of photocatalyst
Dimethyl phthalate $C_{10}H_{10}O_4$	~99%	Alfa Aesar	Photocataytic activity
Nitric acid HNO_3	~65%	R&M Chemicals	Synthesis of photocatalyst
Sodium Carbonate Na_2CO_3	~99%	Acros Organic	Active species analysis
Sodium Hydroxide NaOH	~99%	GENE Chemicals	Synthesis of photocatalyst & Operating parameter study
Sodium Hypochlorite NaOCl	~10% chlorine	Chem Soln	Disinfection of mung bean
Isopropanol $(CH_3)_2CHOH$	AR grade	Chem Soln	Active species analysis
Ammonium oxalate $(NH_4)_2C_2O_4$	ACS reagent	Spectrum	Active species analysis

Table 3.1: Continued.

Chloroform $CHCl_3$	~99.8%	R&M Chemicals	Active species analysis
Sodium sulfate Na_2SO_4	ACS grade	Sigma-Aldrich	Active species analysis
Terephthalic Acid $C_8H_6O_4$	~98%	Merck	Active species analysis
Iron (III) Nitrate $Fe(NO_3)_3 \cdot 9H_2O$	~99%	R&M Chemicals	Synthesis of photocatalyst
Sodium tungstate Na_2WO_4	~99%	Acros Organic	Synthesis of photocatalyst
Potassium nitrate KNO_3	~99%	Bendosen	Operating study
Potassium sulfate K_2SO_4	~99%	Chem Soln	Operating study
Humic acid sodium salt	45-70%	Thermo scientific	Operating study
Barium nitrate $Ba(NO_3)_3$	~99%	Systerm	Synthesis of photocatalyst
Calcium nitrate $Ca(NO_3)_2 \cdot 4H_2O$	~99%	R&M Chemicals	Synthesis of photocatalyst
Strontium nitrate $Sr(NO_3)_2$	~99%	R&M Chemicals	Synthesis of photocatalyst
n-Hexane C_6H_{14}	ACS grade	Merck	Intermediates analysis
Dichloromethane CH_2Cl_2	ACS grade	Chem Soln	Intermediates analysis
Methanol CH_3OH	AR grade	Chem Soln	Intermediates analysis

Table 3.1: Continued.

| Cyclohexane | AR grade | R&M Chemicals | LDPE film |
| C_6H_{12} | | | synthesis |

3.3 FABRICATION OF PHOTOCATALYSTS

3.3.1 Fabrication of Marimo-like ZnO/Bi_2WO_6 Composites (Bi_2WO_6 loadings: 15wt%, 20 wt% and 25 wt%)

Marimo-like Bi_2WO_6 was synthesized using a hydrothermal method. Initially, 6 mmol of $Bi(NO_3)_3.5H_2O$ was dispersed in diluted HNO_3 (0.4M) and the mixture was ultrasonically treated for 10 min. After that, Na_2WO_4 solution (3 mmol) was gradually added into the $Bi(NO_3)_3$ suspension and underwent continuous stirring for 1 h. The mixture was placed in a stainless-steel autoclave lined with Teflon and subjected to a temperature of 175°C for a duration of 16 h. The precipitated compound was separated by filtration., rinsed with deionized water and ethanol alternatively before dried in oven at 65°C for 24h.

Following were typical steps in the synthesis of ZnO/Bi_2WO_6 composites: 4 mmol of $Zn(NO_3)_2 \cdot 6H_2O$ and 0.0462 g of Marimo-like Bi_2WO_6 were dispersed in 80 mL deionized water. The mixture was ultrasonicated for 30 min. Subsequently, NaOH (0.024 mol) was added dropwise into mixture and followed by stirring for 17 h. The precipitate was dried at 65°C until the water was entirely evaporated. The dry powders were calcined at 450°C in a muffle furnace for 2 h under ambient air pressure. The calcined powder was referred to 15BWZ. To examine the relation between the weight ratio of ZnO

and Bi_2WO_6, a series of samples with different amounts of Bi_2WO_6 (20wt% and 25wt%) were synthesized under the same experimental circumstances and the resulting composites were labelled as 20BWZ and 25BWZ, respectively. The bare ZnO was fabricated without loading of Marimo-like Bi_2WO_6.

3.3.2 Preparation of Spinel ferrites/Bi_2WO_6/ZnO Composites (spinel ferrites, SF: $SrFe_2O_4$, $BaFe_2O_4$ and $CaFe_2O_4$)

$Ca(NO_3)_2 \cdot 4H_2O$ and $Fe(NO_3)_3 \cdot 9H_2O$ at 1:2 M molar ratio, were dissolved in 150 mL of distilled water using a magnetic stirrer at room temperature. Then, NaOH was dropped wise into the mixture, which was then adjusted to pH 11. The mixture was stirred for 1 h and transferred to an autoclave and heated at 180 °C for 16 h. The solution was filtered and dried at 65 °C. Finally, the obtained product was labelled as $CaFe_2O_4$. The other spinel ferrites were synthesized under the similar synthesis conditions by replacing the precursor to $Ba(NO_3)_2$ and $Sr(NO_3)_2$, and the obtained composites were denoted as $BaFe_2O_4$ and $SrFe_2O_4$, respectively

The typical synthesis of 10SF20BWZ composites, (SF = $SrFe_2O_4$, $BaFe_2O_4$ and $CaFe_2O_4$) were as follows: 0.2615 g $Zn(NO_3)_2 \cdot 6H_2O$, 0.0654 g of Marimo-like Bi_2WO_6 and 0.0363g of SF were dispersed in 80 mL deionized water. The mixture was ultrasonicated for 30 min. Next, 1.008 g of NaOH was introduced into mixture under stirring condition. The mixture was stirred for another 17 h. The precipitate powders were dried at 65°C until the water was entirely evaporated. The powders were calcined at 450°C using muffle furnace to obtain the 10wt%20BWZ. To examine the relation between the type of SF

and 20BWZ, a series of samples with different types of SF were synthesized under the similar experimental conditions and the resulting catalyst were designated as 10Sr20BWZ, 10Ba20BWZ and 10Ca20BWZ, respectively. In addition, the Sr20BWZ composites with different amounts of $SrFe_2O_4$ (5wt% - 20wt%) were synthesized using fabrication procedure similar to 10Sr20BWZ except for loading of $SrFe_2O_4$ (5wt% -20wt%). The as-prepared catalysts were synthesized and evaluated to determine the optimum loading of $SrFe_2O_4$ in dual Z-scheme composites. The samples were labelled as 5Sr20BWZ, 15Sr20BWZ and 20Sr20BWZ, respectively.

3.4   PREPARATION OF PURE AND COMPOSITE LDPE FILM

Pure LDPE films were prepared by a wet casting method. Firstly, 0.5g LDPE beads were dissolved in 50 mL cyclohexane at 70-80 °C under continuous stirring for 2 h. The suspension was poured into petri dish to obtain bare LDPE film. Composite LDPE films were produced by dissolving desired amount of photocatalyst in the LDPE suspension and poured on glass petri dish and dried overnight at room temperature. The LDPE film was cut into 2 cm x 2 cm square pieces and exposed to sunlight for degradation experiment.

3.5   CHARACTERIZATION OF AS-SYNTHESIZED PRODUCT

3.5.1 X-ray Diffraction (XRD)

X-ray diffraction was employed to examine the crystallographic structure and chemical composition of a material by directing a beam of X-rays at different specific angles. The XRD pattern was obtained using a

diffractometer (Philip PW1820), scanning in the range of 20 to 70°, with Cu Kα radiation and a scanning rate of $2°min^{-1}$. The resulting data were analyzed by referencing the database provided by the Joint Committee on Powder Diffraction Standards (JCPDS). The characterization was conducted at Faculty of Science (FSC), Universiti Tunku Abdul Rahman (UTAR).

3.5.2 Field-Emission Scanning Electron Microscopy (FESEM) and Energy Dispersive X-ray Spectroscopy (EDX)

The surface morphology of the as-produced catalysts were examined through Field Emission Scanning Electron Microscopy (FESEM) analysis, while the elemental composition of the synthesized products was investigated using energy dispersive X-ray spectroscopy (EDX). The FESEM analysis was conducted with a JEOL JSM-6701F model, while the EDX and EDX mapping were performed using Oxford X-max EDX spectroscopy Prior to conducting the analysis, the sample in powder form was uniformly deposited onto carbon double-sided tape, which was then affixed to a circular aluminum stub. Before being subjected to FESEM and EDX analyses, the sample was coated with a layer of platinum together with the stub. The analyses were performed at FSC, UTAR.

3.5.3 Transmission Electron Microscopy (TEM)

Transmission electron microscopy (TEM) analysis enables the observation of the internal structure of samples through capturing images with high magnification. The Tecnai 20 electron microscope was utilized to capture the TEM images. Before analysis, the sample was added to an ethanol solution

and vigorously shaken for a few minutes. Subsequently, the suspension was set aside undisturbed to allow for sedimentation. A tiny amount of the sample was applied onto a copper grid that had been coated with a carbon film and left to dry. The dried sample, which adhered to the copper grid on the sample holder, was then subjected to TEM analysis. The TEM analysis was carried out at Malaysian Institute of Microelectronic Systems (MIMOS), Technology Park, Malaysia.

3.5.4 X-ray Photoelectron Spectroscopy (XPS)

X-ray photoelectron spectroscopy (XPS) is a technique used to analyse the surface chemistry of a material., elemental composition as well as chemical and electronic state within a material. XPS spectra were recorded using Physical Electronics XPS microprobe (PHI Quantera II). The sample was stimulated by mono-energetic Al kα X-rays, leading to the emission of photoelectrons from the surface of the sample. The emitted photoelectrons were measured by analyzer of electron energy. The chemical state and elemental composition were identified based on binding energy and photoelectron peak intensity. The analysis was carried out at Malaysian Institute of Microelectronic Systems (MIMOS), Technology Park, Malaysia.

3.5.5 Fourier Transform Infrared (FTIR) Spectroscopy

The functional group and chemical bonding of a sample can be identified through FTIR analysis. Typically, the photocatalysts and KBr with a ratio 1:5 were mixed and grinded using a mortar. The mixture was compressed into a pellet film using a FTIR compressor. The FTIR pellet was inserted into

FTIR machine and scanned from 400 - 4000 cm^{-1}. The analysis was performed using Perkin Elmer Spectrum RX 1 machine. This measurement took place at the at FSC, UTAR.

3.6. PHOTOCATALYTIC ACTIVITY MEASUREMENT

The photocatalytic performance of the as-synthesized composites was evaluated by degradation of DMP solution under sunlight irradiation. All the photocatalytic experiments were carried out between 12:00 and 14:00 on sunny daytime from November 2021 to February 2022. The average irradiation intensity was found to be about 67×10^3 lx, as measured using a lux meter (E©SUN, LX-101). The UVA and UVC radiation were determined to be ~0.427 mW/cm^2 and ~0.334 mW/cm^2, respectively, as measured by Series 9811 radiometer (Cole-Pamer Instrument Co.). During photocatalytic activities, an appropriate quantity of catalyst was disseminated in 80 ml of DMP solution, where required pH adjustment was performed using 0.1M NaOH or HCl. The solution was agitated in a "blackbox" for 0.5 h to achieve adsorption-desorption equilibrium between the DMP solution and as-prepared photocatalysts. Afterwards, it was exposed to sunlight, DMP samples were routinely collected at predetermined intervals and its concentration was analyed using a UV-vis spectrophotometer at $\lambda = 229$ nm (ThermoSCIENTIFIC: GENESYS 10S UV-Vis).

3.7   OPERATING PARAMETERS

3.7.1 Effect of 10Sr20BWZ Loading

Investigation for different catalyst loading of 10Sr20BWZ composite on photodegradation of DMP was executed in the range of 0.5 - 2.0 g/L. The catalyst loading range was based on references from research articles acquired from the literature review. (Zhang et al., 2019; Xu et al., 2020; Guan et al., 2020). The experimental works were executed using an initial DMP concentration of 5.2μM; sunlight intensity of 67×10^3 lx and at natural pH 6.5.

3.7.2 Effect of Foreign Substances

The effect of foreign susbstances on photocatalytic activity of DMP was investigated by introducing Cl^-, NO_3^-, SO_4^{2-} and humic acids into the solution. The selection of foreign substances was referring to the studies from Sun et al. (2022) and Yang et al. (2019). During the experiments, 1 mM of KCl, KNO_3 and K_2SO_4 and humic acid was added into the solution. The experiment was carried out using 10Sr20BWZ composite at 1.0 g/L; initial DMP concentration at 5.2 μM; pH of DMP at 7 under sunlight intensity of 67×10^3 lx.

3.7.3 Effect of Solution pH

Influnce of pH solution on degradation of DMP was investigated by different pH ranged from pH 5 to pH 11 by referring to literature reports (Li et al. 2021; Reddy et al. 2020). Diluted HCl and NaOH were added to adjust the solution pH into desired pH. The pH of DMP solution was determined using a

pH meter (EUTECH INSTRUMENTS PC2700). The experiment was carried out using 10Sr20BWZ composite at catalyst loading = 1.0 g/L; initial concentration of DMP = 5.2 μM under sunlight intensity of 67×10^3 lx.

3.8   PHOTOELECTROCHEMICAL STUDIES

Photoelectrochemical experiments were performed using the three-electrode scanning potentiostat (Gamry Interface 1000). The working electrode utilized in the experiment was a fluorine-doped tin oxide (FTO) plate coated with the as-synthesized sampleon Briefly, 5 mg of catalyst was mixed with 10 mL of EtOH and sonicated for 1 h. After sonication, the mixture was coated onto the FTO glass to form 2.5cm x 2.5cm coated area and dried in room temperature. 0.5M sodium sulfate (Na_2SO_4) solution was prepared as the electrolyte. Ag/AgCl and platinum wire were acted as the reference and counter electrode, respectively. Transient photocurrent (TPR) was performed with 0.4 V as a step voltage and 0.3 mA was fixed as the maximum limit of current. The frequency range for measurement of electrochemical impedance spectroscopy (EIS) was in the range of 0.01 to 10000 Hz and an amplitude of 5 mV. The Mott-Schottky curves of as-synthesized materials were acquired with starting voltage of 1.2 V, ending voltage of -1.2V and a 1000 Hz frequency. The conduction band is corresponding to the flat band potential while the flat band potential of the material can be obtained through the intersection of tangent and abscissa. The valence band was determined through the equation: $E_{VB} = E_{CB} + E_g$ (Swamy, et al., 2021), where E_{VB} is the valence band; E_{CB} is the conduction band and E_g is the band gap energy.

3.9   ANALYSIS OF ACTIVE SPECIES FORMATION

The roles of photogenerated hydroxyl radical ($\bullet$OH), positive hole (h^+), superoxide anion ($\bullet O_2^-$) and electron (e^-) in the photocatalytic activities were evaluated by adding 1 mM of isopropanol (Gracien et al., 2019; Vione et al., 2011), ammonium oxalate (Castillo-Rodríguez et al., 2023; Wang et al., 2023), chloroform (Li et al., 2020; Mukherjee et al., 2021; Zhang et al., 2022) and Na_2SO_4 (Riaz et al., 2023; Glavaski et al.,2016), respectively. The scavenger experiments were carried out using the similar procedures to those used for the photocatalytic experiment as mentioned in Section 3.6.

Furthermore, the generated $\bullet$OH during photocatalytic reaction were further verified using the terephthalic acid solution. The solution was prepared by dissolving 5×10^{-4} M terephthalic acid in 2×10^{-3} M NaOH solution. This test was carried out in a similar manner to the photodegradation experiment. The collected terephthalic acid solution at different time intervals was examined using a spectrofluorometer (Perkin-Elmer, Lambda S55) through an excitation wavelength set at 315 nm. The generated PL signal was identified as 2-hydroxyterepthalic acid which generated from reaction between terephthalic acid and $\bullet$OH radicals.

3.10 UV-vis Diffuse Reflectance Spectroscopy (UV-vis DRS) Analysis

The optical characteristic of the prepared samples was investigated using UV-vis DRS analysis. During analysis, the spectra of UV-vis DRS of the sample were obtained using a UV-vis spectrometer (Genesys 10S, Thermo Scientific). The spectra were recorded in the range of 350 - 700 nm and $BaSO_4$

was used as the reference standard. This analysis was carried out at FSC, UTAR.

3.11 INTERMEDIATES DETECTION FOR DEGRADATION OF DMP

The intermediate products of photocatalytic degradation of DMP was extracted via organic extraction and analysed by gas chromatography-mass spectrometry (GC-MS). Typically, the sample was extracted 3 times with 10 mL of mixed extraction reagent 1 ($CH_3OH:CH_2Cl_2 = 1:9$). It was followed by extraction for another 3 times using extraction reagent 2 (n-hexane:$CH_2Cl_2 = 3:7$). The obtained organic phase was dehydrated by adding anhydrous sodium sulfate before filtered and concentrated to 2 mL sample. The obtained intemediates samples were analysed by Shimadzu GC-MS QP 2010. The column used was Forte GC capillary column with model BPX5:30 m length; 0.25 mm (i.d.); column oven temp: 35 °C; Injection temperature =280 °C; retention time = 45 min.

3.12 MINERALIZATION STUDY

The degree of mineralization in DMP solution was anlysed by chemical oxygen demand (COD) method, specifically employing the dichromate reactor digestion method derived from HACH Method 8000. Preheating of COD reactor (HI 839800, HANNA Instrument) to 150 °C was necessary before COD vials were inserted for digestion. The COD vials were prepared during preheating process of COD reactor. Particularly, 2 mL of distilled water was

added into the COD digestion vial which worked as an indication for blank. After that, 2 mL of DMP solution was transferred into the COD vial. The COD vial was closed tightly and gently mixed before inserted to COD reactor. The sample was digested for 2 hours and cooled to room temperature prior to measure using COD and multiparameter photometer (HI 83099, HANNA instrument).

3.13 REUSABILITY STUDIES

The stability of the composite with the best performance was tested for four consecutive recycle runs. The solution pH was remained constant at pH 7 and catalyst loading was set at 1.0 g/L. After 90 min irradiation, the DMP solution was collected for analysis. The photocatalyst was filtered, washed with DI water for several times and finally dried at 65 °C in oven. The dried composite was then recycled in the next reaction cycle under the similar experimental conditions.

3.14 PHYTOTOXICITY TEST

Phytotoxicity of photocatalytically treated DMP solution was conducted using seed germination and root growth of *Vigna radiata*. 0.5 % of NaOCl was utilized to sterilize the chosen lively seeds and petri dish. Three petri dishes were labelled as control, degraded and untreated, respectively. In each sterilized petri dish, cotton wool was placed along with 9 *Vigna radiata* seeds. At 12-hour intervals, the petri dish labelled as control was irrigated with 3 mL of distilled water; while the petri dish that marked as degraded and untreated

were irrigated with 3 mL of the treated DMP and untreated DMP, respectively. After 6 consecutive days, the lengths of the radicles were measured to determine the level of phytotoxicity. The phytotoxicity of the sample can be calculated by using the Equation 3.1 (Dugandžić et al., 2017; Zhou et al., 2020).

$$\text{Phytotoxicity (\%)} = \frac{\text{Radicle length of control-Radicle length of sample}}{\text{Radicle length of control}} \times 100 \qquad (3.1)$$

All the photocatalytic experiments were carried out between 12:00 and 14:00 on sunny day from November 2021 to February 2022. The average irradiation intensity was found to be about 67×10^3 lx, as measured using a lux meter (E©SUN, LX-101).

3.15 PHOTODEGRADATION OF LDPE FILM

In addition, the photodegradation of LDPE film was carried out under the solar light. The photodegradation of LDPE film were performed during sunny daytime between 10:00 and 16:00 in February 2022. The irradiation intensity of sunlight was determined as about 67×10^3 lx using a photometer (E©SUN, LX-101). The UVA and UVC radiation were determined to be ~0.427 mW/cm^2 and ~0.334 mW/cm^2, respectively, as measured by Series 9811 radiometer (Cole-Pamer Instrument Co.). The measurement of weight, tensile strength of LDPE film and ATR analysis were performed before and after the photocatalytic treatment. Moreover, the ATR analysis was carried out before and after the photocatalytic analysis to evaluate the functional group of the plastic film.

3.15.1 Weight Measurement of LDPE Film

The weight of LDPE film was measured by weighing balance (LabPRO medel: DT224C) before and after exposed to sunlight irradiation. The platform of balance was cleaned before putting the weighing boat. Zeroing was done before the analysis begin. The plastic film was put on the weighing boat using stainless steel tweezer. The measurement was repeated twice for every sample and the mass of LDPE film was recorded. The weight loss (%) was calculated using Equation 3.2. The analysis was performed at Faculty of Engineering and Green Technology (FEGT), UTAR.

$$\text{Weight loss (\%)} = \frac{\text{Mass of sample before degradation - mass of sample after degradation}}{\text{Mass of sample before degradation}} \times 100 \quad (3.2)$$

3.15.2 Measurement of Tensile Strength

The LDPE film was cut into I shape using Dumbell Press & Cutters machine. The thickness of film was measured by a digital caliper. The film was clipped at the light-weight tensile tester. The tensile strength was analysed using tensile tester that connected to computer installed with "QMAT" software that was ideally for tensile strength analyser. The analysis was performed at FEGT, UTAR.

3.15.3 Attenuated Total Reflectance (ATR) Analysis

ATR analysis was used to identify the functional group and chemical bonding of a sample without grinding and turning the sample into a pellet form. Before sample placement, the analysis stage was wiped with ethanol to eliminate the pollutants from the lens and analysis stage. Then, a suitable knob

was installed and screwed until suitable force. The ATR analysis was started by running the ATR programme installed on computer. The functional groups of LDPE film can be identified by scanning the sample in the range of 400 - 4000 cm^{-1}. The analysis was performed using Perkin Elmer UATR Two machine at FSC, UTAR.

CHAPTER 4

RESULTS AND DISCUSSION

4.1 CHARACTERIZATION STUDIES ON AS-SYNTHESIZED CATALYSTS

4.1.1 X-ray Diffraction (XRD)

The crystalline structure of as-prepared catalysts was explored via X-ray diffraction (XRD) analysis. Figure 4.1 displays the XRD spectra of pure ZnO, Bi_2WO_6 and BWZ composites with various Bi_2WO_6 loadings (15 wt% - 25 wt%). The detected XRD peaks matched with the characteristic peaks sourced from Joint Committee Powder Diffraction Standard (JCPDS) database to identify the plane and structure of the sample. As shown in Figure 4.1a, the observed peaks were correponded to the (100), (002), (101), (102), (110), (103), (200), (112) and (201) planes of ZnO hexagonal wurtzite structure at 2θ angles of 31.8°, 34.4°, 36.3°, 47.6°, 56.6°, 62.9°, 66.4°, 67.9° and 69.1° (JCPDS file no. 0036-1451) (Kumar, Kaushik and Purohit, 2022). The diffraction peaks located at 25.8°, 28.3°, 32.9°, 47.2°, 55.9° and 58.7° were indexed to (111), (131), (002), (202), (133) and (262) planes that matched with Bi_2WO_6 orthorhombic phase (JCPDS File No. 39-0256) (Suryavanshi et al., 2022; Ahsaine et al., 2013; Liu et al., 2020). Additionally, the characteristic peaks associated with ZnO and Bi_2WO_6 were detected in diffraction spectras of as-synthesized composites, indicating the BWZ composites were successfully fabricated. Liu et al. (2020) have synthesized Bi_2WO_6 via a hydrothermal route The crystal structure of as-synthesized catalyst was characterised via XRD

method. Based on the result findings, the XRD plane of as-prepared Bi_2WO_6 was in well agreement with the standard data of orthorhombic phase for Bi_2WO_6.
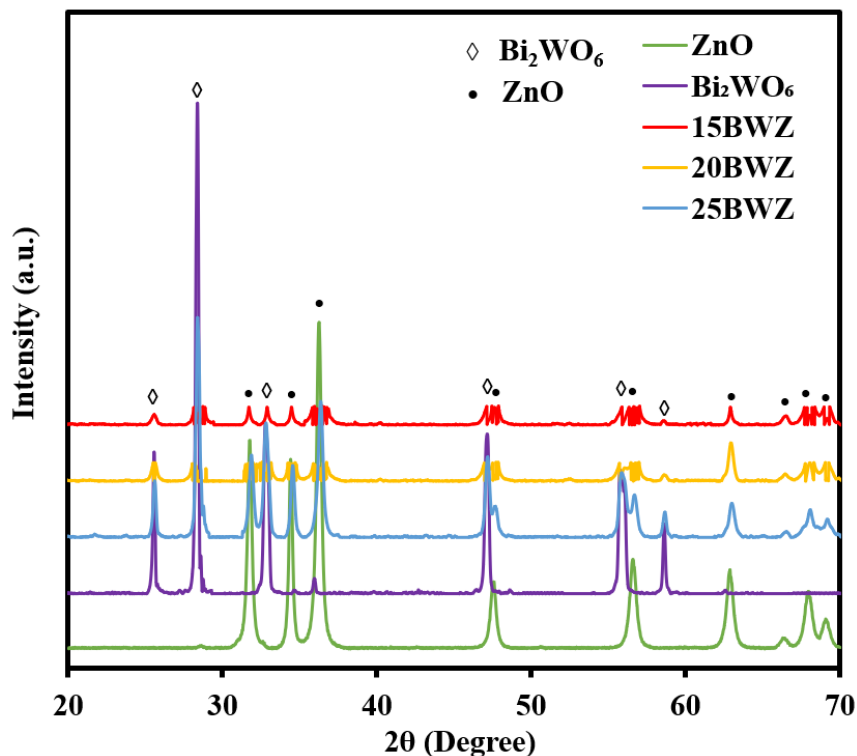
Figure 4.1: XRD patterns of ZnO, Bi_2WO_6 and BWZ composites.

Figure 4.2 shows the XRD diffraction pattern of single ZnO, Bi_2WO_6, $SrFe_2O_4$, $CaFe_2O_4$, $BaFe_2O_4$ and SF20BWZ composites. The diffraction peaks of $CaFe_2O_4$ which observed at 23.9°, 30.9°, 33.4°, 36.6°, 40.6°, 48.2°, 54.0°, 61.9° and 64.0° corresponded to (220), (230), (320), (201), (131), (401), (260), (170) and (261) planes of orthorhombic $CaFe_2O_4$ (JCPDS File No. 32-0168) (Liu et al., 2009; Behera et al., 2019). In $BaFe_2O_4$, the diffraction peaks detected at 24.5°, 34.8°, 42.7°, 45.2° and 47.4° were in accordance with (311), (701), (044), (422) and (214) planes of orthorhombic $BaFe_2O_4$ (JCPDS 46-0113) (Candeia et al., 2007). For $SrFe_2O_4$, the diffraction peaks that appeared at 30.2°, 33.4°, 36.1°, 44.7°, 54.6° and 63.1° matched with (220), (311), (222),

(400), (333) and (440) planes of $SrFe_2O_4$ cubic spinel phase (JCPDS 08-0234) (Zafar et al., 2018). Moreover, it was observed that the diffraction peaks for ZnO and Bi_2WO_6 were observed in all the SF20BWZ composites. In addition to ZnO and Bi_2WO_6, diffraction peaks of $CaFe_2O_4$ were observed in 10Ca20ZBW at 23.9°, 30.9°, 33.4°, 36.6°, 40.6°, 48.2°, 54.0°, 61.9° and 64.0° which corresponded to (220), (230), (320), (201), (131), (401), (260), (170), (600) and (261) planes of orthorhombic $CaFe_2O_4$. The little peaks at (320) and (600) were hardly observed through peak broadening due to overlapping of other peaks such as ZnO and Bi_2WO (Pasuk et al., 2021; Askari and Salarizadeh, 2020; Tan, Cheng and McNeill, 2020). Askari and Salarizadeh (2020) have synthesized $NiFe_2O_4$/rGO via a hydrothermal method and its crystal structure was characterised by XRD. They found that some weak peaks of the XRD diffraction peaks of $NiFe_2O_4$/rGO have disappeared due to overlap with the rGO peaks. Similarly, in 10Ba20ZBW, diffraction peaks other than ZnO and Bi_2WO_6 were detected at 24.5°, 42.7°, 45.2° and 47.4° and in accordance with (311), (044), (422) and (214) planes of orthorhombic $BaFe_2O_4$ (JCPDS 46-0113). However, the weak peak at 34.8° which corresponded to (701) was hard to observe due to overlapping with other characteristic peaks in the composite (Yan et al., 2019; Askari and Salarizadeh, 2020). Yan et al. (2019) have characterised CA/GNs0.5 using XRD analysis. It was reported that one of the diffraction peaks disappeared in XRD pattern due to overlapping of CNs plane. In 10Sr20ZBW composite, diffraction peaks at 30.2°, 33.4°, 36.1°, 44.7°, 54.6° and 63.1° were noticed apart from characteristic peaks of ZnO and Bi_2WO_6, which matched with (220), (311), (222), (400), (333) and (440) planes

of $SrFe_2O_4$ cubic spinel phase (JCPDS 08-0234) (Zafar et al., 2018). The XRD results suggesting that the SF were successfully loaded on 20ZBW composite.
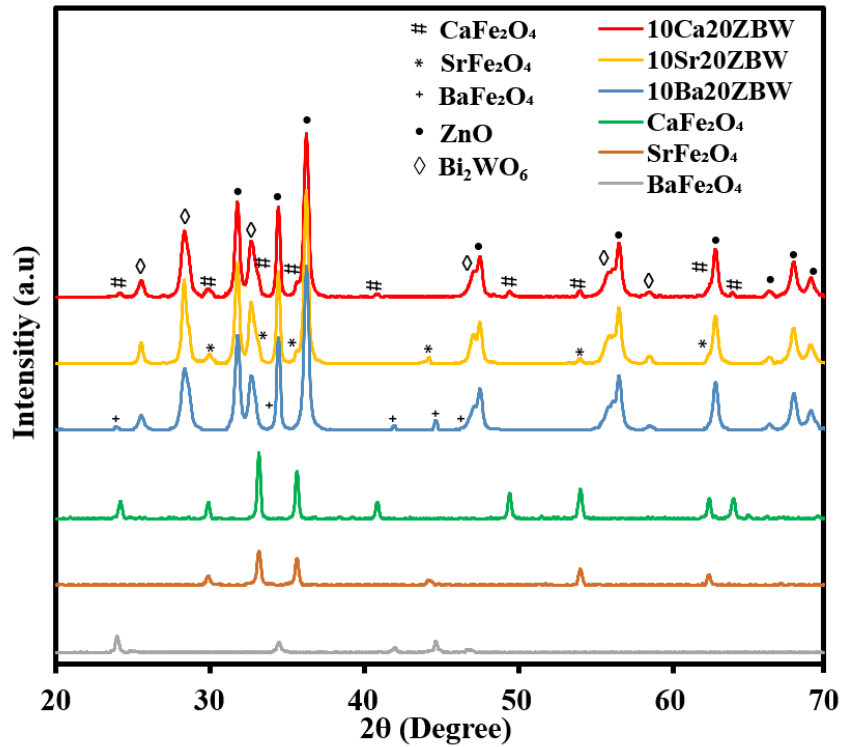
Figure 4.2: XRD patterns of ZnO, Bi_2WO_6, $CaFe_2O_4$, $SrFe_2O_4$, $CaFe_2O_4$ and 10SF20BWZ composites.

Figure 4.3 reveals the XRD pattern of Sr20BWZ composites with various $SrFe_2O_4$ loadings. From the result, it can be observed that the XRD planes of ZnO, Bi_2WO_6 and $SrFe_2O_4$ were detected further indicating the successful incorporation of ZnO, Bi_2WO_6 and $SrFe_2O_4$ into the Sr20BWZ composite. It was noted that the peak intensity of ZnO and Bi_2WO_6 getting broader when the loading of $SrFe_2O_4$ increased. It could be due to overlapping of two planes and crystalline size effect (Holder and Schaak, 2019; Soufi et al. 2022; Nath et al., 2020). Holder and Schaak (2019) have related the peak broadening was due to overlapping of two planes that located close to each other with different peak widths. Similar finding was reported by Soufi et al. (2022). In their study, $CuFe_2O_4/MgFe_2O_4$ composites have been prepared in

101

various $MgFe_2O_4$ loadings for degradation of tartrazine. It was observed that when magnesium ferrites loading increased, the intensities of XRD peaks broaden and reduced which caused by overlapping of two different planes. Another study from Nath et al. (2020) have reported that the diffraction peak gets broader could be due to the crystalline size effect and intrinsic strain effect that originated from physical and instrumental broadening.
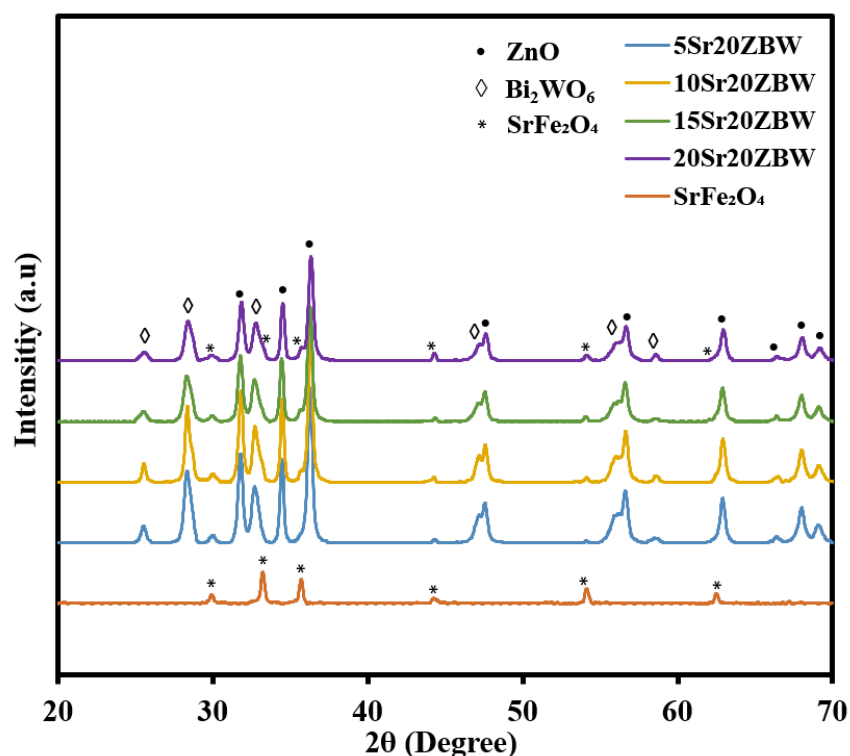
Figure 4.3: XRD patterns of ZnO, Bi_2WO_6, $SrFe_2O_4$ and Sr20BWZ composites with 5 wt%, 10 wt%, 15 wt% and 20 wt% of $SrFe_2O_4$.

4.1.2 Energy Dispersive X-ray (EDX) analysis

To determine the elemental components of the as-prepared samples, energy dispersive X-ray (EDX) analysis was conducted. Figure 4.4 displays the EDX spectra obtained from EDX spectroscopy for 20BWZ, 10Ca20BWZ, 10Ba20BWZ and 10Sr20BWZ composite. The elemental weight composition

of the samples are tabulated in inset of Figure 4.4. From results, elements Zn, O, Bi and W were observed in all samples above by showing their respective spectra and elements in EDX spectrum. Moreover, the presence of Ca, Ba and Sr elements were observed by showing peaks in EDX spectra of 10Ca20BWZ, 10Ba20BWZ and 10Sr20BWZ composites. Besides, the element weight of Ca, Ba and Sr were detected as 6.91, 7.89 and 6.25, respectively.
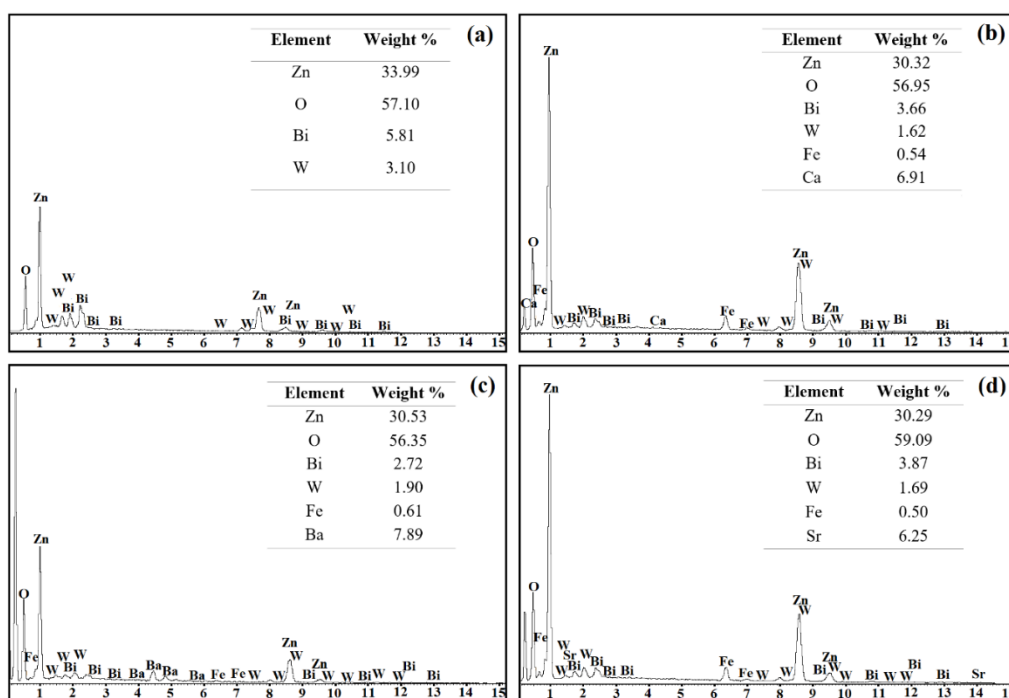
Figure 4.4: EDX spectra of (a) 20BWZ (b) 10Ca20BWZ, (c) 10Ba20BWZ and (d) 10Sr20BWZ composite.

In addition, EDX mapping was used to analyse the existence of elements in catalyst by showing elemental name with respective colour indication. Figure 4.5 shows the results of elemental mapping for 20BWZ and 10SF20BWZ composites. The results revealed the existence of Zn, O, Bi, W and Fe in all the 20BWZ, 10Ca20BWZ, 10Ba20BWZ and 10Sr20BWZ composites. In addition, element Ca, Ba and Sr were found to disperse homogeneously in 10Ca20BWZ, 10Ba20BWZ and 10Sr20BWZ composites. The obtained results consistent with the analysis of the EDX spectrum

discussed earlier, providing further confirmation of the successful fabrication of 20BWZ, 10Ca20BWZ, 10Ba20BWZ and 10Sr20BWZ composites.
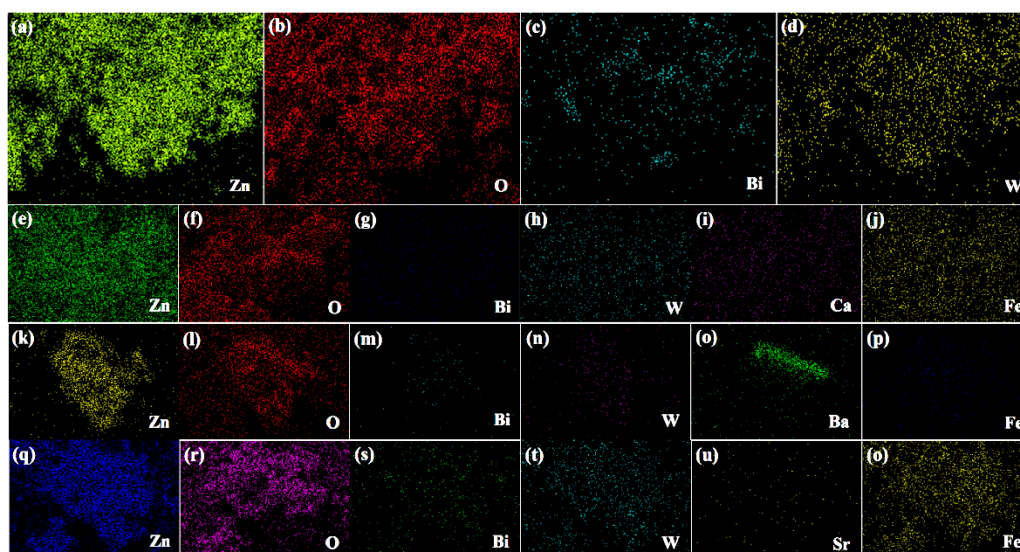
Figure 4.5: EDX mapping of (a-d) 20BWZ composite, (e-j) 10Ca20BWZ, (k-p) 10Ba20BWZ, (q-o) 10Sr20BWZ composite.

4.1.3 Field Emission Scanning Electron Microscopy (FESEM) Analysis

The morphologies and surface of pure ZnO, Bi_2WO_6, 15BWZ and 20BWZ were assessed by FESEM and their images are displayed in Figure 4.6. Figure 4.6a shows the image of FESEM for bare ZnO. ZnO displayed mammillaria-like hierarchical morphology. The average size of ZnO was in the range of 1–4 μm, which consists of lamellar layers that resembled and formed a mammillaria-like hierarchical structure. The image of pure Bi_2WO_6 is displayed in Figure 4.6b. Bi_2WO_6 exhibited a Marimo-like structure with sizes of 2–8 μm that assembled from numerous nanosheets. The image of 20BWZ and 25BWZ are shown in Figure 4.6c and Figure 4.6d, respectively. It was observed that Mammillaria-like ZnO was grew and adhered firmly to the Bi_2WO_6 aperture in both 20 BWZ and 25 BWZ composite. Due to the intimate interface contact between the two photocatalysts, this is beneficial in speed up

the photogenerated charge transfer of as-prepared composites during photocatalytic reaction. Moreover, the increasing in Bi_2WO_6 loading to 25 wt% did not reveal any noticeable modification to the overall morphology.
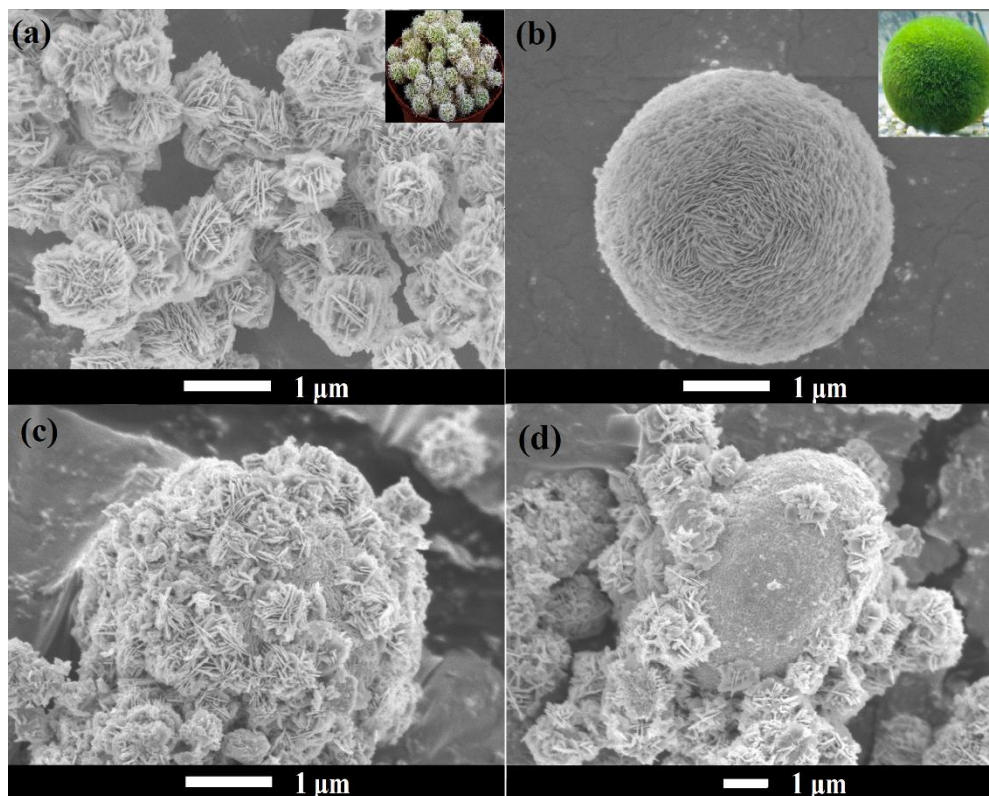
Figure 4.6: FESEM images of (a) pure ZnO (b) pure Bi_2WO_6 (c) 15BWZ and (d) 20BWZ.

Figure 4.7 a-c show the FESEM image of 10Ca20BWZ, 10Ba20BWZ and 10Sr20BWZ composites. All these ternary composites revealed that the Marimo-like Bi_2WO_6 was covered by mammillaria-like ZnO and SF. The SF particles were found perfectly integrated into the remaining slits and porous sites of 20BWZ composite and formed Brassica Oleracea-like structure. The FESEM image with higher Sr loading is displayed in Figure 4.7d. It was noticed that higher loading of Sr (20wt%) did not create major modification in overall morphology of 20BWZ but increasing the amount of Sr rod-like structure on 20BWZ. This makes the surface of 20BWZ rougher and fully occupied the slits and empty gaps of 20BWZ.
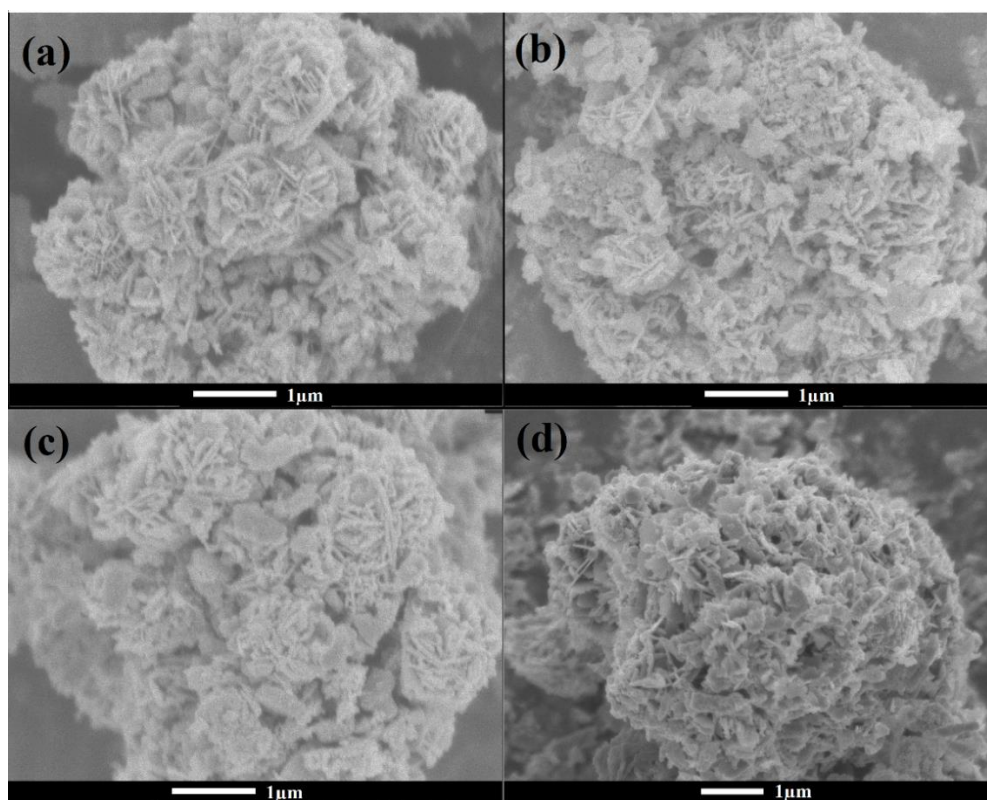
Figure 4.7: FESEM images of (a) 10Ca20BWZ (b) 10Ba20BWZ (c) 10Sr20BWZ (d) 20Sr20BWZ.

4.1.4 Transmission Electron Microscopy (TEM) analysis

TEM images enable the visualization of the internal structure and detailed morphology of the samples through determine the lattice spacing of the material. Figure 4.8a-b and Figure 4.8c-d show the TEM image of 20BWZ and 10Sr20BWZ composites, respectively. The TEM images further confirmed the as-prepared composite was in parallel with the findings from FESEM in terms of size structure and morphology description. ZnO was observed to load on Bi_2WO_6 as shown in Figure 4.8a. Figure 4.8b shows the TEM image of 20BWZ composite where the lattice spacing was determined to be 0.26 nm which corresponded to (002) plane of ZnO. Additionally, the lattice spacing with 0.317 nm was ascribed to (131) plane of Bi_2WO_6. The TEM image from Figure 4.8c revealed that both ZnO and $SrFe_2O_4$ rods lay and gripped tightly on Bi_2WO_6 structure. Moreover, the TEM image from Figure 4.7d also revealed

106

the presence of three different lattice spacings of 0.276nm, 0.317 nm and 0.268 nm in 10Sr20BWZ which corresponding to (100) wurtzite hexagonal plane of ZnO, (131) plane of Bi_2WO_6 and (311) plane of $SrFe_2O_4$, respectively. This confirmed the successful synthesis of 10Sr20BWZ composite via the existence of characters planes ZnO, Bi_2WO_6 and $SrFe_2O_4$.
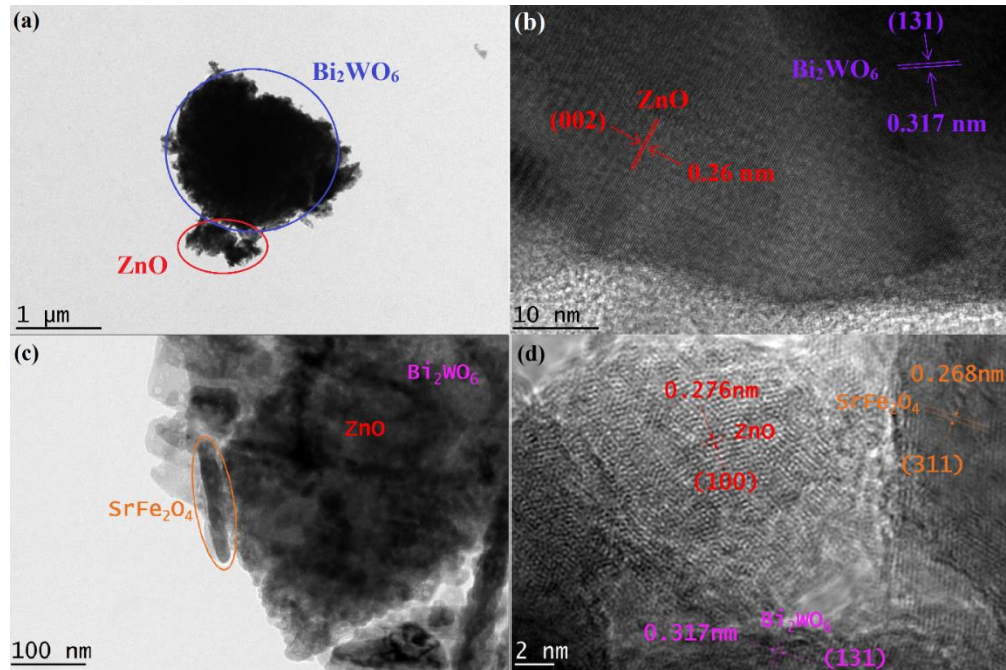
Figure 4.8: TEM images of (a),(b) 20BWZ and (c),(d) 10Sr20BWZ composites.

The findings were in good agreement with the reported literature reviews. Janani et al. (2021) have synthesized $ZnO@CuFe_2O_4$ via a chemical co-precipitation. The as-prepared composite was analysed by TEM and a lattice spacing of 0.26 nm was observed which corresponded to the (002) plane in ZnO. Wang et al. (2021) have synthesized ZnO/Co_3O_4 and a lattice spacing of 0.276 nm was detected in TEM analysis which attributed to (100) plane in ZnO. Atla and Oh (2022) have prepared MoS_2/Bi_2WO_6 via a hydrothermal approach. The microstructure of the MoS_2/Bi_2WO_6 was examined by TEM. The TEM image revealed the lattice fringe with interplanar spacings of 0.371 nm was corresponded to (131) plane of Bi_2WO_6. Ateia et al. (2023) have

reported the lattice fringe of 0.268 nm was corresponded to plane (311) of SrFe$_2$O$_4$. All these results strongly supported the XRD results as discussed in section 4.1.1.

4.1.5 X-Ray Photoelectron Spectroscopy (XPS) Analysis

XPS can be employed to identify the chemical and electronic state within a material. The XPS spectrum of 10Sr20BWZ composite is shown in Figure 4.9. The result revealed that the 10Sr20BWZ composite contained Zn 2p, O 1s, Bi 4f and W 4f elements. Figure 4.9a shows the characteristic peaks of Zn 2p. The characteristic peaks at 1020 eV and 1043 eV of Zn 2p belonged to Zn 2p$_{3/2}$ and Zn 2p$_{1/2}$, respectively, which suggested the chemical states of zinc was in divalent (Girijia et al., 2021). In O 1s spectrum (Figure 4.9b), two binding energies were detected at 528.8 eV and 530.7 eV which can be corresponded to crystal lattice O atom (Li et al., 2015) and surface hydroxyl groups (Zhang et al., 2019), respectively. Similarly, in Figure 4.9c, the XPS spectrum of Bi 4f also displayed two asymmetric peaks with peak energies located at 157.2 and 162.4 eV. These were attributed to the doublets of Bi 4f$_{7/2}$ and Bi 4f$_{5/2}$, respectively (Hu et al., 2019). In Figure 4.9d, the peaks at 26.3 eV and 35 eV were attributed to W4f$_{7/2}$ and W4f$_{5/2}$ shakeup satellites, respectively. This indicated the shifting energy of two W 4f peaks and evidenced the interaction between Bi$_2$WO$_6$, ZnO and SrFe$_2$O$_4$ that lead to occurrence of electronic interaction circumstance and increased the electron density in Bi, W and O elements of 10Sr20ZBW (Sun et al., 2017; Ma et al., 2016; Kitchamsetti et al., 2021; Li et al., 2020). In Figure 4.9e, the characteristic peak that appeared at 137.4 eV was originated from Sr 3d (Yang et al., 2021). From

Figure 4.9f, two binding energies located at 710.8 eV and 721 eV belonged to Fe $2p_{3/2}$ and Fe $2p_{1/2}$, correspondingly, which originated from $SrFe_2O_4$ (Yang et al., 2021).
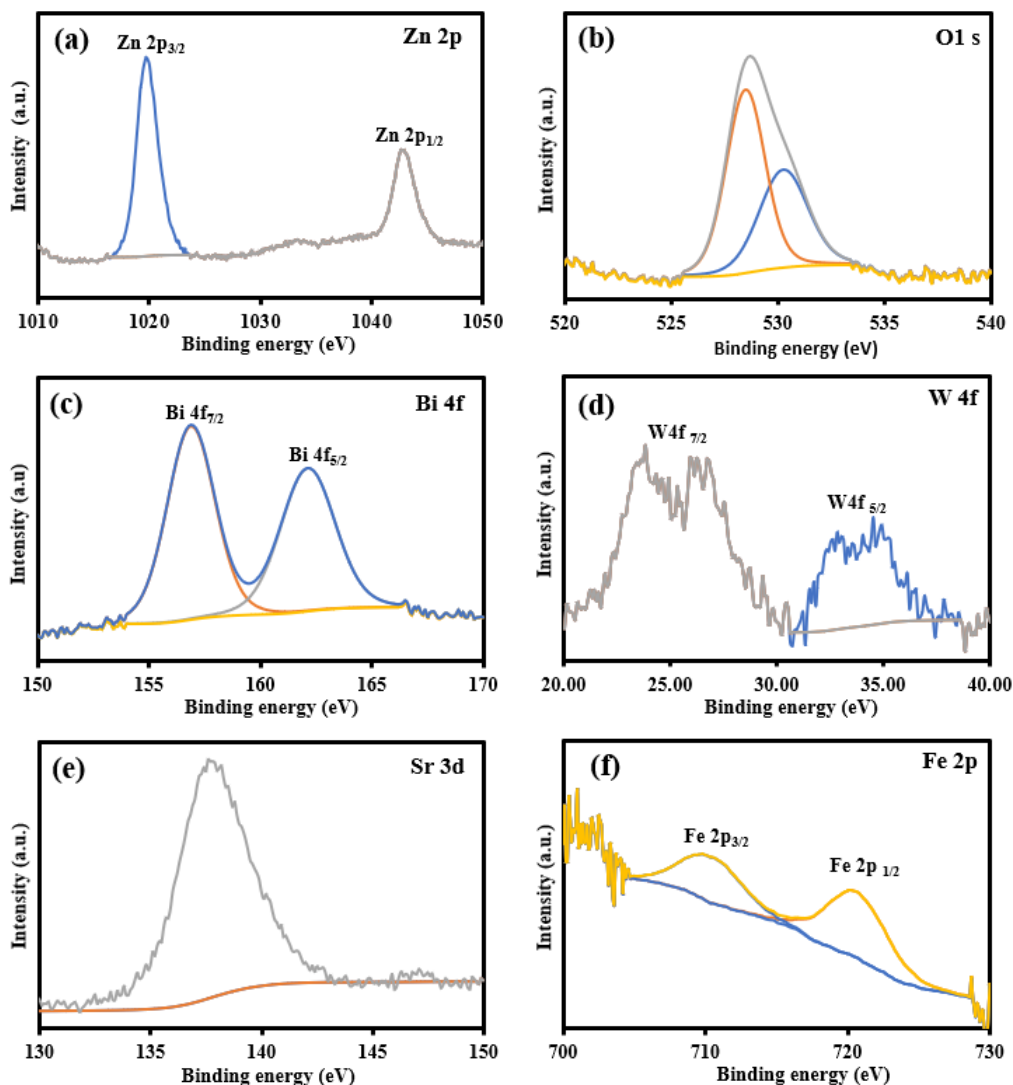
Figure 4.9: XPS spectra of 10Sr20BWZ composite (a) Zn 2p peaks (b) O1 s peaks (c) Bi 4f peaks (d) W 4f peaks (e) Sr 3d peaks and (f) Fe 2p peaks.

Similar observation was reported by Ma et al. (2016) where Z-scheme g-C_3N_4/RGO/Bi_2WO_6 was fabricated by hydrothermal method and the chemical composition was examined through XPS analysis. In their study, energy shifting occurred in characteristic peaks of W 4f in g-C_3N_4/RGO/Bi_2WO_6 composite, where both to $W4f_{7/2}$ and $W4f_{5/2}$ shifting toward lower binding energy, indicating certain electronic interaction between

Bi_2WO_6 and $g\text{-}C_3N_4$/RGO. Wang et al. (2022) have fabricated Bi2WO6 for photocatalysis N2 fixation. In their study, the $W4f_{7/2}$ and $W4f_{5/2}$ were detected at 35.5 and 37.6 eV, respectively. This showed that the $W4f_{7/2}$ and $W4f_{5/2}$ shifting toward lower binding energy in this study.

4.1.6 Fourier Transform Infrared Spectroscopy (FTIR) Analysis

The functional groups of as-prepared samples can be examined through FTIR analysis. The FTIR spectrum of pure ZnO and BWZ composites with different Bi_2WO_6 loadings are displayed in Figure 4.10. The characteristic peaks appeared at 3435 cm^{-1} and 1646 cm^{-1} were attributed to O-H bond stretching and water bending vibration, correspondingly (Zhang et al., 2017; Divya et al., 2019). Besides, the absorption peaks located at 752 cm^{-1} and 567 cm^{-1} can be correlated with W-O-W and Bi-O stretch vibrations in Bi_2WO_6 (Liu et al., 2017; Yi et al., 2014). Additionally, the characteristic band situated at 439 cm^{-1} can be ascribed to stretching vibration of Zn-O (Alamdari et al., 2020). All these characteristic band were found in all the composite which confirmed the successfully synthesis of BWZ composite.
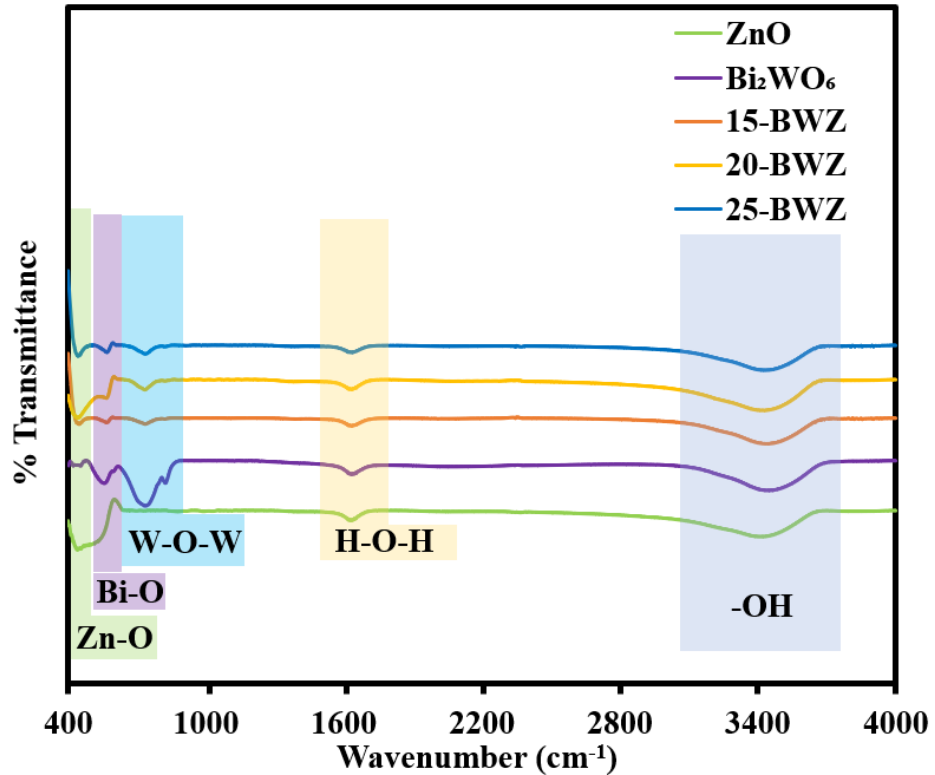
Figure 4.10: FTIR spectra of pure ZnO, Bi_2WO_6 and BWZ composites with different loading of Bi_2WO_6.

The FTIR spectra of SF20BWZ and pure SF are shown in Figure 4.11. A broad absorption band appeared at 3435 cm^{-1} belonged to stretching vibration of O-H, which can be caused by adsorption of water molecules at sample surface (Zhao et al., 2023). The peak emerged at 1650 cm^{-1} was H-O-H bending vibration (Pranoto, Purnawan and Rachmawati, 2021). The peak noticed at 1468cm^{-1} was appeared in $SrFe_2O_4$, $CaFe_2O_4$ and $BaFe_2O_4$ which associated to stretching vibrations of Fe-O. For pure $SrFe_2O_4$, $CaFe_2O_4$ and $BaFe_2O_4$, absorption peaks at 400-900 cm^{-1} were associated to characteristic stretching vibrations of Fe-O, Sr-O, Ca-O, and Ba-O (Bo et al., 2019; Vadivel et al., 2016; Zia and Riaz, 2020; Janani et al., 2022; Kenfoud et al., 2020). Other than the characterisation peaks as discussed above, the characteristic peaks located from 400cm^{-1} to 585cm^{-1} in SF20BWZ composite were

111

attributed to stretching vibrations of Zn-O and Bi-O (Liu et al., 2020; Trandafilović et al., 2017). The results inferred that the composites (10Sr20BWZ, 10Ca20BWZ and 10Ba20BWZ) retained the characteristic peaks of ZnO and Bi_2WO_6 and suggesting that SF were successfully incorporated into ZnO/Bi_2WO_6 composite.
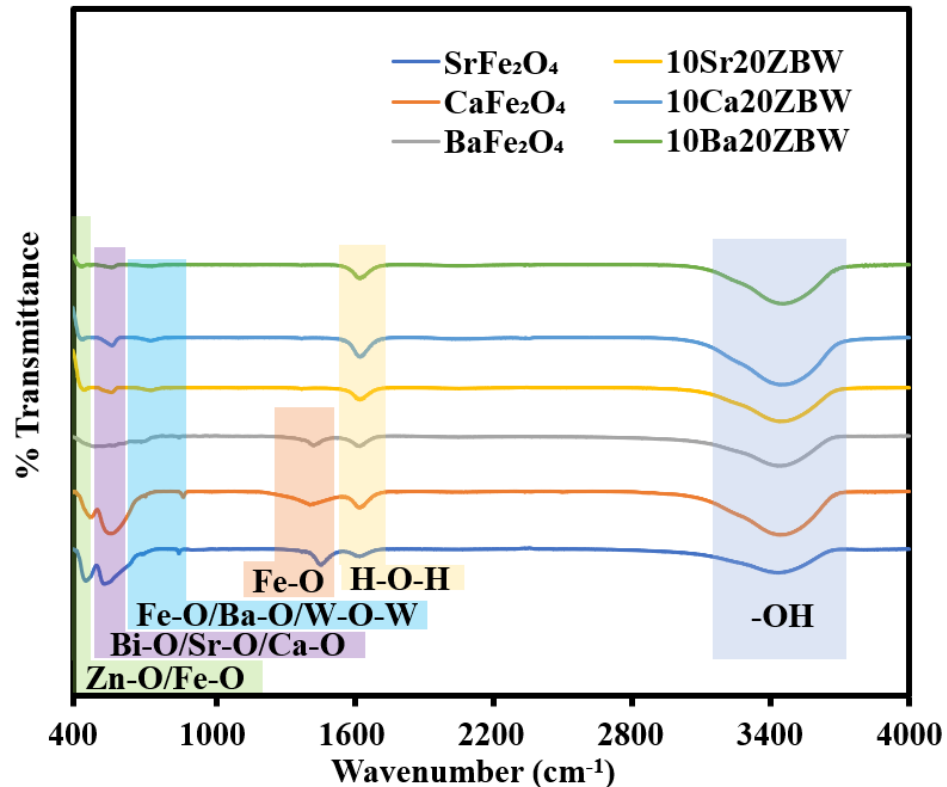
Figure 4.11: FTIR spectra of pure $SrFe_2O_4$, $BaFe_2O_4$, $CaFe_2O_4$ and 10SF20BWZ composites.

The FTIR of Sr20BWZ composites with different $SrFe_2O_4$ loadings (5wt%-20wt%) are exhibited in Figure 4.12. Similar to findings discussed above, absorption peak appeared at 3435 cm^{-1} and 1650 cm^{-1} which belonged to -OH and H-O-H peaks also appeared in all Sr20BWZ composites. The peaks located at 738 cm^{-1} was associated to stretching vibration peak of Fe-O and W-O-W (Liu et al., 2017; Yi and Yan et al., 2013). The peaks at 569 and 452 cm^{-1} mainly attributed to the stretching and bending vibrations of Bi-O, Sr-O, Zn-O

and Fe-O. (Zhao et al., 2023; Bo et al., 2019; Rambabu et al., 2021; Kenfoud et al., 2020). This indicated the presence of ZnO, Bi_2WO_6 and $SrFe_2O_4$ in Sr20BWZ composites. Moreover, the peak position of Sr20BWZ composites with different $SrFe_2O_4$ loadings are similar, revealing the loading of $SrFe_2O_4$ does not alter the chemical bond between ZnO and Bi_2WO_6. The FTIR results further confirmed the successfully synthesis of SF20BWZ composite which was in consistent with findings discussed above.
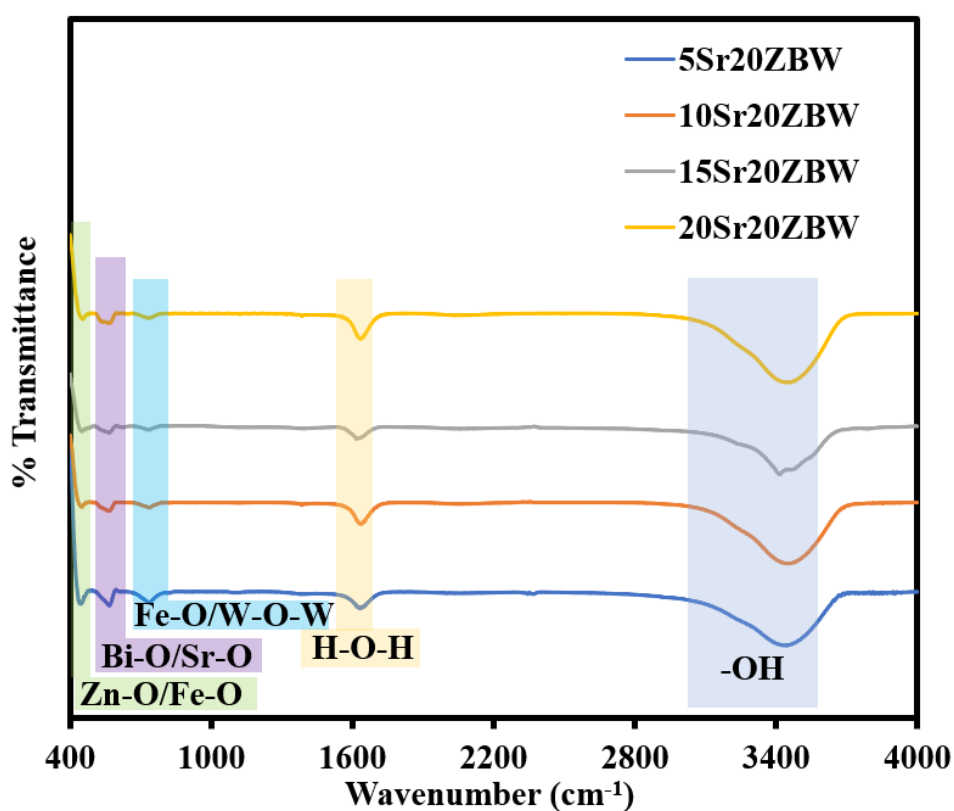
Figure 4.12: FTIR spectra of Sr20BWZ composite with different $SrFe_2O_4$ loading.

The findings above were in consistent with the reported literatures. Alamdari et al., (2020) have synthesized ZnO and identified the functional groups as sample through FTIR method. The results revealed the existence of Zn-O vibrations located at around 546 cm^{-1}. Zhao et al. (2023) also reported the stretching vibrations that appeared in WO_3/Bi_2WO_6 composite which

located at 500–750 cm^{-1} attributed to Bi-O and W-O-W. Vadivel et al. (2016) have prepared CaFe$_2$O$_4$/g-C$_3$N$_4$ for dye degradation. Based on their findings, the O-H stretching vibration was situated at around 3410 cm^{-1} while the prominent peaks that located at 636cm^{-1} and 587 cm^{-1} were corresponded to Fe-O and Ca-O stretching vibrations. Another study from Zia and Riaz (2020) have reported the peaks occurred at 694 cm^{-1} and 647 cm^{-1} were related to stretching vibrations of Fe-O and Ba-O. Bo et al. (2019) have prepared SrFe$_2$O$_4$/g-C$_3$N$_4$ via ultrasonically dispersing and refluxing mixture of SrFe$_2$O$_4$ and g-C$_3$N$_4$. The functional groups in the composite were examined by FTIR analysis. Stretching vibration of Sr-O was appeared at around 800 cm^{-1}. Besides, the characteristic peaks of SrFe$_2$O$_4$ that appeared in all the composites also confirmed the successfully formation of SrFe$_2$O$_4$/g-C$_3$N$_4$.

4.1.7 Vibrating Sample Magnetometry (VSM) Analysis

Vibrating sample magnetometry (VSM) analysis was applied to study the magnetic properties of pure SrFe$_2$O$_4$ and 10Sr20BWZ composite. Figure 4.13a shows the hysteresis loops of pure SrFe$_2$O$_4$ and 10Sr20BWZ composite under an applied field of 8k G. The saturation magnetization (Ms) of 10Sr20BWZ was 0.058 emu/g, which was much smaller than ferromagnetic SrFe$_2$O$_4$ (0.474 emu/g). This can be due to the incorporation of other non-magnetic materials in the composite such as ZnO and Bi$_2$WO$_6$ (Raizada et al., 2017). A study from Zhang et al. (2016) also reported the reduction of 70% in Ms value when another catalyst CaO was introduced in formation of composite with magnetic strontium ferrite. This was due to the introduction of another catalyst can initiate and affect the spins orientation which diminished

magnetization of the composite (Gonçalves et al., 2021). Gonçalves et al. (2021) have also reported the reduction of Ms value in $MoO_3/SrFe_2O_4$ when compared to pure $SrFe_2O_4$. The deterioration of Ms value was related to introduction of MoO_3 and calcination process that could induce changes in orientation of spins and affected magnetization of the composite.
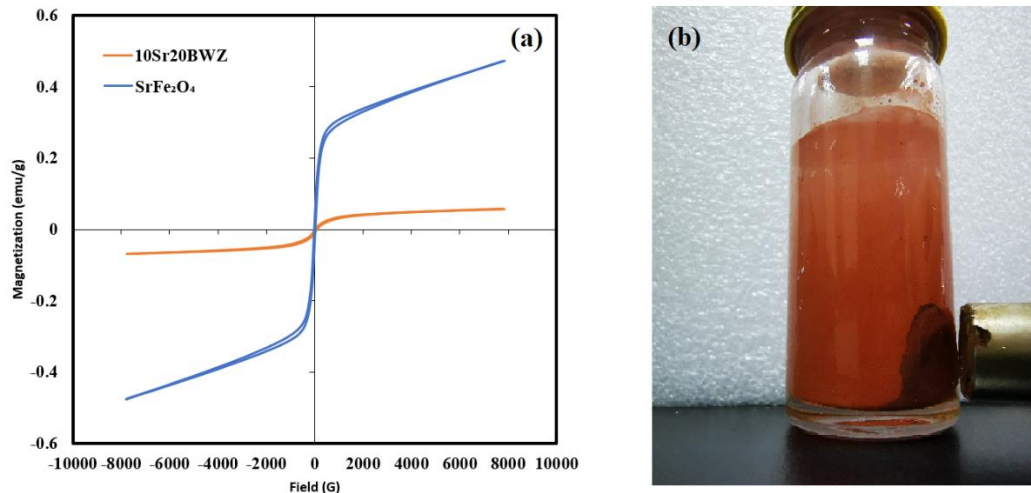
Figure 4.13: (a) Magnetic hysteresis loops for $SrFe_2O_4$ and 10Sr20BWZ; (b) Photo of 10Sr20BWZ was attracted by applying external magnet.

Still, the 10Sr20BWZ composite has shown its magnetic behaviour when a small external magnet was placed near to the bottle stored with 10Sr20BWZ solution. As shown in Figure 4.13b, the suspended 10Sr20BWZ composite was able to be attracted by the external magnet. The results indicated that the composite contained magnetic properties that was useful for magnetic removal and separation after its applications. In addition, the convenience in magnetic separation after application was very useful during recycling work.

4.2 PHOTODEGRADATION OF DMP OVER AS-SYNTHESIZED PHOTOCATALYSTS UNDER SUNLIGHT IRRADIATION

4.2.1 Photodegradation of DMP Over Binary Composites

The photocatalytic performances of as-synthesized pure ZnO, Bi_2WO_6 and BWZ composites with different Bi_2WO_6 loadings were assessed by degradation of DMP with photocatalyst dosage 1g/L, initial DMP concentration of 5.2 μM and at natural solution pH under sunlight irradiation. As shown in Figure 4.14, the DMP removal under photolysis showed negligibly elimination with the increasing time, implying the necessity for the using of photocatalyst in DMP purification. Upon illumination under sunlight for 90 min, the 20BWZ composite revealed the greatest degradation efficacy of DMP, reaching 86.6%. Also, 20BWZ exhibited enhanced degradation efficiencies when compared to pure ZnO (59.5%) and Bi_2WO_6 (27.1%). The degradation percentage of DMP for 15BWZ and 25BWZ were determined to be 66.4% and 47.8%, respectively. This indicated that an appropriate amount of Bi_2WO_6 can improve photocatalytic activity owing to formation of heterostructure. It was reported that decorating with low amount of Bi_2WO_6 can lead to less heterojunctions, while excessive loading of Bi_2WO_6 can make it to be a recombination center for charge carriers (Qin et al., 2020; Zhang et al., 2022).

Qin et al. (2020) reported the application of Bi_2WO_6/In_2O_3 in photodegradation of organic dyes. Similar to this study, the photocatalytic performance was noticed to rise when the loading of Bi_2WO_6 increased and started to decline when the loading amount of Bi_2WO_6 excessed. This proved that an appropriate loading amount of Bi_2WO_6 in the heterojunction system was

116

useful for boosting the photocatalytic performance. Controversy, excessive loading of Bi_2WO_6 resulted in deteriorating the photocatalytic performance as the Bi_2WO_6 turned into the recombination center for charge carriers and caused the electron-hole pair recombination.

Zhang et al. (2022) also reported similar findings in their $Bi_2WO_6/ZnIn_2S_4$ photocatalysis study in the degradation of tetracycline hydrochloride. It was observed that the degradation efficiency was initially increased but deteriorated in the end when the loading content of Bi_2WO_6 increased. The reduction in degradation efficiency was ascribed to shading effect of Bi_2WO_6 which hindered the light absorption ability of another catalyst. Thus, 20BWZ composite was selected for use in subsequent photocatalytic experiments.
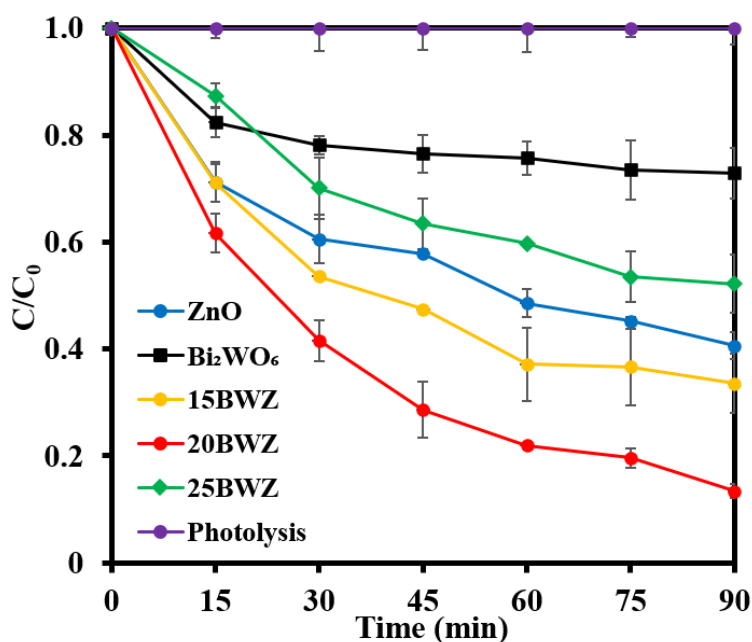
Figure 4.14: Photodegradation of DMP over pure ZnO, Bi_2WO_6, BWZ composites ([DMP]= 5.2 µM; photocatalyst loading = 1 g/L; pH = 6.5).

4.2.2 Photodegradation of DMP Over Ternary Composite

Recent research has revealed that by forming a double Z-scheme composite can further enhance the photocatalytic performance by reducing the

electron-hole recombination rate and boosted the charge transfer efficiency (Zhang et al., 2021; Behineh et al., 2022; Feng et al., 2022; Wang et al., 2022). It was reported that the magnetic candidates such as spinel ferrites with superior chemical stability and ferromagnetic characters have been proverbially applied in photocatalytic research areas (Padervand et al. 2021; Li et al., 2019; Balu et al., 2019; Kumar et al., 2018). In this study, the spinel ferrites ($CaFe_2O_4$, $SrFe_2O_4$ and $BaFe_2O_4$) were selected as the third catalyst to be introduced into the ternary system owing to its magnetic properties and suitable band position for construction of double Z-scheme composites. The photodegradation of DMP was carried out under the following conditions: photocatalyst dosage 1g/L, initial DMP concentration of 5.2 μM and at natural solution pH under sunlight irradiation.

Figure 4.15 displays the degradation performance of DMP over pure ZnO, Bi_2WO_6, SF and 10SF20BWZ composites. In addition, the 10Sr20BWZ composite demonstrated superior performance with degradation efficiency up to 89.1%, which was much higher than pure ZnO (59.5%), Bi_2WO_6 (27.1%), $SrFe_2O_4$ (36.3%), 20BWZ (86.6%), 10Ca20BWZ (76.1%) and 10Ba20BWZ (67.4%). The extraordinary performance can be accredited to the construction of double Z-scheme mechanism which effectively reduced the electron-hole recombination and hence enhanced the photocatalytic performance. Besides, the 10Sr20BWZ composite revealed higher photocatalytic performance compared to the 10Ca20BWZ and 10Ba20BWZ composites. This can be correlated to the high charge carrier separation of 10Sr20BWZ which will be discussed further in Section 4.4.1.
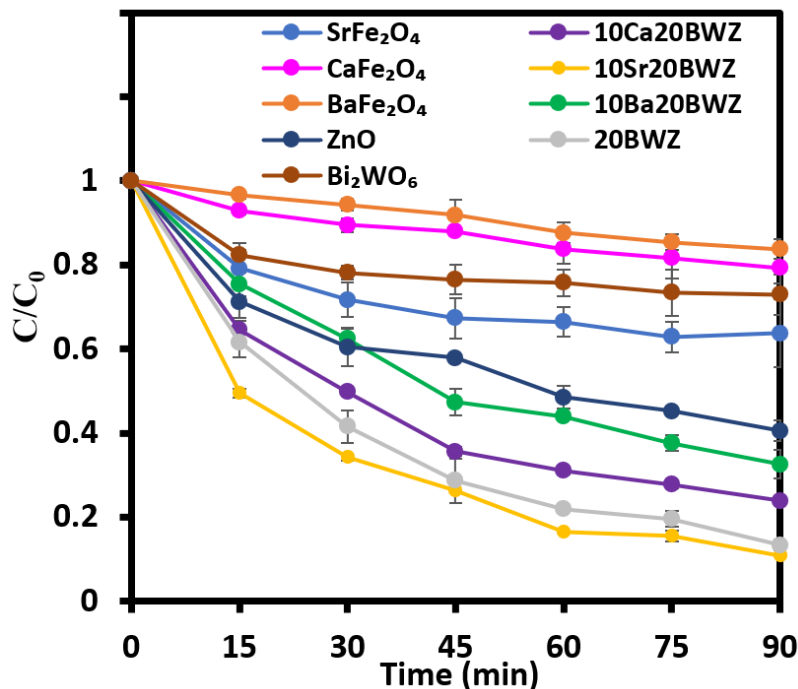
Figure 4.15: Photodegradation of DMP over pure ZnO, Bi$_2$WO$_6$, SF, 10SF20BWZ composites ([DMP]= 5.2 μM; photocatalyst loading = 1 g/L; pH = 6.5).

Behineh et al. (2022) synthesized the dual Z-scheme ZnO/Zn$_2$TiO$_4$/GO for photocatalytic degradation of cefixime. They found that the degradation rate of ZnO/Zn$_2$TiO$_4$/GO was 6.2 times higher than ZnO and 2.7 times higher than ZnO/Zn$_2$TiO$_4$. The improvement of photocatalytic performance was related to the construction double Z-scheme composite which reduced the photogenerated charge carrier from recombination, enhancement of interfacial charge transfer and visible light absorption. Feng et al. (2022) have successfully fabricated a dual Z-scheme g-C$_3$N$_4$QDs-CoTiO$_3$/CoFe$_2$O$_4$ (GCC) composite for photodegradation of oxytetracycline. It was reported the photocatalytic degradation of oxytetracycline effectively improved due to construction of double Z-scheme which led to better separation efficacy of photogenerated charge carriers. The degradation efficiency of oxytetracycline was up to 88% with good reusability. Moreover, the construction of double Z-

scheme composite with ferrites candidate can introduce magnetic properties and eased the recovery process.

Sr20BWZ with different $SrFe_2O_4$ loadings (5wt%−20wt%) were synthesized to examine how $SrFe_2O_4$% loading affects the photodegradation efficiency of DMP. The outcomes were demonstrated in Figure 4.16. It can be noticed that the photocatalytic performance of all Sr20BWZ were greater than the pure $SrFe_2O_4$ and Bi_2WO_6. Additionally, the loading content of $SrFe_2O_4$ has considerable impact on DMP photocatalytic reaction. The order of photodegradation proficiency was found to be 10 wt%> 15 wt% > 20 wt% > 5 wt%. When the loading percentage of $SrFe_2O_4$ increased from 5 % to 10 %, the photocatalytic efficacy also increased from 39.7 % to 89.1%. However, further loading in $SrFe_2O_4$ resulting in photoactivity deterioration. Hence, 10 wt% was identified as the optimum loading content in this study. It was reported that the longer lifespan of electron-hole pairs, leading to the formation of extra amounts of reactive species such as •OH radicals that contributed to enhancement of photocatalytic activity (Rachna et al., 2020; Fakhravar et al., 2020). The degradation efficiency dropped from 89.1 to 45.95% when the loading percentage of $SrFe_2O_4$ increased from 10wt% to 20 wt%. This can be due to the fact that the excess loading amount of $SrFe_2O_4$ can increased the mean path of e^- which eventually induced electron-hole pair recombination and caused deterioration in photocatalytic performance (Xu et al., 2019). In this study, the 10Sr20BWZ revealed the best photocatalytic performance when compared to ZnO (59.45%), Bi_2WO_6 (27.1%), $SrFe_2O_4$ (36.3%) and 20BWZ (86.6%). As discussed above, the boosting effect can be due to the appropriate

loading amount of $SrFe_2O_4$ in development of double Z-scheme composite which able to reduce the electron-hole pair recombination.

Figure 4.16: Photodegradation of DMP over Sr20BWZ composites with various Sr loadings ([DMP]= 5.2 µM; photocatalyst loading= 1 g/L; pH = 6.5)

Fakhravar et al. (2020) designed a dual Z-scheme of $Cu_2S/Ag_2S/BiVO_4$ composite for degradation of metronidazole under visible light. They observed enhanced photodegradation performance resulting from development of the Z-scheme heterojunction structure. Further, the enhanced photocatalytic performance was attributed to efficient charge transportation between the composite and prolonged lifetime of electron-hole pairs. Similar to this study, 20 wt% was identified as optimum Cu_2S loading content in $Cu_2S/Ag_2S/BiVO_4$ composite which revealed its greatest photocatalytic performance among the synthesized composites. Xu et al. (2019) have synthesized Ag/PCNO composites for dyes degradation and found that the Ag loading content can significantly affect the degradation efficiency. When the Ag amount was beyond the optimum amount, the excess amount deposited on composite

121

surface can act as the charge recombination centres and occupied the active sites. This led to deterioration in degradation efficiency.

4.3 EFFECT OF OPERATING PARAMETERS

4.3.1 Effect of Catalyst Loading on DMP Photodegradation

In industrial application, the catalyst loading is one of the important parameters as it affects the cost expenses of the business and the photocatalytic performance. According to literature review, photocatalytic efficiency can be affected by catalyst loading (Zhang et al., 2021; Xu et al., 2020; Wang et al., 2018; Vela et al., 2018). In this study, the effect of catalyst loading (0.5 g/L − 2.0 g/L) on photodegradation of DMP was evaluated over 10Sr20BWZ composite under sunlight irradiation. The experiments were carried out under the conditions: pH = natural pH 6.5; [DMP] = 5.2 μM.

Figure 4.17 shows the result of DMP degradation by introducing different catalyst loadings. The result revealed that the DMP degradation efficiency increased from 54.7 % to 89.1% when the catalyst loading increased from 0.5 g/L to 1.0 g/L. As the catalyst loading increased to 1.5 g/L, the photocatalytic performance started to decline from 89.1% to 63.2% and finally dropped to 39.18% when the catalyst loading further increased to 2.0 g/L. The reason for this is the amount of active sites increased when the catalyst loading increased. Similar scenario was reported by Alothman et al. (2022) in degradation of dyes by TiO_2-g-C_3N_4 composite. In their study, the degradation performance improved when the catalyst loading increased which was due to the increasing number of active sites which responsible for •OH generation. However, when the catalyst loading exceeded 1.0 g/L, the photocatalytic

performance began to decline. The reduction in photocatalytic efficacy was caused by aggregation of photocatalyst at high catalyst loading which eventually led to light scattering effect that shielded the light from penetrating in and hence resulting in photocatalytic performance deterioration.
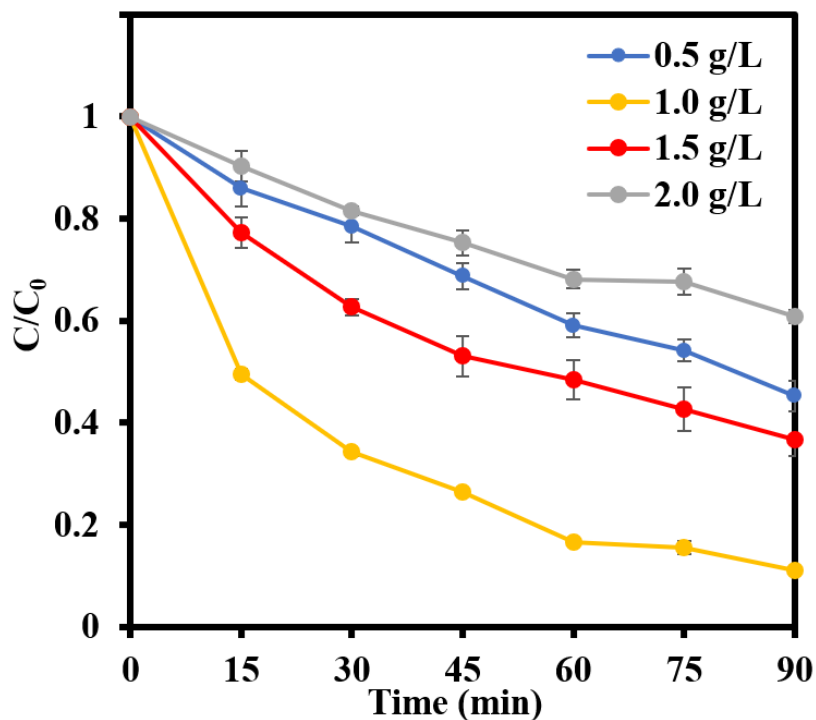
Figure 4.17: Photodegradation of DMP over 10Sr20BWZ composites with different catalyst loadings ([DMP]= 5.2 μM; pH = 6.5).

Guan et al. (2020) also studied the effect of catalyst loading on photodegradation of acid orange 7. In their study, the high catalyst loading was observed to cause a negative effect on photocatalytic performance due to low utilization of light. Mandor et al. (2020) have reported the using of N-doped ZnO in photocatalytic degradation of ammonia and phenol. They studied the effect of catalyst loading by applying various catalyst loadings (0-2g/L) into the pollutant solution. In their study, the catalyst loading with 1g/L achieved the highest degradation efficiency which was similar to this study. Moreover, the effectiveness of degradation started to decline when loading of

photocatalyst beyond 1.0 g/L due to aggregation of catalyst and hindering the light penetration to the active sites.

4.3.2 Effect of Foreign Substances on DMP Photodegradation

In general, the industry wastewater contained mixture of pollutants and foreign substances. Therefore, different co-existing foreign substances such as NO_3^-, Cl^-, SO_4^{2-} and humic acid were introduced into the solution to study the influence of foreign substances on degradation of DMP. Figure 4.18 shows the result of DMP degradation when different foreign substances were introduced into the DMP solution. It was observed that all the foreign substances had negative impact on the photodegradation efficiency of DMP. The negative impact can be arranged in following sequences humic acid> NO_3^- > Cl^->SO_4^{2-}. The inhibitory effect on photodegradation of DMP was caused by the occupied of active sites by foreign substances, thus reducing the number of available active sites and decelerated the degradation efficiency of DMP (Sun et al., 2022). The greatest repressive impact of humic acid on DMP degradation can be due to its complex mixture that composed of humic substances, fulvic acids, humin and microbial metabolites (Guo et al., 2019). This created a much more stressful and competitive environment in occupying the actives sites for DMP degradation, thus resulting in great deterioration of photocatalytic performance. In addition, it was reported that the chromophoric moieties in humic acid competed with other compounds for irradiation absorption which caused spectra overlapping and thus hindering the photocatalysis (Koumaki et al., 2015).
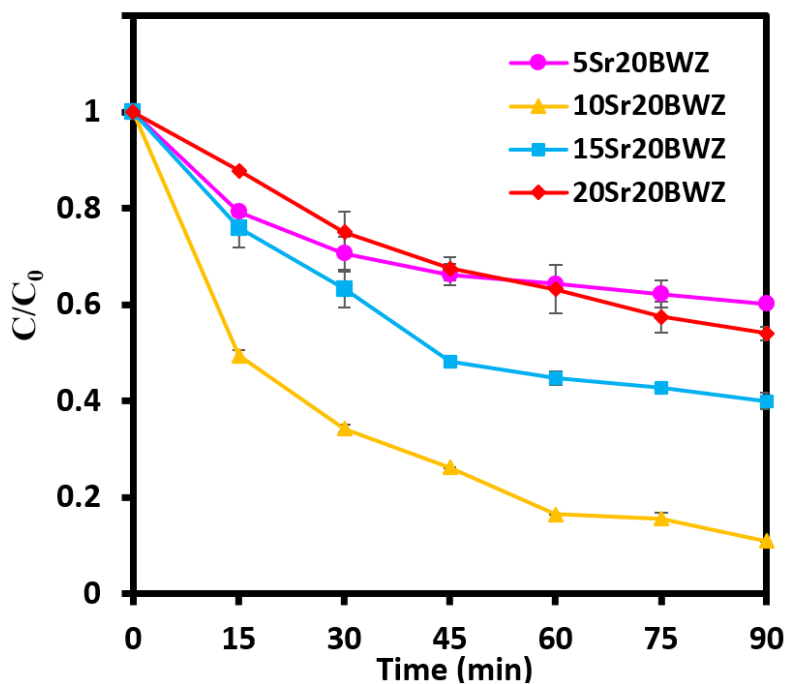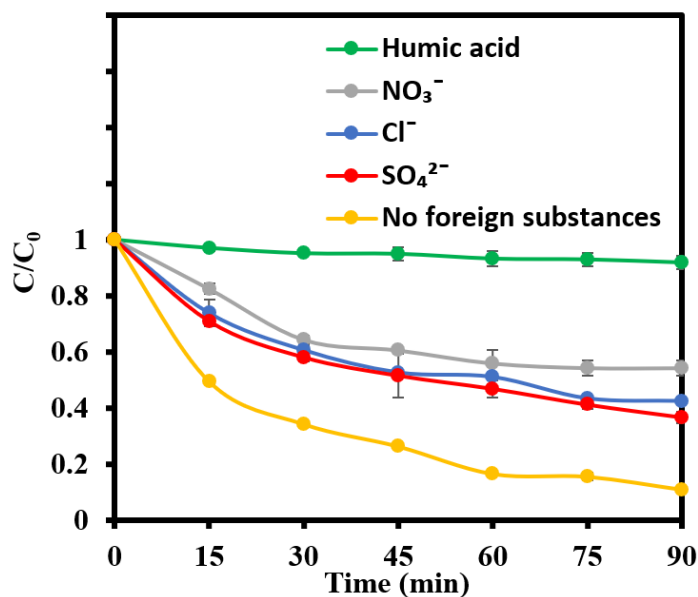
Figure 4.18: Photodegradation of DMP over 10Sr20BWZ composite ([DMP]= 5.2 μM; photocatalyst loading = 1 g/L; pH = 6.5).

Xue et al. (2023) also explored the influence of inorganic anions on photodegradation of ibuprofen by introducing NO_3^- into the system. In their study, the introduction of NO_3^- caused negative impact on degradation of ibuprofen. This was caused by the quenching effect of NO_3^- in generating less reactive NO_2^- and $NO_2^•$ through Equation 4.1 and Equation 4.2. In addition, the redox potential of $NO_2^•$ was reported to be smaller than •OH radical. Therefore, this resulted in decline of photocatalytic activity.

$$2NO_3^- + hv \rightarrow 2NO_2^- + O_2 \tag{4.1}$$

$$•OH + NO_2^- \rightarrow NO_2^• + OH^- \tag{4.2}$$

Dugandžić et al. (2017) have studied the effects of Cl^- and SO_4^{2-} on photodegradation of nicosulfuron. The introduction of Cl^- led to inhibition of photocatalytic activities, which was caused by competitive of Cl^- on active sites and the generation of less reactive radicals through Equation 4.2 – Equation 4.4. Similar to Cl^-, the added SO_4^{2-} also caused negative impact on photocatalytic performance as the SO_4^{2-} will compete with other pollutant for

active sites and formed less redox potential radicals through Equation 4.5−4.6. It was reported that the reduction in photocatalytic activities was due to the fact that the generated $SO_4^{\bullet-}$ has less redox potential than •OH radicals and h^+ due to its bigger size and resonance effect (Dugandžić et al., 2017).

$$Cl^- + h^+ \rightarrow \bullet Cl \tag{4.3}$$

$$Cl^- + \bullet OH \rightarrow \bullet Cl + OH^- \tag{4.4}$$

$$SO_4^{2-} + h^+ \rightarrow SO_4^{\bullet-} \tag{4.5}$$

$$SO_4^{2-} + \bullet OH \rightarrow SO_4^{\bullet-} + OH^- \tag{4.6}$$
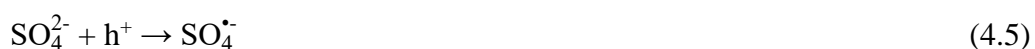
4.3.3 Effect of pH on DMP Photodegradation

Solution pH is one of the priority variables to the degradation efficiency of organic pollutants. In this study, the impact of solution pH on effectiveness of DMP degradation was investigated in the pH range of 5-11 as shown in Figure 4.19. It was noticed that the degradation efficiency increased from pH 5 to pH 7. The DMP removal efficiency of DMP was 47.4%, 89.1%, 100%, 92.8%, 64.1% at pH 5, pH 6.5, pH 7, pH 9 and pH 11, respectively. The DMP was fully degraded by 10Sr20BWZ composite within 60 min at pH=7. Li et al. (2021) also reported that the photocatalytic degradation of DMP reached the highest when the pH was in neutral condition (pH= 7.36). In this study, HCl was added to tune the pH of the solution. The Cl^- introduced by HCl can adsorb on surface of the catalyst and competed with the pollutants for reactive radicals which eventually deteriorated the photocatalytic performance (Chen et al., 2017; Balta and Simsek, 2021). In addition, the lower degradation efficiency in acidic environment could be due to consumption of $\bullet O_2^-$ by h^+ (Di et al., 2019). The Cl^- and h^+ will restrain the production of reactive species for

126

example •OH, which resulted in deterioration of photocatalytic performance. Furthermore, under weakly alkaline condition (7 < pH < 11), the degradation efficiency was excellent, which might be attributed to the increased amounts of •OH formed from the high amount of OH⁻ (Li et al., 2021). On the other hand, when in strong alkaline condition (pH =11), the photocatalytic efficiency was significantly diminished due to high concentration of Na^+ that can compete with the pollutants for reactive species and resulted in reduction of •OH redox potential (Sun et al.,2021; Meenakshi and Sivasamy, 2018).
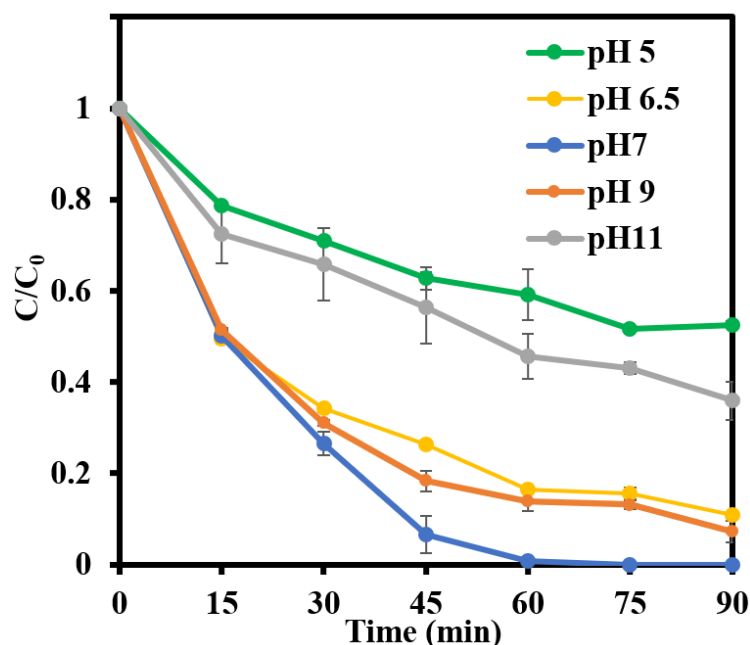
Figure 4.19: Photodegradation of DMP over 10Sr20BWZ under various pH of solution ([DMP]= 5.2 µM; photocatalyst loading = 1 g/L).

Belta and Simsek et al. (2021) have noticed the deterioration occurred in photocatalytic activity when Cl⁻ introduced into the reaction system. It was reported that the Cl⁻ can compete with the local pollutants and quenched the •OH to form •Cl which has less redox potential than the •OH. Similar finding was also reported by Meenakshi and Sivasamy (2018). In their study, the optimum degradation performance occurred at pH 7 for ZnO/SiC composite. When the pH of the medium was less than pH 7, H^+ ions scavenged OH⁻ ions

in the solution and resulted in lower photocatalytic degradation efficiency. Moreover, when the pH of the medium was in highly alkaline conditions (pH > 9), the photocatalytic performance deteriorated due to lower adsorption of pollutants onto the catalyst surface. The lower adsorption was caused by competition of Na^+ ions with foreign pollutants in the medium.

4.4   PROPOSED PHOTOCATALYTIC MECHANISM OF AS-SYNTHESIZED PHOTOCATALYSTS

4.4.1 Photoelectrochemical Experiments

Since electron-hole pair plays an important role in photocatalytic activity, therefore photoelectrochemical experiment was carried out to study the photogenerated electron-hole pair separation and its transfer efficiency. In general, the transient-photocurrent curves with high intensity suggested a better electron-hole pair separation which in return can generate more radicals and hence resulting in higher photocatalytic performance (Liu et al., 2022; Nawaz et al., 2021). Figure 4.20 shows the curve of photocurrent response for ZnO, Bi_2WO_6 and BWZ composites. The 20BWZ composite displayed higher photocurrent intensity than pure ZnO, Bi_2WO_6 and other BWZ composites indicated better electron-hole separation and higher photocatalytic ability.
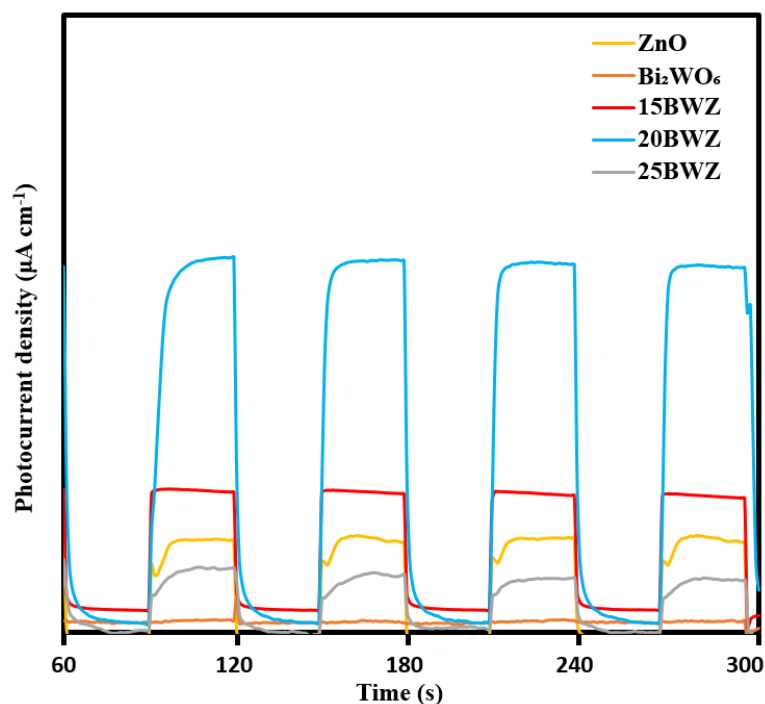
Figure 4.20: Transient-photocurrent curves of pure ZnO, Bi_2WO_6 and BWZ composites.

Figure 4.21 displays the photocurrent response of pure ZnO, Bi_2WO_6, SF, 20BWZ and 10SF20BWZ composites. It was observed that all the 10SF20BWZ composites exhibited higher photocurrent density than the pure ZnO, Bi_2WO_6, $CaFe_2O_4$, $BaFe_2O_4$ and $SrFe_2O_4$. This indicated that all the 10SF20BWZ composites have better electron-hole separation efficiency and hence possessed stronger photocatalytic ability. Among them, 10Sr20BWZ composite revealed the strongest photocurrent intensity, implying 10Sr20BWZ composite has better electron-hole pair separation efficiency than others.
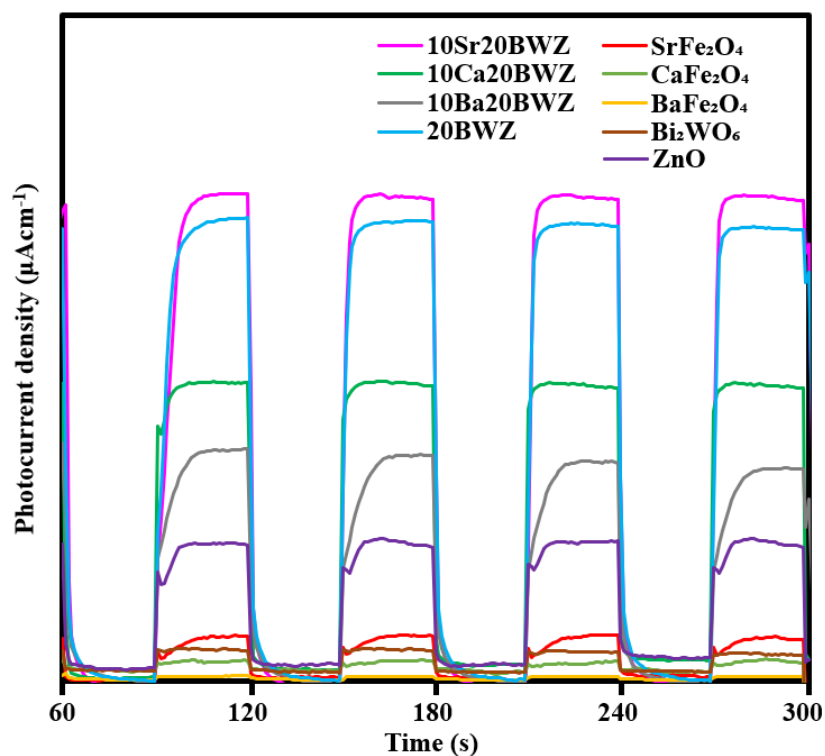
Figure 4.21: Transient-photocurrent curves of pure ZnO, Bi_2WO_6, 20BWZ, SF, 10SF20BWZ composites.

Figure 4.22 shows the transient photocurrent of Sr20BWZ with different loadings of $SrFe_2O_4$. The order of photocurrent intensity was found to be 10 wt%>15 wt% > 20 wt% > 5 wt% which indicated that 10Sr20BWZ composite has the best efficiency in electron-hole pair separation. All the obtained results were in parallel to results from photocatalytic activity as discussed above. The result also implied that the formation of Z-scheme composite can enhance the photocatalytic performance with better electron-hole pair separation that was proven in photocurrent experiment.
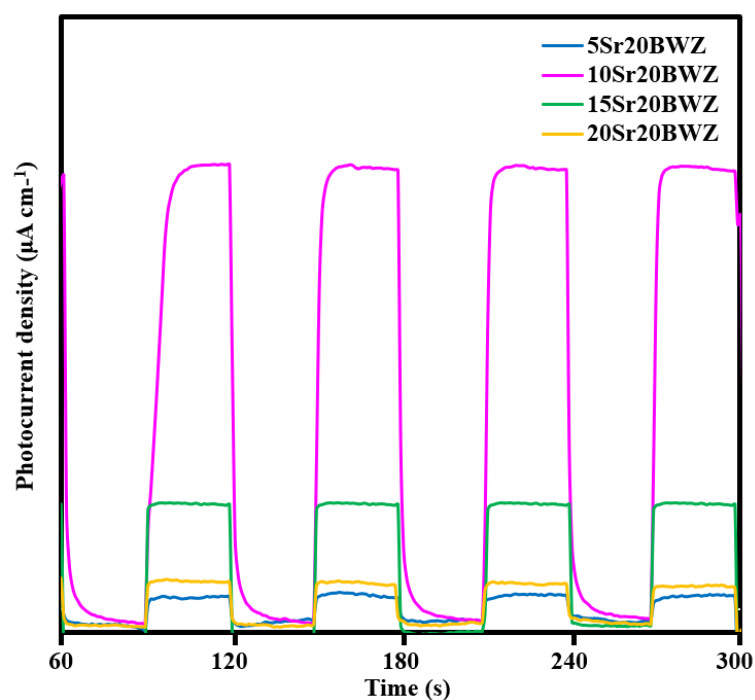
Figure 4.22: Transient-photocurrent curves of pure SF20BWZ composites with different loadings of $SrFe_2O_4$.

Apart from transient-photocurrent test, the electrochemical impedance spectroscopy (EIS) test was also carried out to obtain the Nyquist plot. The EIS analysis can be used to identify the charge transfer behaviour of photogenerated electron-hole pair. In the Nyquist plot, a smaller arc radius represents smaller charge resistance (Kafeshani et al., 2022; Li et al., 2021). Figure 4.23 demonstrates the Nyquist plot of pure ZnO, Bi_2WO_6 and BWZ composites. It was observed that the 20BWZ composite displayed the arc with the smallest radius among the samples. This suggested that the charge with lower resistance resulted in better charge transfer efficiency. Consequently, this turns out 20BWZ composite has higher photocatalytic performance than other samples.
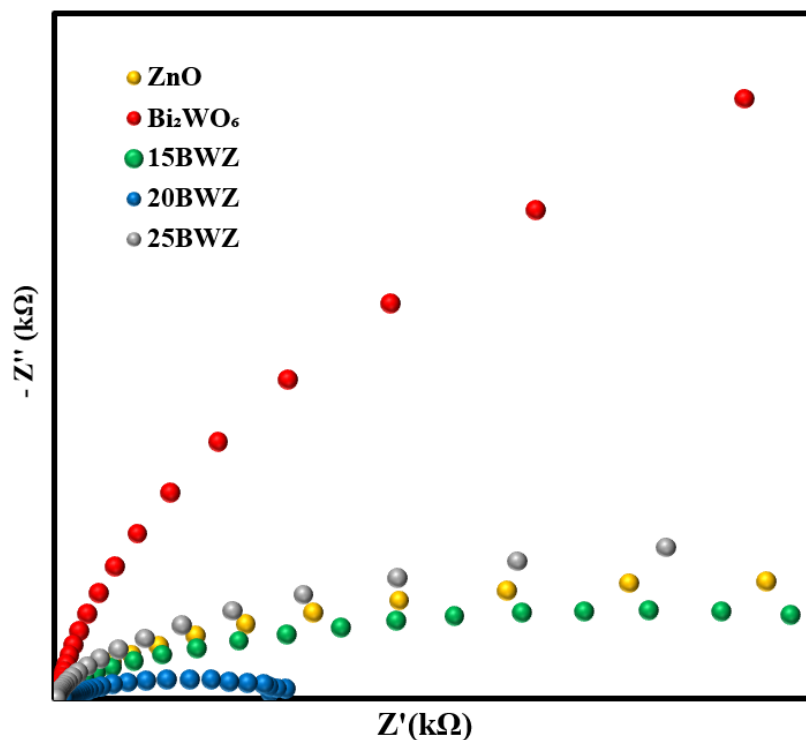
Figure 4.23: EIS Nyquist plot of pure ZnO, Bi_2WO_6 and BWZ composites.

Figure 4.24 shows the Nyquist plot of pure ZnO, Bi_2WO_6, SF and 10SF20BWZ composites. As shown in Figure 4.24, the order of arc radius was arranged as follows: 10Sr20BWZ < 20BWZ < 10Ca20BWZ < 10Ba20BWZ < ZnO < $SrFe_2O_4$ < Bi_2WO_6 < $CaFe_2O_4$ < $BaFe_2O_4$. The results implied that 10Sr20BWZ composite was the composite that has the lowest charge resistance and hence efficient in charge transfer. These criteria made 10Sr20BWZ as an efficient photocatalyst compared to others.
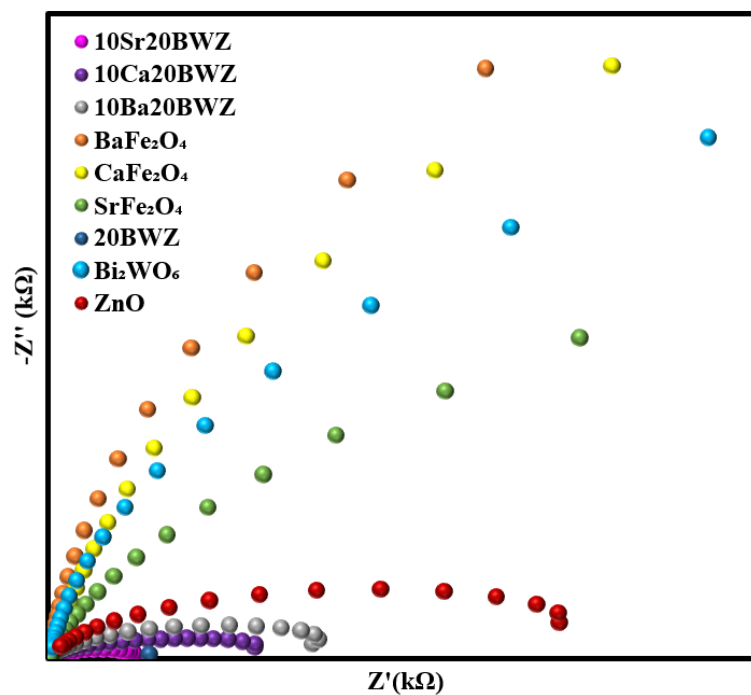
Figure 4.24: EIS Nyquist plot of pure ZnO, Bi$_2$WO$_6$, 20BWZ, SF and 10SF20BWZ composites.

Figure 4.25 reveals the EIS Nyquist plot for Sr20BWZ with different SrFe$_2$O$_4$ loadings. Similar to transient photocurrent response, the 10Sr20BWZ exhibited the smallest arc radius among other composites. Above results indicated that 10Sr20BWZ presented the highest charge carrier separation and migration efficiencies which make it beneficial in photocatalytic treatment.
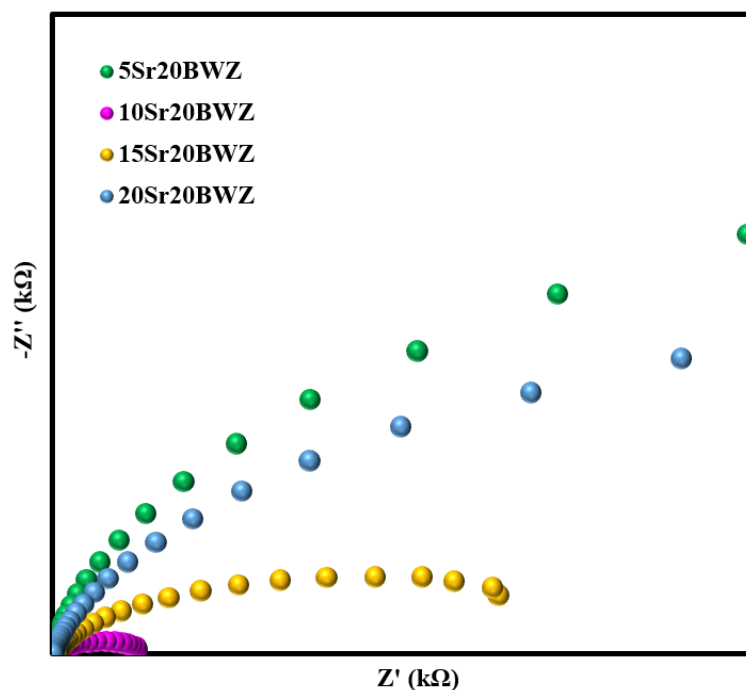
Figure 4.25: EIS Nyquist plot of pure SF20BWZ composites with different loadings of SrFe$_2$O$_4$.

4.4.2 Reactive Species Experiments

A series of control experiments were conducted, with the absence and presence of radical scavengers to ascertain the involvement of active species in the photodegradation of DMP. The predominant role of reactive species such as •OH, h$^+$, O$_2^-$ and e^- were evaluated by introducing different scavengers into the degradation system. In this study, isopropanol (IPA) was introduced to scavenge the •OH radicals, ammonium oxalate was adopted as h$^+$ scavenger, chloroform was adopted as O$_2^-$ scavenger and Na$_2$SO$_4$ was employed to quench e^-. The photodegradation of DMP can be affected and constrained after the scavengers were introduced into the system. The reduction in photocatalytic performance which induced by scavengers reflected the significance of respective reactive species. The scavenger experiment was performed in a similar way to the photocatalytic activity with the exception of introducing a radical scavenger into the solution of DMP. The experiments

were performed under the conditions: catalyst loading = 1.0 g/L; initial DMP

concentration= 5.2 µM; pH = natural solution pH and scavenger concentration

= 0.5 mM.

Figure 4.26 displays the photocatalytic performance of DMP when

different scavengers introduced into reaction system. When ammonium oxalate

(AO) was introduced into the photocatalytic system, the degradation efficiency

was observed to decline from 89.1% to 37.3%, indicating the huge contribution

of h^+ in degradation of DMP. The photocatalytic efficiency also noticed to fall

from 89.1% to 58.4% when isopropanol was added into the photosystem,

which suggesting that •OH was also an important active species that played

predominant role in photodegradation DMP. However, when chloroform and

Na_2SO_4 were added, only minor reduction of photocatalytic efficiency which

revealed that the $•O_2^-$ and e^- played lesser role in photodegradation of DMP.
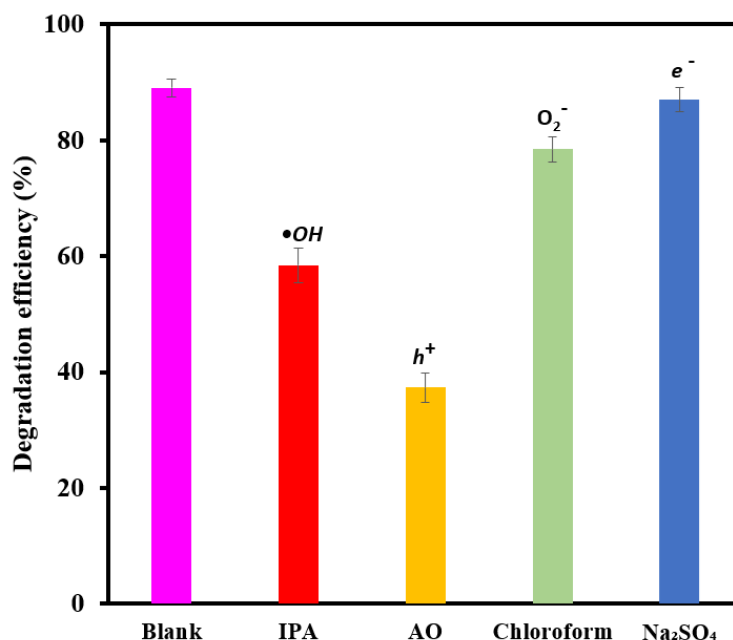
Figure 4.26: Degradation efficiency of DMP under sunlight irradiation with the addition of different scavengers ([DMP]= 5.2 µM; photocatalyst loading = 1 g/L; pH = 6.5).

The suppression of photocatalytic performance was caused by introduction of scavengers which can quench the radicals and formed other intermediates that prevented the main active species from generation and participated in photodegradation activities. It was reported the introduction of isopropanol into the reaction system can scavenge OH radicals by forming hydroxyalkyl radicals with lower potential through Equation 4.7 (Gracien et al., 2019; Vione et al., 2011; Mazellier and Bolte, 2000). Mazellier and Bolte (2000) also reported the using of isopropanol for scavenging the •OH radicals in photodegradation of 2,6-dimethylphenol solution.

$$\bullet OH + CH_3CHOHCH_3 \rightarrow H_2CC\bullet OHCH_3 + H_2O \qquad (4.7)$$

Besides, several studies have reported the introduction of ammonium oxalate (AO) into the system in order to scavenge the h^+ (Castillo-Rodríguez et al., 2023; Wang et al., 2023; Tien, Kapti and Cherly, 2020). Wang et al. (2023) have reported the using of AO in scavenge the h^+ by forming H_2O, CO_2 and $CO_2^{\bullet-}$ and NH_4^+ through Equation 4.8. Besides, it was reported that h^+ can react with H_2O to form •OH radicals through Equation 4.9 (Ng et al., 2017). Hence, the generation of •OH radicals were inhibited when h^+ was scavenged by AO to form lower potential $CO_2^{\bullet-}$ which eventually led to decline in photocatalytic efficiency.

$$(NH_4)_2C_2O_4 + h^+ \rightarrow CO_2 + H_2O + CO_2^{\bullet-} + 2NH_4^+ \qquad (4.8)$$

$$h^+ + H_2O \leftrightarrow \bullet OH + h^+ \qquad (4.9)$$
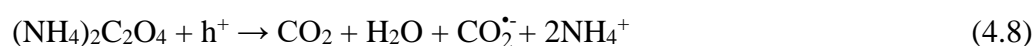
The $\bullet O_2^-$ can be quenched by introduction of chloroform into the photocatalytic system (Li et al., 2020; Mukherjee et al., 2021; Zhang et al., 2022). Li et al. (2020) have reported that the $\bullet O_2^-$ can be converted to H_2O_2 and O_2 when the $\bullet O_2^-$ scavenger was added in the system. However, the H_2O_2 can

react with e^- to form •OH radical through equation 4.10 (Raizada et al.,2020). Therefore, the degradation efficiency was not greatly affected when $•O_2^-$ scavenger was introduced into the system.

$$e^- + H_2O_2 \rightarrow •OH + h^- \tag{4.10}$$

It was reported that Na_2SO_4 can be introduced as e^- scavenger in the system (Riaz et al., 2023; Glavaski et al.,2016). According to Glavaski et al. (2016) and Murugananthan et al. (2010), the Na_2SO_4 can form $SO_4^{•-}$ as intermediates through reaction with •OH as described in Equation 4.11. Then, the $SO_4^{•-}$ scavenged the e^- through Equation 4.12.

$$•OH + 2SO_4^{2-} \rightarrow SO_4^{•-} + OH^- \tag{4.11}$$

$$SO_4^{•-} + e^- \rightarrow SO_4^{2-} \tag{4.12}$$
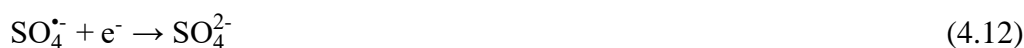
Although $SO_4^{•-}$ is one of the reactive species, but its redox potential was smaller than •OH radicals. As a result, no significant reduction in degradation efficiency was observed, indicating a minor role of this species in the photocatalytic degradation of DMP.

4.4.3 Terephthalic Acid Photoluminescene Probing Test (TA-PL)

Based on the finding discussed above, •OH radical was recognized as one of the prominent active species that exerted a dominant role in photocatalytic degradation of DMP. Hence, the generation of •OH radicals by 10Sr20BWZ under sunlight irradiation was examined by TA-PL test. Upon interaction with the generated •OH radicals in the solution, terephthalic acid underwent a reaction, resulting in the formation of 2-hydroxyterephthalic acid (2-TAOH), which exhibited strong fluorescence characteristics. During analysis, the 2-TAOH can emit a peak at 425 nm when stimulated by 312 nm

excitation wavelength. The spectra intensity reflected the amount of •OH radicals generated in the system. A higher peak intensity indicated a higher quantity of •OH radical produced in the system (Zhang et al., 2019; Kaur et al., 2018). The experiments were performed in the similar procedure of photocatalytic experiment, with the exception of substituting the DMP solution with terephthalic acid solution. The experiments were performed under conditions as follow: catalyst dosage = 1g/L; pH= natural solution pH.

The PL spectrum of 10Sr20BWZ composite at different collection intervals after sunlight irradiation is exhibited in Figure 4.27. The PL spectra were observed for all samples at the wavelength of 425 nm. The intensity of the spectra increased as the irradiation time progressed from 0 to 90 min. This indicated that the amount of generated •OH radicals increased when the irradiation time increased. The result also confirmed the findings of active species as discussed in section 4.4.2 where •OH radicals also played dominant role in photodegradation of DMP. Zhang et al. (2019) has confirmed the generation of •OH radicals in photocatalytic activity through TA-PL experiment. The PL intensity was observed to increase with irradiation time which indicated the generation of •OH radicals during photocatalysis. Kaur et al. (2018) have studied the photocatalytic degradation of ofloxacin and malachite green using CdS. They confirmed the role of •OH radicals through TA-PL technique and found that the amount of •OH radicals was directly proportional to intensity of TA-PL emission peak.
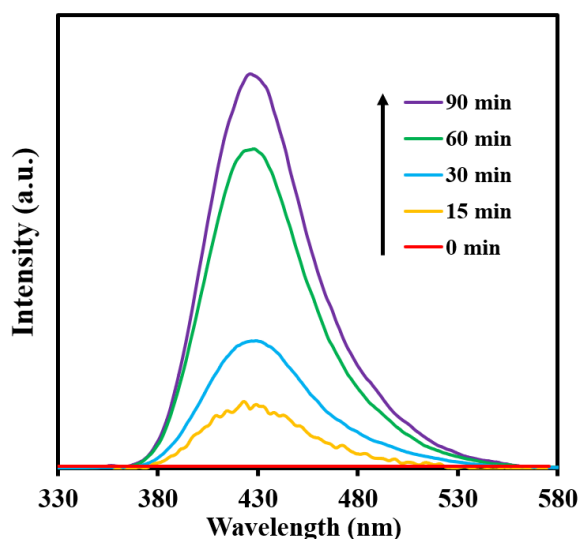
Figure 4.27: PL spectra of terephthalic acid solution collected at different time intervals under excitation of 315 nm.

4.4.4 UV-vis DRS analysis

The optical properties of as-synthesized catalysts were evaluated by UV-vis DRS analysis as shown in Figure 4.28. Figure 4.28a demonstrates the UV-vis spectra of bare ZnO, Bi_2WO_6 and BWZ composites with various loading of Bi_2WO_6. The 20BWZ composite was observed to reveal the outstanding visible light harvesting capacity as compared to pure ZnO after incorporated with Bi_2WO_6. Moreover, it was noticed that the light absorption ranges of BWZ composites shifted to higher wavelengths (visible light region). Figure 4.28b displays the spectra of pure ZnO, Bi_2WO_6, SF and 10SF20BWZ composites. It was noted that the light absorbability of SF20BWZ composites altered drastically when $SrFe_2O_4$ introduced into the 20BWZ composite. Moreover, all the 10SF20BWZ composites revealed boosted visible-light harvesting ability when compared to pure ZnO and Bi_2WO_6, this could be due to the introduction of $SrFe_2O_4$, $CaFe_2O_4$ and $BaFe_2O_4$ into the composite. The result implied that the optical response region of 10SF20BWZ was red shifted

and can be beneficial for the visible light photoreaction. Figure 4.28c shows UV-vis DRS analysis for Sr20BWZ composite with different Sr loadings. The findings revealed that the Sr20BWZ composites displayed enhanced light absorption abilities when Sr loading increased from 5 wt% to 20wt%.
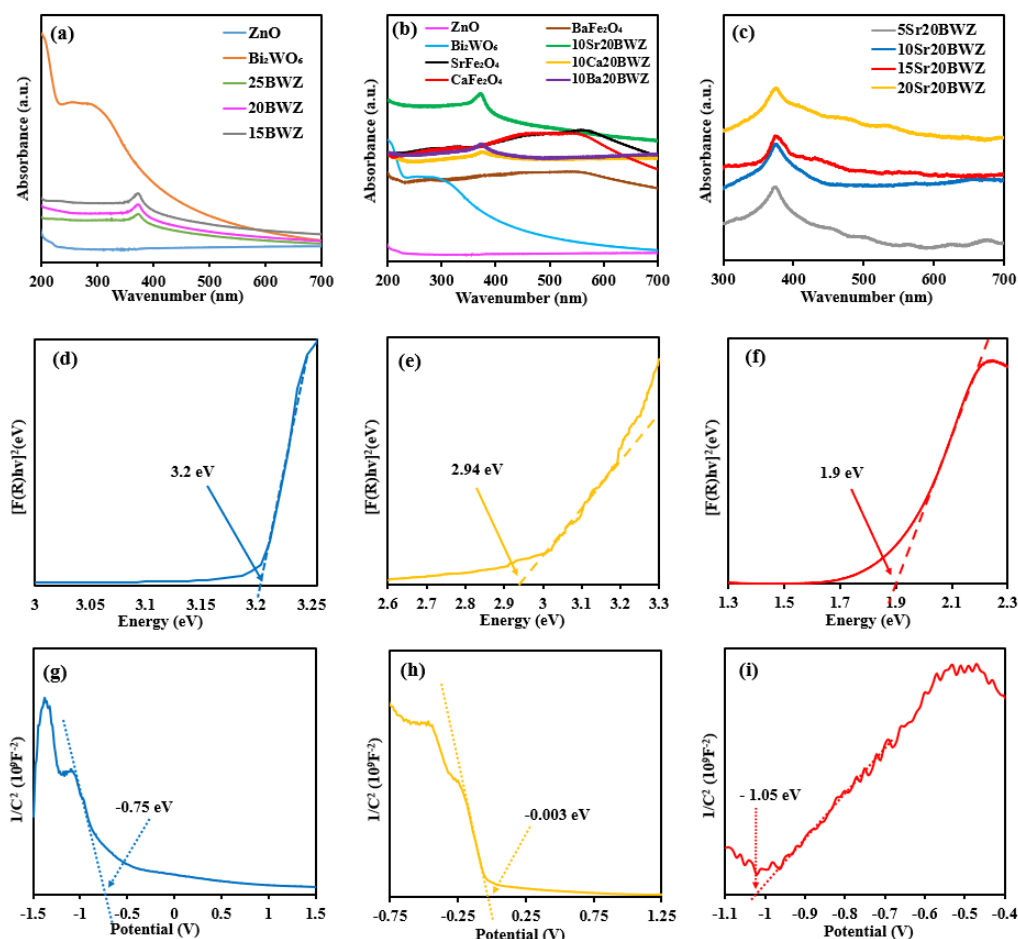
Figure 4.28: UV-vis DRS spectra of (a) ZnO, Bi_2WO_6 and BWZ composites (b) ZnO, Bi_2WO_6, SF, 10SF20BWZ composites and (c) Sr20BWZ composites with various $SrFe_2O_4$ loadings; Kubelka-Munk plot of (d) ZnO, (e) Bi_2WO_6 and (f) $SrFe_2O_4$; Mott-Schottky plots of (g) ZnO, (h) Bi_2WO_6 and (i) $SrFe_2O_4$.

Bandgap energies of the catalyst were important in proposing the mechanism. Therefore, the bandgap energies of ZnO, Bi_2WO_6 and $SrFe_2O_4$ were determined via plotting the Kubelka-Munk function's graph. As illustrated in Figure 4.28d, the energy band gap (E_g) of ZnO was determined to be 3.2 eV by extrapolating the tangent line to y-axis. This was in consistent to the bandgap energy reported in literature review (Krishnamoorthy et al., 2023).

Likewise, the E_g of Bi_2WO_6 and $SrFe_2O_4$ was ascertained to be 2.94 eV (Figure 4.28e) and 1.9 eV (Figure 4.28f), respectively. Similar bandgap energy of Bi_2WO_6 and $SrFe_2O_4$ were also reported in previous literature reviews (Sravandas and Alexander, 2021; Mousavi and Shobegar, 2020). In addition, Mott Schottky analysis was applied to further investigate the band edge position of as-prepared photocatalyst. The flat band potential (E_{fb}) of ZnO, Bi_2WO_6 and $SrFe_2O_4$ were determined through Mott-Schottky test in this study. According to Mishra et al. (2020), the E_{fb} can be determined from intercepts of tangent line from the Mott-Schottky plot. As shown in Figure 4.28g-i, the E_{fb} for ZnO, Bi_2WO_6 and $SrFe_2O_4$ were determined to be -0.75eV, -0.003 eV and -1.05eV, respectively. Considering the fact that CB of semiconductor is situated closed to E_{fb}, which located 0 – 0.1 eV higher than E_{fb} (Yuan et al., 2019; Wan et al., 2020), the E_{CB} of ZnO, Bi_2WO_6 and $SrFe_2O_4$ were estimated as -0.75eV, -0.003 eV and -1.05eV, respectively, by assuming the difference of voltage between band edge and flat band potential as 0V. Since the E_{CB} of ZnO, Bi_2WO_6 and $SrFe_2O_4$ have been determined, their valence band potential (E_{VB}) can be calculated by using formula $E_{VB} = E_{CB} + E_g$ (Mishra et al., 2021). The E_{VB} of ZnO, Bi_2WO_6 and $SrFe_2O_4$ were calculated as 2.45, 2.94 and 0.85eV, respectively. Subsequently, the determined E_g, E_{CB} and E_{VB} were applied in drafting the structure diagram as displayed in Figure 4.29. It can be noted that the Bi_2WO_6 was sandwiched by ZnO and $SrFe_2O_4$, and their staggered alignment was responsible to form a double Z-scheme mechanism for efficient charge carrier separation.
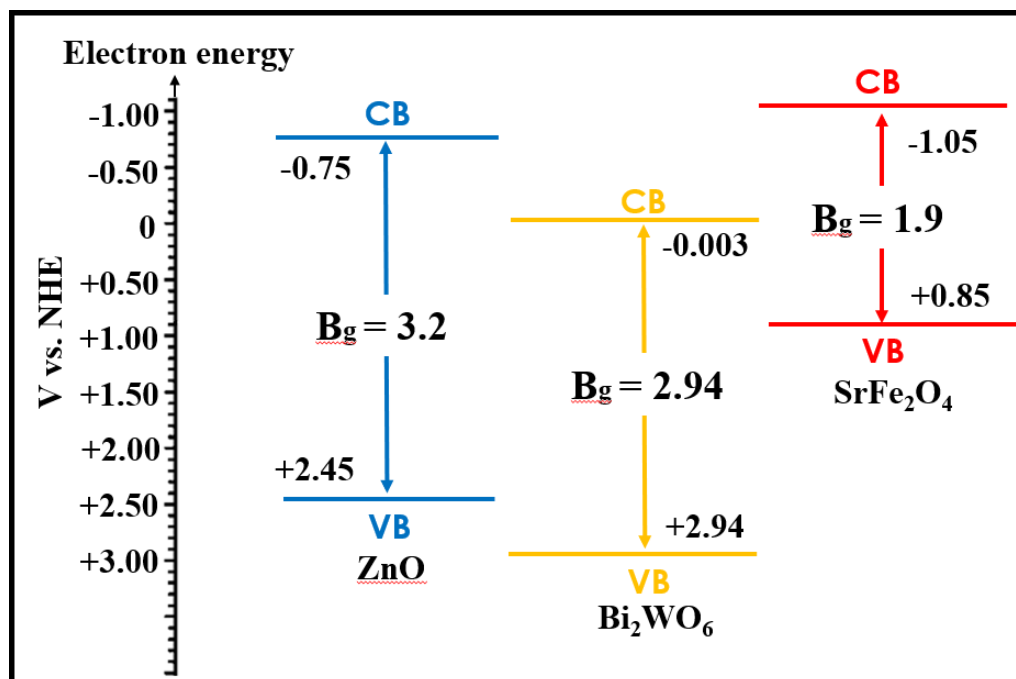
Figure 4.29: Band structure diagram of 10Sr20BWZ composite.

4.4.5 Possible Photocatalytic Mechanism of DMP Degradation Over 10Sr20BWZ

According to the results as described above, a conceivable mechanism of 10Sr20BWZ was postulated and demonstrated in Figure 4.30. Initially, the 10Sr20BWZ composite was presumed to follow the traditional transfer scheme. Based on that assumption, ZnO, Bi_2WO_6 and $SrFe_2O_4$ were activated under sunlight irradiation and produced the photoactivated e^- and h^+ pairs. Since the E_{CB} of Bi_2WO_6 located at a position lower than ZnO and $SrFe_2O_4$, therefore the photogenerated e^- from ZnO and $SrFe_2O_4$ will migrate to E_{CB} of Bi_2WO_6. Concurrently, the h^+ from E_{VB} of Bi_2WO_6 will transfer to E_{VB} of ZnO and $SrFe_2O_4$ since the E_{VB} of ZnO and $SrFe_2O_4$ were smaller than E_{VB} of Bi_2WO_6. In this scenario, the photogenerated e^- gathered in E_{CB} of Bi_2WO_6 while the h^+ accumulated in E_{VB} of ZnO and $SrFe_2O_4$. Unfortunately, the E_{CB} of Bi_2WO_6 (-0.003 V vs NHE) was located at a position that has lower potential than $\bullet O_2^-$ $(O_2/\bullet O_2^-) = -0.33$ eV vs NHE (Zhao et al. 2020; Makola et al., 2022). This

142

means the generation of $\bullet O_2^-$ was not favor and this was not consistent with the findings from active species experiments where $\bullet O_2^-$ played minor role in photodegradation of DMP. Since the transfer mechanism follow the traditional heterojunction transfer scheme was invalid, a dual Z-scheme transfer mechanism was proposed for photodegradation of DMP over 10Sr20BWZ composite.
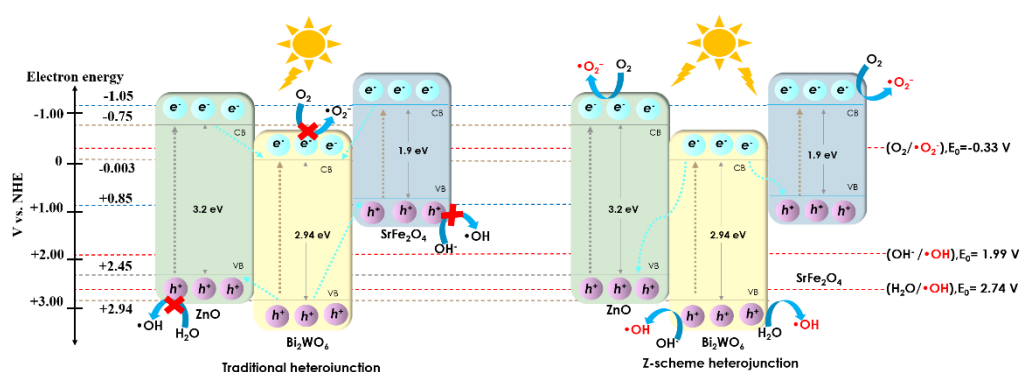
Figure 4.30: Schematic diagram of traditional and Z-scheme transfer mechanism for Sr20BWZ composite.

As usual, the photogenerated electron-hole pair was generated upon the composite exposed to sunlight irradiation. According to dual Z-scheme heterostructure transfer mechanisms, the photogenerated e^- from E_{CB} of Bi_2WO_6 will transfer to E_{VB} of ZnO and $SrFe_2O_4$ due to their E_{VB} located at a position higher than E_{VB} of Bi_2WO_6. These e^- will recombine with the h^+ at E_{VB} of ZnO and Bi_2WO_6. Subsequently, the e^- that remained in E_{CB} of ZnO (-0.75V vs NHE) and $SrFe_2O_4$ (-1.05V vs NHE) have sufficient potential to reduce O_2 into $\bullet O_2^-$. Moreover, the h^+ that remaining in E_{VB} of Bi_2WO_6 able to oxidize the DMP directly and at the same time oxidized OH^- and H_2O into $\bullet OH$ radicals as E_{VB} has enough potential to trigger the generation of $\bullet OH$ ($H_2O/\bullet OH$) = 2.74 eV vs NHE and $\bullet OH$ ($OH^-/\bullet OH$) = 1.99 eV (Graimed et al., 2023; Feng et al., 2023; Fernandes et al., 2022; Xue et al., 2023). Hence, in this

143

study, the photodegradation of DMP was subjected to follow dual Z-scheme mechanism as it was more reasonable and coherent to the findings from scavenger studies where both h^+, •OH and •O_2^- played their role in photodegradation of DMP.

4.5 Photodegradation Pathway of DMP And Intermediates Studies

The photodegradation pathway of DMP over 10Sr20BWZ composite was investigated using GC-MS technique. The experiment was carried out under following conditions: catalyst loadings= 1.0 g/L; [DMP] = 5.2 μM; pH= natural solution pH. The collected sample was sent for GC-MS analysis. The degradation pathways are illustrated according to results obtained from GC-MS analysis and related literature reviews (Zhao et al., 2022; Tan et al., 2020; Xue et al., 2019; Liu et al., 2019; Chen et al., 2009).

The chemical structure and mass value of obtained intermediates were tabulated and displayed in Appendix A. The possible photodegradation pathway were then proposed and presented in Figure 4.31.The major intermediates: dimethyl phthalate, bis(2-ethylhexyl) phthalate, di-n-octyl phthalate, 2,4-di-tert-butylphenol, phenol,3,5-bis(1,1-dimethylethyl)-, Pentanoic acid,5-hydroxy-,2,4-di-t-butylphenyl esters, 3,5-octanedione,2,7-dimethyl-, Nonane,4,5-dimethyl-, propanedioic acid,propyl-, tridecanoic acid are denoted as (1),(5),(6),(7),(8),(9),(10),(11),(12) and (13), respectively. Initially, DMP (1) underwent the radicals attack and generated phthalic acid (2). Under the continuous attack by radicals such as •OH and •O_2^-, phthalic acid would be decarboxylated and produced benzene (3), which would then undergo an addition of OH group on benzene ring to form phenol (4) (Tan et al., 2020).

After that, various intermediates such as bis(2-ethylhexyl) phthalate (5) and di-n-octyl phthalate (6) can be generated through esterification. Simultaneously, the 2,4-di-tert-butylphenol (7) together with phenol,3,5-bis(1,1-dimethylethyl)-(8) were generated and formed pentanoic acid, 5-hydroxy-, 2,4-di-t-butylphenyl esters (9) with the growth of the carbon chain. The generated intermediates were further photodegraded into 3,5-octanedione,2,7-dimethyl-(10), nonane, 4,5-dimethyl- (11), propanedioic acid, propyl- (12) and tridecanoic acid (13) through ring-opening reaction (Zhao et al., 2022) via the continuous attack of generated active radicals. In the end, the intermediates would degrade to small organic substances and eventually mineralized into CO_2 and H_2O.
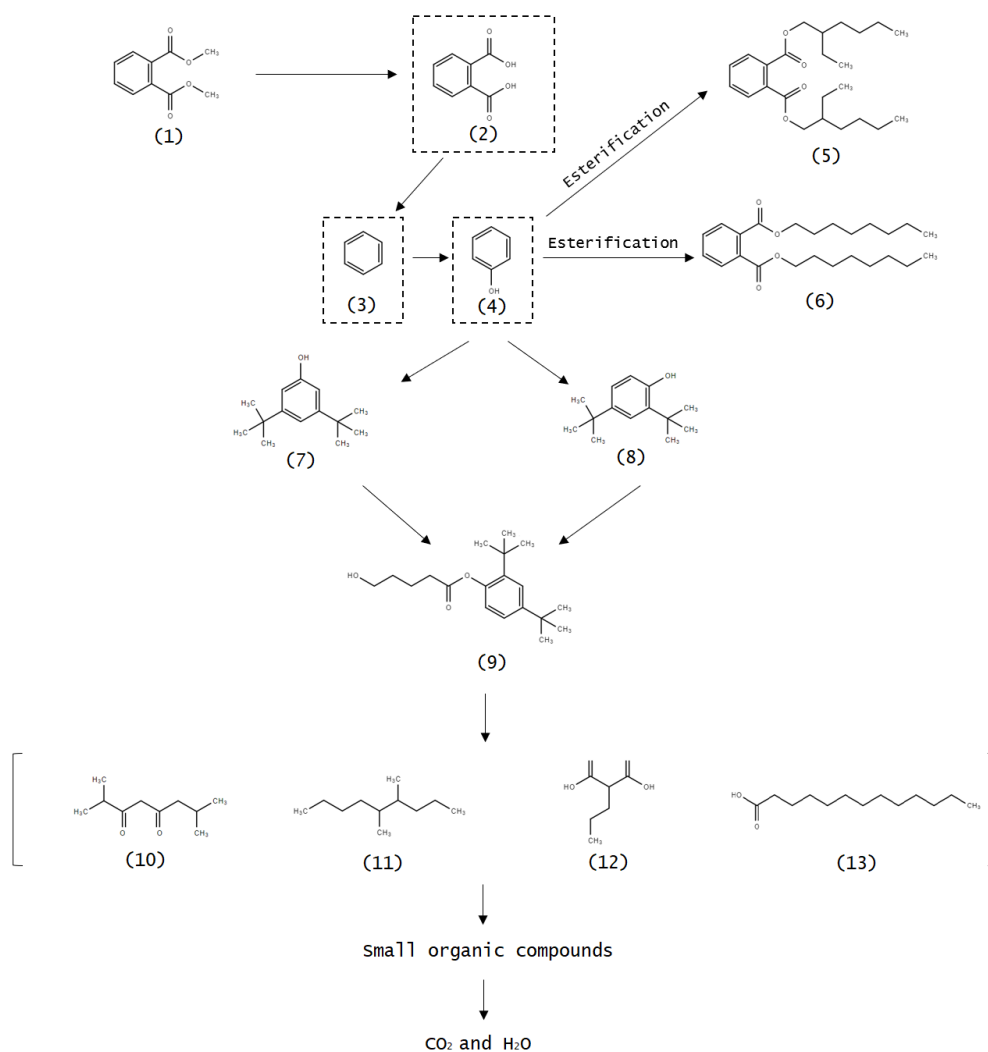
Figure 4.31: Schematic diagram of proposed degradation pathway of DMP over 10Sr20BWZ composite.

Zhao et al. (2022) have synthesized Ag/rGO/BiOBr for photodegradation of 3,6-DMP. The intermediates were determined by GC-MS analysis. Several intermediates have been detected and three possible pathways were proposed for photodegradation of phthalic acid. The first way was through forming small molecular acids and alcohols which eventually degraded into CO_2 and H_2O. The second way was degraded into different phthalate esters and the third way was oxidized from phthalic acid to phenol compound and ends with intermediates with longer carbon chain. The intermediates such as pentanoic acid,5-hydroxy-, 2,4-di-t-butylphenyl esters and Bis(2-ethylhexyl)

phthalate were also appeared in their study. That was in consistent with our results as these two intermediates were also appeared in our GC-MS findings. Tan et al. (2020) has reported that the phthalic acid and phenol were the intermediates that included in the proposed degradation pathway of naphthalene. The naphthalene will be attacked by •OH radicals to form DMP. According to the proposed degradation pathway, phenol will undergo •OH radical attack and formed Phenol, 3,5-bis(1,1-dimethylethyl)- or 2,4-di-tert-butylphenol. Either one of these compounds were further degraded into Pentanoic acid, 5-hydroxy-, 2,4-di-t-butylphenyl esters. These intermediates were also appeared in this study.

4.6 MINERALIZATION STUDY ON PHOTOCATALYTIC DEGRADATION OF DMP

The mineralization study on photocatalytic degradation of DMP over different photocatalysts was evaluated through COD test. The COD experiments were carried out under the following conditions: initial DMP concentration = 5.2 μM; photocatalyst loading = 1g/L; pH of DMP solution = 6.5. Figure 4.32 shows the COD removal of DMP over different photocatalysts. 10Sr20BWZ composite exhibited higher COD removal when compared to 20BWZ and pure catalysts, which was in consistent with the findings from photocatalytic degradation of DMP. Besides, the result revealed that the 10Sr20BWZ composite exhibited 100% COD removal after 90 min of sunlight irradiation. It was observed that the fully removal of COD took longer irradiation period than photodegradation of DMP which implying the presence

of intermediates in DMP solution. However, fully removal of COD was observed after 90 min of irradiation indicating that the DMP was completely mineralized into CO_2 and H_2O.
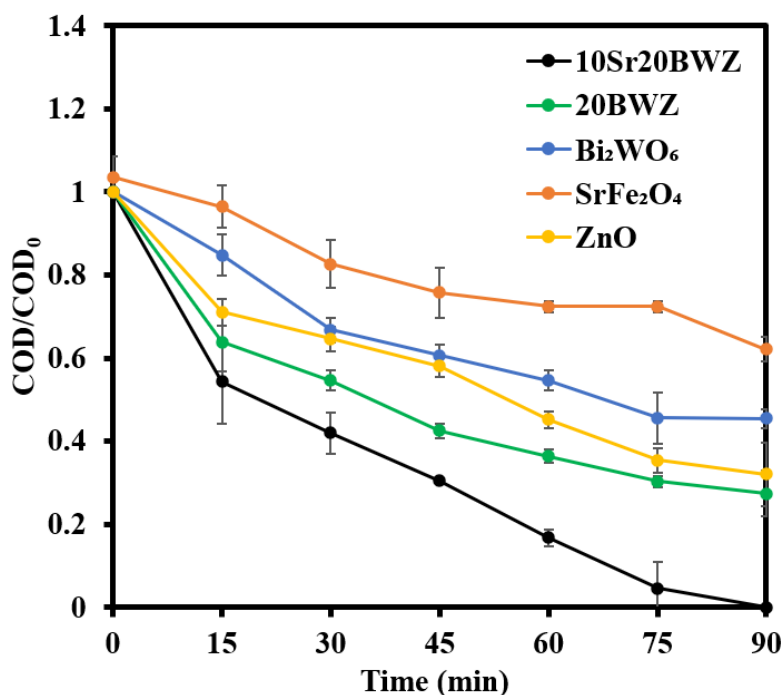
Figure 4.32: Plot of COD/COD_0 versus irradiation time over different photocatalysts ([DMP]= 5.2 µM; photocatalyst loading = 1 g/L; pH = 6.5).

Wang et al. (2011) also reported the similar observation on photocatalytic degradation of DMP using $FeCl_3/NaNO_3$ composite. In their study, the degradation of DMP was up to 96% after 4 days sunlight irradiation, while the COD removal was only 82.8%. This indicated that there were some intermediates existed in the degraded DMP solution which required longer treatment periods to fully remove them.

4.7 REUSABILITY STUDY ON 10SR20BWZ COMPOSITE

It cannot be denied that high reusability of photocatalyst was one of the important criteria that will be valued in practical application. In this study, the

10Sr20BWZ composite was recycled for several cycles to evaluate its stability in degradation of DMP. The experiment was carried out under the following conditions: catalyst loading = 1.0 g/L, [DMP] = 5.2 μM; pH solution = pH 7. After the first application, the 10Sr20BWZ composite can be recovered from used solution with the assistance of magnet bar and filtration paper. The used photocatalyst was rinsed and dried in an oven at 60 °C for the next applications. The dried photocatalyst was again reused in next cycle of photodegradation for fresh DMP solution. The similar procedure was repeated for 3 times and the result was displayed in Figure 4.33.
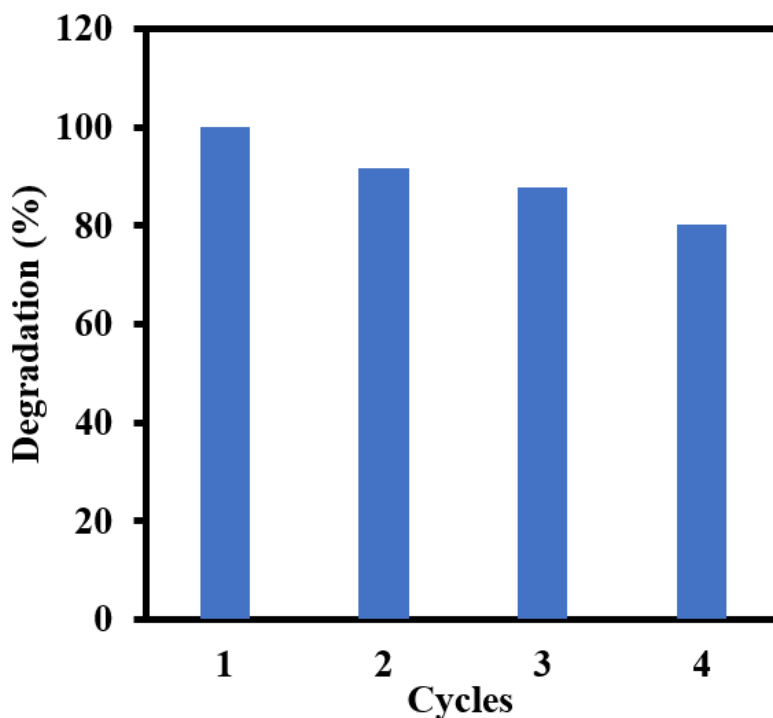
Figure 4.33: Degradation efficiency of 10Sr20BWZ composite for several runs. ([DMP]= 5.2 μM; photocatalyst loading = 1 g/L; pH = 6.5).

Figure 4.33 displays the result of reusability for 10Sr20BWZ composite in DMP degradation. The results revealed that slightly decline in degradation efficiency for 10Sr20BWZ composite in photocatalytic degradation of DMP. The slightly decrease in degradation percentage after 4 cycles could be attributed to the inevitable loss of photocatalyst during the recovery stage.

149

Moreover, the decline in photocatalytic performance could be due to occupying of active sites by DMP molecules (Chang et al., 2014). Moreover, the photocatalytic performance of 10Sr20BWZ composite was observed to maintain its performance over 80.4% after 4 cycles of run. This indicated it has high stability and could be a promising product in clarifying industrial wastewater. In a nutshell, 10Sr20BWZ composite was a potential composite that was high in stability which can be applied in industrial application.

Chang et al. (2014) have fabricated CuPc/TSM for photodegradation of DMP using visible-light irradiation. They reported that the degradation efficiency slightly dropped after reused for several cycles. They claimed that the reduction in degradation efficiency after several runs was due to reduction of active sites caused by occupying of DMP molecules. Rani and Shanker (2018) have synthesized ZnO/ZnHCF for photodegradation of bisphenol A which is one of the endocrine disruptors. In their study, the photocatalytic performance of ZnO/ZnHCF was slightly reduced after several runs probably due to adsorption of the pollutant molecules on catalyst active sites.

Another study from Mukonza et al. (2022) have synthesized F-Sm/TiO$_2$ for photocatalytic degradation of Brilliant Black bis-azo dyes. The photochemical stability of as-synthesized photocatalyst was assessed by recycling the same catalyst for several times. The degradation efficiency was reduced from 64.6% to 31.2% after 5 cycles of run which was caused by loss of photocatalyst in mass during recovery stage. Ahmadpour et al. (2020) have prepared ZnFe$_2$O$_4$/TiO$_2$/Cu nanocomposite for photocatalytic degradation of naproxen. The stability of photocatalyst was assessed by reused the same catalyst for 5 cycles. The results revealed that the degradation efficiency was

150

reduced from 80.7% to 72.3% after 5 cycles, indicating that the catalyst was high in stability and its application in industrial is economically beneficial.

4.8 PHYTOTOXICITY STUDY ON PHOTODEGRADED DMP SOLUTION

In order to evaluate whether the treated solution suitable to be discharged to the environment and used for irrigation without causing negative impact to ecosystem, phytotoxicity test was performed. In this study, phytotoxicity assessment was performed to study the adverse impacts on growth and metabolism of plant caused by DMP solution. The phytotoxicity experiment was carried out by watering the *Vigna radiata* using treated DMP solution, the growth of plant and its length of radicle were recorded and measured as it reflected the degree of phytotoxicity. Three set of *Vigna radiata* seeds were irrigated by distilled water (control), untreated DMP and photocatalytically treated DMP for 6 days. After 6 days of irrigation, the radicle length of *Vigna Radiata* was measured and recorded for calculation in phytotoxicity. The photos of *Vigna Radiata* after irrigated with water (as a control), photocatalytically treated DMP solution and untreated DMP solution for 6 days are shown in Appendix B.

Figure 4.34 displays the length of radicle for *Vigna Radiata* and its respective phytotoxicity for control, untreated DMP and photocatalytically treated DMP. The average length of radicle for *Vigna Radiata* which irrigated by distilled water (control) was 1.8 cm while the radicle length which irrigated by untreated DMP and photocatalytically treated DMP were 0.6cm and 1.5cm,

respectively. Compared to untreated DMP, the radicle length of *Vigna Radiata* after irrigated with photocatalytic treated solution getting longer which indicated the reduction of phytotoxicity. Subsequently, the obtained data was fit into the phytotoxicity equation in order to calculate the phytotoxicity. The phytotoxicity of un-treated DMP was as high as 66.2% while the phototoxicity of control was fixed at 0 %. However, the phytotoxicity of DMP was reduced greatly to 16.6% after going through treatment using photocatalysis. The untreated DMP could induce some sort of inhibition on plant growth, this revealed that the solution was high in phytotoxicity and unsafe to be release to environment. However, the phytotoxicity of DMP reduced greatly after treated using 10Sr20BWZ composite, this was in accordance with the result of photocatalytic activities.
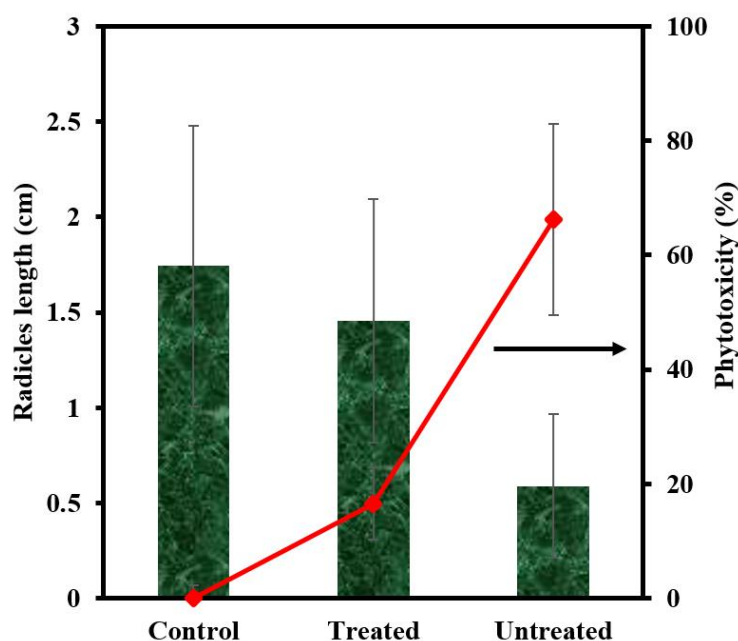
Figure 4.34: Radicle length of *Vigna Radiata* and their relative phytotoxicity (%) irrigated by distilled water (control), photocatalytically treated and untreated DMP solution.

Dugandžić et al. (2017) performed the photocatalytic degradation of weed control herbicide, namely nicosulfuran. In their study, the phytotoxicity

of the samples before and after photocatalytic treatment were examined by *Vigna mungo.* The *Vigna mungo* were irrigated for six days, and their length of radicles were measured and calculated for phytotoxicity. The phytotoxicity of Nicosulfuron was noticed to drop from 56.8% to 14.8% after going through photocatalytic treatment. Zhou et al. (2020) have studied the phytotoxicity of photocatalytically treated sulfamethazine (SMZ) which is one type of antibiotic using Chinese gabbage (*Brassica rapa L.*). The seed radicle length of *Brassica rapa L.* in SMZ was found to be shorter than the blank sample (control). However, the radicle length of *Brassica rapa L.* in photocatalytic treated SMZ was found longer than untreated SMZ solution. This indicated the phytotoxicity of SMZ was reduced greatly after going through photocatalytic treatment.

4.9 KINETIC STUDY

4.9.1 Determination of Kinetic Order

In general, the concept of kinetic is related to the speed of reaction for a particular substance to appear or disappear. Gaya et al. (2014) established a relationship between the rate equation and photocatalytic activities, defining the rate of reaction using a differential rate equation. In this study, Equation 4.13 was employed to express the differential rate law, which quantifies the kinetics of the photocatalytic process., where $-r$ refers to rate of consumption for reactants, k is the rate constant, C_{DMP} is the concentration of DMP, n refers to order and t is reaction time.

$$-r = \frac{dC_{DMP}}{dt} = \text{k [concentration of DMP]}^n \tag{4.13}$$

The order of the reaction was determined by n value, which is 0,1,2 or 3. Hence, the kinetic order for the photodegradation of DMP was determined by fitting the obtained data into integrated equation of 0, 1st, 2nd and 3rd order as displayed in Table 4.1.

Table 4.1: The order of reaction with their relative integrated equations (Gaya et al. 2014)

Order (n)	Reaction	Rate laws	Integrated Equations	Rate constant (k) units
0	Zero order	$-r = kC_{DMP}^0$	$C_{DMP} = -C_{DMP_0} + kt$	$mol \cdot (L \cdot min)^{-1}$
1	First order	$-r = kC_{DMP}^1$	$\ln\frac{C_{DMP_0}}{C_{DMP}} = kt$	$L \cdot min^{-1}$
2	Second order	$-r = kC_{DMP}^2$	$\frac{1}{C_{DMP}} = kt + \frac{1}{C_{DMP_0}}$	$L(mol \cdot min)^{-1}$
3	Third order	$-r = kC_{DMP}^3$	$\frac{1}{C_{DMP}^2} = kt + \frac{1}{C_{DMP_0}^2}$	$(L/mol)^2 \cdot min^{-1}$

Where $-r$ = reaction rate

k = rate constant

C_{DMP_0} = initial concentration of DMP (mg/L)

C_{DMP} = concentration of DMP at reaction time t (mg/L)

t = reaction time (min)

A series of experiment data with catalyst loading (0.5g/L − 2.0 g/L) were substituted into integrated equation and their respective graphs were plotted in order to determine the kinetic order (n value) for photodegradation of DMP. Figure 4.35 depicts the kinetic graph for the 0 order, while Figure 4.36

represents the 1st order, Figure 4.37 displays the 2nd order, and Figure 4.38 illustrates the 3rd order kinetics.
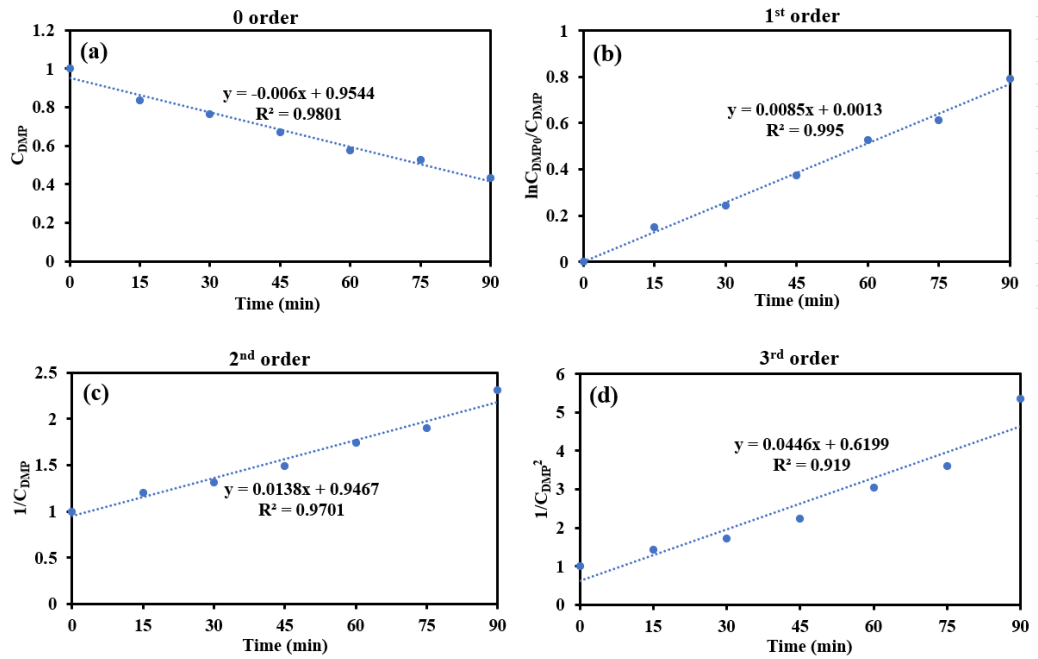
Figure 4.35: Plot of 0 to 3rd order reaction. Conditions: 10Sr20BWZ loading = 0.5 g/L; DMP concentration = 5.2 µM and pH = natural solution pH.
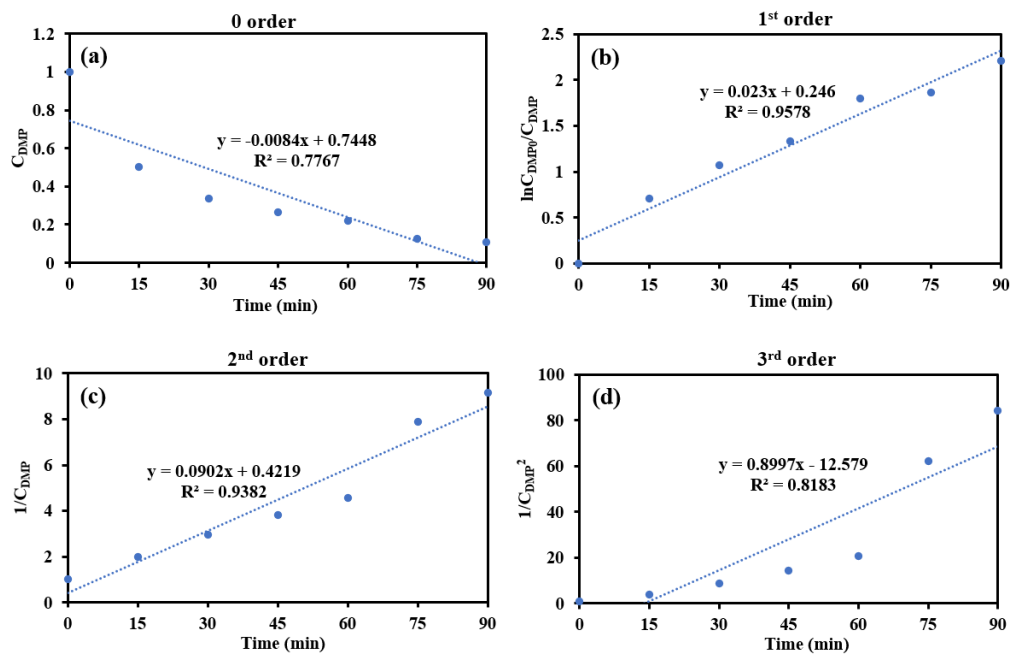
Figure 4.36: Plot of 0 to 3rd order reaction. Conditions: 10Sr20BWZ loading = 1.0 g/L; DMP concentration = 5.2 µM and pH = natural solution pH.
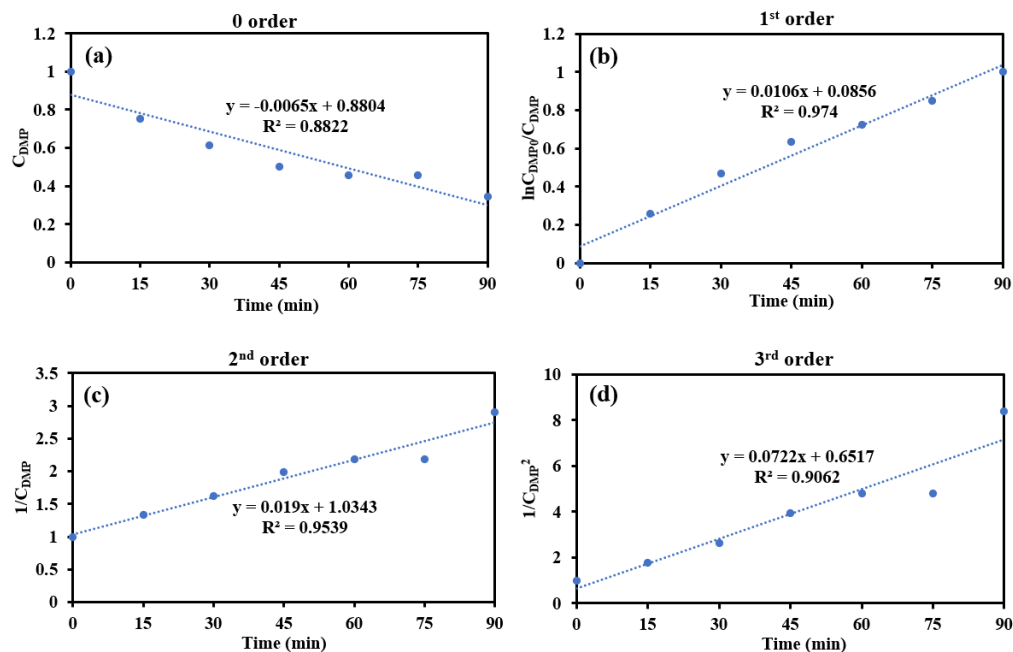
Figure 4.37: Plot of 0 to 3rd order reaction. Conditions: 10Sr20BWZ loading = 1.5 g/L; DMP concentration = 5.2 μM and pH = natural solution pH.
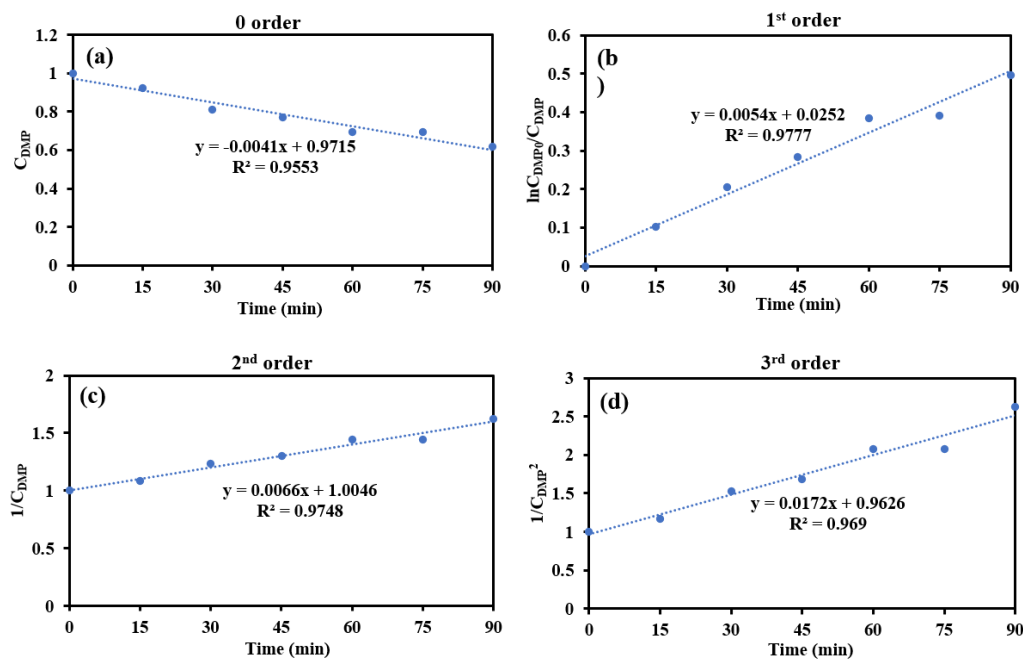
Figure 4.38: Plot of 0 to 3rd order reaction. Conditions: 10Sr20BWZ loading = 2.0 g/L; DMP concentration = 5.2 μM and pH = natural solution pH.

The rate constant (k) together with their coefficient of determination (R^2) for each set of experiment were determined were obtained by analyzing the slope of the best fitting line from the plotted data. The obtained rate

constant (k) and their corresponding coefficients of determination (R^2) are presented in Table 4.2.

Table 4.2: Rate constant of reaction for various 10Sr20BWZ loadings under different orders of reaction.

Reaction order	Catalyst loading of 10Sr20BWZ							
	0.5 g/L		1.0 g/L		1.5 g/L		2.0 g/L	
	k	R^2	k	R^2	k	R^2	k	R^2
0	-0.006	0.9801	-0.0084	0.7767	-0.0065	0.8822	-0.0041	0.9553
1st	0.0085	0.995	0.023	0.9578	0.0106	0.974	0.0054	0.9777
2nd	0.0138	0.9701	0.0902	0.9382	0.019	0.9539	0.0066	0.9748
3rd	0.0446	0.919	0.8997	0.8183	0.0722	0.9062	0.0172	0.969

It can be noted that the determination of coefficient (R^2) for 0 order reaction ranged from $0.7767-0.9801$; the range of R^2 for 1st order reaction was from $0.9578 - 0.995$; R^2 for 2nd and 3rd order were ranged from $0.9382 - 0.9748$ and $0.8183 - 0.969$, respectively. The result clearly demonstrated that the photodegradation of DMP using 10Sr20BWZ composite were best fitted with 1st order reaction as the value of R^2 was found to be the highest in 1st order reaction for all catalyst loadings. Moreover, various literatures also reported that their photocatalytic activity followed the 1st order reaction model in degradation of organic pollutants (Govarthanan et al., 2021; Subramonian et al., 2017).

Subramonian et al. (2017) have synthesized the Fe_2O_3-TiO_2 for degradation of pulp and paper mill effluent. In their study, the kinetic for photodegradation of pulp and paper mill effluent followed the Langmuir-Hinshelwood 1st order reaction model because this model was normally used for plateau-type kinetic curve and well fitted with their results findings with value of R^2 up to 0.9857. Govarthanan et al. (2021) have fabricated MoS_2@MIL-88(Fe) for photocatalytic degradation of Methylene Blue (MB) and RhB dyes under visible light irradiation. The Langmuir Hinshelwood 1st order equation was used to determine the rate constant in photodegradation of dyes. The L-H model was observed fitted well with MB and RhB dye degradation as the regression was found as high as 0.9864.

4.9.2 Kinetic (Langmuir-Hinshelwood) Model

The photodegradation of DMP over 10Sr20BWZ composite was categorised as heterogeneous photocatalytic reaction. It was reported that Langmuir-Hinshelwood (L-H) model was normally adopted for photocatalytic reaction that occurred in heterogeneous systems (Sarani et al., 2021; Orooji et al., 2021). The L-H model made assumption on the reaction occurred linearly dependent on limited single active sites that localised on surface of the adsorbent which affecting the rate of reaction. Since photocatalytic reaction condition was well matched with L-H model, it was commonly adopted by catalytic field researchers in determining the rate of reaction as they able to utilise it for experimental data. Moreover, it was reported that L-H first order model was applied in studying the kinetic rate for photodegradation of DMP

(Jing et al., 2018; Ku et al., 2017). In addition, the reaction order for photocatalytic degradation of DMP was proven to follow first order reaction as discussed in section of reaction order determination above, which also in consistent with the reported literature.

Hence, L-H model was adopted in current research to determine the kinetic profile of DMP photodegradation. Based on L-H kinetic model, the reaction rate equation for photodegradation of DMP is expressed by Equation 4.14.

$$-r = \frac{dC_{DMP}}{dt} = \frac{kKC_{DMP}}{1+KC_{DMP}} \qquad (4.14)$$

Where r = rate of DMP degradation (mg/L•min)

C_{DMP} = concentration of DMP (mg/L)

t = reaction time

k = reaction rate constant (mg/L•min)

K = adsorption equilibrium constant (luc)

Since the photocatalytic degradation of DMP was performed in lab scale and DMP solution was diluted to desired concentration, the KC in Equation 4.14 becomes less than 1 (K<<1) and negligible. Therefore, the denominator equal to 1 and integrated into apparent first order equation as displayed in Equation 4.15. The first order equation also has been confirmed in determination rate reaction section through plotting and fitting the graph using obtained experimental data.

$$\ln \frac{C_{DMP_0}}{C_{DMP}} = kKt = k_{app}t \qquad (4.15)$$

Where kK = k_{app} = apparent rate constant

Figure 4.39 shows the pseudo first order linear plots using equation 4.15 for photodegradation of DMP over 10Sr20BWZ composite at different catalyst loadings. The experiments were carried out under following conditions: [DMP] = 5.2 μM; pH = natural solution pH; catalyst loading = 0.5 – 2.0 g/L. The apparent rate constant (k_{app}) of the degradation activity for different catalyst loadings can be determined from slope of trendline by plotting graph using the set of experimental data. The k_{app} and their coefficient determination (R^2) for different catalyst loadings of 10Sr20BWZ are tabulated in Table 4.3.
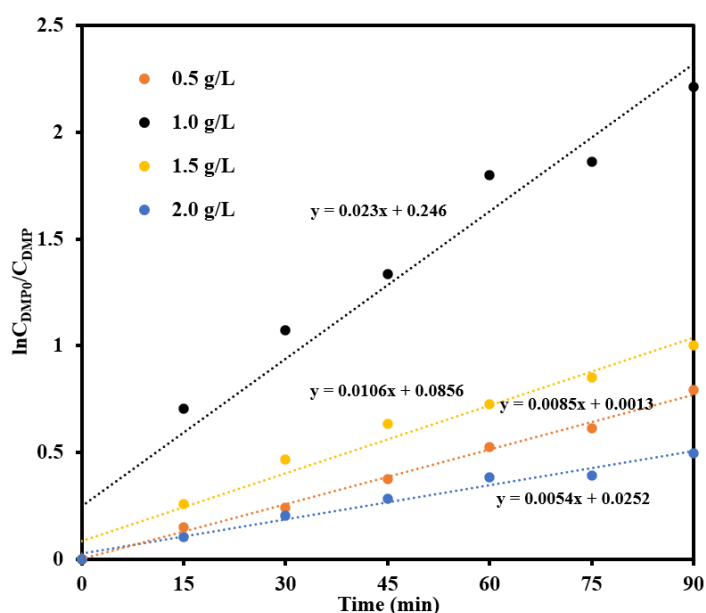
Figure 4.39: Pseudo first order linear plots of ln(C_{DMP_0}/C_{DMP}) versus irradiation time for photodegradation of DMP using 10Sr20BWZ with different loadings (0.5 g/L -2.0 g/L).

Table 4.3: The value of rate constant and their coefficient determination for different catalyst loadings of 10Sr20BWZ using L-H 1st order equation.

Catalyst loading (g/L)	Apparent rate constant (k_{app})	Coefficient determination (R^2)
0.5	0.0085	0.9950
1.0	0.0230	0.9578
1.5	0.0106	0.9740
2.0	0.0054	0.9777

The k_{app} value of the photocatalytic reaction increased when the catalyst dosage raised from 0.5 g/L to 1.0 g/L. The increasing in rate constant with an increase in catalyst loading may be attributed to the augmentation of active sites which was beneficial for the photodegradation of DMP. Therefore, the k_{app} value was observed to increase as the catalyst loading increased from 0.5 g/L to 1.0 g/L. Nonetheless, a reduction in k_{app} value was noticed when loading of catalyst exceeded 1.0 g/L. This was caused by reduction in light transparency during high concentrations. Moreover, the k_{app} values were arranged in an order: 0.5<2.0<1.5<1.0 g/L, which was in consistent with the photocatalytic result as discussed above. In addition, the determination coefficients of all the rate constant were in range of 0.9578−0.9950, which indicating the experimental data was well fitted with L-H 1st order model.

Ku et al. (2017) have studied the degradation behaviour of DMP using TiO₂ under UV irradiation. In their study, they expressed the kinetic of DMP decomposition using Langmuir-Hinshelwood model. Jing et al. (2018) have validated the photodegradation of DMP over TiO₂ followed the Langmuir-Hinshelwood 1st order reaction. In their study, the experimental data was applied in plotted the graph using L-H 1st order equation and a good linear

trendline was obtained with $R^2 = 0.9517$. This further confirmed that the kinetic model in our study was in good agreement with L-H 1st order equation, as the obtained R^2 for our series of data were greater than 0.9578. Similar scenario was reported by Chekir et al. (2016). In their study, TiO_2 and ZnO were utilised in photodegradation of Methylene Blue and the kinetic of photodegradation was expressed using Langmuir-Hinshelwood pseudo-first model. The apparent rate constant of each catalyst loadings was determined by linear regression by plotting ($\ln(C/C_0)$ vs. time). The kinetic rate constant of the degradation was observed to increase with catalyst loading, until it reached the optimum value.

4.10 PHOTOCATALYTIC DEGRADATION OF LDPE FILM

4.10.1 Weight Loss Analysis of LDPE Film

The performance of photodegradation for LDPE film incorporated with as-prepared pure ZnO, Bi_2WO_6, $SrFe_2O_4$, 20BWZ, 10Sr20BWZ composites were assessed by the weight reduction of LDPE film. The experiments were carried out by putting the LDPE film under sunlight irradiation. Figure 4.40 shows the weight loss of pure LDPE film and LDPE film loaded with different photocatalysts under sunlight irradiation. It was noteworthy that all the catalyst loaded LDPE films have higher weight loss compared to pure LDPE film. Moreover, the weight loss of composite loaded LDPE films were higher compared to single loaded catalyst LDPE film. In addition, it was noticed that the LDPE film contained 10Sr20BWZ composite exhibited the greatest weight loss compared to the other LDPE film after photocatalytic treatment. This demonstrated a higher photocatlytic performance of 10Sr20BWZ in LDPE

degradation. The weight reduction for LDPE film loaded with 10Sr20BWZ was up to 27.7% after 225 hrs of sunlight irradiation, which was 16.5 % higher than 20BWZ LDPE film. Under the same conditions, negligible reduction of pure LDPE film, ZnO film, Bi_2WO_6 film and $SrFe_2O_4$ film were noticed, which are only 0%; 3.3%; 0.6% and 1.6%, respectively. This implied that both 20BWZ and 10Sr20BWZ composites can enhance the photodegradation efficiency of LDPE film through the construction of Z-scheme mechanism which can greatly reduce the electron hole pair recombination rate and enhanced the charge carrier transfer efficiency.
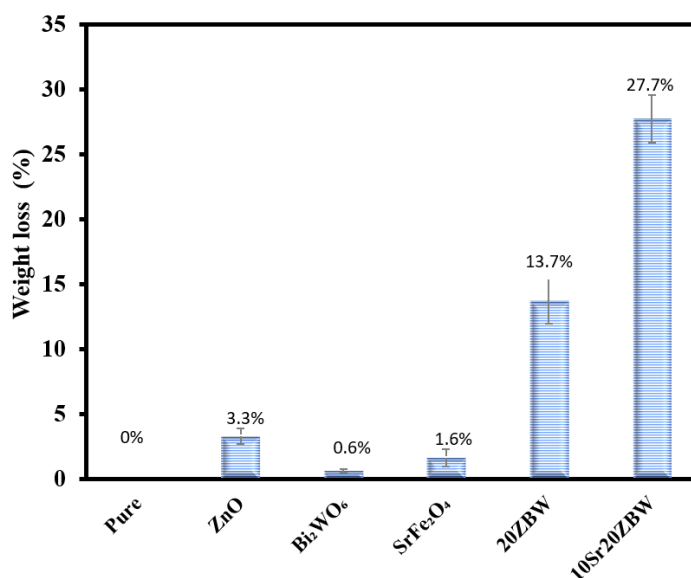
Figure 4.40: Weight reduction of LDPE film under different conditions.

Similar findings were observed and reported by Liang et al. (2013). In their study, PAM-g-TiO_2 composite was incorporated in LDPE film and irradiated under UV irradiation for photocatalytic degradation. It was observed that the PAM-g-TiO_2 LDPE film has higher weight reduction than TiO_2 LDPE film due to higher degradation efficiency of PAM-g-TiO_2 composite. Fa et al. (2008) have embedded the FePc-TiO_2 into polystrene for photodegradation

under visible light irradiation. In their study, the weight loss of FePc-TiO$_2$ film was higher than TiO$_2$ film, verifying the good photoactivity of composite photocatalysts.

4.10.2 Changes of Mechanical Properties In LDPE Film

Tensile strength and break elongation analysis were carried out in order to study the mechanical properties of different LDPE films in this study. The results of tensile strength and break elongation before and after sunlight irriadiation are tabulated in Table 4.4. It was noted that the tensile strength of 20BWZ and 10Sr20BWZ LDPE films were slightly reduced when compared to pure LDPE film before sunlight irradiation. This was caused by the introduction of photocatalyts into the LDPE film which can change the film density (Kavuncuoglu et al., 2023). After sunlight irradiation, reduction in tensile strength and break elongation for all catalyst loaded LDPE films were observed to be greater than pure LDPE film. It has been reported that the loss in tensile strength and reduction in elongation can represent the degradation of film (Liang et al., 2013).

Table 4.4: Tensile strength and break elongation of different LDPE films.

Samples	Tensile strength (Mpa)		Break elongation (%)	
	Before	After	Before	After
Blank	5.8	5.7	71.9	50.8
ZnO	7.8	7.0	88.0	56.9
Bi$_2$WO$_6$	7.6	6.1	69.2	57.3
SrFe$_2$O$_4$	6.0	5.9	98.2	47.3
20BWZ	5.1	4.1	50.4	20.2
10Sr20BWZ	5.4	1.7	71.9	20.0

Kavuncuoglu et al. (2023) also reported that all the composite containing films have bigger reduction in tensile strength values than pure LDPE film and explained by reduction in film crystallinity due to loading of photocatalysts. Ozmihci & Balkose, 2013 have explained the reduction in break elongation value was caused by introduction of photocatalysts into LDPE matrix which resulted in lower chain mobility. In addition, the LDPE film that incorporating with 10Sr20BWZ composite revealed the greatest loss in tensile strength and reduction in elongation after 225 hr of sunlight irradiation. This was explained by higher photocatalytic ability in 10Sr20BWZ composite which has been discussed in photocatalytic activity section. The result was in parallel with the loss in weight as discussed above.

4.10.3 Morphology Analysis of LDPE Film

Figure 4.41 shows the surface morphology of pure LDPE and composite films before and after 225 hr sunlight irradiation. The FESEM images of pure LDPE film before sunlight exposure (Figure 4.39a) and after sunlight exposure (Figire 4.39b) revealed smooth surface with no visible cavities. This proved that the pure LDPE film without incorporated with photocatalyst was not able to biodegrade or undergo self-decomposition. Moreover, it was noticed that the LDPE film that incorporated with ZnO, Bi_2WO_6 and $SrFe_2O_4$ after sunlight exposure (Figure 4.39d,f,h) had higher number of micron sizes cavities, wrinkles and more damage areas when compared to LDPE film before sunlight exposure (Figure 4.39c,e,g). In Figure 4.39i & 4.39k, both the BWZ and Sr20BWZ LDPE films showed uneven and protuding surface before exposed to sunlight. It was reported that the

agglomeration of catalysts in film matrix resulting in alteration of film morphology (Ali et al., 2016). After the sunlight irradiation, a ~10µm diameter cavity was appeared in BWZ LDPE film (Figure 4.39j) while larger cavities with ~30µm diameter and cracks were observed in 20BWZ composite LDPE film (Figure 4.39l). This could be due to the scissoring effect on polymer and the generation of volatile products from the LDPE matrix (Mehmood et al., 2015).
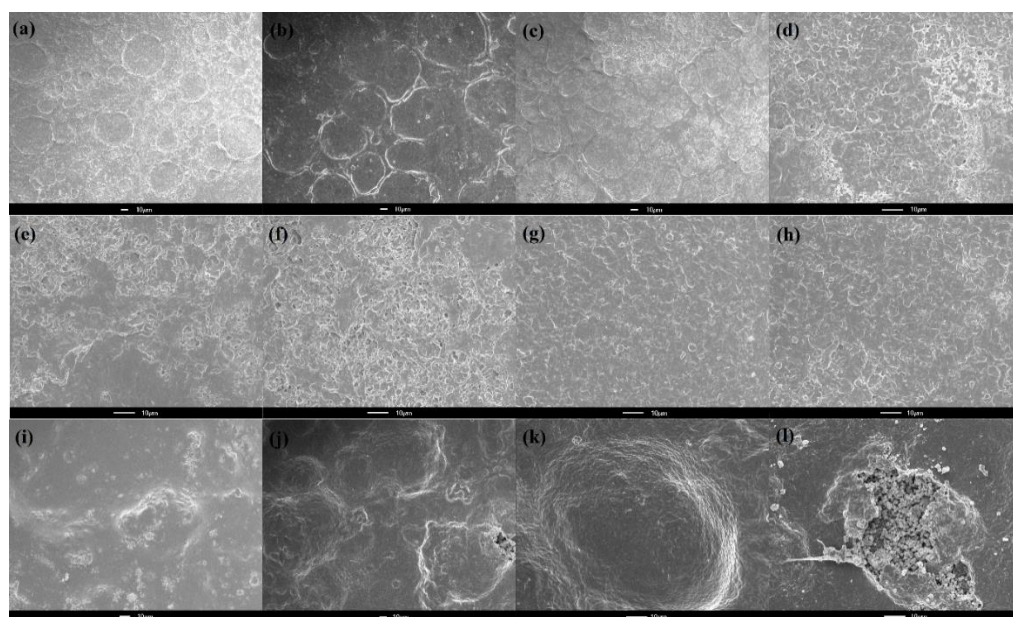
Figure 4.41: FESEM images of (a) pure LDPE film before sunlight irradiation (b) pure LDPE film after sunlight irradiation; LDPE film incorporated with ZnO (c) before sunlight exposre (d) after sunlight exposure; LDPE film incorporated with Bi_2WO_6 (e) before sunlight irradiation (f) after sunlight irradiation; LDPE film incorporated with $SrFe_2O_4$ (g) before sunlight irradiation (h) after sunlight irradiation; LDPE film incorporated with 20BWZ (i) before sunlight irradiation (j) after sunlight irradiation; LDPE film incorporated with 10Sr20BWZ composite (k) before photocatalytic treatment (l) after photocatalytic treatment.

Mehmood et al. (2015) have studied the surface morphology of TiO_2-PE film. It was reported that the micro bubbles and cracks were observed on their surface morphology of the film. They went further to suggest this was caused by evolution of volatile products and scissoring of long chain polymer

from film surface. In addition, the size of cavity in 10Sr20BWZ was found to be larger than in 20BWZ composite which indicated that the oxidation effciency of 10Sr20BWZ in LDPE film was higher than that of the 20BWZ LDPE film. The enhancement of photocatalytic performance in 10Sr20BWZ composite could be attributed to better electron-hole pair separation and low charge resistance that have been discuused in section 4.4.1. Moreover, the result was in consistent with the findings from photocatalytic performance.

4.10.4 Functional Groups Analysis of LDPE Film

ATR analysis was also used to examine the characteristic peaks in LDPE film. Figure 4.42 shows the ATR spectra of all different LDPE films before (B) and after (A) sunlight irradiation. The peak located at region 2915 cm^{-1} – 2850 cm^{-1} was attributed to C-H stretching (Kaewkam et al., 2022). The distinct peak detected at 1466 cm^{-1} and 724 cm^{-1} indicating the CH_2 bending and in-plane rocking vibration of LDPE film, respectively. (Mehmood et al., 2015; Tan et al., 2023). These characteristic peaks were observed across all the unexposed and exposed films which are vital characterisation peaks of PE film. After exposed to sunlight irradiation, the peak at ~1731 cm^{-1} was detected which could be attributed to the carbonyl group's stretching vibration (Ali et al., 2016). This indicated the formation of CO_2 and infered that the photo-oxidation was occurred. In addition, the reduction of band intensity and alteration in spectra can be observed across the LDPE composite after exposed to sunlight irradiation which proved the photocatalytic degradation of LDPE film (Ariza-Tarazona et al., 2019).
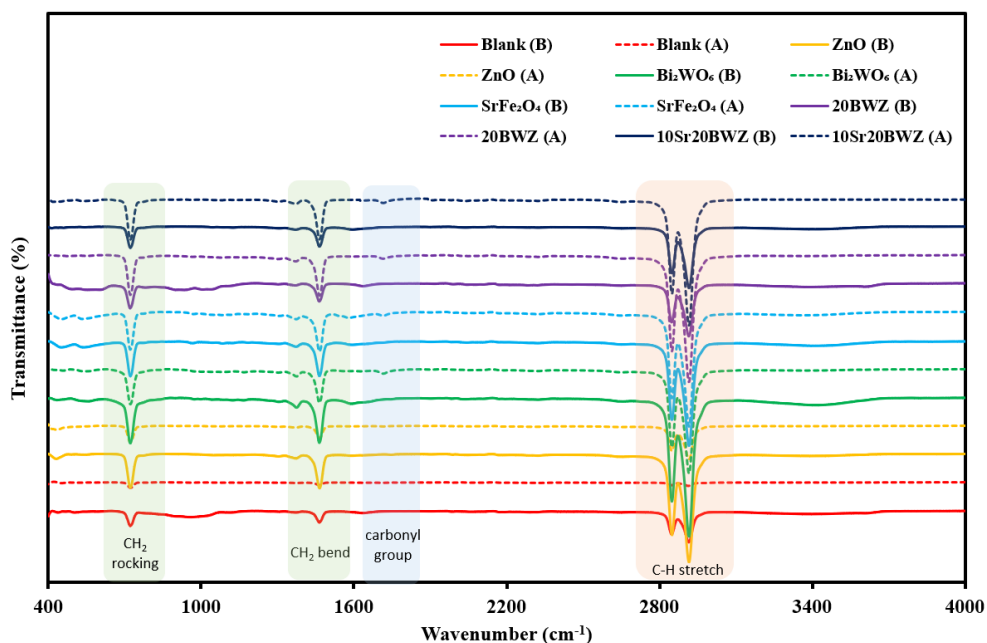
Figure 4.42: ATR spectra of different LDPE composite films.

Kaewkam et al. (2022) reported the degradation of LDPE film using TiO_2. Kaewkam et al. (2022) reported the degradation of LDPE film using TiO_2. In their study, the intensity of transmittance reduced after exposed to UV irradiation. Besides, no major changes were observed in their ATR spectra. This was similar to our research findings. Du et al. (2021) have developed KPF_6/BiOBr for degradation of polyethylene film. Similar to our findings, the functional groups such as CH_2 stretching, carbonyl group, CH_2 bonding and CH_2 recking vibrations were detected. They clamied that appearance of carbonyl group was the evidence of chemical transformation of polyethylene film.

CHAPTER 5

CONCLUSION AND RECOMMENDATIONS

5.1 CONCLUSION

Brassica Oleracea-like SF20BWZ, (SF= $SrFe_2O_4$, $BaFe_2O_4$ and $CaFe_2O_4$) composite have been successfully synthesized using hydrothermal-precipitation route. The as-prepared samples were characterised by XRD, FTIR, FESEM, TEM, EDX, XPS and VSM analyses. The XRD results showed that the as-prepared ZnO exhibited a wurtzite hexagonal structure while Bi_2WO_6 was in orthorhombic structure. The SF characteristic peaks in XRD spectra also confirmed the successful fabrication of SF20BWZ composites. FTIR analysis also revealed the existence of ZnO, Bi_2WO_6 and SF via their respective stretching vibrations. This was further confirmed by FESEM and EDX findings where SF and ZnO were found loaded homogeneously on Marimo-like Bi_2WO_6 and formed Brassica Oleracea-like SF20BWZ composites. The TEM analysis of Sr20BWZ composite proved the presence of ZnO, Bi_2WO_6 and $SrFe_2O_4$ via relative lattice spacing and also demonstrated that the $SrFe_2O_4$ with rod shape structure and ZnO griped tightly on Marimo-like Bi_2WO_6. XPS analysis showed that Sr20BWZ composite comprised of Zn 2p, O 1s, W 4f, Bi 4f, Sr 3d and Fe 2p, which is in parallel of XRD, FTIR and EDX results. Furthermore, VSM analysis has verified that the 10Sr20BWZ composite has magnetic properties and can be attracted by magnet bar.

The photocatalytic performance of as-synthesized catalyst was investigated by photodegradation of DMP under sunlight irradiation. The BWZ composite revealed enhanced photocatalytic performance when compared to pure ZnO and Bi_2WO_6. Since 20wt% was determined as the optimum Bi_2WO_6 loading among the binary composites, therefore it was adopted in constructing ternary composite. Among the 10SF20BWZ composite, 10Sr20BWZ composite demonstrated the best photocatalytic degradation efficiency and was adopted in following photocatalytic experiments. The enhanced photocatalytic performance can be credited to development of dual Z-scheme mechanism which efficiently reduced electron-hole pair recombination and improved the charge transfer efficiencies.

Different operating parameters included catalyst loadings, solution pH and foreign substances were investigated on their effects on photodegradation of DMP. The 10Sr20BWZ composite achieved 100% DMP degradation under the following conditions: catalyst loading = 1g/L and pH =7. Besides, the deterioration effect on photocatalytic performance upon introduction of foreign substances into the DMP solution was caused by competition of reactive sites with parent pollutants.

A plausible mechanism of 10Sr20BWZ composite on photodegradation of DMP was proposed based on findings from photoelectrochemical studies, active species detection, TA-PL test and UV-vis DRS assessment. The TPR and EIS results from photoelectrochemical measurement implied that 10Sr20BWZ composite has the highest electron-hole pair separation efficiency and the lowest charge resistance, which resulting in extraordinary photocatalytic performance. The reactive species study indicated that all •OH,

h^+, $\bullet O_2^-$ and e^- participated in degradation of DMP while $\bullet OH$ and h^+ played major role in DMP degradation. This was further confirmed by TA-PL test where the amount of $\bullet OH$ increased with the increasing in irradiation time. The band gap energies of ZnO, Bi_2WO_6 and $SrFe_2O_4$ were determined as 3.2 eV, 2.94 eV and 3.02 eV, respectively using Kulbelka-Munk plot. Mott-Schottky analysis was used to estimate the band structure of the catalyst. A double Z-scheme mechanism was proposed for photodegradation of DMP over 10Sr20BWZ composite as it was more coherent to the findings from scavenger tests.

The degradation pathway of DMP over 10Sr20BWZ composite was proposed based on findings from GC-MS analysis. Several intermediates such as pentanoic acid,5-hydroxy-, 2,4-di-t-butylphenyl esters and Bis(2-ethylhexyl) phthalate have been detected in GC-MS analysis which was in consistent with the reported studies. Based on findings from GC-MS and literatures, the DMP underwent continuous radical attack by $\bullet OH$ and $\bullet O_2^-$ to form smaller intermediates and finally degraded to CO_2 and H_2O.

Mineralization study revealed the fully removal of COD in DMP solution after 90 min of irradiation. 10Sr20BWZ composite revealed its high stability in photocatalytic applications. The degradation efficiency of 10Sr20BWZ was maintained over 80.4% after 4 cycles of experiment. The phytotoxicity assessment also proved that the toxicity of DMP reduced greatly from 66.2% to 16.6% after going through photocatalytic treatment.

The photodegradation of DMP over 10Sr20BWZ composite was found to follow 1st order kinetic model. The determination of kinetic order was performed by fitting the experiment data into the kinetic equation and verified

by the highest determination of coefficient (R^2). Langmuir-Hinshelwood (L-H) 1st order reaction was adopted in this study to investigate the rate of reaction in photodegradation of DMP over 10Sr20BWZ composite. Based on L-H 1st order equation, the 1.0 g/L showed the highest value of rate constant with 0.023 min^{-1}, which is parallel with the results from photocatalytic activities.

Since 10Sr20BWZ composite revealed its potential in photocatalytic degradation of DMP, therefore it was applied in photodegradation of LDPE film. LDPE composite films were prepared by wet casting method. 10Sr20BWZ LDPE film also showed the greatest reduction in weight loss and tensile strength. Large cavities with ~30µm diameter was found in 10Sr20BWZ LDPE film validated the successful degradation of LDPE film while the surface of pure LDPE film remained smooth after 225 hr sunlight irradiation. Stretching vibration of carbonyl group was detected in 10Sr20BWZ LDPE film indicated the formation of CO_2 and infered that the photo-oxidation was occurred.

The successful degradation of DMP by synthesisized photocatalysts demonstrates the potential for treating phthalate waste in industrial field. Moreover, the incorporation of photocatalyst in LDPE film and its positive findings underscore the potential of the synthesized composites in advancing photocatalysis for plastic waste management and environmental protection via designing sustainable and photodegradable materials.

In the context of wastewater treatment, the 10Sr20BWZ composite offers the potential for effective removal of phthalate-contained wastewater. The operating parameter in the study suggests that the photocatalytic process can be optimized to achieve higher removal rates of phthalate that present in

wastewater. This is particularly promising for industries that generate complex effluents containing a variety of organic pollutants. The practical implication is the development of effective way in wastewater treatment and contributing to protection of environmental and public health from exposing to hazardous pollutant.

Furthermore, this study have significant implications on degradation of plastic pollutants. Plastic waste, especially non-biodegradable plastics, poses hazardous to environment. The synthesized composite in this study has the potential to accelerate the degradation of plastic materials under solar irradiation. This could be one of the breakthrough in addressing the growing issue of plastic pollution in land, terrestrial and aquatic ecosystems. The practical benefit is the development of photodegradable materials for managing plastic waste, which aligns with the United Nations' Sustainable Development Goals (SDGs) include a specific focus on reducing waste, particularly through Goal 12: "Ensure sustainable consumption and production patterns." Target 12.5 under this goal specifically addresses waste reduction. The target is: "By 2030, substantially reduce waste generation through prevention, reduction, recycling, and reuse." This target reflects the global recognition of the need to address the environmental and social impacts of waste generation, including the proliferation of plastic waste, electronic waste, and other forms of pollution.

In summary, Brassica Oleracea-like SF20BWZ (SF= $SrFe_2O_4$, $BaFe_2O_4$, and $CaFe_2O_4$) composites were successfully synthesized through a hydrothermal-precipitation route and characterized using various analytical techniques such as XRD, FTIR, FESEM, TEM, EDX, XPS, and VSM. The

composites exhibited a well-defined structure, confirmed by XRD and FTIR analyses, with SF and ZnO uniformly loaded on Marimo-like Bi_2WO_6. The 10Sr20BWZ composite demonstrated superior photocatalytic performance in the degradation of DMP under sunlight irradiation, attributed to a dual Z-scheme mechanism. The effects of catalyst loadings, solution pH, and foreign substances on the photodegradation were investigated. 10Sr20BWZ composite able to reach 100% degradation under optimum condition. A mechanism proposed based on photoelectrochemical studies, active species detection, TA-PL test, and UV-vis DRS assessment. The degradation pathway of DMP, as determined by GC-MS analysis, highlighted different intermediates could be degraded into CO_2 and H_2O in the end. The composite also demonstrated high stability, maintaining over 80.4% degradation efficiency after four cycles. Application of the 10Sr20BWZ composite in the photodegradation of LDPE film further validated its potential in plastic waste management. The study's implications extend to wastewater treatment, offering effective removal of phthalate-contained wastewater, and addressing the broader issue of plastic pollution in alignment with United nation SDGs, particularly Goal 12.5. The synthesized composite presents a promising solution for advancing photocatalysis in environmental protection and sustainable materials design.

5.2   FUTURE RECOMMENDATIONS

The specific challenges and constraints that might have affected the research outcomes:

Firstly, it is crucial to recognize that the investigation is primarily confined to spinel ferrites and Bi_2WO_6 as components of the ZnO-based double Z-scheme composite. The limitation in material exploration inherently restricts the potential of alternative materials that could exhibit different or extraordinary performances.

Secondly, this study focuses on the application of photocatalysts to the photodegradation of DMP. By solely examining this particular phthalate, the research neglects the the potential effectiveness of the studied photocatalysts against different phthalates. The limitation in single phthalate pollutant could hinder the broader applicability of the findings to diverse environmental scenarios.

Moreover, the study excludes the investigation into other operation parameters beyond those explicitly stated. The understanding of photocatalytic processes could be much more complete with the exploration of additional factors that might affect the efficiency of the photocatalysts. This limitation could impact the practical implementation in real-industrial scenarios where various operational conditions may prevail.

Furthermore, the degradation pathway for LDPE film was not addressing in this study. Offering a comprehensive insight into the degradation pathway of LDPE film is crucial, as it can furnish valuable information for society to tackle the issue of plastic pollution in the environment.

Lastly, the phytotoxicity assessments are confined to the examination of *Vigna Radiata* in the context of DMP exposure, excluding the assessment of phytotoxicity for other species. This could limit the findings regarding the

potential ecological impacts of the photocatalytic treatment on a broader range of plant species.

In conclusion, these outlined the limitations for extrapolating future study. Researchers could take into account these constraints and view them as potential research gaps in the existing reserach when propose a research study to address overarching environmental challenges.

Based on current study, several recommendations and future perspectives were suggested as follow:

1. Apart from spinel ferrites and Bi_2WO_6, other novel materials with suitable bandgap and band position can be adopted in constructing ZnO-based double Z-scheme composite. Potential research questions included selection and fabrication of these novel materials, determining their physicochemical properties, and investigating their compatibility within the double Z-scheme system. The methodology involved photocatalyst synthesis techniques, determination of band structures, and evaluating the resulting composite performance through various tests. The expected outcomes could be the discovery of new materials that can contribute to more efficient ZnO-based double Z-scheme composites for enhanced photocatalytic applications. Possible challenges may arise when the synthesized photocatalyst unsuitable for coupling enhancement, attributed to its bandgap and band positions. To address these challenges, it may be necessary to explore a new selection of materials.

2. In this study, synthetic DMP was used in photocatalytic reaction. In future study, practical applicability of as-prepared photocatalysts can be

examined by using real wastewater as it was a more representative medium. Research questions could be investigating the catalyst performance in degrading pollutants present in actual wastewater, understanding the mechanisms involved in the real-world scenario, and optimizing the photocatalyst for practical applications. Methodologies may include wastewater sample collection, characterization of wastewater, and removal performance under realistic conditions. The outcomes included the insights into the effectiveness of photocatalyst in treating real wastewater and providing valuable solution for potential industrial applications. The potential challenge could be the variability of contaminants and impurities in real-wastewater that might affect the effectiveness of the treatment. Careful considerations should be taken to overcome the obstacles.

3. The SF20BWZ composite can be adapted in other applications such as antibiotic field and air disinfection area. Future research questions could be revolved around exploring the antimicrobial properties of SF20BWZ, optimizing its formulation for specific applications, and evaluating its effectiveness against different microorganisms/bacteria. Different techniques can be carrying out for example microbiological testing and application-specific performance assessments such as zone of inhibition or bacteria counting. Expected outcomes encompass the development of SF20BWZ for novel applications, contributing to improvement in antimicrobial and air purification technologies. The possible challenge could be the difficulty in transition from water-treatment application to antibacterial or air purification treatment. The researcher required to

acquire a new protocol, knowledge and experimental skills that align with the new application.

4. For phytotoxicity studies, the *Vigna Radiata* can be replaced by other species such as *Glycine max* and *Spinacia oleracea*. Besides, toxicity testing in animal can be carried out to identify the possible effects resulting from exposure to phthalates. This can be used to predict the impacts and toxicity of photocatalytically treated phthalates on human. Research questions involve the comparison of response between different plant species and assessing the environmental impact of phthalate on animal life. Methodology includes controlled experiments and ecological monitoring. Expected outcomes include a more comprehensive understanding of the potential impacts and toxicity of photocatalytically treated phthalates on both plant and animal ecosystems, providing insights for predicting side effect of phthalate towards human, wildlife and environment. Possible challenges include the unknown response of new species with various plant physiology and sensitivity that might affect the generalizability of the result findings. A comprehensive literature and study on specific species of plant and animal should be carry out prior to experiment.

5. The photocatalytic performance of as-prepared composites can also be further evaluated via microplastic degradation as an additional assessment criterion. Research questions encompass of investigation of composites efficacy in degrading different types of microplastics to understanding the underlying degradation mechanisms and optimizing the conditions for effective degradation of microplastic. Methodologies could include the simulation of photocatalytic experiment setups, characterization of

microplastics, and monitoring degradation trend. Anticipated outcomes involve insights into the potential application of the composites in addressing the growing concern of microplastic pollution which contributing to solution in environmental remediation technologies. A potential challenge that may arise is the viability in effectiveness when applied to different types and compositions of microplastics.

REFERENCES

Abbas, H.A. and Jamil, T.S., 2016. Nano sized Fe doped strontium titanate for photocatalytic degradation of dibutyl phthalate under visible light. *Advanced Materials Letters*, 7(6), pp.467–471.

Abbasi, A. and Hasanpour, M., 2016. The effect of pH on the photocatalytic degradation of methyl orange using decorated ZnO nanoparticles with SnO_2 nanoparticles, *Journal of Materials Science: Materials in Electronics*, 28, pp.1307-1314.

Abukhadra, M.R., Helmy, A., Sharaf, M.F., El-Meligy, M.A., Soliman, A.T.A., 2020. Instantaneous oxidation of levofloxacin as toxic pharmaceutical residuals in water using clay nanotubes decorated by ZnO (ZnO/KNTs) as a novel photocatalyst under visible light source. *Journal of Environmental Management*, 271, p.111019.

Adgent, M.A., Carroll, K.N., Hazlehurst, M.F., Loftus, C.T., Szpiro, A.A., Karr, C.J., Barrett, E.S., LeWinn, K.Z., Bush, N.R., Tylavsky, F.A., Kannan, K. and Sheela, S., 2020. A combined cohort analysis of prenatal exposure to phthalate mixtures and childhood asthma. *Environment International*, 143, pp.105970–105970.

Ahsaine, H.A., Taoufyq, A., Ezahri, M., Benlhachemi, A., Gavarri, J.R., 2013. *Synthesis and characterization of bismuth tungstate Bi_2WO_6 and its effect towards the degradation of methylene blue*. 13th International Symposium on Nondestructive Characterization of Materials (NDCM-XIII), Le Mans, France, 20-24 May 2013. e-Journal of Nondestructive Testing Vol. 19(4).

Akbari-Adergani, B., Saghi, M.H., Eslami, A., Mohseni-Bandpei, A. and Rabbani, M., 2017. Removal of dibutyl phthalate from aqueous environments using a nanophotocatalytic Fe,Ag-ZnO/VIS-LED system: modeling and optimization. *Environmental Technology*, 39(12), pp.1566–1576.

Alamdari, S., Ghamsari, M.S., Lee, C., Han, W., Park, H.H., Tafreshi, M.J., Afarideh, H. and Ara, M.H.M., 2020. Preparation and characterization of zinc oxide nanoparticles using leaf extract of Sambucus ebulus. *Applied Sciences*, 10(10), p.3620.

Ali, S.S., Qazi, I.A., Arshad, M., Zahiruddin, K., Voice, T.C. and Mehmood, Ch.T., 2016. Photocatalytic degradation of low density polyethylene (LDPE) kfilms using titania nanotubes. *Environmental Nanotechnology, Monitoring & Management*, 5, pp. 44–53.

Alothman, Z.A., Ayub, A., Hachim, S.K., Mohammed, B.M., Hussain, F., Altaf, M., Kadhim, Z.J., Lafta, H.A., Alnassar, Y.S., Shams, M.A., Almuhous, N.A., Ouladsmane, M. and Sillanpaa, M., 2022. Facile synthesis and comparative study of the enhanced photocatalytic degradation of two selected

dyes by TiO_2-g-C_3N_4 composite. *Environmental Science and Pollution Research*, 30, pp.37332–37343.

Amatore C, Arbault S., 2007. *Oxidative Stress at the Single Cell Level. Electrochemical Methods for Neuroscience.* [e-Book] Boca Raton (FL): CRC Press/Taylor & Francis. Available at: <https://www.ncbi.nlm.nih.gov/books/NBK2564/> [Accessed 23 Jan 2023].

Aragon, A.G., Wiggins, T.E. Ma, X. and Geyer, S.M., 2023. Lead-free $Cs_3Bi_2Br_9$ and $Cs_3Bi_{2-x}Sb_xBr_9$ nanocrystals as photocatalysts with enhanced activity for the degradation of rhodamine in aqueous environments. *Journal of Photochemistry and Photobiology A: Chemistry*, 436, p.114391.

Ariza-Tarazona, M.C., Villarreal-Chiu, J.F., Barbieri, V., Siligardi, C. and Cedillo-González, E.I., 2019. New strategy for microplastic degradation: Green photocatalysis using a protein-based porous N-TiO_2 semiconductor. *Ceramics International*, 45, pp.9618–9624.

Asadi, R., Abdollahi, H., Gharabaghi, M. and Boroumand, Z., 2020. Effective removal of Zn (II) ions from aqueous solution by the magnetic $MnFe_2O_4$ and $CoFe_2O_4$ spinel ferrite nanoparticles with focuses on synthesis, characterization, adsorption, and desorption. *Advanced Powder Technology*, 31(4), pp.1480–1489.

Askari, M.B. and Salarizadeh, P., 2020. Binary nickel ferrite oxide ($NiFe_2O_4$) nanoparticles coated on reduced graphene oxide as stable and high-performance asymmetric supercapacitor electrode material. *International Journal of Hydrogen Energy,* 45 (51), pp.27482–27491.

Askari, N., Beheshti, M., Mowla, D., Farhadian, M., 2020. Synthesis of $CuWO_4$/Bi_2S_3 Z-scheme heterojunction with enhanced cephalexin photodegradation. *Journal of Photochemistry and Photobiology A: Chemistry*, 394, p.112463.

Ateia, E.E., Hussien, S. and Mohamed, A.H., 2022. Tuning the structural and magnetic properties of the stuffed framework structures $MeFe_2O_4$ (Me = Ni, Ca, and Sr). *Journal of Inorganic and Organometallic Polymers and Materials*, 33(1), pp.216–227.

Atla, R. and Oh, T.H., 2022. Novel fabrication of the recyclable MoS_2/Bi_2WO_6 heterostructure and its effective photocatalytic degradation of tetracycline under visible light irradiation. *Chemosphere*, 303, p.134922.

Balu, S., Velmurugan, S., Palanisamy, S., Chen, S., Velusamy, V., Yang, T.C.K., El-Shafey, E.I., 2019. Synthesis of α-Fe_2O_3 decorated g-C_3N_4/ZnO ternary Z-scheme photocatalyst for degradation of tartrazine dye in aqueous media. *Journal of the Taiwan Institute of Chemical Engineer*, 99, pp. 258-267.

Barquín, C., Rivero, M.J., Ortiz, I., 2022. Shedding light on the performance of magnetically recoverable TiO_2/Fe_3O_4/rGO-5 photocatalyst. Degradation of S-metolachlor as case study. *Chemosphere*, 307, p.135991.

Behera, A., Kandi, D., Martha, S. and Parida, K., 2019. Constructive interfacial charge carrier separation of a p-$CaFe_2O_4$@n-$ZnFe_2O_4$ heterojunction architect photocatalyst toward photodegradation of antibiotics. *Inorganic Chemistry*, 58(24), pp.16592–16608.

Behineh, E.S., Nazar, A.R.S., Farhadian, M. and Moghadam, M., 2022. Photocatalytic degradation of cefixime using visible light-driven Z-scheme ZnO nanorod/Zn_2TiO_4/GO heterostructure. *Journal of Environmental Management*, 316, p.115195.

Bo, L., Hu, Y., Zhang, Z. and Tong, J., 2019. Efficient photocatalytic degradation of Rhodamine B catalyzed by $SrFe_2O_4$/g-C_3N_4 composite under visible light. *Polyhedron*, 168, pp.94–100.

Candeia, R.A., Souza, M. H.G., Bernardi, M., Maestrelli, S.C., Santos, I.A., Souza, A.G. and Longo, E., 2007. Monoferrite $BaFe_2O_4$ applied as ceramic pigment. *Ceramics International*, 33(4), pp.521–525.

Cao, W., Jiang, C., Chen, C., Zhou, H. and Wang, Y., 2021. A novel Z-scheme CdS/$Bi_4O_5Br_2$ heterostructure with mechanism analysis: Enhanced photocatalytic performance. *Journal of Alloys and Compounds*, 861, p.158554.

Castillo-Rodríguez, J.C., Tzompantzi, F., Tzompantzi-Flores, C., Velásquez-Torres, M.E., Gómez, R., Santolalla-Vargas, C.E., Álvarez Lémus, M.A., Ramos-Ramírez, E. and Ángel, G.D., 2022. High photoactivity of Zr_xO_y-$Bi_2O_2(CO_3)$ composite materials prepared by one-step synthesis for efficient photodegradation of 4-chlorophenol in water. *Journal of Photochemistry and Photobiology A-chemistry*, 435, pp.114285–114285.

Chang, C. and Man, C., 2014. Magnetic photocatalysts of copper phthalocyanine-sensitized titania for the photodegradation of dimethyl phthalate under visible light. *Colloids and Surfaces A: Physicochemical Engineering Aspects*, 441, pp.255–261.

Chang, C.F. and Man, C.Y., 2014. Magnetic photocatalysts of copper phthalocyanine-sensitized titania for the photodegradation of dimethyl phthalate under visible light. *Colloids and Surfaces A: Physicochemical and Engineering Aspects*, 441, pp.255–261.

Chang, C.H., Tsai, Y.A., Huang, Y., Tsai, M.S., Hou J.W., Lin, C.Y., Wang, P., Huang, L., Chen, C.Y., Wu, C.F., Hsieh, C.J., Wu, M.T., Wang, S.M. and Chen, M.L., 2022. The sex-specific association of prenatal phthalate exposure with low birth weight and small for gestational age: A nationwide survey by the Taiwan Maternal and Infant Cohort Study (TMICS). *Science of The Total Environment*, 806, pp.151261–151261.

Chang, T.H., Lü, Y.C., Yang, M., Huang, J.S., Fang, L., Chang, L. and Hsueh, H., 2020. Multibranched flower-like ZnO particles from eco-friendly hydrothermal synthesis as green antimicrobials in agriculture. *Journal of Cleaner Production*, 262, pp.121342–121342.

Chankhanittha, T., Somaudon, V., Photiwat, T., Youngme, S., Hemavibool, K. and Nanan, S., 2021. Enhanced photocatalytic performance of ZnO/Bi_2WO_6 heterojunctions toward photodegradation of fluoroquinolone-based antibiotics in wastewater. *Journal of Physics and Chemistry of Solids*, 153, p.109995.

Chankhanittha, T., Watcharakitti, J., Piyavarakorn, V., Benjamin, J., Bushby, R.J., Chuaicham, C., Sasaki, K., Nijpanich, S., Nakajima, H., Chanlek, N. and Nanan, S., 2023. ZnO/ZnS photocatalyst from thermal treatment of ZnS: Influence of calcination temperature on development of heterojunction structure and photocatalytic performance. *Journal of Physics and Chemistry of Solids*, 179, pp.111393–111393.

Chekir, N., Ouassila, B., Djilali, T., Nadia,A.L. and Fatiha, B., 2016. Photocatalytic degradation of methylene blue in aqueous suspensions using $TiO_2$and ZnO. *Desalination and Water Treatment,* 57, pp.6141–6147.

Chen, F., Yang, Q., Li, X., Zeng, G., Wang, D., Niu, C., Zhao, J., An, H., Xie, T., Deng, Y., 2017. Hierarchical assembly of graphene-bridged $Ag_3PO_4/Ag/BiVO_4(040)$Z-scheme photocatalyst: An efficient, sustainable and heterogeneous catalyst with enhanced visible-light photoactivity towardstetracycline degradation under visible light irradiation. *Applied Catalyst B: Environmental*, 200, pp. 330-342.

Chen, M., Guo, C., Hou, S., Lv, J., Zhang, Y., Zhang, H. and Xu, J., 2020. A novel Z-scheme $AgBr/P-g-C_3N_4$ heterojunction photocatalyst: Excellent photocatalytic performance and photocatalytic mechanism for ephedrine degradation. *Applied Catalysis B: Environmental*, 266, p.118614.

Chen, X., Wu, Z., Liu, D., Gao, Z., 2017. Preparation of ZnO Photocatalyst for the Efficient and Rapid Photocatalytic Degradation of Azo Dyes. *Nanoscale Research Letters*, 12, p.143.

Chen, Y., Ran, M., Zhou, Z., Han, X., Zhu, H. and Gu, J., 2021. Lanthanum/titanium dioxide immobilized onto industrial waste with enhanced photocatalytic activity, and the degradation of dimethyl phthalate. *Journal of Cleaner Production*, 321, p.129041.

Clara, M., Windhofer, G., Hartl, W., Braun, K., Simon, M., Gans, O., Scheffknecht, C. and Chovanec, A., 2010. Occurrence of phthalates in surface runoff, untreated and treated wastewater and fate during wastewater treatment. *Chemosphere*, 78(9), pp.1078–1084.

Cole, M., Lindeque, P.K., Fileman, E., Clark, J., Lewis, C., Halsband, C. and Galloway, T.S., 2016. Microplastics alter the properties and sinking rates of zooplankton faecal pellets. *Environmental Science & Technology*, 50(6), pp.3239–3246.

Cong, B., Liu, C., Wang, L. and Chai, Y., 2020. The impact on antioxidant enzyme activity and related gene expression following adult zebrafish (Danio rerio) exposure to dimethyl phthalate. *Animals*, 10(4), p.717.

Cui, X., Gong, Y., Liu, Y., Yu, H., Qin, W., Huo, M., 2022. Synthesis of a Z-scheme ternary photocatalyst ($Ta_3N_5/Ag_3PO_4/AgBr$) for the enhanced photocatalytic degradation of tetracycline under visible light. *Journal of Physics and Chemistry of Solids*, 170, p.110962.

Dang, J., Guo, J., Wang, L., Guo, F., Shi, W., Li, Y., Guan, W., 2022. Construction of Z-scheme $Fe_3O_4/BiOCl/BiOI$ heterojunction with superior recyclability for improved photocatalytic activity towards tetracycline degradation. *Journal of Alloys and Compounds*, 893, 162251.

Daniel, S.; Laura, H.; Fernando, M.; Gemma, T.; Carlos, P.; Aracely, H.; Jorge Luis, G. Automated on-line monitoring of the TiO_2-based photocatalytic degradation of dimethyl phthalate and diethyl phthalate. *Photochemical & Photobiological Sciences*, 2019, 18, 863–870.

Das, K., Bariki, R., Pradhan, S.K., Majhi, D., Dash, P., Mishra, A., Dhiman, R., Nayak, B., Mishra, B.G., 2022. Boosting the photocatalytic performance of $Bi_2Fe_4O_9$ through formation of Z-scheme heterostructure with In_2S_3: Applications towards water decontamination. *Chemosphere*, 306, 135600.

Deng, Y.L., Yang, P.C., Wang, Y., Liu, C., Luo, Q., Shi, T., Zeng, J.Y., Lu, T., Chen, P., Miao, Y., Zhang, M., Cui, F.P., Lu, W.Q. and Zeng, Q., 2022. Urinary concentrations of polycyclic aromatic hydrocarbon and phthalate metabolite mixtures in relation to semen quality among men attending an infertility clinic. *Environmental Science and Pollution Research*, 29(54), pp.81749–81759.

Di, G., Zhu, Z., Zhang, H., Zhu, J., Qiu, Y., Yin, D., Küppers, S., 2019. Visible-light degradation of sulfonamides by Z-scheme $ZnO/g-C_3N_4$ heterojunctions with amorphous Fe_2O_3 as electron mediator. *Journal of Colloid and Interface Science*, 538, pp.256-266.

Dietrich, M.L., Sarmoria, C., Brandolin, A., Asteasuain, M., 2018. High-pressure polymerization of ethylene in tubular reactors: prediction of the bivariate distributions of molecular weight-branches with a rigorous reactor model. *Computer Aided Chemical Engineering,* 44, pp.1447-1452.

Divya, J., Shivaramu, N.J., Purcell, W., Roos, W.D. and Swart, H.C., 2019. Multifunction applications of $Bi_2O_3:Eu^{3+}$ nanophosphor for red light emission and photocatalytic activity. *Applied Surface Science*, 497, pp.143748–143748.

Dong, S., Ding, X., Guo, T., Yue, X., Han, X., Sun, J., 2017. Self-assembled hollow sphere shaped Bi_2WO_6/RGO composites for efficient sunlight-driven photocatalytic degradation of organic pollutants. *Chemical Engineering Journal*, 316, pp.778-789.

Du, C., Feng, W., Nie, S., Zhang, J., Liang, Y., Han, X., Wu, Y., Feng, J., Dong, S., Liu, H. and Sun, J., 2021. Harnessing efficient in-situ H_2O_2 production via a $KPF_6/BiOBr$ photocatalyst for the degradation of polyethylene. *Separation and Purification Technology*, 279, pp.119734–119734.

Du, C., Yang, L., Tan, S., Song, J., Zhang, Z., Wang, S., Xiong, Y., Yu, G., Chen, H., Zhou, L., Wu, H., Liu, Y., 2021. Reduced graphene oxide modified Z-scheme AgI/Bi_2MoO_6 heterojunctions with boosted photocatalytic activity for water treatment originated from the efficient charge pairs partition and migration. *Environmental Science and Pollution Research*, 28, pp. 66589-66601.

Duan, J., Liu, M., Yueliang Leon Guo, Wang, W., Zhang, Z. and Li, C., 2020. High photocatalytic activity of 2D sheet structure ZnO/Bi_2WO_6 Z-scheme heterojunction under simulated sunlight. *Journal of Physics D: Applied Physics*, 53(16), pp.165101–165101.

Dugandžić, A.M., Tomašević, A.V., Radišić, M.M., Šekuljica, N.Z., Mijin, D.Z., Petrović, S.D., 2017. Effect of inorganic ions, photosensitisers and scavengers on the photocatalytic degradation of nicosulfuron. *Journal of Photochemistry and Photobiology A: Chemistry*, 336, pp.146–155.

Elviera, Yurizar, Y., Apriandanu, D.O.B., Marcony, S.R., 2022. Fabrication of novel $SnWO_4/ZnO$ using Muntingia calabura L. leaf extract with enhanced photocatalytic methylene blue degradation under visible light irradiation. *Ceramics International*, 48, pp.3564-3577.

Fahri, A.N., Ilyas, S., Anugrah, M.A., Heryanto, H., Azlan, M., Ola, A.T.T., Rahmat, R., Yudasari, N., Tahir, D., 2023. Bifunctional Purposes of Composite $TiO_2/CuO/Carbon$ Dots (CDs): Faster photodegradation pesticide wastewater and high performance electromagnetic wave absorber. *Materialia*, 26, p.101588.

Fakhravar, S., Farhadian, M. and Tangestaninejad, S., 2020. Excellent performance of a novel dual Z-scheme $Cu_2S/Ag_2S/BiVO_4$ heterostructure in metronidazole degradation in batch and continuous systems: Immobilization of catalytic particles on α-Al_2O_3 fiber. *Applied Surface Science*, 505, pp.144599–144599.

Fazli, A., Brigante, M., Khataee, A. and Mailhot, G., 2021. Synthesis of a magnetically separable LDH-based S-scheme nano-heterojunction for the activation of peroxymonosulfate towards the efficient visible-light photodegradation of diethyl phthalate. *Applied Surface Science*, 559, p.149906.

Feng, C., Lu, Z.W., Zhang, Y., Liu, C., Zhou, M., Li, X., Yao, C., Li, Z. and Xu, S., 2022. A magnetically recyclable dual Z-scheme GCNQDs-$CoTiO_3/CoFe_2O_4$ composite photocatalyst for efficient photocatalytic degradation of oxytetracycline. *Chemical Engineering Journal*, 435, pp.134833–134833.

Feng, C., Ouyang, X., Deng, Y., Wang, J., Tang, L., 2023. A novel g-C_3N_4/g-$C_{3}N_{4-x}$ homojunction with efficient interfacial charge transfer for photocatalytic degradation of atrazine and tetracycline. *Journal of Hazardous Materials*, 441, p.129845.

Feng, J., Zu, L., Yang, H., Zheng, Y., Chen, Z., Song, W., Zhao, R., Wang, L., Ran, X. and Xiao, B., 2023. Induced abundant oxygen vacancies in $Sc_2VO_{5-\delta}$/g-C_3N_4 heterojunctions for enhanced photocatalytic degradation of levofloxacin. *RSC Advances*, 13(1), pp.688–700.

Ferguson, K.K., McElrath, T.F., Ko, Y.A., Mukherjee, B. and Meeker, J.D., 2014. Variability in urinary phthalate metabolite levels across pregnancy and sensitive windows of exposure for the risk of preterm birth. *Environment International*, 70, pp.118–124.

Fernandes, E., Gomes, J. and Martins, R.P. (2022). Semiconductors application forms and doping benefits to wastewater treatment: a comparison of TiO_2, WO_3, and g-C_3N_4. *Catalysts*, 12(10), pp.1218–1218.

Gad, E.S., Chaudhary, K., Ahmed, A.H., Rafiq, S., Yousif, A.M., Suleman, M., 2023. Hydrothermal synthesis of bifunctional Ag/MnO_2 nanowires decorated with V_2O_5 nanorice: Photocatalytic and electrochemical impedance study for treatment of impurities present in waste water. *Optical Materials*, 135, p.113274.

Gan, Y.X., Jayatissa, A.H., Yu, Z., Chen, X. and Li, M., 2020. Hydrothermal Synthesis of Nanomaterials. *Journal of Nanomaterials*, 2020, pp.1–3.

Geyer, R., Jambeck, J.R., Law, K.L., 2017. Production, use, and fate of all plastics ever made. *Science Advances*, 3, p.e1700782.

Girija, K.G., Shaheera, M., S. and Somasundaram, K., 2021. Correlating the properties of RF sputtered ZnO nanocrystalline films deposited using sintered and powder targets. *Nano-Structures & Nano-Objects*, 26, p.100758.

Glavaski, O.S., Petrovic, S.D., Rajakovic-Ognjanovic, V.N., Zeremski, T.M., Dugandzic, A.M. and Mijin, D.Z., 2016. Photodegradation of dimethenamid-P in deionised and ground water. *Chemical Industry and Chemical Engineering Quarterly*, 22(1), pp.101–110.

Goel, S., Sinha, N. and Kumar, B., 2019. 3D hierarchical Ho-doped ZnO micro-flowers assembled with nanosheets: A high temperature ferroelectric material. *Physica E: Low-dimensional Systems and Nanostructures*, 105, pp.29–40.

Gonçalves, B.R., Della-Flora, A., Sirtori, C., Sousa, R.M.F., Starling, M.C.V.M., Pérez, S., Saggioro, E.M., Sales Junior, S.F., Trovó, A.G., 2023. Influence of water matrix components and peroxide sources on the transformation products and toxicity of tebuthiuron under UVC-based advanced oxidation processes. *Science of The Total Environment*, 859, p.160120.

Gonçalves, M.A., Lourenço Mares, E.K., Zamian, J.R., Narciso da Rocha Filho, G. and Rafael Vieira da Conceição, L., 2021. Statistical optimization of biodiesel production from waste cooking oil using magnetic acid heterogeneous catalyst MoO_3/$SrFe_2O_4$. *Fuel*, 304, p.121463.

Govarthanan, M., Mythili, R., Kim, W., AlFarraj, S., and Sulaiman, A.A., 2021. Facile fabrication of (2D/2D) MoS_2@MIL-88(Fe) interface-driven catalyst for efficient degradation of organic pollutants under visible light irradiation. *Journal of Hazardous Materials*, 414, pp.125522–125522.

Gracien, E.B., Jérémie, M.L., Joseph, L.K.K., Omer, M.M., Antoine, M.K., Hercule, K.M. and Gerard, M.N., 2019. Role of hydroxyl radical scavenger agents in preparing silver nanoparticles under γ-irradiation. *SN Applied Sciences*, 1, p.961.

Graimed, B.H., Okab, A.A., Jabbar, Z.H., Issa, M.A. and Ammar, S.H., 2023. Highly stable β-Bi_2O_3/Ag decorated nanosilica as an efficient Schottky heterojunction for ciprofloxacin photodegradation in wastewater under LED illumination. *Materials Science in Semiconductor Processing*, 156, pp.107303–107303.

Guan, K., Zhou, P., Zhang, J. and Zhu, L., 2020. Synthesis and characterization of ZnO@RSDBC composites and their Photo-Oxidative degradation of Acid Orange 7 in water. *Journal of Molecular Structure*,1203, p.127425.

Guan, K., Zhou, P., Zhang, J., Zhu, L., 2020. Synthesis and characterization of ZnO@RSDBC composites and their Photo-Oxidative degradation of Acid Orange 7 in water. *Journal of Molecular Surface*, 1203, p.127425.

Guan, Z., Li, X., Wu, Y., Chen, Z., Huang, X., Wang, D., Yang, Q., Liu, J., Tian, S., Chen, X., Zhao, H., 2021. AgBr nanoparticles decorated 2D/2D GO/Bi_2WO_6 photocatalyst with enhanced photocatalytic performance for the removal of tetracycline hydrochloride. *Chemical Engineering Journal*, 410, p.128283.

Guo, X., Liu, H. and Wu, S., 2019. Humic substances developed during organic waste composting: Formation mechanisms, structural properties, and agronomic functions. *Science of The Total Environment*, 662, pp.501–510.

He, Q., Liu, X., Li, F., Li, F., Tao, L., Yu, C., 2022. Effect of light and heavy rare earth doping on the physical structure of $Bi_2O_2CO_3$ and their performance in photocatalytic degradation of dimethyl phthalate. *Catalysts*, 12, p.1295.

Hejda, S., Buzek, D., Kluson, P. and Bajt, O., 2023. Fenton-like photocatalyzed degradation of dibutyl phthalate with goethite and carboxylic acids. *International Journal of Environmental Science and Technology,* [online] Available at:< https://doi.org/10.1007/s13762-023-04781-4> [Assessed 23 Jan 2023].

Holder, C.F. and Schaak, R.E., 2019. Tutorial on Powder X-ray Diffraction for Characterizing Nanoscale Materials. *ACS Nano*, 13(7), pp.7359–7365.

Hong, J., Cho, K.-H., Presser, V. and Su, X., 2022. Recent advances in wastewater treatment using semiconductor photocatalysts. *Current Opinion in Green and Sustainable Chemistry*, 36, p.100644.

Hu, K., Chen, C., Zhu, Y., Zeng, G., Huang, B., Chen, W., Liu, S., Lei, C., Li, B., Yang, Y., 2019. Ternary Z-scheme heterojunction of Bi_2WO_6 with reduced graphene oxide (rGO) and meso-tetra (4-carboxyphenyl) porphyrin (TCPP) for enhanced visible-light photocatalysis. *Journal of Colloid and Interface Science*, 540, pp.115-125.

Hu, K., Chen, C., Zhu, Y., Zeng, G., Huang, B., Chen, W., Liu, S., Lei, C., Li, B., Yang, Y., 2019. Ternary Z-scheme heterojunction of Bi2WO6 with reduced graphene oxide (rGO) and meso-tetra (4-carboxyphenyl) porphyrin (TCPP) for enhanced visible-light photocatalysis. *Journal of Colloid and Interface Science*, 540, pp.115-125.

Hu, L., Zhang, Y., Lu, W., Lu, Y. and Hu, H.M., 2019. Easily recyclable photocatalyst Bi_2WO_6/MOF/PVDF composite film for efficient degradation of aqueous refractory organic pollutants under visible-light irradiation. *Journal of Materials Science*, 54(8), pp.6238–6257.

Huang, D., Li, J., Zeng, G., Xue, W., Chen, S., Li, Z., Deng, R., Yang, Y. and Cheng, M., 2019. Facile construction of hierarchical flower-like Z-scheme AgBr/Bi2WO6 photocatalysts for effective removal of tetracycline: Degradation pathways and mechanism. *Chemical Engineering Journal*, 375, p.121991.

Huang, L., Zhu, X., Zhou, S., Cheng, Z., Shi, K., Zhang, C. and Shao, H., 2021. Phthalic acid esters: natural sources and biological activities. *Toxins*, 13(7), p.495.

Huang, X., Guo, Q., Yan, B., Liu, H., Chen, K., Wei, S., Wu, Y. and Wang, L., 2021. Study on photocatalytic degradation of phenol by BiOI/Bi2WO6 layered heterojunction synthesized by hydrothermal method. *Journal of Molecular Liquids*, 322, p.114965.

Huang, Z., Wu, P., Lu, Y., Wang, X., Zhu, N., Dang, Z., 2013. Enhancement of photocatalytic degradation of dimethyl phthalate with nano-TiO_2 immobilized onto hydrophobic layered double hydroxides: A mechanism study. *Journal of Hazardous Materials*, 246-247, pp.70-78.

Hung, C., Yuan, C., Li, H., 2017. Photodegradation of diethyl phthalate with PANi/CNT/TiO_2 immobilized on glass plate irradiated with visible light and simulated sunlight—Effect of synthesized method and pH. *Journal of Hazardous Materials*, 322, pp.243–253.

Hunge, Y.M., Yadav, A.A., Liu, S. and Mathe, V.L., 2019. Sonochemical synthesis of CZTS photocatalyst for photocatalytic degradation of phthalic acid. *Ultrasonics Sonochemistry*, 56, pp.284–289.

Janani, B., Balakrishnaraja, R., Elgorban, A.M., Bahkali, A.H., Varma, R.S., Syed, A., Sudheer Khan, S., 2023. Eco-friendly cubic-ZnS coupled Cu_7S_4 spines on chitosan matrix: Unravelling defect-engineered nanoplatform for the photodegradation of p-chlorophenol. *Journal of Environmental Management*, 326, p.116615.

Janani, B., Syed, A., Thomas, A.M., Al-Rashed, S., Elgorban, A.M., Raju, L.L. and Khan, S.S., 2021. A simple approach for the synthesis of bi-functional p-n type ZnO@CuFe$_2$O$_4$ heterojunction nanocomposite for photocatalytic and antimicrobial application. *Physica E: Low-dimensional Systems and Nanostructures*, 130, p.114664.

Janani,B., Al-amri, S.S., Okla, M.K., Mohebaldin, A., Soufan, W., Almunqedhi, B., Abdel-Maksoud, M.A., AbdElgawad, H., Thomas, A.J., Raju, L.L. and Khan, S., 2022. High performing p-n system of CaFe$_2$O$_4$ coupled ZnO for synergetic degradation of Rhodamine B with white-light photocatalysis and bactericidal action. *Journal of The Taiwan Institute of Chemical Engineers*, 133, pp.104271–104271.

Jiang, J., Wang, H., Xiao Dong Chen, Li, S., Xie, T., Wang, D. and Lin, Y., 2017. Enhanced photocatalytic degradation of phenol and photogenerated charges transfer property over BiOI-loaded ZnO composites. *Journal of Colloid and Interface Science*, 494, pp.130–138.

Jiao, H., Zhou, X., Song, S., Jin, J., Zhang, X., Tang, Y., Zhap, K., 2023. Barium titanate (1 0 1)/silver nanocomposite: Preparation, photocatalytic activity, and mechanism based on Density Functional Theory. *Materials Science and Engineering B: Solid-State Materials for Advanced Technology*, 288, p.116137.

Jing, W.W., Li, D.M., Li, J.C., Li, X., Wu, Z. and Liu, Y.W., 2018. Photodegradation of dimethyl phthalate (DMP) by UV–TiO$_2$ in aqueous solution: operational parameters and kinetic analysis. *International Journal of Environmental Science and Technology*, 15(5), pp.969–976.

John, K.I., Omorogie, M.O., Bayode, A.A., Adeleye, A.T., Helmreich,B., 2022. Environmental microplastics and their additives—a critical review on advanced oxidative techniques for their removal. *Chemical Papers*, 77, pp.657–676.

Joudi, F., Naceur, J.B., Ouertani, R. and Chtourou, R., 2018. A novel strategy to produce compact and adherent thin films of SnO$_2$/TiO$_2$ composites suitable for water splitting and pollutant degradation. *Journal of Materials Science: Materials in Electronics*, 30(1), pp.167–179.

Joy, M., Chandrasekharan, G., Ahmed Khan, M., Arunachalapandi, M., Chellapandi, T., Harish, D., Chitra, D., Roopan, S.M., 2022. Citrus lemon mediated green synthesis of ZnTiO$_3$ nanospheres for the degradation of petrochemical wastewater. *Environmental Quality Management*, 32, pp.159-169.

Kaewkam, P., Kanchanapaetnukul, A., Khamyan, J., Phadmanee, N., Andrew, K.L., Krisana, K. and Sirivithayapakorn, S., 2022. UV-assisted TiO$_2$ photocatalytic degradation of virgin LDPE films: Effect of UV-A, UV-C, and TiO$_2$. *Journal of Environmental Chemical Engineering*, 10, pp.108131–108131.

Kafeshani, M.A., Mahdikhah, V. and Sheibani, S., 2022. Facile preparation and modification of $SrTiO_3$ through Ni–Cd co-doping as an efficient visible-light-driven photocatalyst. Optical Materials, 133, pp.113080–113080.

Kaur, M., Mehta, S.K. and Kansal, S.K., 2018. Visible light driven photocatalytic degradation of ofloxacin and malachite green dye using cadmium sulphide nanoparticles. *Journal of Environmental Chemical Engineering*, 6(3), pp.3631–3639.

Kenfoud, H., Nasrallah, N., Baaloudj, O., Meziani, D., Chaabane, T. and Trari, M., 2020. Photocatalytic reduction of Cr(VI) onto the spinel $CaFe_2O_4$ nanoparticles. *Optik*, 223, p.165610.

Keshu, Rani, M., Shanker, U., 2022. Efficient removal of plastic additives by sunlight active titanium dioxide decorated Cd–Mg ferrite nanocomposite: Green synthesis, kinetics and photoactivity. *Chemosphere*, 290, p.133307.

Khodami, Z. and Ejhieh, A.N., 2015. Investigation of photocatalytic effect of $ZnO–SnO_2$/nano clinoptilolite system in the photodegradation of aqueous mixture of 4-methylbenzoic acid/2-chloro-5-nitrobenzoic acid. *Journal of Molecular Catalysis A: Chemical*, 409, pp.59–68.

Kim, D. and Yong, K., 2021. Boron doping induced charge transfer switching of a C_3N_4/ZnO photocatalyst from Z-scheme to type II to enhance photocatalytic hydrogen production. *Applied Catalysis B: Environmental*, 282, p.119538.

Kishimoto, M., Latiff, H., Kita, E. and Yanagihara, H., 2019. Structure and magnetic properties of Co–Ni spinel ferrite particles synthesized via co-precipitation and hydrothermal treatment at different temperatures. *Materials transactions*, 60(4), pp.485–489.

Kitchamsetti, N., Ramteke, M.M., Rondiya, S.R., Mulani, S.R., Patil, M., Cross, R.R., Dzade, N.Y. and Devan, R.S., 2021. DFT and experimental investigations on the photocatalytic activities of NiO nanobelts for removal of organic pollutants. *Journal of Alloys and Compounds*, 855, pp.157337–157337.

Koch, H.M., Wittassek, M., Brüning, T., Angerer, J. and Heudorf, U., 2011. Exposure to phthalates in 5–6 years old primary school starters in Germany—A human biomonitoring study and a cumulative risk assessment. *International Journal of Hygiene and Environmental Health*, 214(3), pp.188–195

Koniecki, D., Wang, R., Moody, R.P. and Zhu, J., 2011. Phthalates in cosmetic and personal care products: Concentrations and possible dermal exposure. *Environmental Research*, 111(3), pp.329–336.

Koumaki, E., Mamais, D., Noutsopoulos, C., Nika, M.C., Bletsou, A.A., Thomaidis, N.S., Eftaxias, A. and Stratogianni, G., 2015. Degradation of emerging contaminants from water under natural sunlight: The effect of season, pH, humic acids and nitrate and identification of photodegradation by-products. *Chemosphere*, 138, pp.675–681.

Krishnamoorthy, N., Sivasankarapillai, V.S., Natarajan, V.K., Eldesoky, G.E., Wabaidur, S.M., Eswaran, M. and Dhanusuraman, R., 2023. Biocidal activity of ZnO NPs against pathogens and antioxidant activity - a greener approach by Citrus hystrix leaf extract as bio-reductant. *Biochemical Engineering Journal*, 192, pp.108818–108818.

Ku, Y., Shiu, S.J. and Wu, H.C., 2017. Decomposition of dimethyl phthalate in aqueous solution by UV–LED/TiO_2 process under periodic illumination. *Journal of Photochemistry and Photobiology A: Chemistry*, 332, pp.299–305.

Kumar, A., Prajapati, P.K., Pal, U., Jain, S.L., 2018. Ternary rGO/InVO4/Fe2O3 Z-Scheme Heterostructured Photocatalyst for CO_2 Reduction under Visible Light Irradiation. *ACS Sustainable Chemistry & Engineering*. 6, pp.8201-8211.

Kumar, R., George, L., Zhao, J., Mukherji, S., 2022. Photocatalytic activity of graphene oxide-TiO_2 nanocomposite on dichlorvos and malathion and assessment of toxicity changes due to photodegradation. *Chemosphere*, 308, p.136402.

Kumar, S., Kaushik, R.D. and Purohit, L.P., 2022. ZnO-CdO nanocomposites incorporated with graphene oxide nanosheets for efficient photocatalytic degradation of bisphenol A, thymol blue and ciprofloxacin. *Journal of Hazardous Materials*, 424, pp.127332–127332.

Kumar, S., Kaushik, R.D., Upadhyay, G.K. and Purohit, L.P., 2021. rGO-ZnO nanocomposites as efficient photocatalyst for degradation of 4-BP and DEP using high temperature refluxing method in in-situ condition. *Journal of Hazardous Materials,* 406, p.124300.

Kumar, S., Maivizhikannan, V., Drews, J., Krishnan, V., 2019. Fabrication of nanoheterostructures of boron doped ZnO-MoS_2 with enhanced photostability and photocatalytic activity for environmental remediation applications. *Vacuum*, 163, pp.88-98.

Kumar, S., Sharma, V., Bhattacharyya, K. and Krishnan, V., 2016. Synergetic effect of MoS_2–RGO doping to enhance the photocatalytic performance of ZnO nanoparticles. *New Journal of Chemistry*, 40(6), pp.5185–5197.

Kumaresan, N., Sinthiya, M.M.A., Ramamurthi, K., Babu, R.R., Sethuraman, K., 2020. Visible light driven photocatalytic activity of ZnO/CuO nanocomposites coupled with rGO heterostructures synthesized by solid-state method for RhB dye degradation. *Arabian Journal of Chemistry*. 13, pp. 3910-3928.

Kumari, V., Yadav, S., Jindal, J., Sharma, S., Kumari, K. and Kumar, N., 2020. Synthesis and characterization of heterogeneous ZnO/CuO hierarchical nanostructures for photocatalytic degradation of organic pollutant. *Advanced Powder Technology*, 31(7), pp.2658–2668.

Lai, C., Xu, F., Zhang, M., Li, B., Liu, S., Yi, H., Li, L., Qin, L., Liu, X., Fu, Y., An, N., Yang, H., Huo, X., Yang, X. and Yan, H., 2021. Facile synthesis of CeO_2/carbonate doped $Bi_2O_2CO_3$ Z-scheme heterojunction for improved visible-light photocatalytic performance: Photodegradation of tetracycline and photocatalytic mechanism. *Journal of Colloid and Interface Science*, 588, pp.283–294.

Laksono, A.D., Damastuti, R., Amanah, N.L., Assa, M.H., Cheng, Y., Ernawati, L., Nugroho, A., Abdullah, H., 2023. *Photocatalytic and Adsorptive Removal of Liquid Textile Industrial Waste with Carbon-Based Nanomaterials. Green Energy and Technology,* [e-Book] Singapore: Springer. Available at: <https://doi.org/10.1007/978-981-19-6748-1_1> [Accessed 23 Jan 2023].

Latif, S., Liaqat, A., Imran, M., Javaid, A., Hussain, N., Jesionowski, T., Bilal, M., 2023. Development of zinc ferrite nanoparticles with enhanced photocatalytic performance for remediation of environmentally toxic pharmaceutical waste diclofenac sodium from wastewater. *Environmental Research*, 216, p.114500.

Lee, J., Tan, X.Y. Ng, B., Kong, X., Chai, S., Tan, L., 2023. Cyano group modified graphitic carbon nitride with K intercalation for sustainable photodegradation of pharmaceutical waste. *Journal of the Taiwan Institute of Chemical Engineering*, 142, p.104617.

Li, B., Lai, C., Zeng, G., Qin, L., Yi, H., Huang, D., Zhou, C., Liu, X., Cheng, M., Xu, P., Zhang, C., Huang, F. and Liu, S., 2018. Facile hydrothermal synthesis of Z-Scheme $Bi_2Fe_4O_9$/Bi_2WO_6 heterojunction photocatalyst with enhanced visible light photocatalytic activity. *ACS Applied Materials & Interfaces*, 10, pp.18824-18836.

Li, M., Song, C., Wu, Y., Wang, M., Pan, Z., Sun, Y., Meng, L., Han, S., Xu, L., Gan, L., 2019. Novel Z-scheme visible-light photocatalyst based on $CoFe_2O_4$/BiOBr/Graphene composites for organic dye degradation and Cr(VI) reduction. *Applied Surface Science*, 478, pp.744-753.

Li, P., Wang, X., Su, M., Zou, X., Duan, L. and Zhang, H., 2020. Characteristics of plastic pollution in the environment: a review. *Bulletin of Environmental Contamination and Toxicology*, 107, pp.577-584.

Li, S., Chen, J., Hu, S., Wang, H., Jiang, W., Chen, X., 2020. Facile construction of novel Bi_2WO_6/Ta_3N_5 Z-scheme heterojunction nanofibers for efficient degradation of harmful pharmaceutical pollutants. *Chemical Engineering Journal*, 402, p.126165.

Li, S., Lai, C., Li, J., Zhong, J.-T., He, Z., Peng, Q., Liu, X. and Ke, B., 2021. Enhanced photocatalytic degradation of dimethyl phthalate by magnetic dual Z-scheme iron oxide/mpg-C_3N_4/BiOBr/polythiophene heterostructure photocatalyst under visible light. *Journal of Molecular Liquids*, 342, pp.116947–116947.

Li, S., Zhang, R., Ma, X., Qiao, J., Zhang, H., Wang, J. and Song, Y., 2019. Preparation of ortho-symmetric double (OSD) Z-scheme $SnO_2\backslash CdSe/Bi_2O_3$ sonocatalyst by ultrasonic-assisted isoelectric point method for effective degradation of organic pollutants. *Journal of Industrial and Engineering Chemistry*, 72, pp.157–169.

Li, W., Zhuang, C., Li, Y., Gao, C., Jiang, W., Sun, Z. and Qi, K., 2021. Anchoring ultra-small TiO_2 quantum dots onto ultra-thin and large-sized Mxene nanosheets for highly efficient photocatalytic water splitting. *Ceramics International*, 47(15), pp.21769–21776.

Li, X., Liu, D., Zhu, B., Wang, J., Lang, J., 2019. Facile preparation of ZnO/Ag_2CO_3 heterostructured nanorod arrays with improved photocatalytic activity. *Journal of Physics and Chemistry of Solids,* 125, pp. 96-102.

Li, X., Zhu, F. and Zeng, Z., 2021. Effects of different extraction methods on antioxidant properties of blueberry anthocyanins. *Open Chemistry*, 19(1), pp.138–148.

Li, Z., Sun, L., Zhang, J., Tang, S., 2022. Facile green synthesis of nickel-ferrite-rGO ($NiFe_2O_4/rGO$) nanocomposites for efficient water purification under direct sunlight. *Inorganic Chemistry Communications*, 146, p.110073.

Li. S., Lai, C., Li, C., Zhong, J., He, Z., Peng, Q., Liu, X., Ke, B., 2021. Enhanced photocatalytic degradation of dimethyl phthalate by magnetic dual Z-scheme iron oxide/mpg-C_3N_4/BiOBr/polythiophene heterostructure photocatalyst under visible light. *Journal of Molecular Liquids,* 342, p.116947.

Liang, W., Luo, Y., Song, S., Dong, X. and Yu, X., 2013. High photocatalytic degradation activity of polyethylene containing polyacrylamide grafted TiO_2. *Polymer Degradation and Stability*, 98, pp. 1754–1761.

Liccardo, L., Bordin, M., Sheverdyaeva, P.M., Belli, M., Moras, P., Vomiero, A. and Moretti, E., 2023. Surface defect engineering in colored TiO_2 hollow spheres toward efficient photocatalysis. *Advanced Functional Materials*, pp.2212486–2212486.

Lin, D.J., Lin, H.L., Haung, S.M., Liu, S.M. and Chen, W.C., 2021. Effect of pH on the in vitro biocompatibility of surfactant-assisted synthesis and hydrothermal precipitation of rod-shaped nano-hydroxyapatite. *Polymers*, 13, p.2994.

Liu, H., Liu, G., Fan, J., Zhou, Q., Zhou, H., Zhang, N., Hou, Z., Zhang, M., He, Z., 2011. Photoelectrocatalytic degradation of 4,4′-dibromobiphenyl in aqueous solution on TiO_2 and doped TiO_2 nanotube arrays. *Chemosphere*, 82, pp.43-47.

Liu, R.F., Li, W.B. and Peng, A., 2018. A facile preparation of TiO_2/ACF with C Ti bond and abundant hydroxyls and its enhanced photocatalytic activity for formaldehyde removal. *Applied Surface Science*, 427, pp.608–616.

Liu, J., Nie, Q., Tan, Z., Luo, Y., Wang, S. and Yu, H., 2020. Insights into the impurities of Bi_2WO_6 synthesized using the hydrothermal method. *RSC Advances*, 10(67), pp.40597–40607.

Liu, K., Li, N., Ding, J., Chen, N., Wang, S., Wang, Q., Yao, X., Li, X., Wang, J. and Yin, H., 2023. One-step synthesis of $Bi_2O_2CO_3/Bi_2S_3$ S-scheme heterostructure with enhanced photoactivity towards dibutyl phthalate degradation under visible light. *Chemosphere*, 324, p.138357.

Liu, M., Xue, X., Yu, S., Wang, X., Hu, X., Tian, H., Chen, H. and Zheng, W., 2017. Improving photocatalytic performance from $Bi_2WO_6@MoS_2$/graphene hybrids via gradual charge transferred pathway. *Scientific Reports*, 7(1), p.3637.

Liu, Y., Chen, Z., Shen, J., 2013. Occurrence and Removal Characteristics of Phthalate Esters from Typical Water Sources in Northeast China. *Journal of Analytical Methods in Chemistry*, 8, p. 419349.

Liu, Z., Hao, W., Yuan, C., Ruan, W., Jiang, W. and Teng, F., 2022. Substantially updating photocatalytic reaction by in-situ generated SO_4^- through directly exciting SO_4^{2-}. *Journal of water process engineering*, 48, pp.102912–102912.

Liu, Z., Zhao, Z.-G. and Miyauchi, M., 2009. Efficient visible light active $CaFe_2O_4/WO_3$ based composite photocatalysts: effect of interfacial modification. *The Journal of Physical Chemistry C*, 113(39), pp.17132–17137.

Long, G., Ding, J., Xie, L., Sun, R., Chen, M., Zhou, Y., Huang, X., Han, G., Li, Y., Zhao, W., 2018. Fabrication of mediator-free $g-C_3N_4/Bi_2WO_6$ Z-scheme with enhanced photocatalytic reduction dechlorination performance of 2,4-DCP. *Applied Surface Science*, 455, pp.1010-1018.

Lung, C.W., Zheng, Z., Lo, I.M.C., 2023. Solar-driven photocatalytic chlorine activation for the simultaneous degradation of pharmaceuticals and personal care products and the inactivation of Escherichia coli in drinking water. *Chemosphere*, 311, p.137019.

Luo, Y., Wang, Y., Hua, F., Xue, M., Xie, X., Xie, Y., Yu, S., Zhang, L., Yin, Z., Xie, C., Hong, Z., 2023. Adsorption and photodegradation of reactive red 120 with nickel-iron-layered double hydroxide/biochar composites. *Journal of Hazardous Materials*, 443, p.130300.

Lv, P., Tao, Y., Zhang, N., Yang, Y., Wu, X., Li, Q.X., Hua, R., 2023. Cyanidin-3-O-glucoside mediated photodegradation of profenofos in water. *Chemosphere*, 308, p.136170.

Ma, D., Wu, J., Gao, M., Xin, Y., Ma, T. and Sun, Y., 2016. Fabrication of Z-scheme $g-C_3N_4$/RGO/Bi_2WO_6 photocatalyst with enhanced visible-light photocatalytic activity. *Chemical Engineering Journal*, 290, pp.136–146.

Ma, F., Yang, Q., Wang, Z., Liu, Y.-H., Xin, J., Zhang, J., Hao, Y. and Li, L., 2018. Enhanced visible-light photocatalytic activity and photostability of

Ag_3PO_4/Bi_2WO_6 heterostructures toward organic pollutant degradation and plasmonic Z-scheme mechanism. *RSC Advances*, 8(28), pp.15853–15862.

Ma, Y., Qian, X., Muhammad, A., Xia, J., Fan, H., Luo, J., He, G., Chen, H., 2023. Z-scheme $Bi_4O_5Br_2$/MIL-88B(Fe) heterojunction for boosting visible light catalytic oxidation of tetracycline hydrochloride. *Applied Surface Science*, 611, p.155667.

Makola, L. C., Moeno, S., Ouma, C.N.M., Sharma, A., Vo, D.N. and Dlamini, L.N., 2022. Facile fabrication of a metal-free 2D–2D $Nb_2CTx@g-C_3N_4$ MXene-based Schottky-heterojunction with the potential application in photocatalytic processes. *Journal of Alloys and Compounds*, 916, pp.165459–165459.

Mandor, H., El-Ashtoukhy, E-S.Z., Abdelwahab, O., Amin, N.K. and Kamel, D.A., 2022. A flow-circulation reactor for simultaneous photocatalytic degradation of ammonia and phenol using N-doped ZnO beads. *Alexandria Engineering Journal*, 61(5), pp.3385–3401.

Manna, M. and Sen, S., 2023. A novel oxygen-deficient core–shell $ZA@ZnO_{1-x}$ nanocomposite for enhanced degradation of multiple polyaromatic hydrocarbons. *Applied Surface Science*, 630, p.157523.

Mansouri, L., Tizaoui, C., Geissen, S.-U. and Bousselmi, L., 2019. A comparative study on ozone, hydrogen peroxide and UV based advanced oxidation processes for efficient removal of diethyl phthalate in water. *Journal of Hazardous Materials*, 363, pp.401–411.

Masula, K., Bhongiri, Y., Rao, G.R., Kumar, P.V., Pola, S., Basude, M., 2022. Evolution of photocatalytic activity of CeO_2–Bi_2O_3 composite material for wastewater degradation under visible-light irradiation. *Optical Materials*, 126, p.112201.

Mazellier, P. and Bolte, M., 2000. Heterogeneous light-induced transformation of 2,6-dimethylphenol in aqueous suspensions containing goethite. *Journal of Photochemistry and Photobiology A-chemistry*, 132(1-2), pp.129–135.

Meenakshi, G., Sivasamy, A., 2018. Nanorod ZnO/SiC nanocomposite: An efficient catalyst for the degradation of an endocrine disruptor under UV and visible light irradiations. *Journal of Environmental Chemical Engineering*, 6, pp.3757-3769.

Mehmood, C.T., Qazi, I.A., Baig, M.A., Arshad, M. and Quddos, A., 2015. Application of photodegraded polythene films for the treatment of Drimarene Brilliant Red (DBR) dye. *International Biodeterioration & Biodegradation*, 102, pp. 31–39.

Mestre-Martinez, R.M., Marrugo-Pautt, I., Correa-Turizo, R.R., Severiche Sierra, C.A., Baldiris-Navarro, I., 2020. Degradation of Cyanide from Gold Mining Wastewater Using Photocatalysis. *IOP Conference Series: Materials Science and Engineering*, 844, p.012012.

Miao, B., Chu, Y., Zheng, X. and Su, H., 2021. Sb_2WO_6/Bi_2WO_6 composite photocatalyst prepared by one-step hydrothermal method: Simple synthesis and excellent visible-light photocatalytic performance. *Materials Science in Semiconductor Processing*, 125, p.105636.

Miao, F., Gao, M., Yu, X., Xiao, P., Wang, M., Wang, Y., Wang, S., Wang, X., 2020. TiO_2 electrocatalysis via three-electron oxygen reduction for highly efficient generation of hydroxyl radicals. *Electrochemistry Communications*, 113, p.106687.

Mishra, P., Behera, A., Kandi, D., Ratha, S., Parida, K., 2020. Novel magnetic retrievable visible-light-driven ternary Fe_3O_4@$NiFe_2O_4$/phosphorus-doped g-C_3N_4 nanocomposite photocatalyst with significantly enhanced activity through a double-z-scheme system. *Inorganic Chemistry*, 59, pp. 4255-4272.

Mishra, S., Kumari, S., Kumar, P. and Samanta, S.K., 2021. Microwave synthesized strontium hexaferrite 2D sheets as versatile and efficient microwave catalysts for degradation of organic dyes and antibiotics. *Science of The Total Environment*, 790, p.147853.

Moses, A., Komandur, J., Maarisetty, D., Mohapatra, P., Barul, S.S., 2022. A review on photocatalytic hydrogen production potential from paper and pulp industry wastewater. *Biomass Conversion and Biorefinery*, [online] Available at: <https://doi.org/10.1007/s13399-022-02658-z> [Assessed 23 Jan 2023].

Mousavi, S.E. and Mohammadzadeh, E.S. 2020. An investigation of the ethylene glycol surfactant on the structural, microstructure, magnetic and optical properties of $SrFe_2O_4$ nanoparticles. *Journal of Magnetism and Magnetic Materials*, 495, pp.165866–165866.

Mphahlele, I.J., Malinga, S.P. and Dlamini, L.N., 2022. Combined biological and photocatalytic degradation of dibutyl phthalate in a simulated wastewater treatment plant. *Catalysts*, 12(5), p.504.

Muenhor, D., Moon, H.-B., Lee, S. and Goosey, E., 2017. Organophosphorus flame retardants (PFRs) and phthalates in floor and road dust from a manual e-waste dismantling facility and adjacent communities in Thailand. *Journal of Environmental Science and Health*, 53(1), pp.79–90.

Mukherjee, I., Cilamkoti, V., Dutta, R.K., 2021. Sunlight-driven photocatalytic degradation of ciprofloxacin by carbon dots embedded in ZnO nanostructures. *ACS Applied Nano Material*, 4, pp. 7686–7697.

Mukonza, S.S., Chaukura, N. and Mishra, A.K., 2022. Photocatalytic activity and reusability of F,Sm^{3+} Co-Doped TiO_2/MWCNTs hybrid heterostructure for efficient photocatalytic degradation of Brilliant Black Bis-Azo Dye. *Catalysts*, 13(1), p.86.

Murali, A., Sarswat, P.K. and Free, M.L., 2020. Minimizing electron-hole pair recombination through band-gap engineering in novel ZnO-CeO_2-rGO ternary

nanocomposite for photoelectrochemical and photocatalytic applications. *Environmental Science and Pollution Research*, 27(20), pp.25042–25056.

Musial, J., Mlynarczyk, D.T., Stanisz, B.J., 2023. Photocatalytic degradation of sulfamethoxazole using TiO_2-based materials – Perspectives for the development of a sustainable water treatment technology. *Science of The Total Environment*, 856, p.159122.

Nath, D., Singh, F. and Das, R., 2020. X-ray diffraction analysis by Williamson-Hall, Halder-Wagner and size-strain plot methods of CdSe nanoparticles- a comparative study. *Materials Chemistry and Physics*, 239, p.122021.

Nandi, P. and Das, D., 2019. Photocatalytic degradation of Rhodamine-B dye by stable ZnO nanostructures with different calcination temperature induced defects. *Applied Surface Science*, 465, pp.546–556.

Nawaz, A., Goudarzi, S., Saravanan, P. and Zarrin, H., 2021. Z-scheme induced $g\text{-}C_3N_4/WS_2$ heterojunction photocatalyst with improved electron mobility for enhanced solar photocatalysis. *Solar Energy,* 228, pp.53–67.

Net, S., Sempéré, R., Delmont, A., Paluselli, A. and Ouddane, B., 2015. Occurrence, fate, behavior and ecotoxicological state of phthalates in different environmental matrices. *Environmental Science & Technology*, 49(7), pp.4019–4035.

Neto, B.J.A., Gaylarde, C., Beech, I., Bastos, A.C., Silva Quaresma, V.D. and Carvalho, D.G.C., 2019. Microplastics and attached microorganisms in sediments of the Vitória bay estuarine system in SE Brazil. *Ocean & Coastal Management*, 169, pp.247–253.

Ng, K.H., Khan, M.R., Ng, Y.H., Hossain, S.S. and Cheng, C.K., 2017. Restoration of liquid effluent from oil palm agroindustry in Malaysia using UV/TiO_2 and UV/ZnO photocatalytic systems: A comparative study. *Journal of Environmental Management*, 196, pp.674-680.

North, M.L., Takaro, T.K., Diamond, M.L. and Ellis, A.K., 2014. Effects of phthalates on the development and expression of allergic disease and asthma. *Annals of Allergy, Asthma & Immunology*, 112(6), pp.496–502.

Ong, C.B., Ng, L.Y. and Mohammed, A.W., 2018. A review of ZnO nanoparticles as solar photocatalysts: Synthesis, mechanisms and applications. *Renewable and Sustainable Energy Reviews*, 81, pp.536–551.

Orroji, Y., Bahareh, T., Ali, A., Soheil, H.T., Marzieh, A., Fatemeh, F.B., Fatemeh, K., Sadegh, S., Jalal, R., Safoora, A., Mika, S., Rozhin, D., Hassan, K.M., 2021. Heterogeneous UV-switchable Au nanoparticles decorated tungstophosphoric acid/TiO_2 for efficient photocatalytic degradation process. *Chemosphere*, 281, pp.130795–130795.

Ozmihci, F., and Balkose, D., 2013. Effects of particle size and electrical resistivity of filler on mechanical, electrical, and thermal properties of linear

low density polyethylene–zinc oxide composites. *Journal of Applied Polymer Science*, 130, pp. 2734–2743.

Padervand, M., Rhimi, B., Wang, C., 2021. One-pot synthesis of novel ternary $Fe_3N/Fe_2O_3/C_3N_4$ photocatalyst for efficient removal of rhodamine B and CO_2 reduction. *Journal of Alloys and Compounds*, 852, p.156955.

Pang, X., Skillen, N., Gunaratne, N., Rooney, D.W. and Robertson, P.K.J., 2021. Removal of phthalates from aqueous solution by semiconductor photocatalysis: A review. *Journal of Hazardous Materials*, 402, p.123461.

Pang, X., Sarvothaman, V.P., Skillen, N., Wang, Z., Rooney, D.W., Ranade, V.V.and Robertson, P.K.J., 2022. Kinetic modelling of the photocatalytic degradation of Diisobutyl phthalate and coupling with acoustic cavitation. *Chemical Engineering Journal*, 444, p.136494.

Parra-Marfil, A., López-Ramón, M.V., Aguilar-Aguilar, A., García-Silva, I.A., Rosales-Mendoza, S., Romero-Cano, L.A., Bailón-García, E., Ocampo-Pérez, R., 2023. An efficient removal approach for degradation of metformin from aqueous solutions with sulfate radicals. *Environmental Research*, 217, p.114852.

Pasuk, I., Neațu, F., Neațu, Ș., Florea, M., Istrate, C.M., Pintilie, I. and Pintilie, L., 2021. Structural details of $BaTiO_3$ nano-powders deduced from the anisotropic XRD peak broadening. *Nanomaterials*, 11(5), p.1121.

Porcu, S., Secci, F. and Ricci, P.C., 2022. Advances in Hybrid Composites for Photocatalytic Applications: A Review. *Molecules*, 27(20), p.6828.

Pranoto, Purnawan, C. and Rachmawati, C., 2021. Photodegradation of Rhodamine B using composite andisoi/TiO_2. *Journal of physics*, 1912(1), pp.012039.

Qiang, Z., Liu, X., Li, F., Li, T., Zhang, M., Singh, H., Huttula, M. and Cao, W., 2021. Iodine doped Z-scheme $Bi_2O_2CO_3/Bi_2WO_6$ photocatalysts: Facile synthesis, efficient visible light photocatalysis, and photocatalytic mechanism. *Chemical Engineering Journal*, 403, p.126327.

Qin, Y., Li, H., Lu, J., Ding, Y., Ma, C., Liu, X., Meng, M. and Yan, Y., 2020. Fabrication of Bi_2WO_6/In_2O_3 photocatalysts with efficient photocatalytic performance for the degradation of organic pollutants: Insight into the role of oxygen vacancy and heterojunction. *Advanced Powder Technology,* 31(7), pp.2890–2900.

Qu, J., Xia, W., Qian, X., Wu, Y., Li, J., Wen, S. and Xu, S., 2022. Geographic distribution and time trend of human exposure of Di(2-ethylhexyl) phthalate among different age groups based on global biomonitoring data. *Chemosphere*, 287, p.132115.

Rachna, Rani, M. and Shanker, U., 2020. Sunlight assisted degradation of toxic phenols by zinc oxide doped prussian blue nanocomposite. *Journal of Environmental Chemical Engineering*, 8(4), p.104040.

Rachna, Rani, M. and Shanker, U., 2019. Sunlight active ZnO@FeHCF nanocomposite for the degradation of bisphenol A and nonylphenol. *Journal of Environmental Chemical Engineering*, 7(3), p.103153.

Raizada, P., Kumari, J., Shandilya, P., Dhiman, R., Pratap Singh, V. and Singh, P., 2017. Magnetically retrievable Bi_2WO_6/Fe_3O_4 immobilized on graphene sand composite for investigation of photocatalytic mineralization of oxytetracycline and ampicillin. *Process Safety and Environmental Protection*, 106, pp.104–116.

Raizada, P., Parwaz Khan, A.A.and Singh, P., 2020. Construction of carbon nanotube mediated Fe doped graphitic carbon nitride and Ag_3VO_4 based Z-scheme heterojunction for H_2O_2 assisted 2,4 dimethyl phenol photodegradation. *Separation and Purification Technology*, 247, p.116957.

Raji, R. and Gopchandran, K.G., 2017. ZnO nanostructures with tunable visible luminescence: Effects of kinetics of chemical reduction and annealing. *Journal of Science: Advanced Materials and Devices*, 2(1), pp.51–58.

Ramachandra, M., Rajendra Pai, S.D.K., Jadan, R., J., UC., Sephan, P., 2020. Improved photocatalytic activity of g-C_3N_4/ZnO: A potential direct Z-scheme nanocomposite. *Chemistry Select*, 5, pp.11986-11995.

Rambabu, K., Bharath, G., Banat, F. and Show, P.L., 2021. Green synthesis of zinc oxide nanoparticles using Phoenix dactylifera waste as bioreductant for effective dye degradation and antibacterial performance in wastewater treatment. *Journal of Hazardous Materials*, 402, p.123560.

Rani, M. and Shanker, U., 2018. Insight into the degradation of bisphenol A by doped ZnO@ZnHCF nanocubes: High photocatalytic performance. *Journal of Colloid and Interface Science*, 530, pp.16–28.

Rapti, I., Kosma, C., Albanis, T., Konstantinou, I., 2022. Solar photocatalytic degradation of inherent pharmaceutical residues in real hospital WWTP effluents using titanium dioxide on a CPC pilot scale reactor. *Catalysis Today*, [online] Available at: <https://doi.org/10.1016/j.cattod.2022.08.026> [Assessed 23 Jan 2023].

Rashid, J., Karim, S., Kumar, R., Barakat, M.A., Akram, B., Hussain, N., Bin, H.B. and Xu, M., 2020. A facile synthesis of bismuth oxychloride-graphene oxide composite for visible light photocatalysis of aqueous diclofenac sodium. *Scientific Reports*, 10(1), p.14191.

Reddy, N.S., Reddy, N.L., Nissy, S.M., Pallavi, G., Vangalapati, M., 2020. Degradation of dicofol by synthesized ZnO nanoparticles as catalyst. *Materials Today:Proceedings*, 26, pp.1694-170.

Riaz, U., Gaffar, S., Hauser, K. and Yan, F., 2023. Visible-light induced degradation of diphenyl urea and polyethylene using polythiophene decorated $CuFe_2O_4$ nanohybrids. *Scientific Reports*, 13, pp.4975–4975.

Rupa, E.J., Kaliraj, L., Abid, S., Yang, D.C. and Jung, S.K., 2019. Synthesis of a zinc oxide nanoflower photocatalyst from sea buckthorn fruit for degradation of industrial dyes in wastewater treatment. *Nanomaterials*, 9(12), p.1692.

Rusek, J., Baudys, M., Toker, O., Paušová, Š., Paz, Y., Krýsa, J., 2023. Composite TiO_2 films modified by CeO_2 and SiO_2 for the photocatalytic removal of water pollutants. *Photochemical & Photobiological Sciences,* 21, pp.2127-2138.

Sabri, M., Habibi-Yangjeh, A., Ghosh, S., 2020. Novel $ZnO/CuBi_2O_4$ heterostructures for persulfate-assisted photocatalytic degradation of dye contaminants under visible light. *Journal of Photochemistry and Photobiology A: Chemistry*, 391, p.112397.

Sarani, M., Bazookar Joshaghani, A., Najafidoust, A., Abbasi Asl, E., Kazemi Hakki, H., Bananifard, H. and Sillanpaa, M., 2021. Sun-light driven photo degradation of organic dyes from wastewater on precipitation Ag_2CrO_4 over SiO_2-aerogel and nano silica. *Inorganic Chemistry Communications*, 133, p.108877.

Saravanakumar, K. and Park, C.M., 2021. Rational design of a novel $LaFeO_3/g\text{-}C_3N_4/BiFeO_3$ double Z-scheme structure: Photocatalytic performance for antibiotic degradation and mechanistic insight. *Chemical Engineering Journal*, 423, p.130076.

Sathasivam, M., Aparna, R.S.L., Prasad, R.G.S.V. and Cheok, K.Y., 2013. Photocatalytic effect of titanium dioxide nanoparticles and effect of copper as a dopant in degradation of dibutyl pthalate and butylhydroxyanisole. *Journal of Bionanoscience*, 7(5), pp.568–574.

Sattam, F.A., Masood, A.A., Abdulaziz, I.A., Abdulrhman, F.A., Khaled, T.A., Sultan, A., Sharma, K., Ahmed, N.A., 2022. Constructing a $ZnO/CuCo_2O_4$ p-n heterojunction photocatalyst for efficiently hexavalent chromium–phenol detoxification and nitrogen fixation. *Journal of Physics and Chemistry of Solids*, 172, pp.111057–111057.

Selvaraj, S., Patrick D, S., Vangari, G.A., Mohan, M.K., S, P. and C, M., 2022. Facile synthesis of Sm doped ZnO nanoflowers by Co-precipitation method for enhanced photocatalytic degradation of MB dye under sunlight irradiation. *Ceramics International*.48 (19), pp.29049-29058.

Sharma, S., Sharma, A., Chauhan, N.S., Tahir, M., Kumari, K., Mittal, A., Kumar, N., 2023. $TiO_2/Bi_2O_3/PANI$ nanocomposite materials for enhanced photocatalytic decontamination of organic pollutants. *Inorganic Chemistry Communications*, 146, p.110093.

Shivani, Gadi, R., Sharma, S.K., Mandal, T.K., Kumar, R., Mona, S., Kumar, S. and Kumar, S., 2018. Levels and sources of organic compounds in fine ambient aerosols over national capital region of India. *Environmental Science and Pollution Research*, 25(31), pp.31071–31090.

Shivani, V., Harish, S., Archana, J., Navaneethan, M., Ponnusamy, S. and Hayakawa, Y., 2019. Highly efficient 3-D hierarchical Bi_2WO_6 catalyst for environmental remediation. *Applied Surface Science*, 488, pp.696–706.

Shuai, W.; Liu, C.; Fang, G.; Zhou, D.; Gao, J.,2018. Nano-α-Fe_2O_3 enhanced photocatalytic degradation of diethyl phthalate ester by citric Acid/UV (300–400 nm): A mechanism study. *Journal of Photochemistry and Photobiology A: Chemistry*, 360, pp.78–85.

Škrbić, B.J., Ji, Y., Đurišić-Mladenović,N. and Zhao, J., 2016. Occurence of the phthalate esters in soil and street dust samples from the Novi Sad city area, Serbia, and the influence on the children's and adults' exposure. *Journal of Hazardous Materials*, 312, pp.272–279.

Smith, M., Love, D.C., Rochman, C.M. and Neff, R.A., 2018. Microplastics in seafood and the implications for human health. *Current Environmental Health Reports*, 5(3), pp.375–386.

Song, C., Wang, L., Ren, J., Lv, B., Sun, Z., Yan, J., Li, X. and Liu, J., 2015. Comparative study of diethyl phthalate degradation by UV/H_2O_2 and UV/TiO_2: kinetics, mechanism, and effects of operational parameters. *Environmental Science and Pollution Research*, 23(3), pp.2640–2650.

Soufi, A., Hajjaoui, H., Elmoubarki, R., Abdennouri, M. and Barka, N., 2022. Sol-gel auto-combustion synthesis of $Cu_{1-x}Mg_xFe_2O_4$ nanoparticles and their heterogenous Fenton-like activity towards tartrazine. *Inorganic Chemistry Communications*, 142, pp.109717–109717.

Sravandas, P. and Alexander, L.K., 2021. Facile hydrothermal synthesis and sonophotocatalytic performance of novel Bi_2WO_6 structure on the degradation of rhodamine B. *Materials Today: Proceedings*, 46, pp.2925–2929.

Subramaniam, M.N., Goh, P.S., Lau, W.J., Ismail, A.F., 2021. Photocatalytic degradation of aerobically treated palm oil mill effluent using titania nanotubes prepared via hydrothermal technique. *Materials Today:Proceeding*, 46, pp.1813-1817.

Subramonian, W., Wu, T.Y. and Chai, S.P., 2017. Photocatalytic degradation of industrial pulp and paper mill effluent using synthesized magnetic Fe_2O_3 - TiO_2: Treatment efficiency and characterizations of reused photocatalyst. *Journal of Environmental Management*, 187, pp.298–310.

Sulaiman, N.H., Ghazali, M.J., Yunas, J., Rajabi, A., Majlis, B.Y. and Razali, M., 2018. Synthesis and characterization of $CaFe_2O_4$ nanoparticles via co-precipitation and auto-combustion methods. *Ceramics International*, 44(1), pp.46–50.

Sun, D.S., Yan, X. and Xue, W., 2012. Oxidative degradation of dimethyl phthalate (DMP) by persulfate catalyzed by Ag^+ combined with microwave irradiation. *Advanced Material Research*, 610-613, pp.1209–1212.

Sun, H., Zou, C., Liao, Y., Tang, W., Huang, Y., Chen, M., 2023. Modulating charge transport behavior across the interface via g-C_3N_4 surface discrete modified BiOI and Bi_2MoO_6 for efficient photodegradation of glyphosate. *Journal of Alloys and Compound*, 935, p.168208.

Sun, J., Shen, C., Guo, J., Guo, H., Yin, Y., Xu, X., Fei, Z., Liu, Z. Wen, X., 2021. Highly efficient activation of peroxymonosulfate by Co_3O_4/Bi_2WO_6 p-n heterojunction composites for the degradation of ciprofloxacin under visible light irradiation. *Journal of Colloid and Interface Science*, 588, pp.19–30.

Sun, J., Shen, C., Guo, J., Guo, H., Yin, Y., Xu, X., Fei, Z., Liu, Z. and Niu, C.G., 2021. Highly efficient activation of peroxymonosulfate by Co_3O_4/Bi_2WO_6 p-n heterojunction composites for the degradation of ciprofloxacin under visible light irradiation. *Journal of Colloid and Interface Science*, 588, pp.19–30.

Sun, L., Wang, Y., Qiao, L., Qu, Y., Bai, L. and Jing, L., 2017. Enhanced photoelectrochemical activities for water oxidation and phenol degradation on WO_3 nanoplates by transferring electrons and trapping holes. *Scientific Reports*, 7(1), pp.1303–1303.

Sun, X., Huang, L., Wang, G., Feng, H., Zhou, S., Zhao, R., Wang, D., Li, Z., 2022. Efficient degradation of tetracycline under the conditions of high-salt and coexisting substances by magnetic $CuFe_2O_4$/g-C_3N_4 photo-Fenton process. *Chemosphere*, 308, p.136204.

Sun, X., Huang, L., Wang, G., Feng, H., Zhou, S., Zhao, R., Wang, D. and Li, Z., 2022. Efficient degradation of tetracycline under the conditions of high-salt and coexisting substances by magnetic $CuFe_2O_4$/g-C_3N_4 photo-Fenton process. *Chemosphere*, 308, pp.136204–136204.

Suryavanshi, R.D., Babar, P.V., Narewadikar, N.A. and Rajpure, K.Y., 2022. Sunlight assisted novel spray deposited Bi_2WO_6 photoelectrode for degradation of organic pollutants. *Journal of Physics and Chemistry of Solids*, 168, pp.110786–110786.

Swamy, C.K., Hezam, A., Mavinakere Ramesh, A., Habbanakuppe Ramakrishnegowda, D., K. Purushothama, D., Krishnegowda, J., Kanchugarakoppal S., R. and Shivanna, S., 2021. Microwave hydrothermal synthesis of copper induced ZnO/gC_3N_4 heterostructure with efficient photocatalytic degradation through S-scheme mechanism. *Journal of Photochemistry and Photobiology A: Chemistry*, 418, p.113394

Tan, S.Y., Chong, W.C., Sumathi, S., Pang, Y.L., Sim, L.C. and Mahmoudi, E., 2023. Optimisation of aqueous phase low density polyethylene degradation by graphene oxide-zinc oxide photocatalysts. *Chemical Engineering Research & Design*, 190, pp.550–565.

Tan, T.L., Lee, K.L., Chin, W.L., Zhang, Z. and Suraya, S.R., 2020. Photocatalytic degradation mechanisms of dimethyl phthalate esters by

MWCNTs-anatase TiO_2 nanocomposites using the UHPLC/Orbitrap/MS technique. *Advanced Powder Technology*, 31, pp.533–547.

Tan, T.L.; Lai, C.W.; Hong, S.L.; Rashid, S.A., 2018. New insights into the photocatalytic endocrine disruptors dimethyl phathalate esters degradation by UV/MWCNTs-TiO$_2$ nanocomposites, *Journal of Photochemistry and Photobiology A: Chemistry*, 364, pp.177–189.

Tan, W., Cheng, Y.B. and McNeill, C.R., 2020. Direct assessment of structural order and evidence for stacking faults in layered hybrid perovskite films from X-ray scattering measurements. *Journal of materials chemistry. A, Materials for energy and sustainability*, 8(25), pp.12790–12798.

Teodóra, N., Shahnazarova, G., Lukács, I.E., Szabó, A., Hernadi, K., Igricz, T., László, K., Szilágyi, I.M. and Pokol, G., 2019. Effect of pH in the Hydrothermal Preparation of Bi_2WO_6 Nanostructures. *Materials*, 12(11), pp.1728–1728.

Theerakarunwong, C.D., Phothi, R., 2018. Community Refinery Wastewater Photodegradation by Fe-Doped TiO_2 Films. *Water, Air and Soil Pollution*, 229, p.231.

Thomas, R.T., Nair, V., Sandhyarani, N., 2013. TiO_2 nanoparticle assisted solid phase photocatalytic degradation of polythene film: A mechanistic investigation. *Colloids and Surface A: Physicochemical and Engineering Aspects*, 422, pp.1-9.

Tofa, T.S., Kunjali, K.L., Paul, S. and Dutta, J., 2019. Visible light photocatalytic degradation of microplastic residues with zinc oxide nanorods. *Environmental Chemistry Letters*, 17, pp.1341-1346.

Trandafilović, L.V., Jovanović, D.J., Zhang, X., Ptasińska, S. and Dramićanin, M.D., 2017. Enhanced photocatalytic degradation of methylene blue and methyl orange by ZnO:Eu nanoparticles. *Applied Catalysis B: Environmental*, 203, pp.740–752.

Trung, D.Q., Tran, M.T., Tu, N., Thu, L.T.H., Huyen, N.T., Hung, N.D., Viet, D.X., Kien, N.D.T. and Huy, P.T., 2022. Synthesis, structural and optical properties of ZnS/ZnO heterostructure-alloy hexagonal micropyramids. *Optical Materials*, 125, pp.112077–112077.

Uddin, M. T., Hoque, M. E., Bhoumick, M.C., 2020. Facile one-pot synthesis of heterostructure SnO_2/ZnO photocatalyst for enhanced photocatalytic degradation of organic dye. *RSC Advances*, 10, pp.23554-23565.

Vadivel, S., Maruthamani, D., Habibi-Yangjeh, A., Paul, B., Siddhartha, S.D. and Selvam, K., 2016. Facile synthesis of novel $CaFe_2O_4$/g-C_3N_4 nanocomposites for degradation of methylene blue under visible-light irradiation. *Journal of Colloid and Interface Science*, 480, pp.126–136.

Vavilapalli, D.S., Melvin, A.A., Bellarmine, F., Mannam, R., Velaga, S., Poswal, H.K., Dixit, A., Ramachandra Rao, M.S. and Singh, S., 2020. Growth

of sillenite $Bi_{12}FeO_20$ single crystals: structural, thermal, optical, photocatalytic features and first principle calculations. *Scientific Reports*, 10, p.22052.

Vela, N., Calín, M., Yáñez-Gascón, M.J., Garrido, I., Pérez-Lucas, G., Fenoll, J. and Navarro, S., 2018. Photocatalytic oxidation of six endocrine disruptor chemicals in wastewater using ZnO at pilot plant scale under natural sunlight. *Environmental Science and Pollution Research*, 25(35), pp.34995–35007.

Venkata Reddy, Ch., Koutavarapura, R., Rahava Reddy, K., Shetti, N.P., Aminabhavi, T.M., Shim, J., 2020. Z-scheme binary 1D $ZnWO_4$ nanorods decorated 2D $NiFe_2O_4$ nanoplates as photocatalysts for high efficiency photocatalytic degradation of toxic organic pollutants from wastewater. *Journal of Environmental Management*, 268, p.110677.

Venkataramana, C., Botsa, S.M., Shyamala, P. and Muralikrishna, R., 2021. Photocatalytic degradation of polyethylene plastics by $NiAl_2O_4$ spinels-synthesis and characterization. *Chemosphere*, 265, p.129021.

Vione, D., Sur, B., Dutta, B.K., Maurino, V. and Minero, C., 2011. On the effect of 2-propanol on phenol photonitration upon nitrate photolysis. *Journal of Photochemistry and Photobiology A-chemistry*, 224(1), pp.68–70.

Vuppala, S. and Stoller, M., 2020. Nanocomposites photocatalysis application for the purification of phenols and real olive mill wastewater through a sequential process. *Applied Sciences,* 10, pp.1–12.

Wan, C., Zhou, L., Sun, L., Xu, L., Cheng, D., Chen, F., Zhan, X. and Yang, Y., 2020. Boosting visible-light-driven hydrogen evolution from formic acid over AgPd/2D $g-C_3N_4$ nanosheets Mott-Schottky photocatalyst. *Chemical Engineering Journal*, 396, pp.125229–125229.

Wang, C., Du, L., Xing, X., Feng, D., Tian, Y., Li, Z., Zhao, X. and Stephen, 2022. Radial ZnO nanorods decorating Co_3O_4 nanoparticles for highly selective and sensitive detection of the 3-hydroxy-2-butanone biomarker. *Nanoscale*, 14(2), pp.482–491

Wang, D., Han, D., Shi, Z., Wang, J., Yang, J., Li, X. and Song, H., 2018. Optimized design of three-dimensional multi-shell $Fe_3O_4/SiO_2/ZnO/ZnSe$ microspheres with type II heterostructure for photocatalytic applications. *Applied Catalysis B: Environmental*, 227, pp.61–69.

Wang, G., Chen, Q., Liu, Y., Ma, D., Xin, Y., Ma, X. and Zhang, X., 2018. In situ synthesis of graphene/WO_3 co-decorated TiO_2 nanotube array photoelectrodes with enhanced photocatalytic activity and degradation mechanism for dimethyl phthalate. *Chemical Engineering Journal*, 337, pp.322–332.

Wang, G., Zhang, Q., Chen, Q., Ma, X., Xin, Y., Zhu, X., Ma, D., Cui, C., Zhang, J. and Xiao, Z., 2019. Photocatalytic degradation performance and mechanism of dibutyl phthalate by graphene/TiO_2 nanotube array photoelectrodes. *Chemical Engineering Journal*, 358, pp.1083–1090.

Wang, H., Zhang, T., Ji, Y., Lu, J., 2023. Photodegradation of phenylurea herbicides sensitized by norfloxacin and the influence of natural organic matter. *Journal of Hazardous Materials*, 442, p.130135.

Wang, J., Tang, L., Zeng, G., Deng, Y., Liu, Y., Wang, L., Zhou, Y., Guo, Z., Wang, J., Zhang, C., 2017. Atomic scale g-C_3N_4/$Bi_2WO_6$2D/2D heterojuction with enhanced photocatalytic degradation of ibuprofen under visible light irradiation. *Applied Catalysis B: Environmental*, 209, pp.285-294.

Wang, T., Feng, C., Liu, J., Wang, D., Hu, H., Hu, J., Chen, Z., Xue, G., 2021. Bi_2WO_6 hollow microspheres with high specific surface area and oxygen vacancies for efficient photocatalysis N_2 fixation. *Chemical Engineering Journal*, 414, pp.128827–128827.

Wang, Q., Wang, L., Zheng, S., Tan, M., Yang, L., Fu, Y., Li, Q., Du, H. and Yang, G., 2023. The strong interaction and confinement effect of Ag@NH_2-MIL-88B for improving the conversion and durability of photocatalytic Cr(VI) reduction in the presence of a hole scavenger. *Journal of Hazardous Materials*, 451, p.131149.

Wang, Y., Xing, Z., Zhao, H., Song, S., Liu, M., Li, Z. and Zhou, W., 2021. MoS_2@In_2S_3/Bi_2S_3 Core-shell dual Z-scheme tandem heterojunctions with Broad-spectrum response and enhanced Photothermal-photocatalytic performance. *Chemical Engineering Journal*, 431, p.133355.

Wang, Y., Yang, L., Zou, R., Lan, J., Yao, A., Xiao, H., Lin, S., 2022. Z-scheme CeO_2/Ag/CdS heterojunctions functionalized cotton fibers as highly recyclable and efficient visible light-driven photocatalysts for the degradation of dyes. *Journal of Cleaner Production*, 380, p. 135012.

Wong, H., Zhou, J., Zhang, J., Jin, H., Kakushima, K. and Iwai, H., 2014. The interfaces of lanthanum oxide-based subnanometer EOT gate dielectrics. *Nanoscale Research Letters*, 9(1), p.472.

Wu, J., Li, J., Gary, O., Chen, Z., 2023. Toward green nano adsorbents and catalysts: Highly active Fe/Mn nanoparticles for enhanced oxidation of oxytetracycline and levofloxacin. *Journal of Colloid and Interface Science*, 632, pp. 299-310.

Wu, L., Yan, X., Yang, L., Shen, S., Yang, S., He, L., Chen, Y., Yang, S., Zhang, Z., 2023. Simultaneous efficient degradation and dechlorination of chloramphenicol using UV/sulfite reduction: Mechanisms and product toxicity. *Chemical Engineering Journal*, 452, p.139161.

Wu, Q. and Song, Y., 2023. Enhanced interfacial charge migration through fabrication of p-n junction in $ZnIn_2S_4$/$NiFe_2O_4$/biochar composite for photocatalytic doxycycline hydrochloride degradation. *Chemical Engineering Journal*, 453, p.139745.

Xia, P., Urso, M. and Pumera, M., 2023. Metal oxide single-component light-powered micromotors for photocatalytic degradation of nitroaromatic pollutants. *npj Clean Water*, 6, p.21.

Xiao, J., Dong, W., Song, C., Yu, Y., Zhang, L., Li, C. and Yin, Y., 2015. Nitrogen oxide gas-sensing characteristics of hierarchical Bi_2WO_6 microspheres prepared by a hydrothermal method. *Materials Science in Semiconductor Processing*, 40, pp.463–467.

Xing, G., Zhang, L., Zhao, Y., Li, S., Li, T., Lv, T., Yu, C., Zhao, C., 2023. Sb_2X_3 (X = S, Se) nanowires/graphene aerogel monoliths for effective photodegradation of dye/drug under visible light irradiation. *Journal of Molecular Structure*, 1274, p.134409.

Xu, J., Gao, Q., Bai, X., Wang, Z. and Zhu, Y., 2019. Enhanced visible-light-induced photocatalytic degradation and disinfection activities of oxidized porous g-C_3N_4 by loading Ag nanoparticles. *Catalysis Today*, 332, pp.227–235.

Xu, L., Qi, L., Sun, Y. Gong, H., Chen, Y., Pei, C., Gan, L., 2020. Mechanistic studies on peroxymonosulfate activation by g-C_3N_4 under visible light for enhanced oxidation of light-inert dimethyl phthalate. *Chinese Journal of Catalysis*, 41, pp. 322–332.

Xu, L., Yang, X., Guo, Y., Ma, F., Guo, Y., Yuan, X. and Huo, M., 2010. Simulated sunlight photodegradation of aqueous phthalate esters catalyzed by the polyoxotungstate/titania nanocomposite. *Journal of Hazardous Materials*, 178(1-3), pp.1070–1077.

Xu, L.; Qi, L.; Sun, Y.; Gong, H.; Chen, Y.; Pei, C.; Gan, L., 2020. Mechanistic studies on peroxymonosulfate activation by g-C_3N_4 under visible light for enhanced oxidation of light-inert dimethyl phthalate. *Chinese Journal Catalysis*, 41, pp.322–332.

Xu, M., Deng, Y., Li, S., Zheng, J., Liu, J., Tremblay, P., Zhang, T., 2023. Bacterial cellulose flakes loaded with Bi_2MoO_6 nanoparticles and quantum dots for the photodegradation of antibiotic and dye pollutants. *Chemosphere*, 312, p.137249.

Xu, P., Wang, P., Wang, Q., Wei, R., Li, Y., Xin, Y., Zheng, T., Hu, L., Wang, X., Zhang, G., 2021. Facile synthesis of Ag_2O/ZnO/rGO heterojunction with enhanced photocatalytic activity under simulated solar light: Kinetics and mechanism. *Journal of Hazardous Materials*, 403, p.124011.

Xu, Q., Zhang, L., Yu, J., Wageh, S., Al-Ghamdi, A.A. and Jaroniec, M., 2018. Direct Z-scheme photocatalysts: Principles, synthesis, and applications. *Materials Today*, 21(10), pp.1042–1063.

Xu, Z., Xiong, X., Zhao, Y., Xiang, W. and Wu, C., 2020. Pollutants delivered every day: Phthalates in plastic express packaging bags and their leaching potential. *Journal of Hazardous Materials*, 384, p.121282.

Xue, H., Li, J., Zhang, G., Li, M., Liu, B. and Kang, C., 2023. Hydroxyl radical dominated ibuprofen degradation by UV/percarbonate process: Response surface methodology optimization, toxicity, and cost evaluation. *Chemosphere*, pp.138681–138681.

Yadav, A., Raj, A., Purchase, D., Ferreira, L.F.R., Saratale, G.D. and Bharagava, R.N., 2019. Phytotoxicity, cytotoxicity and genotoxicity evaluation of organic and inorganic pollutants rich tannery wastewater from a Common Effluent Treatment Plant (CETP) in Unnao district, India using Vigna radiata and Allium cepa. *Chemosphere*, 224, pp.324–332.

Yan, Y., Shi, M., Zou, Y., Wei, Y., Chen, L., Fan, C., Yang, R. and Xu, Y., 2019. Tunable hierarchical porous carbon aerogel/graphene composites cathode matrix for Li-S batteries. *Journal of Alloys and Compounds*, 791, pp.952–961.

Yang, L., Liang, L., Wang, L., Zhu, J., Gao, S., Xia, X., 2019. Accelerated photocatalytic oxidation of carbamazepine by a novel 3D hierarchical protonated $g-C_3N_4$/BiOBr heterojunction: Performance and mechanism. *Applied Surface Science*, 473, pp.527-539.

Yang, Q., Guo, E., Lu, Q., Wei, M., Ma, J., Xu, X., Li, Q., 2021. Hierarchical $CoTiO_3$@NiO core–shell sub-microbelts as direct Z-scheme photocatalyst for efficient visible-light-driven tetracycline degradation. *Applied Surface Science*, 546, p.148892.

Yang, X., Xing, X.J., Liu, Y., Mu, C., Hao Van Bui, Zhang, Z.W., Agathopoulos, S., Xu, X. and Mahmood, N., 2021. A new thermal degradation mechanism of red $Sr_2Si_5N_8$:Eu phosphor: From the view of microstructural evolution. *Optical Materials*, 121, p.111506.

Yang, Y., Zhao, S., Bi, F., Chen, J., Li, Y., Cui, L., Xu, J. and Zhang, X., 2022. Oxygen-vacancy-induced O_2 activation and electron-hole migration enhance photothermal catalytic toluene oxidation. *Cell reports physical science*, 3(8), pp.101011.

Yang, Z., Liu, P., Wang, J., Ding, L., Li, L., Jia, H., Wang, T., Guo, X., Gao, S., 2023. Microplastics-derived dissolved organic matters accelerate photodegradation of sulfamethazine in wastewater ultraviolet disinfection process. *Chemical Engineering Journal*, 454, p.140301.

Ye, Q., Liu, C., Wu, P., Wu, J., Lin, L., Li, Y., Ahmed, Z., Rehman, S., Zhu, N., 2023. Insights into photocatalytic degradation of phthalate esters over $MSnO_3$ perovskites (M = Mg, Ca): Experiments and density functional theory. *Journal of Environmental Management*, 307, p.114511.

Ye, Q., Liu, C., Wu, P., Wu, J., Lin, L., Li, Y., Ahmed, Z., Rehman, S. and Zhu, N., 2022. Insights into photocatalytic degradation of phthalate esters over $MSnO_3$ perovskites (M = Mg, Ca): Experiments and density functional theory. *Journal of Environmental Management*, 307, p.114511.

Yi, K., Lei, M., Peng, L., Chen, A. and Luo, S., 2021. Sunlight-driven degradation of diethyl phthalate via magnetically modified biochar catalysts in water: Internal electron transfer mechanism. *Chemosphere*, 269, p.129366.

Yi, W. and Yan, C., 2013. A Novel visible-light-driven photocatalyst: Pt surface modified Bi_2WO_6-WO_3 composite. *Applied Mechanics and Materials*, 448-453, pp.178–181.

Yuan, X., Shen, D., Zhang, Q., Zou, H., Liu, Z., Peng, F., 2019. Z-scheme Bi_2WO_6/$CuBi_2O_4$ heterojunction mediated by interfacial electric field for efficient visible-light photocatalytic degradation of tetracycline. *Chemical Engineering Journal*, 369, pp. 292-301.

Yuan, X., Shen, D.-Y., Zhang, Q., Zou, H., Liu, Z. and Yu, H., 2019. Z-scheme Bi_2WO_6/$CuBi_2O_4$ heterojunction mediated by interfacial electric field for efficient visible-light photocatalytic degradation of tetracycline. *Chemical Engineering Journal*, 369, pp.292–301.

Zafar, M., Amjad, M., Tabassum, M., Ahmad, I. and Zubair, M., 2018. $SrFe_2O_4$ nanoferrites and SrFe2O4/ground eggshell nanocomposites: Fast and efficient adsorbents for dyes removal. *Journal of Cleaner Production*, 199, pp.983–994.

Zarezadeh, S., Habibi-Yangjeh, A. and Mousavi, M., 2019. BiOBr and AgBr co-modified ZnO photocatalyst: A novel nanocomposite with p-n-n heterojunctions for highly effective photocatalytic removal of organic contaminants. *Journal of Photochemistry and Photobiology A: Chemistry*, 379, pp.11–23.

Zhang, D., Lv, S., Luo, Z., 2019. A study on the photocatalytic degradation performance of a $[KNbO_3]_{0.9}$ -$[BaNi_{0.5}Nb_{0.5}O3-_\delta]_{0.1}$ perovskite. *Royal Society of Chemistry*, 10, pp.1275-1280.

Zhang, G., Chen, D., Li, N., Xu, Q., Li, H., He, J., Lu, J., 2019. Fabrication of Bi_2MoO_6/ZnO hierarchical heterostructures with enhanced visible-light photocatalytic activity. *Applied Catalysis B: Environmental*, 250, pp.313-324.

Zhang, L., Wang, F., Ji, Y., Jiao, J., Zou, D., Liu, L., Shan, C., Bai, Z. and Sun, Z., 2014. Phthalate esters (PAEs) in indoor PM_{10}/$PM_{2.5}$ and human exposure to PAEs via inhalation of indoor air in Tianjin, China. *Atmospheric Environment*, 85, pp.139–146.

Zhang, M., Lai, C., Li, B., Huang, D., Zeng, G., Xu, P., Qin, L., Liu, S., Lai, C., Yi, H., Li, M., Chu, C. and Chen, Z., 2019. Rational design 2D/2D BiOBr/CDs/g-C_3N_4 Z-scheme heterojunction photocatalyst with carbon dots as solid-state electron mediators for enhanced visible and NIR photocatalytic activity: Kinetics, intermediates, and mechanism insight. *Journal of Catalysis*, 369, pp.469–481.

Zhang, P., Shi, M., Liu, Y., Fan, M. and Dong, Y., 2016. Sr doping magnetic CaO parcel ferrite improving catalytic activity on the synthesis of biodiesel by transesterification. *Fuel*, 186, pp.787–791.

Zhang, Q., Han, F.X., Yan, Y., Dai, Q., Proctor, G., Cheah, P., Avijit, P., Chandra, R.P., Kang, N., Hu, M. and Yao, B., 2019. Preparation and properties of visible light responsive RGO/In_2TiO_5 nanobelts for photocatalytic degradation of organic pollutants. *Applied Surface Science*, 485, pp.547–553.

Zhang, R., Han, Q., Li, Y., Zhang, T., Liu, Y., Zeng, K., Zhao, C., 2020. Solvothermal synthesis of a peony flower-like dual Z-scheme $PANI/BiOBr/ZnFe_2O_4$ photocatalyst with excellent photocatalytic redox activity for organic pollutant under visible-light. *Separation and Purification Technology*, 234, p.116098.

Zhang, S., Wei, Y., Metz, J., He, S., Alvarez, P.J.J. and Long, M., 2022. Persistent free radicals in biochar enhance superoxide-mediated Fe(III)/Fe(II) cycling and the efficacy of CaO_2 Fenton-like treatment. *Journal of Hazardous Materials*, 421, pp.126805–126805.

Zhang, T., Wang, Y., Xie, X., Shao, Y., Zeng, Y., Zhang, S., Yan, Q. and Li, Z., 2021. Dual Z-scheme 2D/3D carbon-bridging modified g-$C_3N_4/BiOI$-Bi_2O_3 composite photocatalysts for effective boosting visible-light-driven photocatalytic performance. *Separation and Purification Technology*, 277, p.119443.

Zhang, X., Wang, Y., Wei, C., Hu, Y., 2022. One-step synthesis of N-doped porous wall TiO_2 nanotube arrays for efficient removal of dibutyl phthalate under visible light. *Journal of Photochemistry and Photobiology A: Chemistry,* 430, p.113975.

Zhang, X.J., Yu, S., Liu, Y., Zhang, Q. and Zhou, Y., 2017. Photoreduction of non-noble metal Bi on the surface of Bi_2WO6 for enhanced visible light photocatalysis. *Applied Surface Science*, 396, pp.652–658.

Zhang, Y., Jiao, Y., Li, Z., Tao, Y. and Yang, Y., 2021. Hazards of phthalates (PAEs) exposure: A review of aquatic animal toxicology studies. *Science of The Total Environment*, 771, p.145418.

Zhang, Y., Lin, L., Cao, Y., Chen, B., Zheng, L. and Ge, R.S., 2009. Phthalate levels and low birth weight: a nested case-control study of chinese newborns. *The Journal of Pediatrics,* 155(4), pp.500–504.

Zhang, Y., Ma, H., Chen, X., Wang, W., Li, F., Qiang, T., Shen, Y., Cong, Y., 2023. CQDs improved the photoelectrocatalytic performance of plasma assembled WO_3/TiO_2-NRs for bisphenol A degradation. *Journal of Hazardous Materials*, 443, p.130250.

Zhang, Y., Tan, P., Yang, L., Zhou, B.P. and Pan, J., 2022. Electrostatic self-assembly of 2D/2D $Bi_2WO_6/ZnIn_2S_4$ heterojunction with enhanced

photocatalytic degradation of tetracycline hydrochloride. *Journal of Solid State Chemistry*, 314, pp.123408–123408.

Zhang, Y., Yu, H., Li, S., Wang, L., Huang, F., Guan, R., Li, J., Jiao, Y. and Sun, J., 2021. Rapidly degradation of di-(2-ethylhexyl) phthalate by Z-scheme Bi_2O_3/TiO_2@reduced graphene oxide driven by simulated solar radiation. *Chemosphere*, 272, p.129631.

Zhang, Y., Zhou, B., Chen, H., Yuan, R., 2023. Heterogeneous photocatalytic oxidation for the removal of organophosphorus pollutants from aqueous solutions: A review. *Science of the Total Environment,* 856, p.159048.

Zhao, B., Shao, N., Chen, X., Ma, J., Gao, Y. and Chen, X., 2023. Construction of novel type II heterojunction WO_3/Bi_2WO_6 and Z-scheme heterojunction CdS/Bi_2WO_6 photocatalysts with significantly enhanced photocatalytic activity for the degradation of rhodamine B and reduction of Cr(VI). *Colloids and Surfaces A: Physicochemical and Engineering Aspects*, 663, pp.131072–131072.

Zhao, F., Gao, D., Zhu, X., Dong, Y., Liu, X. and Li, H., 2022. Rational design of multifunctional C/N-doped ZnO/Bi_2WO_6 Z-scheme heterojunction for efficient photocatalytic degradation of antibiotics. *Applied Surface Science*, 587, pp.152780–152780.

Zhao, L., Liu, Y., Xi, X., Shen, Y., Wang, J., Liu, Y. and Nie, Z., 2022. $Bi/Bi_2O_3/WO_3$ composite: A bifunctional plasmonic heterostructure for detection and degradation pollutions in wastewater. *Journal of environmental chemical engineering*, 10(3), pp.107643–107643.

Zhao, W., Wei, Z., Zhang, X., Ding, M., Huang, S. and Yang, S., 2020. Magnetic recyclable $MnFe_2O_4/CeO_2/SnS_2$ ternary nano-photocatalyst for photo-Fenton degradation. *Applied Catalysis A: General*, 593, p.117443.

Zhao, Y., Zhang, F., Zhang, J., Zou, K., Zhang, J., Chen, C., Long, M., Zhang, Q., Wang, J., Zheng, C., Shou, W. and Wang, D., 2021. Preparation of composite photocatalyst with tunable and self-indicating delayed onset of performance and its application in polyethylene degradation. *Applied Catalysis B: Environmental*, 286, p.119918.

Zhou, C., Zeng, G., Huang, D., Wang, F., Cheng, M., Liu, Y., Xiong, W., Yang, Y., Song, B., Wang, W., Shao, B. and Li, Z., 2020. Distorted polymeric carbon nitride via carriers transfer bridges with superior photocatalytic activity for organic pollutants oxidation and hydrogen production under visible light. *Journal of Hazardous Materials*, 386, pp.121947–121947.

Zhou, T., Shi, J., Li, G., Liu, B., Hu, B., Che, G., Liu, C., Wang, L., 2023. Advancing n-π* electron transition of carbon nitride via distorted structure and nitrogen heterocycle for efficient photodegradation: Performance, mechanism and toxicity insight. *Journal of Colloid and Interface Science*, 632, pp. 285-298.

Zhou, T., Wang, J., Chen, S., Bai, J., Li, J., Zhang, Y., Li, L., Xia, L., Rahim, M., Xu, Q., Zhou, B., 2020. Bird-nest structured ZnO/TiO_2 as a direct Z-scheme photoanode with enhanced light harvesting and carriers kinetics for highly efficient and stable photoelectrochemical water splitting. *Applied Catalysis B: Environmental*, 267, p.118599.

Zhou, X., Wu, S., Li, C., Yan, F., Bai, H., Shen, B., Zeng, H., Zhai, J., 2019. Piezophototronic effect in enhancing charge carrier separation and transfer in $ZnO/BaTiO_3$ heterostructures for high-efficiency catalytic oxidation. *Nano Energy*, 66, p.104127.

Zhu, D. and Zhou, Q., 2019. Action and mechanism of semiconductor photocatalysis on degradation of organic pollutants in water treatment: A review. *Environmental Nanotechnology, Monitoring & Management*, 12, p.100255.

Zhu, L., Li, H., Xia, P., Liu, Z., Xiong, D., 2018. Hierarchical ZnO decorated with CeO_2 nanoparticles as the direct Z-Scheme heterojunction for enhanced photocatalytic activity. *ACS Applied Materials & Interfaces,* 10, pp. 39679–39687.

Zhu, P., Luo, D., Duan, M., Feng, L., Zhang, S. and Liu, M., 2022. Based on a dual Z-scheme heterojunction and magnetically separable $CoFe_2O_4/g$-$C_3N_4/Bi_4Ti_3O_{12}$ flower-like composite for efficient visible-light photocatalytic degradation of organic pollutants. *Journal of Alloys and Compounds*, 911, p.164907.

Zhu, Y., Cui, Y., Xiao, B., Ou-yang, J., Li, H., Chen, Z., 2021. Z-scheme 2D/2D g-C_3N_4/Sn_3O_4 heterojunction for enhanced visible-light photocatalytic H_2 evolution and degradation of ciprofloxacin. *Materials Science in Semiconductor Processing*, 129, p.105767.

Zia, J. and Riaz, U., 2020. Studies on the spectral, morphological and magnetic properties of PCz-PPy copolymer encapsulated $BaFe_2O_4$ nanohybrids. *Journal of Materials Science: Materials in Electronics*, 31(24), pp.22856–22865.

Detected intermediates in photodegradation of DMP using GC-MS analysis.

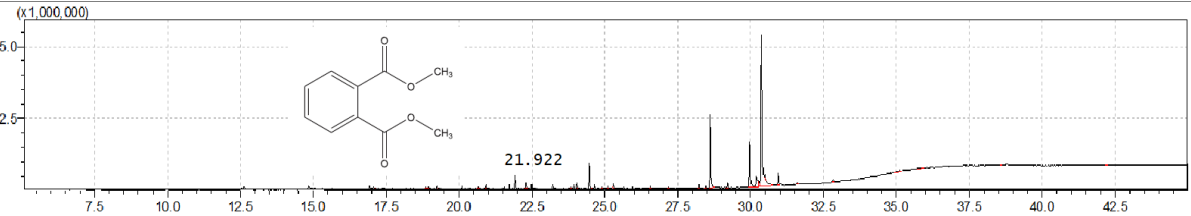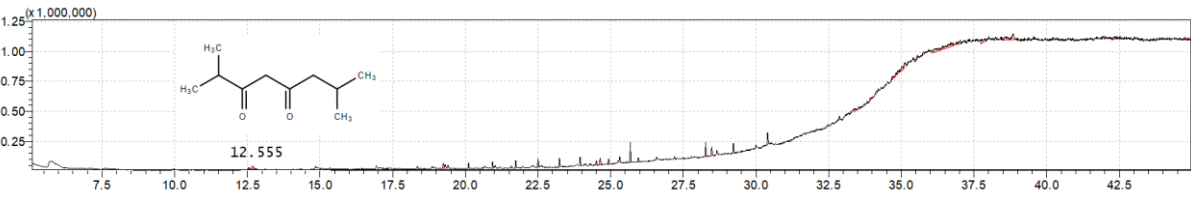Table A: Detected intermediates with their relative molecular formula, mass spectrum and retention time.

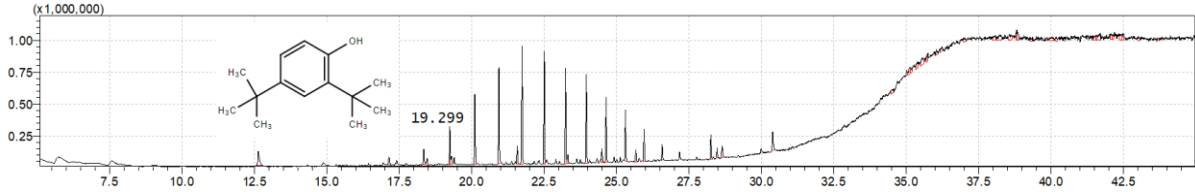| Compound	Molecular formula	GC-MS spectra	Mass spectrum (m/z)
Dimethyl phthalate	$C_{10}H_{10}O_4$		194.18
3,5-Octanedione, 2,7-dimethyl-	$C_{10}H_{18}O_2$		170.25

Table A: Continued.
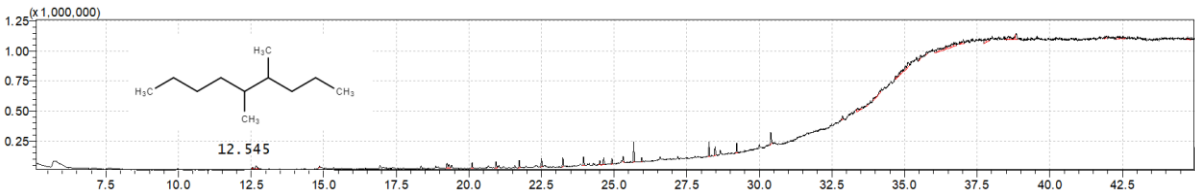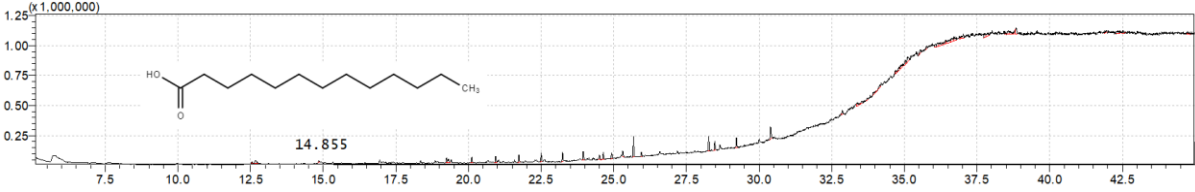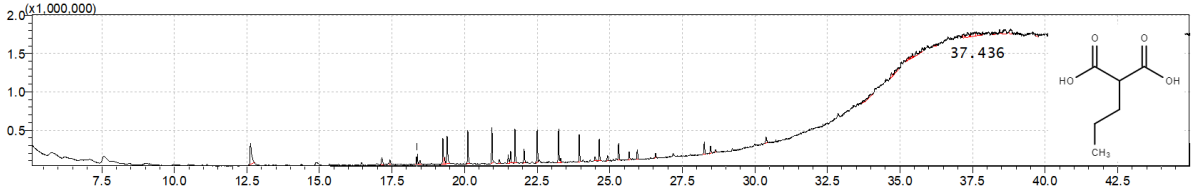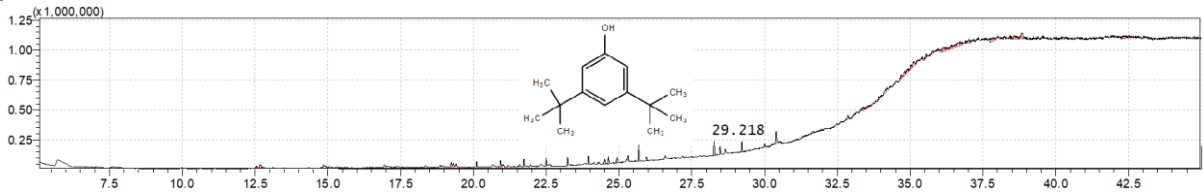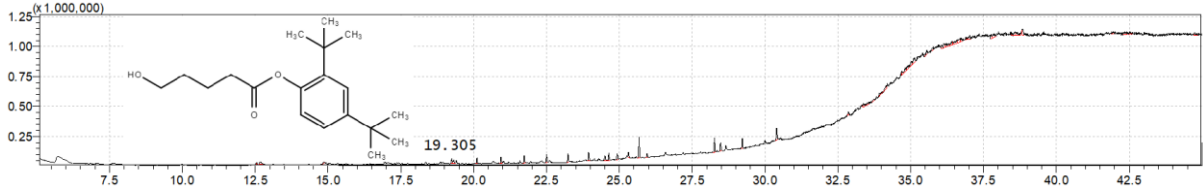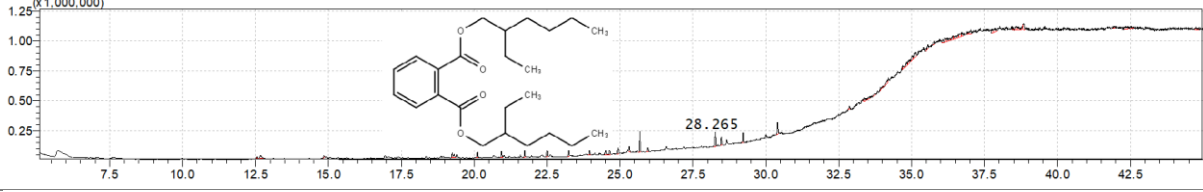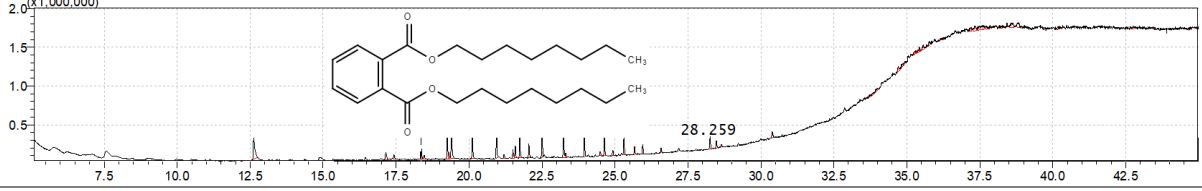
Nonane, 4,5-dimethyl-	$C_{11}H_{24}$		156.31
Tridecanoic acid	$C_{13}H_{26}O_2$		214.34
Propanedioic acid, propyl-	$C_6H_{10}O_4$		146.14
2,4-Di-tert-butylphenol	$C_{14}H_{22}O$		206.32

Table A: Continued.

Phenol, 3,5-bis(1,1-dimethylethyl)-	$C_{14}H_{22}O$		206.32
Pentanoic acid, 5-hydroxy-, 2,4-di-t-butylphenyl esters	$C_{19}H_{30}O_3$		306.44
Bis(2-ethylhexyl) phthalate	$C_{24}H_{38}O_4$		390.56
Di-n-octyl phthalate	$C_{24}H_{38}O_4$		390.56

APPENDIX B

Phytotoxicity test of DMP using *Vigna Radiata*.

Figure B: Radicle length of *Vigna radiata* irrigating by (left) distilled water as control; (middle) degraded DMP solution via 10Sr20BWZ photocatalysis and (right) untreated DMP solution.

LIST OF PUBLICATION

1. Chin, Y.H., Sin, J.C., Lam, S.M., Zeng, H., Lin, H., Li, H., Huang, L., Mohamed, A.R., 2022. 3-D/3-D Z-Scheme heterojunction composite formed by Marimo-like Bi_2WO_6 and Mammillaria-like ZnO for expeditious sunlight photodegradation of dimethyl phthalate. *Catalysts*, 12(11), p. 1427.

2. Chin, Y.H., Sin, J.C. and Lam, S.M., Zeng, H., Lin, H., Li, H., Mohamed, A.R., 2022. 0-D/3-D heterojunction composite constructed by decorating transition metal oxide nanoparticle on peony-like ZnO hierarchical microstructure for improved photodegradation of palm oil mill effluent. *Optik*, 260, p. 169098.

3. Chin, Y.H., Sin, J.C. and Lam, S.M., 2021. Facile synthesis of hierarchical ZnO structure for photocatalytic degradation of dimethyl phthalate. *IOP Conference Series: Earth and Environmental Science*, 945, p. 012017.

4. Sin, J.C., Chin, Y.H., Lam, S.M., Zeng, H., Lin, H., Li, H., Mohamed, A.R., 2022. MXenes and their composites: a promising material for hydrogen storage. *Mxenes and their composites*, pp. 397-422.

5. Lam, S.M., Yong, Z.J., Choong, M.K., Sin, J.C., Chin, Y.H., Tan, J.H., 2021. Construction of MXene-Based Photocatalysts. *Mxene-Based Photocatalysts*, pp. 69-101.